



**HAL**  
open science

# Impact of air infiltration on buildings' performance : focus on the experimental study within timber-frame walls

Nolwenn Hurel

► **To cite this version:**

Nolwenn Hurel. Impact of air infiltration on buildings' performance : focus on the experimental study within timber-frame walls. Civil Engineering. Université Grenoble Alpes, 2016. English. NNT : 2016GREAA018 . tel-01528910

**HAL Id: tel-01528910**

**<https://theses.hal.science/tel-01528910v1>**

Submitted on 30 May 2017

**HAL** is a multi-disciplinary open access archive for the deposit and dissemination of scientific research documents, whether they are published or not. The documents may come from teaching and research institutions in France or abroad, or from public or private research centers.

L'archive ouverte pluridisciplinaire **HAL**, est destinée au dépôt et à la diffusion de documents scientifiques de niveau recherche, publiés ou non, émanant des établissements d'enseignement et de recherche français ou étrangers, des laboratoires publics ou privés.

## **THÈSE**

Pour obtenir le grade de

### **DOCTEUR DE L'UNIVERSITÉ GRENOBLE ALPES**

Spécialité : **Génie Civil et Sciences de l'Habitat**

Arrêté ministériel : 7 août 2006

Présentée par

**Nolwenn HUREL**

Thèse dirigée par **Monika Woloszyn** et  
co-dirigée par **Mickaël Pailha**

préparée au sein du **Laboratoire LOCIE UMR CNRS 5271**  
dans **l'École Doctorale SISEO**

## **Impact of air infiltration on buildings' performance: focus on the experimental study within timber-frame walls**

Impact des infiltrations d'air sur les performances des bâtiments : focus sur l'étude expérimentale dans les parois ossature bois

Thèse soutenue publiquement le **21 Novembre 2016**,  
devant le jury composé de :

**M. Eric ARQUIS**

Professeur, Bordeaux INP, Président

**M. Christian INARD**

Professeur, Université de La Rochelle, Rapporteur

**M. Mickaël PAILHA**

Maître de Conférences, Université Savoie Mont Blanc, Encadrant

**M. Staf ROELS**

Professeur, Katholieke Universiteit Leuven (Belgique), Rapporteur

**M. Gilles RUSAOUEN**

Maître de Conférences, Université de Lyon, Examineur

**M. Max H. SHERMAN**

Directeur de Recherche, Lawrence Berkeley National Laboratory (USA),  
Examineur

**Mme Monika WOLOSZYN**

Professeure, Université Savoie Mont Blanc, Directrice de thèse









# Remerciements

( Acknowledgement )

Cette thèse fut pour moi une riche expérience non seulement d'un point de vue scientifique mais également humain. Je souhaite remercier du fond du cœur toutes les personnes qui m'ont encadrée, soutenue, aidée, ou qui ont simplement contribué à mon bien-être durant ces trois années.

En premier lieu, je tiens à remercier très chaleureusement ma directrice de thèse, Monika Woloszyn qui m'a donné sa confiance pour mener à bien ce projet et qui a toujours su se rendre disponible lorsque j'en avais besoin. Ses nombreux conseils, son expertise scientifique mais également ses grandes qualités humaines ont été plus que précieux pour moi. Un grand merci également à mon co-encadrant Mickaël Pailha pour son soutien, sa disponibilité et son aide très utile, notamment sur les expériences PIV.

J'adresse aussi mes sincères remerciements à Christian Inard et Staf Roels pour avoir accepté d'être les rapporteurs de cette thèse et pour leurs commentaires et échanges très constructifs qui ont permis d'améliorer la qualité scientifique et la compréhension de ce manuscrit. Je souhaite également exprimer ma profonde reconnaissance envers les autres membres du jury, Eric Arquis en qualité de président, Max Sherman et Gilles Rusaouën qui m'ont fait l'honneur d'assister à ma soutenance et qui ont pris le temps d'examiner mon travail.

Cette thèse a été principalement réalisée au laboratoire LOCIE de l'Université Savoie Mont Blanc et financée par l'Agence Nationale de la Recherche à travers le projet MOB-AIR. Je remercie vivement l'équipe technique pour son support inestimable durant ces trois années. Un très grand merci tout particulièrement à Thierry qui a mis toute son énergie, son savoir-faire et sa patience pour m'aider à construire les différents dispositifs expérimentaux. Nous avons presque toujours réussi à « tenir Murphy à distance », et travailler ensemble a été tout aussi instructif qu'agréable pour moi. Merci également à Cédric pour sa précieuse aide sur l'instrumentation et à Jonathan pour son investissement et ses explications sur la partie chimique liée à la fluorescéine. Je tiens aussi à remercier l'équipe administrative : Elisabeth, Martine et Isabelle qui m'ont donné un grand confort de travail.

Un travail de recherche mêle souvent des problèmes de différentes spécialités, et il a été précieux pour moi de pouvoir échanger avec d'autres scientifiques, experts sur mes problématiques, ou me donnant simplement du recul sur mes travaux. Je remercie pour cela tout particulièrement Yves Gonthier, Evelyne Gonze, Michel Ondarts, Géraldine Garnier, Serge Buseyne, Denis Covalet, Anne-Cécile Grillet, Benoît Stutz, Simon Rouchier mais aussi des amis (post-) doctorants Clément Belleudy, Gaëlle Guyot et Wout Parys.

Je tiens également à remercier chaleureusement les stagiaires qui se sont impliqués dans ce projet sur de plus ou moins longues durées. Merci à Alice Falatin à la bonne humeur communicative pour sa précieuse aide sur la finalisation du banc expérimental et le développement d'un protocole de mesure de la concentration de fluorescéine. Merci à Guillaume Lasjuilliaris et Rudy Forey pour leur grand investissement sur la caractérisation des capteurs, l'instrumentation des parois et leur aide durant les tests. Enfin *Grazie mille* à Marco Freschi pour son travail consciencieux sur une partie des tests de fluorescéine à petite échelle, et son aide lors des expériences utilisant la thermographie infrarouge et la PIV. J'espère qu'il a été aussi agréable pour vous que pour moi de travailler ensemble.

J'ai également eu la chance d'effectuer un séjour au Lawrence Berkeley National Laboratory financé par la bourse Exploradoc de la Région Rhône Alpes. Je tiens à remercier très sincèrement Max Sherman et Iain Walker pour m'avoir accueillie et encadrée durant ces 4 mois. Ce fût à la fois un privilège et un plaisir de me joindre à leur équipe de recherche, de bénéficier de leur grande expertise dans le domaine de l'étanchéité à l'air, et de découvrir le fonctionnement d'un autre laboratoire. Merci aussi à Brennan Less pour sa précieuse aide sur l'utilisation des logiciels REGCAP et R. Enfin, ce séjour n'aurait pas été aussi inoubliable sans la présence de Sara Ticci, mais aussi Ryan, Tim, Stéphanie, Simone, toute l'équipe de Triple Rock, ma formidable *landlady* Renate Lohmann et tant d'autres. *Thank you* !

Un merci du fond du cœur à mes amis de longue date qui m'apportent toujours autant de joie et de soutien: Louise, Benjamin, Ludovic, Guillaume, Nicolas, Victoria, Betty, Amélie, Marta, Leah. A tous les doctorants du LOCIE et autres amis de Chambéry qui ont toute ma gratitude pour avoir rendu ces trois années exceptionnelles pour moi et ponctuées de mémorables sorties en montagne. Je pense notamment à Ranime, Léa, Nicolas, Lauren, Cédric, Benoît, Elsa, Thomas, Téo, Jean-François, Lorena, Zakaria, Ismail, Yannis, Bastian, Mohammad, Lama, Lucile et Alessandro. Un merci tout particulier à mes coloc' Marion et Clément qui ont mis tant de sourires et d'énergie dans mon quotidien.

Mes plus douces pensées vont à ma famille si chère à mon cœur. En particulier un énorme merci à mes parents. Quelques mots ne seront jamais assez pour décrire tout ce que vous m'avez transmis durant ces 25 années, mais Papa, pour ta curiosité scientifique, Maman pour ta créativité, ce travail est en partie le vôtre. A mes deux sœurs génialissimes en tous points, Laura et Morgane, je vous suis immensément reconnaissante pour tout ce que vous apportez dans ma vie. Une dernière pensée enfin pour mes deux adorés (plus si) petits prince et princesse : Pierre-Louis et Antonia.

*"Les yeux sont aveugles.  
Il faut chercher avec le cœur."*

- Antoine de Saint-Exupéry

# Abstract

Poor airtightness in buildings can lead to an over-consumption of energy and to many issues such as moisture damage and poor indoor climate. Timber frame constructions are particularly subject to air leakage and further knowledge in this field is needed to meet the regulation requirements tightened by the development of low-energy and passive houses. This study focuses on the impact of air infiltration on the buildings' performance, both at the building and the wall assembly scales.

The air infiltration through the envelope can disrupt the proper functioning of mechanical ventilation and increase the global energy load. This issue was first investigated numerically at the building scale on a wide range of housing and weather conditions. Simplified models working across the whole airtightness spectrum were established for the inclusion of natural infiltration in buildings' total ventilation rate calculations. The airtightness was then considered at a smaller scale with the experimental characterization of timber frame wall assemblies, components and construction details, in particular with an original test set-up built for this purpose. A number of pressurization tests enabled to quantify the additional leakage air flow induced by specific airtightness defects and may be of use for building scale numerical simulations.

The impact of air infiltration on the hygro-thermal performance of a wall is closely linked to the air dispersion inside it, but there is a lack of experimental studies and methods for the air path investigation. A new technique has therefore been developed, consisting in an innovative use of fluorescein micro-particles as tracer inside the insulation material. It was first applied to specific configurations: straight/angled air channels in contact with porous media. A simple analysis of the fluorescein concentration mappings enabled to investigate the impact of parameters such as the flow velocity, the insulation material and the geometry on the air infiltration in the glass wool, and gave evidences of phenomena such as the appearance of thin air gaps between the components of the wall. A fluorescein transport model was developed and coupled to a CFD model for finer analysis.

Finally a case study on simple wall assemblies was carried out to compare experimental techniques, to verify their applicability to the air path study and to provide data for possible numerical model validation. The air dispersion at the inlet/outlet of the insulation was studied with both infrared thermography and the PIV. The air path inside the insulation layer was investigated using three experimental approaches: a temperature monitoring with thermocouples; a relative humidity monitoring with capacitive sensors SHT 75; and the use of fluorescein tracer micro-particles. The respective benefits and limitations of the various methods were identified to help in the selection of the most appropriate one for further studies.





# Résumé

( French abstract )

Une mauvaise étanchéité à l'air dans un bâtiment peut entraîner des surconsommations énergétiques et poser un certain nombre de problèmes tels que l'apparition de moisissures dans les murs ou encore une mauvaise qualité de l'air intérieur. Les constructions à ossature bois sont particulièrement sujettes aux infiltrations d'air, d'où la nécessité de mieux comprendre ces phénomènes et leurs conséquences afin que ces bâtiments puissent respecter les normes d'étanchéité de plus en plus strictes. Cette étude contribue par plusieurs aspects et à différentes échelles à l'évaluation de l'impact des infiltrations d'air sur les performances d'un bâtiment.

Les infiltrations d'air à travers l'enveloppe peuvent perturber le bon fonctionnement de la ventilation mécanique et augmenter les pertes thermiques. Cette problématique est d'abord traitée numériquement à l'échelle du bâtiment, avec l'étude d'une grande variété de maisons et de conditions météorologiques. Des modèles simplifiés applicables à tout niveau d'étanchéité ont été établis pour la prise en compte des infiltrations naturelles dans les calculs de débit total de ventilation. Une plus petite échelle est ensuite considérée pour l'étude de l'étanchéité à l'air, avec la caractérisation expérimentale de parois ossature bois, de matériaux et de détails de construction, notamment grâce à la construction d'un banc d'essai adapté. Un certain nombre de tests de pressurisation ont permis de quantifier les fuites d'air induites par des défauts d'étanchéité spécifiques et peuvent être utilisés pour les simulations numériques à l'échelle du bâtiment.

L'impact des infiltrations d'air sur les performances hygrothermiques d'une paroi est intimement lié à la dispersion de l'air à l'intérieur de celle-ci, mais il y a actuellement un manque d'études et de techniques expérimentales pour la déterminer. Une nouvelle méthode a donc été développée, à savoir l'utilisation de microparticules de fluorescéine comme traceur à l'intérieur des isolants. L'établissement de cartographies de la concentration en fluorescéine a permis d'étudier l'impact de certains paramètres tels que la vitesse d'air, le matériau isolant ou encore la géométrie sur les infiltrations d'air, et a mis en évidence des phénomènes tels que l'apparition de lames d'air entre les composants de la paroi. Par ailleurs un modèle du transport des particules de fluorescéine a été développé et couplé à un modèle CFD pour des analyses plus fines du chemin de l'air.

Enfin, une étude de cas a été effectuée sur des parois simplifiées afin de comparer les différentes méthodes expérimentales, de vérifier leur applicabilité à l'étude du chemin de l'air, et d'obtenir des données pour la validation de modèles numériques. La dispersion de l'air en entrée/sortie de l'isolant a été étudiée par thermographie infrarouge et PIV. Le chemin de l'air à l'intérieur de l'isolant a lui été étudié par 3 techniques : des mesures de température avec des thermocouples ; d'humidité relative avec des capteurs capacitifs SHT 75 ; et l'utilisation de microparticules de fluorescéine. Les avantages et inconvénients de chaque méthode ont été identifiés pour aider à sélectionner la plus adaptée pour de futures études.



# Résumé détaillé

(French detailed summary)

## 1. Introduction

Dans un contexte global de raréfaction des ressources, de réchauffement climatique menaçant l'équilibre de la planète et d'une population mondiale en forte croissance, un défi majeur se présente à nous pour repenser notre relation à l'énergie, favoriser l'utilisation de ressources renouvelables, mais aussi diminuer nos consommations. Le secteur du bâtiment représente à lui seul entre 20 et 40% de la demande énergétique mondiale dans les pays développés et a donc un rôle important à jouer dans cette transition. La construction de maisons à basse consommation, passives, voire à énergie positive se répand à travers le monde, poussée par des réglementations thermiques de plus en plus contraignantes, à l'image de la RT 2012 en France.

Une bonne étanchéité à l'air de l'enveloppe est un des critères déterminants pour atteindre ces niveaux de performance, les infiltrations d'air pouvant être responsables jusqu'à 25% des consommations de chauffage. Elles ont d'autres effets néfastes tels que le risque de moisissure dû à des infiltrations d'air humide, une dégradation de l'isolation sonore et potentiellement de la qualité de l'air intérieur, ainsi qu'une perturbation du bon fonctionnement de la ventilation mécanique avec l'apparition de zones sous-ventilées. Une perméabilité minimale à l'air est donc recherchée, mais il est actuellement impossible d'atteindre une parfaite étanchéité à l'air. Afin de comprendre et pouvoir prédire l'impact de ces infiltrations sur les performances d'un bâtiment, des études à la fois numériques et expérimentales sont nécessaires.

La construction à ossature bois présente de nombreux avantages qui justifient son essor actuel mais elle est particulièrement sensible à cette problématique d'étanchéité à l'air. Elle est en effet structurellement plus complexe que la maçonnerie, avec la présence de plusieurs couches, membranes et de multiples joints. Ce secteur est donc devant la nécessité d'optimiser le processus d'étanchéification pour suivre les réglementations de plus en plus contraignantes sans y consacrer du temps et des moyens excessifs. Un projet ANR « MOB-AIR » (Maîtriser les transferts d'AIR et leur impact sur le comportement hygrothermique des Maisons à Ossature Bois) rassemble des centres de recherche, des centres techniques et des bureaux d'études pour travailler sur cette problématique.

L'étude présentée ici s'inscrit dans le cadre de ce projet. Son objectif est de contribuer à l'évaluation de l'impact des infiltrations d'air sur les performances d'un bâtiment. Après la présentation de la littérature consacrée aux études expérimentales, une étude numérique est effectuée sur une grande variété de maisons et de conditions météorologiques afin d'établir des modèles simplifiés pour la prise en compte des infiltrations naturelles dans le calcul des débits globaux de ventilation. La problématique de l'étanchéité à l'air est ensuite abordée à une plus petite échelle avec des mesures de perméabilité sur différentes parois ossatures bois, matériaux et détails de constructions. Enfin,

une attention particulière est portée au chemin de l'air à l'intérieur de la paroi. Une méthode expérimentale est développée et testée, utilisant des microparticules traceuses qui se déposent dans l'isolant le long du passage de l'air. Un modèle de filtration est implémenté pour faire le lien entre la cartographie des concentrations de particules mesurées et les champs de vitesse d'air dans la paroi. Cette technique est ensuite comparée à d'autres méthodes expérimentales et à des résultats numériques lors d'une étude de cas.

## **2. Revue des méthodes expérimentales et des études en laboratoire sur l'étanchéité à l'air des bâtiments : focus sur les constructions à ossature bois**

### **2.1. Méthodes expérimentales pour l'étude de l'étanchéité à l'air d'une paroi**

Un certain nombre de méthodes expérimentales permettent l'étude de l'étanchéité à l'air de l'enveloppe des bâtiments, des parois ou des composants de celle-ci. En fonction de l'échelle considérée mais aussi de l'objectif recherché, le choix de la technique la plus appropriée peut varier. Un tableau résumant les caractéristiques, les avantages et les limites de ces différentes méthodes est présenté ci-dessous.

Pour des tests réalisés in situ la méthode la plus répandue pour déterminer le débit des infiltrations d'air hors ventilation consiste à effectuer un test de pressurisation avec une porte soufflante en suivant une norme telle que l'EN ISO 9972. Des paliers de pressions sont imposés entre l'extérieur et l'intérieur du bâtiment ( $\Delta P$ ) et le débit d'air induit ( $Q$ ) est mesuré. Il est ainsi possible d'obtenir une loi débit-pression caractérisant la perméabilité de l'enveloppe:

$$Q = c. \Delta P^n$$

Cette méthode permet de comparer facilement les niveaux d'étanchéité à l'air de différents bâtiments entre eux, mais aussi par rapport aux valeurs seuils imposées par certaines normes. Cependant, si d'importants écarts de pression sont nécessaires pour s'affranchir de l'effet du vent et diminuer les incertitudes de mesure, ils entraînent également un risque de déformation artificielle des défauts d'étanchéité.

L'utilisation de gaz traceurs permet en revanche une caractérisation de la perméabilité à l'air dans des conditions réelles de pression. Le débit d'infiltration est déduit de l'évolution de la concentration du gaz dans le temps. Les mesures sont cependant dépendantes des conditions météorologiques le jour du test. De plus il est à noter que cette technique convient davantage aux petits volumes puisque le gaz doit initialement être mélangé de manière homogène avec l'air intérieur.

L'approche acoustique est une autre alternative pour des mesures in situ en conditions naturelles. Elle se base sur une mesure de l'atténuation d'un son lors de son passage à travers une paroi et présente l'avantage de sa simplicité de mise en œuvre et d'un faible coût matériel. Elle est difficilement applicable à l'échelle de l'enveloppe mais peut convenir pour des études plus locales. Un travail préalable, expérimental ou théorique, est cependant nécessaire pour obtenir une valeur de référence correspondant à une paroi parfaitement étanche.

Pour une détection des zones de défauts d'étanchéité par lesquels l'air entre ou sort de la paroi, la thermographie infrarouge ou l'utilisation d'un générateur de fumée sont utilisés à la fois pour un diagnostic in situ et pour des tests en laboratoire. La thermographie infrarouge est la technique la plus répandue car elle ne nécessite pas de mettre sous pression le bâtiment. Une caméra capture l'énergie infrarouge émise et réfléchiée par une surface et la convertit en un champ de température. Plus l'écart de température entre les deux côtés de la paroi est important, plus il est facile de visualiser les infiltrations et meilleure est la précision de la mesure. La visualisation des défauts par la génération de fumée est facile à mettre en œuvre en complément d'un test de pressurisation mais donne une information seulement qualitative.

En ce qui concerne les mesures expérimentales en laboratoire sur la problématique de l'étanchéité à l'air, les méthodes précédemment mentionnées sont également utilisées pour des études plus locales, notamment le test de pressurisation grâce à la construction de caissons étanches.

Afin d'identifier le chemin de l'air à l'intérieur de la paroi, il est possible de placer un relativement grand nombre de capteurs de température et/ou d'humidité entre les couches. En imposant une atmosphère différente en amont de la paroi, le passage de cet air par exemple plus chaud ou plus humide dans la paroi peut être enregistré par ces capteurs. Cette technique est cependant intrusive et basée sur des mesures locales.

Enfin, dans les années 80 des études utilisant l'interférométrie holographique ont également été effectuées afin de visualiser l'écoulement à proximité de défauts d'étanchéité. Cette technique permet de mieux comprendre l'impact des infiltrations sur la circulation de l'air intérieur mais elle est cependant complexe à mettre en œuvre et donne des résultats sous forme d'hologrammes qui peuvent être difficiles à interpréter.

Plusieurs de ces techniques sont utilisées dans cette étude. Comme présenté dans le Chapitre 4, des tests de pressurisation sont effectués pour une caractérisation globale de l'étanchéité à l'air de certaines compositions de paroi, matériaux et détails de construction. Concernant l'étude du chemin de l'air dans la paroi, un manque d'études et de techniques disponibles a été souligné. Une nouvelle approche utilisant des microparticules traceuses est donc développée et testée dans le Chapitre 5. Enfin, dans le chapitre 6, cette nouvelle technique est comparée avec l'utilisation de capteurs de température et d'humidité relative dans une étude de cas. La thermographie infrarouge est également utilisée pour des mesures complémentaires sur la dispersion de l'air à l'entrée/sortie de l'isolant. Ces résultats sont comparés avec les champs de vitesse mesurés par PIV (Particle Image Velocimetry), une technique de laboratoire courante mais dont l'utilisation pour ce type d'application est également innovante.

Ces tests en laboratoire ont nécessité la construction de bancs expérimentaux ainsi qu'une instrumentation permettant de mesurer des températures, humidités relatives, pressions différentielles, débits volumiques et vitesses d'air. Une revue non exhaustive des dispositifs expérimentaux pour l'étude des transferts d'air-chaleur-humidité a servi d'inspiration pour le design et la construction d'un nouveau caisson expérimental présenté dans le paragraphe 4.1.2. Une étude détaillée de l'instrumentation mise en œuvre a également permis une familiarisation avec les différentes technologies de capteurs, et dans certains cas, la sélection de la plus appropriée, comme les thermocouples pour les mesures de température dans la paroi.

Méthode	In situ	Lab.	Frequ.	Objectifs	Echelle	Paramètres	Avantages	Limites
Test de pressurisation	x		++	Caractérisation de l'étanchéité à l'air	pièce / zone / bâtiment	- $\Delta P$ (généralement entre 10 et 100 Pa) - Débit des infiltrations d'air	- Indépendant des conditions climatiques - Très répandu: exigé dans certaines normes	- Ouvertures artificiellement déformées ( $\Delta P \neq$ conditions naturelles)
		x	+		paroi / composant	- $\Delta P$ (potentiellement > 500 Pa) - Débit des infiltrations d'air	- Contrôle des conditions limites - Possibilité d'atteindre la rupture - Possibilité de modéliser les défauts d'étanchéité	- Plus éloigné des conditions réelles - Complexe à mettre en œuvre (caissons expérimentaux)
Approche acoustique	x	x	-		paroi / composant	-Perte de transmission sonore menant au calcul du débit des infiltrations d'air	- Débit d'infiltration calculé pour des pressions usuelles (naturelles) - Mesures rapides - Economique: peu d'équipement	- Travail en amont nécessaire (mesure en laboratoire ou étude théorique) - Peu étudié
Gaz traceur	x		+	Mesure du taux de renouvellement d'air	pièce / zone / petit bâtiment	- Concentration en gaz menant au calcul du débit des infiltrations d'air	- Débit d'infiltration calculé pour des pressions usuelles (naturelles)	- Dépendant des conditions climatiques - Adapté pour de petits volumes (mélange homogène initial) - Complexe à mettre en œuvre
Capteurs de température et d'humidité		x	-	Cartographie du passage de l'air dans la paroi	paroi	- Température - Humidité	- Possibilité d'étudier le chemin des infiltrations d'air dans la paroi	- Méthode intrusive - Mesures locales - Complexe à mettre en œuvre
Thermographie infrarouge	x	x	++	Détection des défauts d'étanchéité	façade de bâtiment / paroi / composant	Energie infrarouge émise par une surface menant au champ de température apparente	- Facilité de mise en œuvre - Très répandu	- L'interprétation nécessite une certaine expérience - Température apparente (dépendante de l'émissivité du matériau) - Etude seulement surfacique - important $\Delta T$ nécessaire entre l'intérieur et l'extérieur
Générateur de fumée	x	x	+		pièce / zone / bâtiment	Diagnostic visuel	- Facilité de mise en œuvre	- Informations qualitatives - Surpression nécessaire
Interférométrie holographique	x	x	-	Etude de l'écoulement résultant des infiltrations d'air	Défaut d'étanchéité	Diagnostic visuel	- Non-intrusif	- Complexe à mettre en œuvre - Interprétation difficile

## 2.2. Tests d'étanchéité sur les parois à ossature bois

Il existe une large variété de compositions de parois à ossature bois, avec au minimum trois couches :

- Une isolation thermique incorporée entre la structure bois. Différents isolants peuvent être choisis tels que la laine de verre, la fibre de bois, la cellulose, etc. Les poutres en bois sont les éléments porteurs et elles sont habituellement espacées de 40 à 60 cm.
- Un parement extérieur augmente la résistance aux vents latéraux. Il est généralement constitué de panneaux de particules tels que l'OSB (oriented strand board)
- Un parement intérieur généralement en plâtre.

Différents éléments peuvent être ajoutés à cet assemblage de base. Le pare-vapeur a pour but d'empêcher l'humidité de pénétrer dans la paroi. C'est une membrane importante pour la protection de la paroi puisque la baisse de température à travers celle-ci peut entraîner de la condensation entre deux matériaux. Une lame d'air entre le parement intérieur et le pare-vapeur est recommandée pour éviter les percements de cette membrane.

Un bardage peut également être ajouté du côté extérieur afin d'améliorer la résistance aux conditions météorologiques et donner l'apparence souhaitée par le client, avec par exemple l'utilisation de briques, pierres ou de bois. Une lame d'air est là aussi recommandée entre le bardage et le parement extérieur pour permettre à l'eau de pluie de s'évacuer et diminuer l'humidité par ventilation.

Enfin un pare-pluie peut-être agrafé du côté extérieur pour empêcher l'humidité de pénétrer dans la paroi pendant la phase de construction et ensuite de la protéger contre la pluie entraînée par de forts vents.

L'ensemble de ces possibilités de compositions de paroi, ajouté à la variété de matériaux disponibles pour chaque couche signifie qu'il n'existe pas de « paroi type » pouvant représenter la majorité des constructions à ossature bois. L'étude bibliographique en apporte confirmation puisque les parois testées pour l'étude des transferts d'air-chaleur-humidité diffèrent toutes entre elles (Table 2.8)<sup>1</sup>. De même chacun des nombreux défauts d'étanchéité habituellement rencontrés peut se décliner en une infinité de variantes géométriques, et il est donc impossible de caractériser chacun d'eux. Ainsi, l'étude expérimentale de certaines configurations (Table 2.9) peut être utile non seulement pour une caractérisation locale de l'impact d'un défaut donné, mais également pour valider des outils numériques afin de pouvoir simuler un plus grand nombre de configurations particulières.

Par ailleurs il est à noter que les résultats de précédentes études expérimentales sont utilisés pour valider les premiers résultats obtenus avec notre nouveau banc d'essai.

---

<sup>1</sup> Dans ce résumé les figures et tableaux cités font référence au corps de texte débutant p.39



### 3. Prise en compte des infiltrations d'air naturelles dans le calcul du débit total de ventilation d'un bâtiment

#### 3.1. Contexte

Dans ce chapitre, la problématique de l'étanchéité à l'air est abordée à l'échelle du bâtiment à travers l'étude des débits de ventilation dans des maisons individuelles. La perméabilité globale de l'enveloppe est caractérisée par le coefficient  $n_{50}$  correspondant au nombre de renouvellements d'air à l'heure pour une surpression de 50 Pa. La force du vent et le tirage thermique créent des écarts de pressions locaux entre les côtés intérieurs et extérieurs de l'enveloppe (Figure 3.1). L'association de ces forces de pression naturelles et de la perméabilité des parois crée des infiltrations d'air à travers l'enveloppe.

L'objectif de cette première partie est de développer des modèles globaux pour prédire la façon dont ces infiltrations naturelles d'air s'ajoutent aux débits de ventilation mécanique pour estimer le taux de ventilation totale du bâtiment. Une ventilation double-flux impacte peu le champ de pression intérieur, et ces deux débits vont donc simplement s'additionner. En revanche, les systèmes de ventilation par extraction ou insufflation reposent respectivement sur la mise en surpression ou en dépression du bâtiment, ce qui a un impact sur les débits d'infiltrations induits par les forces naturelles (Figure 3.2). La combinaison des débits est dite sous-additive, c'est-à-dire inférieure à la somme des débits pris séparément.

Afin d'éviter à la fois les consommations excessives d'énergie et une mauvaise qualité d'air intérieur, il est nécessaire de prédire de manière fiable le débit total de ventilation dû aux effets combinés des infiltrations naturelles et de la ventilation mécanique. Pour cela il est possible d'utiliser des modèles de bilan de masse de type « réseaux de pression » pour calculer la pression intérieure qui permet d'équilibrer les débits d'infiltrations et d'exfiltrations. Cette approche est efficace mais elle nécessite un grand nombre de paramètres d'entrée et peut s'avérer trop longue pour certaines applications telles que les normes de ventilation ou les modélisations paramétriques simplifiées.

L'autre alternative est l'utilisation de modèles simplifiés empiriques, appelés modèles de superposition. Dans les années 80s un certain nombre de modèles ont ainsi été proposés (Table 3.1) et testés lors d'études numériques ou expérimentales. Ces résultats n'ont pas permis d'identifier un unique modèle qui ferait consensus, probablement parce qu'ils étaient basées sur des données restreintes notamment en terme de niveaux d'étanchéité, d'où la nécessité d'une nouvelle étude.

Il est à noter que chaque modèle peut être utilisé de manière directe (*forward*) pour calculer le débit total de ventilation  $Q_t$  en fonction des débits d'infiltration naturelle  $Q_{inf}$  et de ventilation mécanique  $Q_f$ , ou *inverse* pour estimer  $Q_f$  en fonction de  $Q_t$  et  $Q_{inf}$ . De plus ces modèles peuvent être utilisés pour des calculs à un pas de temps horaire ou annuel, d'où les 4 applications possibles :

- (1) Horaires, Cas direct: pour la prédiction des taux de renouvellement d'air annuels utilisés notamment pour le calcul des besoins énergétiques et celui des expositions aux polluants.
- (2) Annuel, Cas direct: pour la prédiction de la ventilation effective annuelle en fonction de la perméabilité à l'air de l'enveloppe et du débit de ventilation mécanique, utilisé notamment pour les problématiques de qualité de l'air intérieur.

- (3) Horaires, Cas inverse: pour l'adaptation du débit de ventilation mécanique heure par heure pour maintenir un débit de ventilation total constant et compenser les infiltrations d'air fluctuantes.
- (4) Annuel, Cas inverse: pour dimensionner un système de ventilation mécanique qui, combiné aux infiltrations, permettra d'atteindre le débit total de ventilation souhaité. Cette application est particulièrement intéressante pour les réglementations telles que la norme ASHRAE 62.2.

### 3.2. Approche

Le logiciel REGCAP a été utilisé pour créer une base de données par simulation couvrant une grande variété de conditions météorologiques et de types de maisons (Table 3.2) : 4 niveaux d'étanchéité à l'air ( $0.6 < n_{50} < 10$ ) ; deux types de systèmes de ventilation (extraction et soufflage) ; trois types de fondations et des données météorologiques de 8 zones climatiques différentes. Cet éventail de paramètres permet de tester 864 différentes configurations, soit environ 7.5 millions de données horaires qui peuvent servir de référence pour l'évaluation des modèles de superposition.

Pour chaque jeu de paramètres, deux simulations ont été effectuées : une première sans ventilation mécanique pour connaître  $Q_{inf}$  puis une seconde avec une ventilation mécanique (débit  $Q_f$  fixe calculé avec la norme ASHRAE 62.2) pour obtenir également  $Q_t$ . De cette manière il était ensuite possible de comparer les débits  $Q_t/Q_f$  prédits par les modèles à ceux respectivement obtenus et utilisés dans les simulations.

Onze différents modèles ont été testés, les équations sont données dans Table 3.3. Trois d'entre eux proviennent de la littérature :

- *Additivity model* : correspondant à la simple addition de  $Q_{inf}$  et  $Q_f$ , c'est le modèle actuellement utilisé par la norme ASHRAE 62.2
- *Simple quadrature model* : modèle actuel du ASHRAE Handbook of Fundamentals
- *Half Fan model* : utilisé dans des versions antérieures du ASHRAE Handbook of Fundamentals

Les huit autres ont été développés pour cette étude avec des formes d'équations différentes mais pour chacun d'eux une constante déterminée de manière empirique.

### 3.3. Comparaison des modèles

Les différents modèles simplifiés ont été évalués en comparant les débits prédits ( $Q_{model}$ ) avec ceux obtenus par simulation ( $Q_{sim}$ ). Pour le modèle direct permettant l'estimation du débit total de ventilation  $Q_t$ , l'erreur est donnée par :

$$E_{fw} = \frac{Q_{t,model} - Q_{t,sim}}{Q_{t,sim}}$$

De la même manière, l'erreur induite par les modèles inverses repose sur la différence entre les débits prédits et simulés de la ventilation mécanique :

$$E_{inv} = \frac{Q_{f,model} - Q_{f,sim}}{Q_{t,sim}}$$

Ces erreurs sont représentées graphiquement en fonction de taux d'infiltration (Figure 3.6 et Figure 3.7) et leurs caractéristiques sont données dans les tableaux ci-dessous.

Erreurs sur la prédiction des modèles pour les données horaires

Modèle	Erreur directe				Erreur inverse				
	Biais	RMS	Max. Med.	Max. 90%	Biais	RMS	Max. Med.	Max. 90%	
Additivity	21.2%	22.1%	33.1%	34.4%	-21.2%	22.1%	33.1%	34.4%	
Simple quadrature	-3.67%	6.44%	11.6%	12.5%	7.67%	10.9%	23.3%	24.8%	
Advanced quadrature	$\beta=0.3$	0.53%	5.92%	7.45%	9.81%	0.88%	8.18%	11.9%	14.6%
	$\beta=0.6$	4.54%	7.20%	11.8%	12.1%	-4.68%	8.54%	12.3%	13.8%
Half-fan	-2.61%	4.60%	9.7%	8.72%	3.89%	7.41%	14.9%	14.7%	
Half-smaller	4.64%	7.62%	13.9%	13.1%	-4.45%	8.88%	13.9%	14.6%	
Constant coefficient system	9.34%	13.0%	19.3%	21.3%	-12.4%	16.1%	24.3%	26.6%	
SFSA	-0.75%	5.71%	7.57%	10.0%	2.69%	8.44%	14.9%	16.7%	
SISA	3.55%	5.59%	7.47%	9.64%	-4.44%	7.26%	8.51%	12.6%	
EFSA	-0.89%	4.02%	3.78%	7.72%			-		
EISA			-		-0.92%	5.60%	2.31%	10.8%	
MLSA	0.82%	8.15%	10.7%	12.9%			-		

Erreurs sur la prédiction des modèles pour les données annuelles

Modèle	Erreur directe			Erreur inverse			
	Biais	RMS	Max.	Biais	RMS	Max.	
Additivity	17.6%	17.8%	30.9%	-17.6%	17.8%	30.9%	
Simple quadrature	-7.28%	7.70%	18.1%	11.5%	12.0%	32.2%	
Advanced quadrature	$\beta=0.3$	-3.06%	5.10%	12.7%	5.17%	7.32%	21.2%
	$\beta=0.6$	0.94%	4.22%	10.3%	-0.29%	5.18%	12.7%
Half-fan	-6.18%	6.38%	20.3%	9.60%	9.9%	31.6%	
Half-smaller	0.86%	5.49%	12.3%	0.42%	6.83%	18.6%	
Constant coefficient system	5.52%	8.77%	17.9%	-7.92%	11.0%	22.6%	
SFSA	-4.31%	5.35%	13.9%	6.73%	7.87%	23.4%	
SISA	0.11%	2.15%	6.18%	0.46%	2.81%	8.65%	
EFSA	-0.05%	1.60%	5.55%				
EISA				0.04%	2.14%	8.85%	
MLSA	1.08%	6.79%	13.6%				

Le biais est l'erreur moyennée sur l'ensemble des points de la base de données. La moyenne quadratique (RMS) représente l'erreur moyenne pour une maison et une zone climatique spécifiques. Pour les données annuelles le maximum de l'erreur est également renseigné, mais cette valeur n'est que peu significative pour les données horaires étant donné le très grand nombre de points. En revanche, la médiane maximale parmi les 20 groupes de données est précisée, ainsi que la valeur en dessous de laquelle se situent 90% des erreurs calculées.

### 3.4. Conclusion

Les meilleurs modèles pour chacune des 4 applications sont comparés Figure 3.8. Il ressort de cette étude que les modèles exponentiels (EFSa et EISA) sont ceux donnant les meilleures prédictions, avec des biais proches ou inférieurs à 1%, des moyennes quadratiques entre 1.5% et 5.5%, et des erreurs maximales proches ou inférieures à 10%. Leurs expressions (incluant la constante déterminée empiriquement) sont données ci-dessous :

	Forward	Inverse
<b>Hourly</b>	$Q_t = Q_f + \exp\left(-\frac{2}{3} \frac{Q_f}{Q_{inf}}\right) Q_{inf}$	$Q_f = Q_t - \exp\left(-\left(\frac{Q_t}{Q_{inf}} - 1\right)\right) Q_{inf}$
<b>Annual</b>	$Q_t = Q_f + \exp\left(-\frac{4}{9} \frac{Q_f}{Q_{inf}}\right) Q_{inf}$	$Q_f = Q_t - \exp\left(-\frac{2}{3} \left(\frac{Q_t}{Q_{inf}} - 1\right)\right) Q_{inf}$

Une amélioration certaine est apportée en comparaison avec les modèles présents dans la littérature, notamment avec le *simple additivity model* dont les erreurs présentent un biais et une moyenne quadratique d'environ 20%, et des valeurs maximales au-dessus de 30%.

## 4. Tests de pressurisation pour la caractérisation de l'étanchéité à l'air à l'échelle de la paroi

Dans ce chapitre la perméabilité à l'air n'est plus évaluée à l'échelle du bâtiment mais du défaut d'étanchéité, avec des tests de pressurisation sur des parois ou composants à trois échelles différentes.

### 4.1. Bancs expérimentaux

Deux bancs expérimentaux ont été construits pour cette étude (SAPI et APIE), et le banc AEV du CSTB de Grenoble a été utilisé.

La SAPI box (Small Air Path Investigation box) est utilisée pour caractériser à petite échelle la perméabilité à l'air de matériaux seuls ou d'assemblages simples (Figure 4.1). Les petites dimensions intérieures (150 cm x 150 mm) permettent un temps de mise en œuvre très court et donc l'obtention rapide de résultats. La répétabilité des mesures est bonne, mais si cela assure une certaine précision en relatif, la précision en absolue est quant à elle plus discutable.

L'APIE box (Air Path In Envelopes box) a été construite pour des études sur des parois de plus grandes dimensions (0.7 m x 2 m), correspondant approximativement à l'espacement entre deux poteaux de l'ossature bois (Figure 4.2). Elle a été dimensionnée par simulation CFD sous OpenFoam pour assurer une homogénéité du champ de pression le long de la paroi testée (Figure 4.3). Des tests préliminaires ont montré une très bonne répétabilité des mesures (Figure 4.5). De plus une comparaison avec des résultats de la littérature a permis de valider la cohérence des résultats pour ces deux nouveaux bancs expérimentaux (Figure 4.6).

Enfin le banc AEV du CSTB permet de tester la perméabilité à l'air de parois à taille réelle, allant jusqu'à 10 m x 5.5 m, en suivant la norme EN 1026 (Figure 4.4). Les résultats sont donc facilement utilisables à l'échelle du bâtiment, mais la mise en place et les tests en eux-mêmes sont à la fois plus longs, complexes et coûteux. L'ensemble des tests d'étanchéité réalisés pour cette étude comprend dans un premier temps une caractérisation de l'isolant, l'élément le plus perméable dans la paroi ; puis des assemblages simples pour l'étude de détails de construction ; et enfin une paroi ossature bois réelle pour la caractérisation de détails de construction de plus grande échelle tels que l'étanchéité du pare-vapeur ou d'une fenêtre.

#### **4.2. Caractérisation de l'isolant**

Plusieurs tests de pressurisation sont effectués pour la caractérisation de l'isolant. Il est dans un premier temps montré que le choix de celui-ci peut avoir un impact non négligeable sur la perméabilité à l'air. Une laine de verre souple de faible densité (HPGW) a en effet une perméabilité à l'air près de 3 fois plus importante qu'une autre laine de verre rigide (LPGW) alors que ses propriétés thermiques sont similaires. La direction de l'écoulement par rapport au plan des fibres a aussi son importance : pour la HPGW la perméabilité est 2.4 fois plus élevée parallèlement aux fibres que perpendiculairement.

L'effet de la compression de l'isolant est également étudié, avec deux couches de HPGW testées pour des épaisseurs de 11, 9 et 7 cm (Figure 4.9). La perméabilité à l'air diminue logiquement avec le taux de compression. Les résultats de tous les tests de perméabilité sur la laine de verre (de différents types, épaisseur, compression) ainsi que ceux trouvés dans la littérature ont permis d'établir une relation empirique entre la perméabilité  $k$  et la masse volumique ( $\rho$ ) :

$$k = 1.94.10^{-8} \times \rho^{-0.89}$$

Le coefficient de corrélation  $R^2$  est seulement de 0.83, puisque la perméabilité est également dépendante d'autres paramètres tels que le diamètre des fibres, la porosité et la tortuosité. Cette relation peut cependant être utile pour une première approximation puisque contrairement à ces autres paramètres, la masse volumique est très facilement mesurable.

#### **4.3. Parois simplifiées**

Différents assemblages de composants ont été testés avec la SAPI box. Tout d'abord, une étude a été effectuée sur l'impact de l'interface entre une couche étanche avec un passage d'air (ici un carton plastifié avec un orifice de 20 mm de diamètre) et l'isolant (HPGW). Quatre assemblages ont été testés : avec de la colle sur toute l'interface et une étanchéité sur les pourtours de la paroi (a) ; avec un rond de colle autour de l'orifice et une étanchéité (b) ; sans colle mais avec étanchéité (c) ; et enfin sans colle ni étanchéité (d) (Figure 4.11). Les cas (a) et (b) donnent une loi linéaire entre le débit

et la pression, avec cependant une perméabilité plus importante pour le cas (b). Le cas (c) montre l'apparition d'une lame d'air entre les deux composants et dans le cas (d) le déplacement de l'isolant et la création d'un passage d'air entre celui-ci et la SAPI box (Figure 4.12).

Par la suite, l'addition progressive de différentes couches a été étudiée avec des tests de perméabilité entre chaque ajout de composant. Un premier assemblage de paroi comprend une couche étanche avec un orifice de 20 mm de diamètre au centre, 2 couches de laine de verre et une autre couche étanche avec le même orifice centré. Les résultats (Figure 4.13) montrent que la première couche seule induit un écoulement turbulent (exposant proche de 0.5) ; l'ajout d'une épaisseur de HPGW réduit considérablement le débit et linéarise l'écoulement ; une deuxième couche a un impact moins significatif, contrairement à la dernière couche « étanche » qui a aussi pour effet d'augmenter à nouveau la turbulence. Un deuxième assemblage, similaire au premier mais avec des orifices excentrés, a également été testé (Figure 4.14). Les conclusions sont semblables mais avec une perméabilité globalement réduite du fait d'une dispersion de l'air dans l'isolant réduite dans deux directions.

Enfin, un test a été effectué pour évaluer l'impact de la direction de l'écoulement dans la paroi testée. Il est connu que les tests d'étanchéité peuvent donner des résultats légèrement différents en fonction de s'ils sont effectués en pression ou en dépression. Cette différence est notamment attribuée à la présence d'adhésifs, par exemple pour lier les bandes de pare-vapeur entre elles, qui peuvent se décoller dans un sens. Cependant, avec ce test qui ne comprend qu'une couche étanche avec un orifice de 20 mm et une couche d'isolant, il s'avère qu'à de fortes pressions ( $> 300$  Pa), une différence est également observée (Figure 4.15). L'exposant de la loi débit-pression est en effet plus proche de 1 (0.85 au lieu de 0.72) lorsque la divergence de l'air plutôt que sa convergence se fait dans l'isolant.

#### **4.4. Tests sur une paroi réelle à ossature bois**

L'étanchéité à l'air d'une paroi réelle (5 m x 2.6 m) a été testée sur le banc AEV. Elle est composée (de l'intérieur vers l'extérieur) de 15 mm de plâtre ; d'un pare-vapeur ; 2 couches de 80 mm de fibre de bois et d'un panneau MFP (Figure 4.16). Dans un premier temps, un test de pressurisation est fait sans étanchéité entre les 8 plaques de plâtre ni entre le pare-vapeur et la lisse basse de la paroi, et sans fenêtre. Un scotch aluminium a ensuite été utilisé pour étanchéifier les jonctions entre les plaques de plâtre, différents niveaux d'étanchéité de la liaison avec le pare-vapeur ont été testés, et enfin l'étanchéité du fenêtrage triple vitrage a été étudiée (Figure 4.17).

Pour chaque configuration, la perméabilité à l'air est mesurée à 10 seuils de pression (20-30-40-50-60-70-80-90-100 et 150 Pa), et une moyenne est faite entre les résultats pour une surpression et pour une dépression.

L'ajout de scotch aluminium entre les plaques de plâtre réduit légèrement la perméabilité à l'air de la paroi, de moins de 10% à 150 Pa (Figure 4.18). Cette différence n'est pas très significative en comparaison de la longueur de jonction étanchéifiée d'environ 19 m. Cela peut s'expliquer par une très bonne étanchéité du côté extérieur de la paroi qui réduit l'impact d'éventuels défauts du côté intérieur de celle-ci.

De manière similaire, l'étanchéité entre le pare-vapeur et la lisse basse de la paroi a un impact également restreint sur la perméabilité de la paroi. Deux types d'étanchéité ont été testés : des points de colle tous les 20 cm pour éviter un décollement complet du pare-vapeur, et du mastic tout le long de la jonction (Figure 4.19). Il s'est avéré que les points de colle n'ont pas d'effet significatif par rapport aux incertitudes de mesure, et que l'étanchéité sur toute la jonction (5 m) permet une réduction d'en moyenne 7% de la perméabilité à l'air. La même explication que pour les précédents tests s'applique : l'étanchéité du côté extérieur est suffisamment efficace pour éviter d'importants débits d'infiltration, quel que soit le niveau d'étanchéité du côté intérieur.

En revanche, l'ajout d'une fenêtre modifie plus radicalement la perméabilité de la paroi (Figure 4.20). Malgré l'ajout de polyuréthane du côté extérieur pour améliorer l'étanchéité, la perméabilité à l'air est plus que doublée, avec par exemple un débit de 7.6 m<sup>3</sup>/h mesuré à 150 Pa au lieu de 3.2 m<sup>3</sup>/h sans fenêtre. Par contre, l'ajout d'un ruban adhésif côté intérieur diminue considérablement cet impact, avec à 150 Pa un débit de 3.7 m<sup>3</sup>/h. Ainsi, lorsque des défauts d'étanchéité traversants sont créés, une bonne étanchéité des deux côtés devient nécessaire pour limiter leur impact.

## 5. Etude expérimentale du chemin de l'air à travers un défaut d'étanchéité par l'utilisation d'un traceur

Dans ce chapitre, une technique non-intrusive est développée pour l'étude du chemin de l'air dans la paroi grâce à des microparticules traceuses.

### 5.1. Méthodologie

La fluorescéine est choisie parmi les différents types de traceur pour sa très bonne solubilité dans l'eau, sa forte fluorescence dans celle-ci, son bas coût et faible toxicité. Des particules solides sont introduites dans l'air et filtrées par l'isolant le long du passage de l'air dans celui-ci. La quantité de particules dans un petit volume d'isolant est ensuite mesurée en l'immergeant dans l'eau et en mesurant l'absorbance de la solution résultante. Une cartographie de la concentration en fluorescéine dans l'isolant constitue une indication du chemin de l'air dans celui-ci. Le diamètre des particules est un paramètre important dans ce processus. Il y a une taille optimale, habituellement entre 0.1 et 0.2 µm, pour laquelle l'efficacité de filtration du milieu poreux est la plus basse. Etant donné que l'objectif est de tracer le chemin de l'air sur une distance aussi longue que possible, les particules de fluorescéine doivent être dans ces dimensions. Un générateur de fluorescéine SETRA GP92 produisant des particules d'une taille moyenne de 0.18 µm est donc utilisé (Figure 5.1).

La masse de fluorescéine présente dans une solution correspond à la quantité de particules filtrées par l'échantillon d'isolant plongé dans celle-ci. Or, la couleur de la solution varie en fonction de cette concentration en fluorescéine, passant d'une solution presque transparente (10<sup>-4</sup> g/L) à un jaune vif (10<sup>-2</sup> g/L). L'absorbance (A) de chaque solution est mesurée par spectroscopie pour relier sa coloration à sa concentration en fluorescéine (C<sub>fluo</sub>). Une calibration est effectuée pour relier ces deux grandeurs (Figure 5.4):

$$C_{fluo} = 1.077 \cdot 10^{-2} \times A^{0.8537}$$

Les mesures sont faites à une longueur d'onde de 489 nm correspondant au pic d'absorbance de la fluorescéine (Figure 5.3).

Afin de ne pas perturber les mesures de concentration en fluorescéine, l'isolant doit colorer aussi peu que possible l'eau, notamment à une longueur d'onde de 489 nm. Cela impose certaines limitations pour l'utilisation de cette technique expérimentale. Il a été vérifié que la laine de verre convient pour cette étude grâce à sa faible coloration de l'eau (Figure 5.5), avec une mesure d'absorbance presque négligeable ( $A=0.008$ ). En comparaison de la fibre de bois ( $A = 0.195$ ) induit une trop forte coloration mais la laine de roche est une autre option possible ( $A = 0.009$ ). Parmi les différentes laines de verre, l'HPGW convient par sa forte perméabilité à l'air qui minimise l'efficacité de filtration.

Le protocole expérimental pour chaque test est le suivant (Figure 5.6):

- (1) La « paroi » testée est exposée au flux d'air chargé en microparticules de fluorescéine pendant plusieurs heures. La durée exacte est choisie en fonction de l'importance de la dispersion de l'air pour avoir des concentrations significatives en fluorescéine ( $>10^{-4}$  g/L).
- (2) L'isolant est découpé en petits volumes (5 x 5 cm).
- (3) Chaque échantillon est immergé dans un volume donné d'eau distillée ( $V_{water}$ ) et compressé plusieurs fois (environ 30s) pour évacuer l'air et dissoudre toute la fluorescéine.
- (4) La solution colorée est versée dans des petites fioles plastiques et placée dans une centrifugeuse à 22000 tr/min pendant 5 minutes pour que les résidus de fibres de laine de verre se déposent au fond du récipient.
- (5) L'absorbance de la solution est mesurée avec un spectromètre à 489 nm.
- (6) La concentration en fluorescéine ( $C_{fluo}$ ) est calculée avec la loi de calibration.
- (7) Le pourcentage de la masse ( $MP_{fluo}$ ) par rapport à la quantité totale de fluorescéine dans la couche d'isolant est calculé pour chaque échantillon (i) de la manière suivante:

$$(MP_{fluo})_i = \frac{(C_{fluo} \times V_{water})_i}{\sum_{i,layer} (C_{fluo} \times V_{water})_i} \times 100$$

## 5.2. Tests préliminaires

Un certain nombre de tests préliminaires ont été effectués à petite échelle dans la SAPI box pour valider l'utilisation de microparticules de fluorescéine pour tracer le chemin de l'air dans les parois à ossature bois. Les mêmes composants ont été utilisés que pour les tests d'étanchéité à petite échelle : des couches étanches avec un orifice de 20 mm de diamètre situé soit au centre soit dans un coin, et de la laine de verre (HPGW) d'une épaisseur originale de 620 mm mais compressée à 40 mm. Pour une analyse 3D, la laine de verre est coupée en deux dans son épaisseur. Les huit différents tests et leurs résultats sont présentés sur la Figure 5.8.

Ils ont permis de confirmer la pertinence de cette technique, avec une bonne répétabilité et cohérence des résultats. Il a par exemple été montré que la présence de colle entre les composants réduit significativement la dispersion de l'air dans l'isolant, tout comme l'ajout d'une couche « étanche » en sortie. Une limitation importante a cependant été identifiée avec une efficacité de filtration relativement élevée : l'absence de fluorescéine peut non seulement être due à une vitesse



d'air nulle à cet endroit, mais aussi à une filtration totale des particules en amont. Le transport des particules implique en effet deux phénomènes physiques : l'advection qui permet de faire le lien avec le chemin de l'air mais aussi la filtration par les fibres de l'isolant. Afin de faciliter l'interprétation des résultats expérimentaux, cet effet de filtration est étudié plus en détails.

### 5.3. Modèle de filtration des microparticules

L'efficacité de filtration d'une fibre d'isolant  $\eta$  résulte de l'action simultanée de différents phénomènes physiques de filtration. Pour cette application, seules l'interception ( $\eta_i$ ), l'impaction ( $\eta_r$ ) et la diffusion ( $\eta_d$ ) sont considérées, l'effet de tamis et la sédimentation étant négligeables pour des aérosols de faible diamètre. Une particule est arrêtée par interception si son centre de gravité suivant une ligne de courant passe à moins d'un rayon d'une fibre. L'impaction résulte de l'inertie d'une particule lorsque celle-ci ne suit pas la ligne de courant déviée par la présence d'une fibre. Enfin, l'arrêt par diffusion est dû au mouvement Brownien des particules de petits diamètres qui ne suivent alors pas rigoureusement les lignes de courant (Figure 5.9).

Plusieurs modèles ont été proposés pour estimer ces différentes composantes d'efficacité de filtration. Celui de Miecret et Gustavsson est communément utilisé pour des filtres fibreux et a donc été choisi pour cette étude. L'efficacité de filtration d'une fibre s'exprime comme la somme des efficacités de chaque mécanisme de filtration ( $\eta_j$ ) avec un terme additionnel ( $\eta_{dr}$ ) correspondant à l'interaction entre les phénomènes de diffusion et d'interception (cf nomenclature):

$$\left\{ \begin{array}{l} \eta = \sum \eta_j + \eta_{dr} \\ \eta_i = 2.4 (1 - \varphi)^{1/3} R^{1.75} \\ \eta_d = 1.5 Pe^{-\frac{2}{3}} \\ \eta_r = \frac{1}{\left(1 + \frac{1.53 - 0.23 \ln(Re_f) + 0.0167(\ln Re_f)^2}{Stk}\right)^2} \\ \eta_{dr} = 1.24 Ku^{-0.5} \cdot R^{2/3} \cdot Pe^{-0.5} \end{array} \right.$$

En intégrant cette efficacité de filtration d'une fibre sur l'ensemble du filtre d'épaisseur  $t_{filter}$ , l'efficacité totale de filtration (CE) est alors :

$$CE = \frac{\text{concentration amont}}{\text{concentration aval}} = \exp\left(-4 \eta \frac{(1 - \varphi) t_{filter}}{\varphi \pi d_f}\right)$$

Ce modèle repose sur un certain nombre de paramètres, notamment le diamètre des particules de fluorescéine, celui des fibres du filtre (ici l'isolant) ainsi que la porosité du milieu. Le diamètre des particules est évalué à 0.18  $\mu\text{m}$  grâce à des études antérieures utilisant le même générateur de particules. Sa distribution n'est cependant pas connue, et il a été vérifié par microscopie à balayage électronique que des particules plus grosses étaient également générées, jusqu'à 1  $\mu\text{m}$  de diamètre (Figure 5.11). Le diamètre des fibres de verre moyen est évalué expérimentalement à 5.7  $\mu\text{m}$  sur plus de 100 mesures avec un microscope optique (Figure 5.12 et Figure 5.13). La porosité est également évaluée expérimentalement sur 15 échantillons à 0.994 pour une épaisseur initiale de 6 cm, soit 0.99 pour une compression à 4 cm. Une étude paramétrique a mis en évidence une grande sensibilité du modèle à ces différents paramètres ce qui souligne l'importance de la précision des valeurs utilisées (Figure 5.14 à Figure 5.16). Il a également été vérifié qu'un minimum d'efficacité de filtration était

atteint pour des diamètres de particule proches de 0.18  $\mu\text{m}$  lorsque la vitesse de l'écoulement est inférieure à 2 m/s.

Ce modèle est implémenté dans le logiciel COMSOL Multiphysics® et couplé avec un module CFD pour les écoulements dans les milieux poreux. La concentration en fluorescéine  $C_{\text{fluo}}$  est calculée avec une équation d'advection-diffusion dont le dernier terme représente le dépôt de particules :

$$\frac{dC_{\text{fluo}}}{dt} = D\nabla^2 C_{\text{fluo}} - \vec{v}\nabla C_{\text{fluo}} - \ln(CE_1) \vec{v}C_{\text{fluo}}$$

L'efficacité de filtration utilisée dans ce modèle ( $CE_1$ ) est calculée par le modèle théorique de Miecret et Gustavsson pour une épaisseur d'isolant d'1 mètre, et est fonction de la vitesse de l'écoulement. Une vérification expérimentale a été effectuée pour des vitesses comprises entre 0.2 et 1.5 m/s. Un nouveau dispositif expérimental sous forme de tube a été construit dans ce but (Figure 5.17), permettant le passage de l'air chargé en fluorescéine à travers 20 cm d'isolant. Celui-ci est ensuite divisé en 10 échantillons et la concentration en fluorescéine est mesurée dans chacun d'eux pour identifier l'efficacité de filtration (Figure 5.19 et Figure 5.20). Les résultats expérimentaux ont confirmé la pertinence du modèle théorique pour cette gamme de vitesse (Figure 5.21).

#### 5.4. Ecoulement d'air canal en contact avec un milieu poreux

Cette méthode d'utilisation de microparticules traceuses de fluorescéine est ensuite utilisée pour l'étude des écoulements d'air dans des canaux en contact avec un milieu poreux (isolant). Cette configuration peut en effet être étudiée numériquement mais les résultats ont besoin d'être validés expérimentalement. La dispersion de l'air dans l'isolant est étudiée expérimentalement avec la SAPI box pour trois cas distincts (Figure 5.23) : un canal formant un coude avec d'abord une entrée d'air restreinte au canal (1) puis libre également en amont de l'isolant (2); ainsi qu'un canal droit (sans coude) (3). De plus, certains paramètres sont modifiés pour l'étude de leur impact, tels que la densité de l'isolant, son épaisseur, son sens et la vitesse de l'écoulement. Le détail des 10 tests expérimentaux réalisés est présenté dans Table 5.3.

Une simple analyse de la répartition de la concentration en fluorescéine renseigne dans un premier temps sur la présence et le chemin des infiltrations de l'air dans l'isolant. L'étude du cas (1) a permis de mettre en évidence une infiltration de l'air dans l'isolant le long du canal, notamment dans l'intérieur du coude (Figure 5.26). Une relativement bonne répétabilité a été démontrée malgré la précision limitée lors du découpage de l'isolant. Le test avec un isolant plus dense (LPGW au lieu de HPGW) a montré une infiltration moins importante et moins profonde de l'air dans l'isolant. Lorsqu'une deuxième épaisseur d'isolant a été ajoutée, les résultats ont mis en évidence un passage d'air entre les deux couches malgré la compression de l'isolant. Enfin, une réduction par deux de la vitesse dans le canal a nettement diminué la pénétration de l'air dans l'isolant. Les résultats expérimentaux du cas (2) ont permis quant à eux de distinguer clairement deux passages préférentiels de l'air correspondant aux extrémités de l'isolant. Pour le cas (3) du canal droit, de l'air s'infiltré également dans l'isolant mais moins profondément que pour la configuration (1) (Figure 5.27). Les tests avec deux couches d'isolant montrent également une infiltration de l'air entre elles. De plus, il a été vérifié que pour cette configuration aussi une réduction de la vitesse dans le canal diminue les infiltrations d'air.

Dans un second temps ces résultats expérimentaux sont confrontés aux résultats numériques, à savoir les champs de vitesses obtenus par CFD mais également les concentrations en fluorescéine prédites grâce au modèle de filtration (Table 5.6 à Table 5.10). Cette approche permet une analyse plus fine et une éventuelle validation des modèles numériques. Pour le cas (1), les résultats expérimentaux et numériques sont semblables en termes de profondeur d'infiltration de l'air dans l'isolant, mais expérimentalement cette infiltration est plus concentrée au niveau de l'intérieur du coude. Concernant l'ajout d'une deuxième couche d'isolant, la discontinuité à l'interface n'est pas présente numériquement et le passage de l'air entre les deux couches ne paraît donc pas. Quant à la diminution de la vitesse de l'écoulement, elle entraîne bien une diminution des infiltrations mais de manière moins prononcée qu'expérimentalement. Le cas (2) révèle une différence significative de comportement de l'écoulement, avec numériquement une répartition presque homogène de l'air dans l'isolant qui ne correspond pas aux résultats expérimentaux. Le cas (3) est un autre exemple de différence significative puisque la solution numérique ne montre pas ou très peu d'infiltration d'air dans l'isolant.

Dans l'ensemble ces résultats démontrent la pertinence de l'utilisation de cette méthode expérimentale, à la fois pour une indication du chemin de l'air dans l'isolant et pour une confrontation avec des modèles numériques.

## **6. Evaluation des performances des méthodes expérimentales pour l'étude de la dispersion de l'air dans les parois**

Dans ce dernier chapitre, cinq techniques expérimentales différentes sont testées pour l'identification du chemin de l'air dans les parois légères. L'identification des entrées et sorties d'air est d'abord effectuée par IRT (thermographie infrarouge) et PIV (particle image velocimetry). Le chemin à l'intérieur même de la paroi est ensuite étudié. Un quadrillage 3D de capteurs de température puis d'humidité relative est mis en œuvre dans les parois testées pour tracer respectivement les infiltrations d'air chaud puis humide. Enfin, la technique développée précédemment d'utilisation de microparticules traceuses de fluorescéine est également testée.

Ces différentes méthodes sont comparées entre elles et avec un modèle numérique pour identifier leurs avantages et limitations respectifs. Pour chacune d'elles, deux niveaux d'analyse sont possibles. Les champs de température, d'humidité et de concentration en fluorescéine peuvent être utilisés directement comme indicateurs du chemin de l'air. Pour une analyse plus fine, il est également possible de coupler un modèle d'écoulement d'air avec les autres phénomènes physiques impactant les mesures : transferts de chaleur, d'humidité ou transport des particules de fluorescéine. Ces couplages facilitent la comparaison des résultats expérimentaux avec les champs de vitesse obtenus numériquement et permettent la validation des modèles qui peuvent ensuite être appliqués à une grande variété de configurations. Dans cette étude, seul le transport de fluorescéine est couplé avec l'écoulement de l'air en raison du caractère innovant de la technique. Des modèles de couplage air-chaleur-humidité sont cependant présents dans la littérature et peuvent être utilisés dans cet objectif.

## 6.1. Description des configurations testées

Pour la comparaison des méthodes expérimentales, trois configurations principales ont été identifiées (Figure 6.1), bien que certaines techniques (IRT et PIV) aient nécessité des adaptations et/ou additions de cas testés. Pour chacune d'elles, deux couches de laine de verre (HPGW) d'une épaisseur totale de 8 cm sont placées entre deux plaques de plâtre non perméables à l'air mais avec un orifice de 20 mm de diamètre. D'un côté (aval) le plâtre et l'isolant sont collés entre eux, mais l'interface entre ces deux matériaux du côté amont diffère selon les configurations. La première (1) correspond à la présence d'un vide technique se traduisant par une lame d'air de plusieurs centimètres à cette interface. Les deux matériaux sont ensuite simplement juxtaposés (2) puis collés entre eux similairement à l'interface aval (3).

Ces trois configurations sont modélisées numériquement sous COMSOL (Figure 6.2). L'écoulement dans l'isolant est décrit par la loi de Darcy et dans les lames d'air par les équations de Navier et Stokes. Les paramètres des simulations sont présentés dans Table 6.1 et les conditions aux limites dans Table 6.2.

## 6.2. Identification des entrées et sorties d'air par IRT et PIV

Les tests pour l'identification des entrées/sorties d'air se font sur la configuration (1) puisque ces dernières sont clairement identifiables (orifice de 20 mm) pour les deux autres configurations.

La thermographie infrarouge permet d'obtenir un champ de température surfacique. L'air est donc chauffé dans le caisson amont de la paroi, et une caméra IR enregistre ce champ côté aval pour évaluer la dispersion de l'air en sortie de l'isolant. Un premier test (a) est réalisé avec une couche d'isolant, puis une 2<sup>ème</sup> couche est ajoutée (b), et enfin l'isolant est compressé pour réduire l'épaisseur totale de 8 cm à 6 cm (c). L'évolution du diamètre de la « zone chaude » (WA) ainsi que la température au cœur de celle-ci sont tracées pour ces 3 cas dans la Figure 6.4.

Il est montré que l'ajout d'une deuxième couche augmente de manière significative la dispersion de l'air, avec un diamètre de WA qui passe de 26 cm à 34 cm soit un facteur de 1.7 en termes de surface. Le fait de compresser ces deux couches d'isolant réduit cependant fortement la WA et donc la dispersion de l'air avec un diamètre de 28 cm. Les résultats expérimentaux et numériques coïncident pour le cas (a) puisque la simulation prévoit une dispersion de 25 cm en prenant comme limite  $v > 0.95v_{\max}$ . Par contre la dispersion évaluée par IRT pour le cas (b) est nettement inférieure à la prédiction numérique de 50 cm. Il est possible que cette différence soit liée aux plus faibles vitesses d'air dans le cas (b) résultant de la plus grande dispersion. En effet, de plus faibles débits mettent plus de temps pour chauffer les fibres de verre le long de leur passage. De plus, si les vitesses en sortie de l'isolant sont du même ordre de grandeur que l'écoulement induit par convection naturelle le long de la paroi, la laine de verre est simultanément refroidie par l'air ambiant.

L'IRT est donc une technique certes facile à mettre en œuvre et adapté pour des diagnostics globaux à grande échelle, mais qui présente aussi des limites pour une mesure précise de la zone d'infiltration/exfiltration de l'air. Le chemin de l'air est en effet étudié à travers les transferts de chaleur ce qui pose deux difficultés : l'inertie thermique qui ralentit la montée en température de l'isolant et les transferts par conduction qui peuvent entraîner une surestimation de la dispersion de l'air.

En complément des tests sont réalisés par PIV. Cette technique repose sur l'utilisation d'un laser qui éclaire les particules introduites dans l'air, d'une caméra qui prend deux photos à un intervalle de temps très court, et d'un post traitement par cross-corrélation qui permet de calculer le déplacement le plus probable des particules entre les deux images, et donc le champ de vitesse dans l'écoulement (Figure 6.7).

Une première étude similaire au cas (a) est réalisée mais avec deux orifices espacés de 15 cm ouverts tour à tour et simultanément (Figure 6.8). Les résultats coïncident avec l'IRT et la simulation avec une dispersion de 25 cm observée lorsqu'un seul des orifices est ouvert. Lorsque les deux orifices sont ouverts simultanément, le profil de vitesse observé correspond approximativement au maximum en tout point des deux profils des ouvertures tour à tour (Figure 6.10). Les vitesses ne s'additionnent donc pas dans la zone d'interaction entre les deux orifices, ce qui signifie que le débit global est inférieur à la somme des débits individuels pour cet espacement de défauts d'étanchéité. Les cas (b) et (c) n'ont pas pu être étudiés avec cette technique car la plus grande dispersion d'air rendait les vitesses trop faibles en comparaison des phénomènes de convection.

Les tests sont répétés plusieurs fois avec des temps d'enregistrement plus ou moins longs afin d'à la fois valider la répétabilité de la technique et de vérifier que les particules traceuses (gouttes d'huile) ne produisent pas un phénomène d'obstruction pour des plus longues périodes d'enregistrement (Figure 6.11).

Une deuxième étude a été réalisée correspondant à la configuration (3) mais avec à nouveau deux orifices ouverts tour à tour, l'un en face de la sortie, l'autre excentré de 15 cm. Les résultats ont permis de valider la cohérence de la technique dans le cas d'entrée d'air bien définie géométriquement ainsi que de vérifier sa faisabilité pour de fortes vitesses (15 cm/s) lorsque le risque d'obstruction est plus élevé (Figure 6.13).

### **6.3. Mesures de température suivant un quadrillage 3-D**

Par la suite l'intérêt est porté sur le chemin de l'air à l'intérieur même de la paroi pour les 3 configurations décrites précédemment. Pour cela un quadrillage 3D avec des thermocouples (TC) est réalisé dans un premier temps. Comme pour l'IRT, l'air est chauffé dans le caisson amont, et la cartographie de la température est représentative de la dispersion de l'air chaud. Des tests préliminaires ont permis de valider la bonne précision et réactivité des capteurs ainsi que leur faible intrusivité. Pour les tests à grande échelle, 60 TC sont répartis sur trois plans correspondant aux interfaces entre les différentes couches de la paroi, et suivent un quadrillage avec un espacement de 5 cm entre deux capteurs (Figure 6.15).

Les résultats sont présentés sous forme de cartographie de l'écart relatif de température, correspondant à l'augmentation en température mesurée pour chaque capteur divisée par l'écart maximal parmi tous les TC du plan de l'interface (Figure 6.18 à Figure 6.20). Ils sont cohérents entre eux et une bonne répétabilité est observée. Pour la configuration (1) une dispersion d'environ 25 cm est mesurée entre les deux couches d'isolant, ce qui est cohérent avec les précédents résultats expérimentaux. Les configurations (2) et (3) donnent des résultats relativement similaires, avec cependant une dispersion en entrée logiquement légèrement inférieure pour le cas (3) où de la colle améliore le contact entre les deux matériaux à cette interface.

Une comparaison est également effectuée avec les profils de vitesse obtenus par simulation numérique (Figure 6.22). Les résultats sont en relativement bon accord pour les trois configurations à l'exception de l'interface « entrée » entre la plaque de plâtre amont et la première couche de laine de verre. Cela peut s'expliquer par l'intrusivité des TC plus importante à cette interface qu'aux deux autres pour plusieurs raisons : le côté plâtre étant rigide, il est moins aisé d'éviter des « trous d'air » qu'entre deux isolants ; l'ensemble des 60 fils de TC passent entre cette plaque de plâtre amont et les parois de l'APIE box et une étanchéité parfaite n'est pas réalisable ; enfin la pression de l'écoulement écarte l'isolant du plâtre à cet interface, contrairement au côté aval où le phénomène inverse se produit.

En conclusion ces tests ont confirmé la faisabilité de l'utilisation de TC pour l'étude du chemin de l'air, avec une bonne précision et réactivité des capteurs, ainsi qu'une bonne répétabilité. Un certain nombre de limites ont cependant été soulevées. Le grand nombre de capteurs peut créer des passages d'air le long de leurs fils, notamment aux interfaces avec des surfaces planes et rigides. Une réduction du nombre de capteurs serait bénéfique en ce sens mais est difficilement envisageable compte tenu du caractère local de la mesure. Les températures sont en effet mesurées à des points précis, ce qui augmente les imprécisions dues aux fluctuations spatio-temporelles de l'écoulement et à la non-homogénéité de l'isolant. De plus, tout comme l'IRT, cette technique repose sur l'étude des transferts de chaleur, ce qui pose les mêmes problèmes d'inertie thermique et de conductions pouvant compliquer l'interprétation des résultats.

#### **6.4. Mesures d'humidité relative suivant un quadrillage 3-D**

Comme alternative aux thermocouples, des capteurs hybrides température-humidité relative (SHT 75) sont utilisés pour une étude du chemin de l'air à travers les transferts d'humidité. De la vapeur d'eau est introduite dans le caisson amont pour que l'air approche de la saturation, et que son passage dans la paroi soit ainsi enregistré par les capteurs. Ce modèle de capteur a été choisi notamment pour ses petites dimensions mais des tests préliminaires à petite échelle ont révélé une intrusivité malgré tout non négligeable.

Un nombre restreint de capteurs (22) ont donc été disposés dans la paroi (Figure 6.26) pour les tests à grande échelle sur les 3 configurations. La comparaison de la perméabilité de chaque paroi en fonction de la pression entre les tests avec TC et ceux avec les capteurs SHT montre cependant une intrusivité significative de ces capteurs (Figure 6.28).

Les résultats sont présentés sous la forme de cartographie de l'écart relatif de la pression de vapeur saturante (Figure 6.29 à Figure 6.31). En effet, l'introduction de vapeur chaude rend l'écoulement anisotherme et, l'humidité relative variant avec la température pour une même valeur absolue, cette grandeur n'est pas appropriée pour représenter le transport de la vapeur d'eau.

Pour chacune des trois configurations, la dispersion ainsi observée est nettement plus grande que pour l'utilisation de TC, avec des montées en humidité non négligeables enregistrées à 1 m de l'orifice. Ces différences ne peuvent pas être uniquement expliquées par le changement de la grandeur physique mesurée puisque la mesure simultanée de la température donne également des dispersions nettement plus grandes que lors des tests avec les TC seuls. Ces résultats confirment donc l'importance de la problématique de l'intrusivité pour cette technique.

Il est cependant noté que contrairement à l'étude par les transferts de chaleur, les transferts d'humidité posent moins le problème de l'inertie. En effet, les pics d'humidité relative enregistrés au milieu de la paroi coïncident presque temporellement avec le pic mesuré dans le caisson amont. Cette technique présente donc l'avantage d'une corrélation plus aisée entre la cartographie des pressions de vapeur saturante et les champs de vitesse, même si le chemin de l'air est malheureusement fortement impacté par la présence de ces capteurs.

### **6.5. Utilisation de microparticules traceuses de fluorescéine**

La dernière méthode expérimentale testée est celle développée dans le chapitre 5, à savoir l'utilisation de microparticules traceuses de fluorescéine. Elle est également appliquée aux trois différentes configurations. Les débits d'air sont choisis pour éviter des efficacités de filtration trop élevées ( $v < 3$  m/s), et le temps de génération de fluorescéine est de 7h (Table 6.9). Pour l'analyse des résultats, chaque couche d'isolant est découpée en deux dans son épaisseur, puis en carrés de 5 cm x 5 cm.

Les résultats sont présentés sous une forme similaire à ceux des deux études précédentes, avec des cartographies de concentrations relatives de fluorescéine. Chaque valeur correspond cependant à une moyenne sur un volume et non plus à une mesure locale au centre de celui-ci.

Une comparaison est d'abord effectuée entre les trois configurations pour la couche la plus en amont (Figure 6.34). Le cas (1) de la lame d'air est logiquement celui pour lequel la plus grande dispersion d'air est observée avec 30% de la concentration maximale mesurée à 15 cm de l'orifice et 10% à 40 cm. Les deux autres configurations présentent des dispersions plus petites avec dans les deux cas moins de 5% de la concentration maximale mesurée à 15 cm de l'orifice. Pour le cas (3) avec de la colle, la dispersion est encore plus restreinte mais non nulle à 5 cm de l'orifice. Cela s'explique par l'expansion du jet d'air dans les 2 cm de l'isolant, mais aussi potentiellement par un contact qui, malgré la colle, n'est pas parfait avec la plaque de plâtre.

La dispersion de l'air dans l'isolant autour du chemin le plus direct entre l'entrée et la sortie est également étudiée pour les configurations (2) et (3) (Figure 6.35). Celle-ci ne fait que diminuer à l'approche de la sortie pour la configuration (2), et augmente légèrement avant de diminuer pour la dernière configuration. Dans ces deux cas, la fluorescéine n'a pas été déposée plus loin que 15 cm autour du chemin le plus direct.

Une comparaison de ces résultats est effectuée avec la simulation numérique (Figure 6.36). Le modèle de transport des particules de fluorescéine développé précédemment et couplé au module CFD permet de comparer directement les concentrations de fluorescéine mesurées expérimentalement et celles théoriquement obtenues avec le champ de vitesse prédit par le modèle numérique.

Dans l'ensemble les résultats expérimentaux et numériques coïncident d'avantage que pour l'utilisation de TC et de SHT75. Les profils sont également plus lisses puisque les mesures sont des moyennes spatiales sur les volumes de laine de verre et temporelles sur les 7 heures de génération. En entrée d'isolant, les concentrations en fluorescéine expérimentales et numériques sont semblables mais diffèrent des profils de vitesse, ce qui semble confirmer l'importance du couplage avec le modèle de filtration. Cependant, pour les deux couches les plus en aval, certains écarts sont

observés entre les deux profils de concentration et la courbe expérimentale est légèrement au-dessus des profils de vitesse tandis que la concentration numérique légèrement en dessous.

Il apparaît donc que le modèle de filtration facilite la comparaison des résultats expérimentaux et numériques et pour les 3 cas testés ces résultats étaient cohérents entre eux. Le modèle a été validé seulement pour une gamme de vitesse restreinte (0.2 – 1.5 m/s), mais avec des vitesses maximales de 2.5 m/s, la majeure partie de l'écoulement se situe dans cet intervalle. Cependant, si le diamètre moyen des particules est de 0.18  $\mu\text{m}$ , sa distribution n'est pas connue. Etant donné que le modèle est relativement sensible à ce paramètre, il serait intéressant de déterminer la distribution de la taille des particules de fluorescéine et de l'ajouter comme entrée du modèle.

## **6.6. Comparaison des méthodes**

En conclusion, l'étude du chemin de l'air à l'intérieur des parois n'est pas aisée, mais les méthodes présentées dans cette étude ont donné des résultats cohérents. Chacune d'elles présente des avantages et des inconvénients (résumés dans le tableau ci-dessous) qui ont été révélés par ces tests et par la comparaison avec la simulation numérique. Par conséquent, la technique la plus adaptée dépend de l'objectif recherché et des paramètres de l'étude.



Méthode	Thermographie infrarouge (IRT)	Particle image velocimetry (PIV)	Thermocouples (TC)	Capteurs d'humidité relative (SHT)	Fluorescéine
Objectif	Identification des entrées/sorties d'air		Etude du chemin de l'air à l'intérieur de la paroi		
Précision de la mesure	+	+	+	-	+
Non-intrusivité	++	-	-	--	++
Facilité de mise en œuvre	++	-	+	-	--
Destructif?	Non	Oui	Non	Non	Oui
Mesures locales/moyennées	Locales <sup>2</sup>	Locales <sup>1</sup>	Locales	Locales	Moyennées (volume)
Facilité de corrélation avec le chemin de l'air	-	+	-	+	-
Avantage principal	Non-intrusif	Champ de vitesse obtenu près de la paroi	Bonne précision et réactivité des capteurs	Facilité de corrélation avec le chemin de l'air	Non-intrusif
Limitation principale	Inertie thermique & conduction	Mise en œuvre difficile	Inertie thermique & conduction	Intrusivité	Effet de filtration
Comparaison avec la simulation (écoulement isotherme seulement)	Bon accord pour une couche de laine de verre ; sous-estimation de la dispersion de l'air pour 2 couches	Bon accord (comparaison sur un cas seulement)	Relativement bon accord ; problème d'intrusivité mis en évidence pour l'interface « entrée »	Mauvais accord: forte surestimation de la dispersion de l'air due à une importante intrusivité des capteurs	Bon accord à l'exception de l'interface « entrée » <sup>3</sup>

<sup>2</sup> Pour l'IRT et la PIV, les mesures sont locales mais les champs respectivement de température et de vitesse sont obtenus directement, contrairement aux TC et SHT qui ne donnent qu'une mesure par capteur.

<sup>3</sup> Avec le modèle de filtration: bon accord pour la moitié amont de l'écoulement mais pas pour la partie aval.

## **Apports du travail et perspectives**

Cette étude contribue par plusieurs aspects et à différentes échelles à l'évaluation de l'impact des infiltrations d'air sur les performances d'un bâtiment.

### **Modèles pour prédire l'addition des infiltrations d'air naturelles et de la ventilation mécanique**

A l'échelle du bâtiment, des modèles ont été développés pour prédire la manière dont s'additionnent les débits d'infiltrations d'air naturelles et ceux d'une ventilation mécanique simple flux. Ils peuvent être utilisés pour différentes applications en fonction de si l'échelle de temps considérée est annuelle ou horaire, et de si le problème est direct ou inverse. On peut par exemple citer le cas annuel inverse qui correspond au dimensionnement de la ventilation mécanique pour assurer un débit de ventilation totale réglementaire en connaissant le niveau d'étanchéité d'un bâtiment.

### **Détermination des débits d'infiltration d'air induits par certains détails de constructions**

Les résultats des tests de pressurisation présentés dans cette étude peuvent être directement utilisés pour évaluer l'impact de parois ou de détails de construction spécifiques sur la perméabilité à l'air d'un bâtiment. Par exemple, le débit d'air supplémentaire induit par une absence d'étanchéité entre deux plaques de plâtre peut être exprimé en fonction de la longueur de cette jonction, et ainsi être utilisé pour des simulations numériques à l'échelle du bâtiment.

### **Etude de faisabilité pour des techniques expérimentales de tracé du chemin de l'air dans la paroi**

Le nombre d'études expérimentales sur l'étude du chemin de l'air à l'intérieur des parois étant très restreint, plusieurs méthodes ont été développées et/ou testées pour cette application. La fluorescéine est communément utilisée en tant que particules traceuses, mais la possibilité de l'utiliser pour tracer le chemin de l'air dans un isolant poreux a été vérifiée, et un protocole expérimental spécifique a été mis en place. Il a également été vérifié que la PIV pouvait être utilisée pour visualiser les infiltrations d'air en entrée de la paroi sans obstruction dues à la présence des particules traceuses.

### **Aide à la sélection de la méthode expérimentale la plus adaptée pour l'étude du chemin de l'air**

Cette étude a montré que chaque méthode expérimentale présente à la fois des avantages et des inconvénients, la méthode parfaite pouvant être appliquée à n'importe quel cas d'étude n'existe donc pas. Le choix de la technique la plus appropriée dépend fortement de l'objectif recherché et des paramètres de l'étude. A titre d'exemple, pour les mesures in situ, l'IRT sera préféré à la PIV, et s'il est possible d'instrumenter une paroi pendant la phase de construction, l'utilisation de la fluorescéine n'est pas envisageable étant donné le caractère destructif de cette méthode. En revanche, les mesures par fluorescéine peuvent être préférées pour des études en laboratoire pour éviter l'intrusivité des capteurs ou si des résultats moyennés dans le temps et dans l'espace sont préférés à des mesures locales et ponctuelles.

## **Validation de modèles numériques**

Il a été souligné que les parois à ossature bois peuvent être très différentes d'un bâtiment à l'autre, et si les principales sources d'infiltrations d'air sont connues, chaque défaut d'étanchéité est unique. Il n'est donc pas envisageable de caractériser chacun d'eux expérimentalement, mais des mesures fiables sur certains d'entre eux sont nécessaires pour valider des modèles numériques. Il n'est cependant pas possible de mesurer directement les champs de vitesse à l'intérieur de la paroi puisque les capteurs seraient trop intrusifs. Un certain nombre de méthodes alternatives ont été proposées et testées, reposant sur la mesure d'une autre grandeur physique, à savoir la température, l'humidité relative et la concentration en fluorescéine. Un modèle de filtration a été développé pour faciliter la comparaison entre les mesures expérimentales et les résultats numériques. Des améliorations peuvent encore y être apportées, notamment avec une caractérisation de la dispersion de la taille des microparticules, et des couplages similaires avec des modèles air-chaleur-humidité peuvent également être effectués pour les deux autres méthodes.

De plus, dans cette étude un certain nombre de configurations expérimentales ont été testées, et pour chacune d'elles les différents paramètres ont été explicités. Il est donc possible de simuler ces tests avec un modèle numérique quelconque pour une comparaison avec les résultats expérimentaux.

## **Transport de contaminants extérieurs à travers la paroi**

Enfin, en ouverture, une autre application pratique de ce travail concerne le domaine de la qualité de l'air intérieur, et plus précisément le transport de contaminants extérieurs par les infiltrations d'air à travers les parois. Cet aspect n'a pas été évoqué dans cette étude, mais la problématique scientifique est intimement liée à celle du transport des particules de fluorescéine. Les résultats des tests avec la méthode de la fluorescéine peuvent être utilisés avec le détail des caractéristiques de la laine de verre pour valider des modèles de filtration. Le modèle de Miecret et Gustavsson sélectionné pour cette étude semble montrer que le pourcentage de particules traversant 10 cm de laine de verre (HPGW) est non négligeable (>5%) seulement pour des tailles de particule comprises entre 0.05  $\mu\text{m}$  to 0.5  $\mu\text{m}$ , et pour des vitesses d'écoulement entre 0.1 m/s et 3 m/s. Ce type de modèle peut être appliqué à différents isolants, épaisseurs, vitesses d'infiltration et polluants pour évaluer le risque de contamination par l'air extérieur dans des configurations spécifiques.

# Contents

Remerciements (Acknowledgement).....	1
Abstract .....	3
Résumé (French abstract) .....	5
Résumé détaillé (French detailed summary) .....	7
1. Introduction.....	41
1.1. Context and problem statement.....	41
1.2. Aim and methodology.....	44
2. A review of experimental methods and laboratory studies on building airtightness: focus on timber frame constructions .....	47
2.1. Experimental approaches for wall airtightness study.....	47
2.1.1. Building air permeability indicators .....	47
2.1.2. Air permeability measurement methods.....	48
2.1.3. Complementary experimental methods for air permeability study .....	53
2.1.4. Synthesis.....	56
2.2. Experimental research on HAM transfer using built-up boxes.....	59
2.2.1. Experimental setups review .....	59
2.2.2. Instrumentation .....	59
2.3. Airtightness tests on timber frame wall assemblies .....	65
2.3.1. Tested wall assemblies.....	65
2.3.2. Tested airtightness defects .....	68
2.4. Conclusion .....	69
3. Inclusion of natural infiltration in building total ventilation rate calculations .....	71
3.1. Superposition background .....	71
3.1.1. Superposition issue .....	71
3.1.2. Prior work.....	73
3.1.3. Cases of interest .....	76

3.2.	Approach .....	76
3.2.1.	REGCAP simulation .....	76
3.2.2.	Simplified models .....	78
3.3.	Model comparison .....	83
3.3.1.	Simulation results .....	83
3.3.2.	Simplified models errors .....	83
3.3.3.	Discussion .....	84
3.4.	Conclusion .....	90
4.	Pressurization tests for airtightness characterization at the wall scale on timber frame construction .....	93
4.1.	Experimental setups .....	93
4.1.1.	Small scale – SAPI box .....	93
4.1.2.	Intermediate scale – APIE box .....	95
4.1.3.	Big scale – AEV test bench .....	96
4.1.4.	Verification of the experimental results reliability .....	97
4.1.5.	Synthesis and overview of the tests .....	99
4.2.	Insulation characterization .....	100
4.2.1.	Permeability measurements .....	100
4.2.2.	Impact of the density .....	103
4.3.	Simple wall assemblies .....	105
4.3.1.	Bond between the wall assembly materials .....	105
4.3.2.	Additivity of layers in a wall assembly .....	106
4.3.3.	Flow direction .....	108
4.4.	Tests on a real timber frame wall assembly .....	109
4.4.1.	Sealing between the gypsum boards .....	110
4.4.2.	Sealing of the vapor barrier .....	111
4.4.3.	Sealing of a window .....	112
4.4.4.	Use of the results for building scale simulations .....	112
4.5.	Conclusions .....	113
5.	Experimental investigations of the air path through an airtightness defect using a tracer technique .....	115
5.1.	Methodology .....	115
5.1.1.	Tracer selection .....	115
5.1.2.	Fluorescein micro-particles generator .....	116

5.1.3.	Fluorescein concentration measurement .....	116
5.1.4.	Insulation material .....	120
5.1.5.	Experimental protocol.....	120
5.2.	Preliminary tests.....	121
5.3.	Fluorescein micro-particles filtration model.....	124
5.3.1.	Theoretical study of the collection efficiency .....	124
5.3.2.	Coupled air flow-filtration model.....	133
5.3.3.	Experimental collection efficiency of the HPGW .....	134
5.4.	Air channel in contact with a porous medium .....	138
5.4.1.	Tests description .....	138
5.4.2.	Results .....	142
5.4.3.	Comparison with the simulation .....	146
5.5.	Conclusions.....	152
6.	Assessing the performance of different experimental methods to evaluate air dispersion in wall assemblies .....	155
6.1.	Description of the tested configurations .....	155
6.1.1.	Experimental study.....	155
6.1.2.	Numerical study .....	157
6.2.	Air inlet and outlet identification with IRT and PIV.....	159
6.2.1.	Infrared thermography.....	160
6.2.2.	PIV.....	164
6.2.3.	Comparison with the numerical simulation .....	172
6.3.	3-D grid temperature monitoring.....	173
6.3.1.	Preliminary tests.....	174
6.3.2.	Description of the tests .....	175
6.3.3.	Results .....	177
6.3.4.	Comparison with the numerical study .....	180
6.3.5.	Conclusion .....	182
6.4.	3-D grid relative humidity monitoring.....	183
6.4.1.	Preliminary tests.....	183
6.4.2.	Description of the tests .....	185
6.4.3.	Results .....	188
6.4.4.	Comparison with thermocouples and with numerical studies .....	190
6.4.5.	Conclusion .....	191

6.5. Fluorescein study.....	192
6.5.1. Fluorescein tests.....	192
6.5.2. Comparison with the numerical study .....	195
6.6. Comparison of the methods and discussion .....	197
Conclusion .....	201
Publications .....	207
References.....	209
Appendices .....	219
A. Optimization of the advanced quadrature model .....	221
B. Optimization of the exponential models .....	223
C. Impact of the simulation parameters on the sub-additivity coefficients.....	225
D. APIE box sizing using CFD (OpenFoam).....	227
E. Full results of the CETT fluorescein tests.....	230
F. Full results of the COMSOL simulation for the air channel study .....	232
G. COMSOL simulation results .....	243
H. Full results of IR thermography tests.....	246
I. Full results of PIV Tests.....	248
J. Full results of the 3-D thermocouple grid tests .....	255
K. Full results of the 3-D relative humidity sensors grid tests.....	258
L. Full results of the fluorescein tests.....	261

# Nomenclature

## Roman symbols

A	absorbance	-
ACH	air change per hour	$h^{-1}$
c	leakage coefficient	$m^3/(hPa^n)$
C	concentration	$kg/m^3$
$C_c$	Cunningham correction factor	-
CE	collection efficiency	-
d	diameter	m
D	diffusion coefficient	$m^2/s$
DR	density ratio	-
E	relative error between the model and the simulation	-
f	frequency	$s^{-1}$
J <sub>i</sub>	junction i	-
k	intrinsic permeability	$m^2$
$k_B$	Boltzmann constant	J/K
$k_d$	deposition factor	$s^{-1}$
$k_{fw}$	forward exponential model coefficient	-



$k_{inv}$	inverse exponential model coefficient	-
Ku	Kuwabara hydrodynamic factor	-
L	length	m
m	mass	kg
MP	mass percentage	%
n	flow exponent	-
N	number of particles collected	-
$n_{ppi}$	number of pairs of particle images	-
P	pressure	Pa
$p_v$	vapor pressure	Pa
$p_{vs}$	saturation vapor pressure	Pa
Q	leakage rate through the envelope or building component	$m^3/h$
$r_{SD}$	radius of the simulated domain	m
S	cross-sectional area to flow	$m^2$
t	time	s
t	thickness	m
T	temperature	K
v	flow velocity	m/s
V	volume	$m^3$

### **Greek symbols**

$\alpha$	infiltration fraction	-
----------	-----------------------	---

$\beta$	advanced quadrature coefficient	-
$\eta$	collection efficiency of a single fiber	-
$\lambda$	mean free path	m
$\Omega$	filtration surface	m <sup>2</sup>
$\mu$	dynamic viscosity	Pa/s
$\nu$	kinematic viscosity	m <sup>2</sup> /s
$\Phi$	sub-additivity coefficient	-
$\rho$	density	kg/m <sup>3</sup>
$\varphi$	porosity	-

## Subscripts

//	parallel
⊥	perpendicular
0	initial
50	at a reference pressure of 50 Pa
a	annual (Chapter 3)
a	air
AC	air channel
AG	air gap
acqu	acquisition
f	fan (Chapter 3)
f	fiber

fluo	fluorescein
fw	forward problem
h	hourly
in	inlet
inf	infiltration
inv	inverse problem
m	measurement
out	outlet
p	particle
r	relative
sim	simulation
t	total

### **Dimensionless numbers**

Pe	Peclet number
Re	Reynolds number
Stk	Stokes number

### **Abbreviations**

CFD	Computational fluid dynamic
GB	gypsum board
GW	glass wool

HAM	heat air moisture
HPGW	high permeability glass wool
IRT	infrared thermography
LPGW	low permeability glass wool
MFP	multifuncional plate
OSB	oriented strand board
PIV	particle image velocimetry
PCC	plastic-coated cardboard
RH	relative humidity
TC	thermocouple
VB	vapor barrier
WA	warm area



# Chapter 1

## Introduction

### 1.1.Context and problem statement

#### Over consumption of energy resources

In 2000 the Earth Overshoot Day was in October, in 2016 it fell on August 8<sup>th</sup>. We have used in only eight months the resources needed to live sustainably for a year and since then we are maintaining our ecological deficit by consuming local resource stocks and by accumulating CO<sub>2</sub> in the atmosphere. This is one of many reminders that we are living well beyond our means, with serious consequences already apparent such as the occurrence of extreme weather events (droughts, storms, floods), the loss of animal and plant species, and the sea level rise threatening entire island nations.

With the population growing rapidly, the situation is increasingly alarming. We are facing a major challenge to rethink our relationship with energy, to rely more on renewable resources but also to decrease our global energy demand. Some people, scientists and governments are meeting this challenge at all scales and by a wide range of actions. In 2015 99% of Costa Rica's electricity came from renewables; Sweden announced recently an ambitious goal of having 100% of its energy consumption coming from renewables by 2040 and in France a study [1] by the government agency ADEME stated that a 100% renewable power system is not only feasible but also economically attractive. In December 2015, 195 countries signed the Paris agreement in an attempt to limit global warming to below 2°C.

The energy demand in the building sector is steadily increasing with the world population, the level of desired indoor comfort and the time spent inside buildings, reaching between 20% and 40% of energy consumption in developed countries [2]. This sector has therefore an active role to play in the efforts towards a reduction of the global energy demand. Net-zero energy buildings (NZEB) are emerging around the world with an energy production meeting the needs over the course of a year. They require the implementation of renewable energy systems, often photovoltaic panels, but also highly efficient buildings designed to minimize energy requirements.

## Air permeability issue in buildings

The air permeability of the envelope is one of the crucial parameters for this purpose. It characterizes the building's ability to permit air leakage which is the unintended air flow through the envelope due to a pressure difference between the inside and outside. Up to 53% of the ventilation heating energy in buildings is indeed lost due to uncontrolled air leakage [4] and a bad airtightness can lead to a 25% over-consumption of energy for high performance buildings [3]. Logue et al. [4] found that improving airtightness of all homes in USA at current average retrofit performance levels would decrease the annual energy consumption by 0.74 EJ (206 TWh) and upgrading all homes to be as airtight as the top 10% of similar homes would double the savings, leading to roughly \$22 billion in annual savings in energy bills. Jones et al. [5] found that the unintended infiltration is responsible for 3-5% of total UK energy demand, 11-15% of UK housing stock energy demand, and 10-14% of UK housing stock carbon emissions. As a result, standards for highly efficient buildings such as Passivhaus, Minergie-P and Effinergie generally include a minimum airtightness level. This is also more and more the case for national building codes with airtightness testing mandatory in some countries such as the United Kingdom, Ireland, France, Denmark and Portugal.

There is a large variety of airtightness defects allowing the air to go through walls either by infiltration (outdoor air entering the building) or exfiltration (indoor air leaking out) depending on the pressure gradient direction. Measurement campaigns such as the one carried out in France by the CETE [6] enable to identify the most common ones (cf. Figure 1.1). They can either provide a direct air path between the exterior and the indoor (e.g. windows and doors edges) or just allow the air to enter the wall assembly. In the latter case the air can then circulate between the layers and through porous media such as insulation materials until finding a way out. One should note that airtightness defects may either exist from the construction of the building or emerge over time with for example the drying and shrinking of the framing.

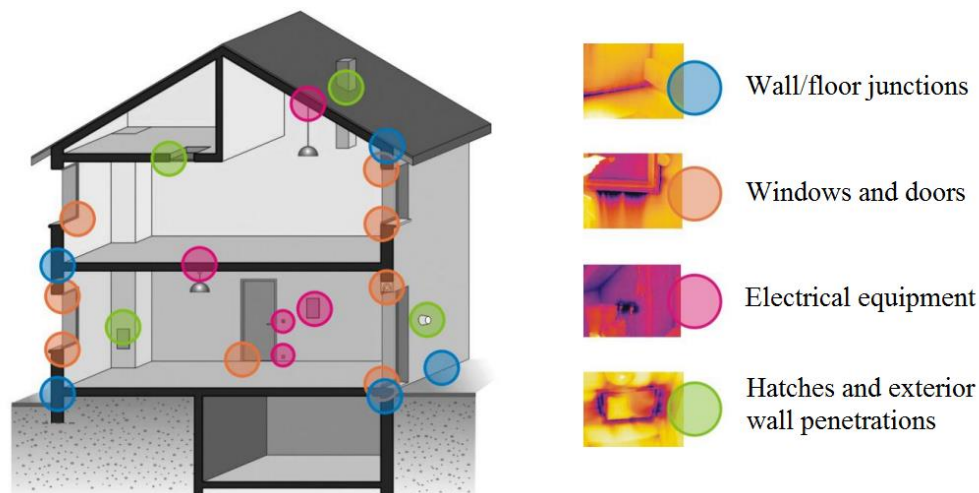


Figure 1.1 – Typical locations of air leakage in dwellings [6]

The airtightness issue affects not only the heating load but also the indoor air quality since the air can introduce outdoor pollutants or pick them up (fibers, dust, mold, volatile organic compounds, etc.) when passing through the wall [3]. As an example field measurements in Finland [7] revealed the presence of fungal spores indoors that had been transported from a crawl space. Moisture damages

can also occur because of leakages, thus increasing the heat transfer and threatening the longevity of the building itself [8]. Air leakage also affects the acoustic insulation regarding to outside noise [9]. Finally, it can disrupt the proper functioning of mechanical ventilation and create under-ventilated areas.

There is therefore a need of both modeling and experimental studies to understand and predict the airtightness of a building, its interactions with wall assemblies, and find solutions to improve it.

### **Timber frame buildings and air permeability**

As its name implies, timber frame is a method of construction with a load-bearing structure made of timber instead of a steel frame or concrete blocks. It is one of the oldest forms of construction that still exists today. It is widely used in the United States and in Europe, especially for houses and low-rise buildings. Tykkä et al. [10] pointed out that it is the most common method of building in some regions such as in Scotland or Sweden. In France 12% of newly-built individual houses were timber frame in 2013 against a few percent in 2000 [11].

Timber frame buildings had a period of decline with the industrial and technical development during the 19<sup>th</sup> and 20<sup>th</sup> century. The growing environmental concerns are however giving this method of building a new impetus. In western countries people tend to seek to live closer to the nature and give increasing importance to ecology, quality of life and genuine comfort. Timber is a natural and renewable resource that does not release toxic chemicals in the ambient air. Moreover its use for constructions generally results in lower energy use and CO<sub>2</sub> emissions than does the use of concrete [12]. As an example, Goverse et al. [13] stated that an increased share of wood use in the Dutch residential construction sector can lead to a 12% CO<sub>2</sub> emission reduction in the short term.

The timber frame construction has other advantages than the ecological aspect, including the flexibility of design; the possibilities of prefabrication, modular construction, and mass-production; a good fire resistance and the fact that it can be rapidly erected (in a few days rather than a few weeks for an average-sized house). Last but not least, the insulation material is contained within the depth of the structure, which allows thinner walls or more energy efficient envelopes for the same thickness.

Despite its various benefits, the timber frame method of building has also some disadvantages, including the tight tolerances requiring a high degree of accuracy during the construction. It is structurally more complicated than a masonry building, with many layers, control membranes and joints. Air barrier systems combined with the sealing of all the joints and intersections in the interior sheathing enable to meet very high airtightness levels [14] but the process is time-consuming and require a number of controls during the construction. Hrubá et al. [15] recorded multiple incidents of permeability during the insulation process of a passive building. The complexity of the structure can indeed easily lead to assembly problems and defects in the moisture or airtightness protection.

This construction method is therefore facing a challenge to meet the gradually tighter building codes on airtightness requirements while optimizing the sealing process to avoid an excessive amount of time dedicated to this task.



## 1.2.Aim and methodology

### MOB-AIR research project

The work presented here is part of a 4-year research project called MOB-AIR (*Maîtriser les transferts d'AIR et leur impact sur le comportement hygrothermique des Maisons à Ossature Bois*). MOB-AIR aims at investigating the air transfer in timber frame houses and its impact on the hygrothermal behavior of the envelope. It is funded by the French National Agency of Research ANR and brings together several research centers besides LOCIE and several companies: CETHIL (The Center for Thermal Sciences of the Université de Lyon) ; EDF R&D (Electricity of France) ; CSTB (Scientific and Technical Center for Buildings) ; FCBA (French Institute of Technology for forest based and furniture sectors) ; Aldes (Manufacturer of ventilation products and systems) ; Albedo Energie (engineering consultancy company in sustainable structures) and Wigwam (engineering consultancy company in environmental optimization of buildings).

The objective of the project is three-fold:

- (1) Collect experience feedback from the timber frame construction professionals in order to identify both typical airtightness issues and potential innovations to simplify its implementation.
- (2) Carry out a number of experimental studies to improve knowledge on the heat air and moisture transfer and to provide data for numerical models validation.
- (3) Developing models both at the wall and at the building scales to investigate the air transfer inside timber frame assemblies and its impact on the hygro-thermal behavior of the building envelope.

### Aim of the present study

The present study contributes mainly to the second objective of this research project with the experimental investigation of the air transfer and more specifically the air path inside timber frame wall assemblies.

It is indeed currently impossible to achieve a perfect sealing of the envelope. Despite specific attention paid on airtightness during the construction, there will always be air infiltrating the wall and impacting its performance. As mentioned before, one consequence is the occurrence of moisture damages increasing the heat transfer and threatening the longevity of the building. Paradoxically, the tightest envelopes are not necessarily the one with the lowest risks since the air also exits less easily the wall assembly once infiltrated.

As a result there is not only a need for finding technical solutions to improve air permeability but also for evaluating the impact of air leakage on the performance of wall assemblies. This latter aspect has been less studied so far. The physics is complex with coupled heat air and moisture transfer, both diffusion and convection phenomena and a mix of porous, airtight, hygroscopic and non-hygroscopic materials. A few numerical models have been developed, but reliable experimental data are required to validate them. This study contributes to this end, with the development, testing, and comparison of various experimental methods for the air transfer investigation inside wall assemblies.

## **Methodology**

A review of experimental methods and studies on building airtightness is first presented in Chapter 2. It provides a background for the rest of the study on several aspects, such as the choice of experimental techniques, the design of the experimental set-up, the appropriate instrumentation and the previously studied airtightness defects on timber frame wall assemblies.

The air permeability issue is then first investigated at the building scale in Chapter 3. A numerical study is carried out on a wide range of housing and weather conditions to establish models for the inclusion of natural infiltration in building total ventilation rate calculations. The study was carried out as a visiting researcher at the Lawrence Berkeley National Laboratory.

In Chapter 4 the air permeability is no longer considered at the building scale, but measured for specific timber frame wall assemblies, components and construction details. Two experimental set-ups are built up and are used together with a third existing one for pressurization tests carried out at three different scales.

In the last two chapters the experimental studies are even finer with a focus on the air path investigation inside the timber frame wall assemblies. It is relatively easy to identify the air inlets and outlets in the wall but there are very few experimental studies on the flow behavior inside it. In Chapter 5 an innovative method is developed and tested, using tracer micro-particles to track the air flow inside the insulation layer. A filtration model is also developed to facilitate the comparison between the tracer particles concentration mapping and the velocity field. Finally, in Chapter 6 a case study is presented with a comparison between this method, other experimental ones and a numerical model.



## Chapter 2

# A review of experimental methods and laboratory studies on building airtightness: focus on timber frame constructions

This chapter is a review of the experimental methods and laboratory set-ups implemented for the wall airtightness study, with a particular focus on the timber frame assemblies. The advantages, drawbacks and scope of the various experimental approaches, both quantitative and qualitative, are discussed. This provides a background on the choice of the experimental techniques for the present study and points out the lack of studies and methods for the air path investigation inside the wall assembly.

The heat and moisture transfer are also of interest, even if they are monitored for the air path investigation only. The instrumentation and the experimental set-ups implemented in laboratories for the heat air and moisture (HAM) transfer studies are therefore also presented. Finally the case of timber frame buildings is detailed further with a review of the wall assemblies and the airtightness defects tested so far.

### 2.1. Experimental approaches for wall airtightness study

In this section the focus is on the experimental setups implemented for the airtightness study of building envelopes, wall assemblies or wall components. Several techniques are available and the most appropriate one depends if the aim is to measure the air permeability, identify the location of air leakage, study the air path inside the wall or characterize the air flow resulting from infiltrations.

#### 2.1.1. Building air permeability indicators

One can characterize the airtightness of a component by measuring the crossing air flow for a given pressure difference. At the building scale, the leakage rate through the whole envelope  $Q$  is conventionally measured for a pressure difference between the interior and exterior sides  $\Delta P$  of 50 Pa or 4 Pa. Under natural conditions the wind load  $\Delta P_w$  (Pa) is expressed as:

$$\Delta P_w = C_p \frac{\rho_a v_a^2}{2} \quad (2.1)$$

Where  $\rho_a$  is the air density ( $\text{kg/m}^3$ ),  $v_a$  (m/s) the wind velocity and  $C_p$  the pressure coefficient (-) which depends on the size and shape of the building, the wind direction and the shielding effect by surrounding topography or buildings. As an indication for low-rise buildings, 4 Pa corresponds to a pressure difference generated by a light breeze (about 10 km/h) whereas a 50 Pa difference occurs in case of stronger winds (>30 km/h). The average pressure under natural conditions is close to 1 Pa but the measure has to be taken at higher pressure values to minimize the impact of the wind and the stack effects.

In order to compare the airtightness performance of buildings and to set norms and standards, the leakage rate measured can be divided by the:

- Internal building volume  $V_{\text{build}}$ : the resulting indicator is the air change rate, noted  $n_{50}$  or  $\text{ACH}_{50}$  if taken at 50 Pa ( $\text{h}^{-1}$ )
- Envelope area  $A_{\text{env}}$  : the resulting indicator is called the air permeability and is noted  $q_{50}$  ( $\text{m}^3/(\text{h}.\text{m}^2)$ ) at 50 Pa and  $q_4$  at 4 Pa.
- Floor area  $A_{\text{floor}}$ : the resulting indicator is the specific leakage rate, noted  $w_{50}$  ( $\text{m}^3/(\text{h}.\text{m}^2)$ ) at 50 Pa.

A more visual indicator is the effective leakage area (ELA). It corresponds to the area of a unique orifice through which, for a given pressure difference, the air flow would be the same as the envelope leakage rate measured.

Some very low energy labels have minimum requirements for building airtightness. By way of example, the standards *Passivhaus* and *Minergie-P* require an airtightness  $n_{50} \leq 0.6 \text{ h}^{-1}$ , which corresponds approximately to  $q_4 = 0.16 \text{ m}^3/(\text{h}.\text{m}^2)$  and to an ELA of  $56 \text{ cm}^2$  [16]. In France, the airtightness performance of a new building is systematically tested at 4 Pa and has to meet a reference value (RT 2012):  $q_4 < 0.6 \text{ m}^3/(\text{h}.\text{m}^2)$  for individual houses and  $q_4 < 1 \text{ m}^3/(\text{h}.\text{m}^2)$  for collective dwellings.

The various experimental methods used to measure the air leakage are described below.

### 2.1.2. Air permeability measurement methods

#### Pressurization test

Studies are multiplying on the buildings airtightness characterization and various experimental techniques are emerging. The most commonly used one is the pressurization test which consists in generating incremental pressures between the interior and exterior sides of the tested wall or envelope  $\Delta P$  (Pa) in order to measure the induced volumetric flow rate  $Q$  ( $\text{m}^3/\text{h}$ ) [17]:

$$Q = c. \Delta P^n \quad (2.2)$$

Where  $c$  ( $\text{m}^3/(\text{hPa}^n)$ ) is the leakage coefficient characterizing the air permeability and  $n$  (-) is the flow exponent ranging from 0.5 to 1 and giving an information on the flow regime. Values close to 0.5 correspond to turbulent flows obtained with large leaks such as orifices whereas values close to 1 indicate laminar flow conditions. For a building envelope  $n$  is normally found to be in the vicinity of 0.65 [18].

During the pressurization tests applied pressure differences are higher than those encountered under natural conditions to ensure that measured air flow rates are greater than uncertainties. A usual range is from +/- 10 Pa to +/- 100 Pa [19]. However one should be careful with the fact that the higher the pressure is, the more artificially distorted the openings become and the larger the extrapolation error becomes [20]. Moreover for in-situ measurements the test should be conducted during periods of low wind speed to improve the accuracy ([21] and [22]).

- **In-situ tests**

The pressurization test on existing buildings is usually carried out using a blower door installed in the frame of an exterior door ([23],[24],[25],[26] and [27]). As illustrated in Figure 2.1, it is a device composed of a powerful variable-speed fan capable of creating a significant positive or negative pressure difference between the inside and outside and a manometer measuring this pressure difference induced for a given air flow rate. All the ventilation openings are previously sealed, the exterior windows and doors closed, so that the air is forced to go only through the envelope airtightness defects. The repeatability of this technique was tested several times in the past decades ([21], [28] and [29]) and with up to 48 pressurization tests carried out on the same house in a 5 months period [30]. The results of these studies are in rather good agreement with each other, the standard deviation is found to be between 1.1% and 2.7% and a maximum variation between 3.5% and 7.7%.

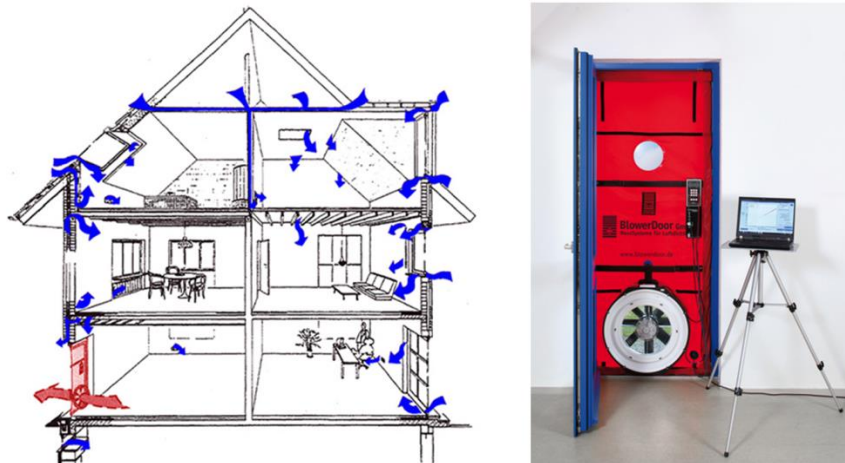


Figure 2.1 – Pressurization test with a blower door (Source: BlowerDoor GmbH)

One can note that this technique can also be applied for multizone air leakage measurements in order to determine the air leakage between adjacent zones or to the outside from a single unit. This enables a finer analysis than a single envelope permeability measurement and it has been found in different studies ([31], [32] and [33]) that the air leakage is not uniform as often assumed ([34] and [35]). Several methods can be applied for this multizone approach but the two-door tests seems to give lower uncertainties [36].

In order to also take into account the infiltrations through the exterior door, it is possible to use a Permeascope developed by the company Aldes [37]. The difference with the blower door is the fact that the fan is located inside the building and blows the air in the ventilation ducts. As a result it has the advantage to also take into account the air leakage through the exterior door where the blower door would have been installed, which is often the greater source of leakage for small buildings.

In case of large scale buildings, the fan is sometimes not powerful enough to significantly pressurize the building. It is then possible to use the supply fan of the air-handler as a complement or instead of the blower door for the building pressurization ([38] and [39]).

- **Laboratory measurements**

Specific materials or wall assemblies are also tested in laboratories thanks to the pressurization technique ([40], [41], [42] and [43]). As further discussed in paragraph 2.2.1, this requires the construction of airtight boxes linked with a fan to either pressurize or depressurize it. The tested wall or material can serve as a side wall of the box, the transfer being made with the ambient air, or can subdivide the box into two controlled atmospheres. The air transfer study is often linked with the heat and humidity ones (HAM transfer).

Compared with in-situ tests, laboratory measurements enable to have more local measurements for example on an individual window but they have the disadvantage of swaying from the real conditions. However on research purposes it is often necessary to be able to control the atmosphere, add sensors in the wall assembly, use destructive methods, and so on. Tests with a single layer can also constitute a way of characterizing a material airtightness.

As an example of the possibilities offered by laboratories studies, in the research program called PREBAT MININFIL [44] 4 pairs of airtightness defects (exterior panel – interior panel) were modeled with given numbers of calibrated holes inducing the same pressure-flow rate phenomenological laws than those found in the literature :

- Wall/floor junction (50 holes) - Wall/ceiling junction (50 holes)
- Wall/exterior joinery junction (25 holes) - Electrical outlet (25 holes)
- Wall/exterior joinery junction (25 holes) - Wall/ceiling junction (50 holes)
- Electrical panel (100 holes) - Electrical outlet (25 holes)

The holes diameter is set to obtain the right flow exponent  $n$  (2mm for 0.6) whereas the number of holes will enable to reach the right leakage coefficient. An insulation layer is then added between the two wall panels to study the changes induced on the phenomenological laws.

- **Unsteady pressurization tests**

One should note that if such steady pressurization tests are the most common ones; there are also a number of alternative unsteady methods:

- The oscillation (AC) method uses a cylinder and piston assembly sealed into a door or window to generate sinusoidal pressure fluctuations. This technique was developed by Sherman et al. [45] and implemented in a number of studies ([46] and [47]). The interior pressure response is measured synchronously to the volume oscillation in order to eliminate the pressure fluctuations caused by the weather. Sharples and Thompson [48] have however found that the average flow under fluctuating pressure differentials does not differ significantly from the flow which would occur if the mean pressure differential were imposed.

- The decay method for which the air flow pressurizing the building is stopped suddenly and the leak rate is calculated based on the change in pressure over a certain period of time ([49] and [50]). The main advantage of this method is that it requires the measurement of only one physical parameter (the pressure difference) and it is also less time-consuming. It has however a number of limitations such as the necessity of a device to seal quickly the channel through which the building is pressurized, the high amount of measurement points required per second (>20/s for large air flow rates), and the sensitivity to pressure-dependent deformations of the envelope.
- Similarly, pulse methods are based on the measurement of the pressure difference over time. Carey et al. [51] used a simple gravity driven piston device and found that the steady pressurization test was preferable for most buildings, with the exception of large ones for which the steady technique becomes increasingly inaccurate. Cooper et al. have however improved the system by using a compressed air supply tank [52] and a nozzle pressurization technique [53]. They found that their device was giving more accurate low pressure leakage measurements than the blower door technique. It has the advantage of being compact, portable and of not needing to penetrate the building envelope. It can however only pressurize the building (no depressurization possible) and does not generate enough flow to identify individual leakage pathways using smoke or thermography. It could be a promising technique but it is not commercialized yet.

### **Tracer gas**

Tracer gas can be used for air change rate measurements in a building by monitoring the evolution of their concentration with time and hence evaluating the rate of air flow between seeded and unseeded zones ([37] and [19]). The main advantage of this technique is that the flow is measured under real conditions, without forcing it with a pressurization or depressurization of the building. However, depending on the study purposes, this advantage can also turn into a disadvantage since the result is more strongly dependent on the exterior conditions such as the wind velocity.

The tracer gas has to be inert, non-toxic, measurable at low concentrations and not normally present in the atmosphere. Several gases meet these criteria including nitrous oxide, sulfur hexafluoride and various per fluoro tracers. Carbon dioxide gas is present in the atmosphere but it is also used mainly because it is the cheapest solution.

In order to avoid errors in the measurements, the tracer gas has to be evenly mixed throughout the volume. It can be difficult for large buildings which makes the technique more appropriate to small building envelope characterization or multizone analysis. A study estimated the uncertainty of the calculated air flows due to errors in the measurements of tracer gas data lower than 10% for multizone analysis [54]. Several measurement techniques can be used depending on the application:

- Concentration decay: measurement of the tracer concentration evolution over time. It is easy to set up and gives good results, which makes it the most commonly used method
- Constant concentration: measurement of the rate at which the tracer needs to be released to maintain a target concentration. This method can give more accurate results but is also more expensive



- Constant emission: the air-leakage rates are obtained from a tracer gas balance. It requires a high amount of gas consumption but it can be appropriate to long-term observations

As pressurization tests, tracer gas enable also to characterize the airtightness of a single building component or a single construction layer [55].

There is a rule of thumb attempting to relate the blower door data for a 50 Pa pressurization and the air flow under natural conditions obtained with tracer gas measurements [56]:

$$ACH_4 \sim \frac{ACH_{50}}{20} \quad (2.3)$$

Correction factors can be applied depending on the building height, but this relation can be used only as an approximation.

A study on the airtightness of 20 single-family buildings in Greece [57] was carried out using both the tracer gas decay method (natural ventilated building) and the blower door test method (50 Pa pressure difference). The average number of air changes per hour was 0.6 ACH for the first one and 7 ACH for the second one. For each test the houses were classified into three categories namely low, medium and high airtightness, but only 6 houses were in the same category according to the two methods. It points out that both tests give valuable information for qualitative comparison but they are not equivalent.

### **Acoustical method**

A characterization of the walls airtightness is also possible by an acoustical method, measuring the sound wave attenuation induced by the passage through the wall. Experiments have been carried out in the eighties ([58] and [59]) without determining useful correlation laws.

More recently Lordache and Catalina [9] have done a measurement campaign on a building façade with double pane wooden windows. The experimental set-up is presented in Figure 2.2: the sound transmission loss was measured with sonometers (between 27 and 33dB) and the infiltration air flow rate was measured using a blower door (between 2 and 10 ACH depending on the windows sealing). They found that the two phenomena are inverse correlated and their relation is described by a second degree polynomial function with a correlation coefficient  $R = -0.9958$ . The error of this acoustical measurement was estimated to be around 5% which is in the range of a usual standardized building airtightness measurement [17] and [54].

They pointed out that this method is faster and more economical than the use of a blower door since it only requires a noise source and two sonometers, and it has the advantage to decrease the results dependence on weather conditions. However even if the developed mathematical model can then replace permeability measurements, the fact that it is a semi-empirical one prevents from a generalization to other building components.

Hassan [60] established a more general model to evaluate the air infiltration rate as well as the leakage area of a building component. The determination of the sound absorption requires the reverberation time of the building component, but if laboratory measurements are not possible a theoretical value may be calculated. This can however be tedious since the overall influence of surface materials, furniture items and decorations in the room must be considered.

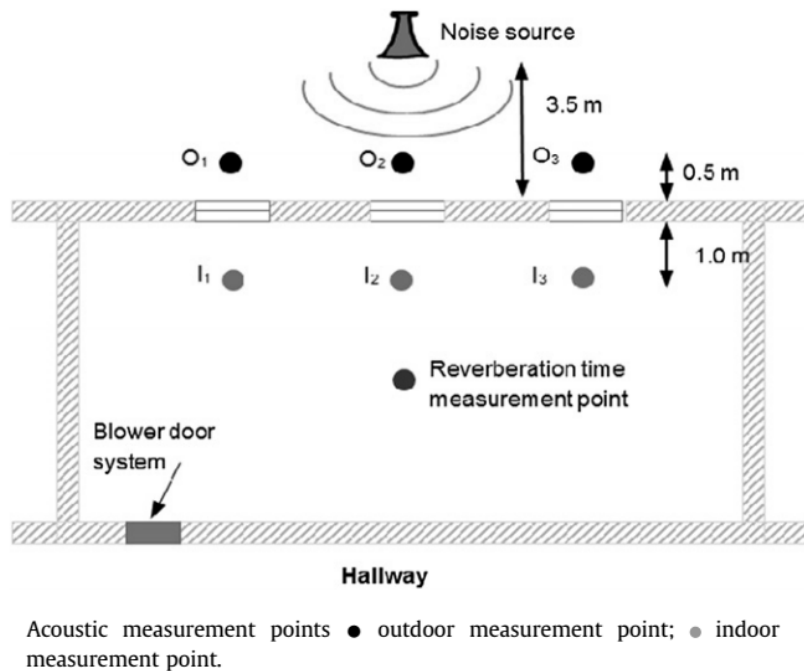


Figure 2.2 – Experimental set-up for a dual window permeability characterization - air and noise transfer study [7]

Varshney et al. [61] have also used acoustic for the study of the infiltration through various types of holes and cracks. They developed a correlation between sound transmission loss and air infiltration through small apertures. This correlation obtained in laboratory was tested in 5 buildings and the results were in good agreement with the blower door tests. It is applicable only to individual small airtightness defects which can be an advantage for finer air permeability studies but makes difficult the global building envelope characterization. As pointed out in the study, there might be holes in the building which are not easily visible or which exist only on one side of the envelope and in that case the air infiltration cannot be measured using this method. Moreover, this technique can hardly be performed in a noisy environment.

### 2.1.3. Complementary experimental methods for air permeability study

#### Infra-red thermography

The previously listed techniques enable to possibly quantify the total air leakage and the induced heat losses but they don't give information on the location of these leakages. For that purpose it is possible to use infra-red cameras detecting insulation defects, thermal bridges, and the airtightness defects.

Infrared thermography is based on the capture of the infrared energy emitted and reflected by the surface of an object and its conversion into a thermal image (thermographs) giving the apparent temperature field [62]. This is a popular and widely employed non-destructive method for building diagnostics, which is easy and fast to carry out. One can distinguish two approaches: the passive one measuring the temperature differences under normal conditions and the active one using an external heat source to generate or increase the temperature differences [63]. The greater the difference of temperature between the two sides of the wall is, the better the accuracy is [64]. This test can also be combined with the pressurization method in order to increase the leakage and therefore facilitate their detection.

As shown in Figure 2.3, thermography can be a valuable tool during the construction process to enable early identification of thermal performance issues and carry out appropriate remedial work [65].

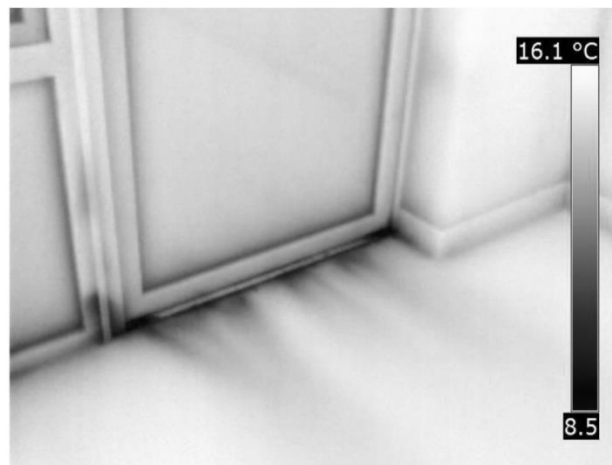


Figure 2.3 – Air leakage below a balcony door identified using thermography [65]

### Smoke visualization

Another way of identifying the location of air leakage is to combine a pressurization test with the emission of smoke from a smoke stick or puffer next to potential sources of leaks. The pressure difference should be high enough to clearly identify the flow of smoke from inside to outside [14] and [19].

### Temperature and moisture sensors

Air transfer through wall assemblies can also be studied coupled with heat and moisture transfer. A laboratory study from Concordia University ([66] and [67]) showed the correlation between air leakage paths induced by various airtightness defects and these two other transfer by monitoring the temperature (3D grid) and moisture (2D grid) fields inside the wall. As shown in Figure 2.4 three air leakage paths within exterior walls were studied, namely a long, a direct and a diffused one. Both interior and exterior conditions were controlled, with different temperature and humidity conditions. The air exfiltration modified the hygrothermal fields along its path, giving information on the location of the air flow.

192 thermocouples were installed on two planes within the assembly corresponding to the warm and cold sides of the insulation layer. They monitored the warming of the materials in contact with exfiltrating air. The differential isotherms generated give therefore valuable information on the air trajectory. The temperature maps obtained with this method can be considered similar to infrared thermographic images that would have been taken inside the wall rather than at its surface. It was possible to compare them with temperature fields calculated without the air leakage, thus providing quantitative information on the effect of air leakage on temperatures.

The moisture content was monitored in the fiberboard sheathing thanks to a two-dimensional grid of 144 removable gravimetry samples (38 mm in diameter). The results are displayed in the form of

isohygrons (contour lines of equal moisture content). It was established that the measurement of the moisture actually stored in the material provides more reliable information on the air path than the measurement of the temperature which is more sensitive to the actual air temperature and rapid variations in the air path.

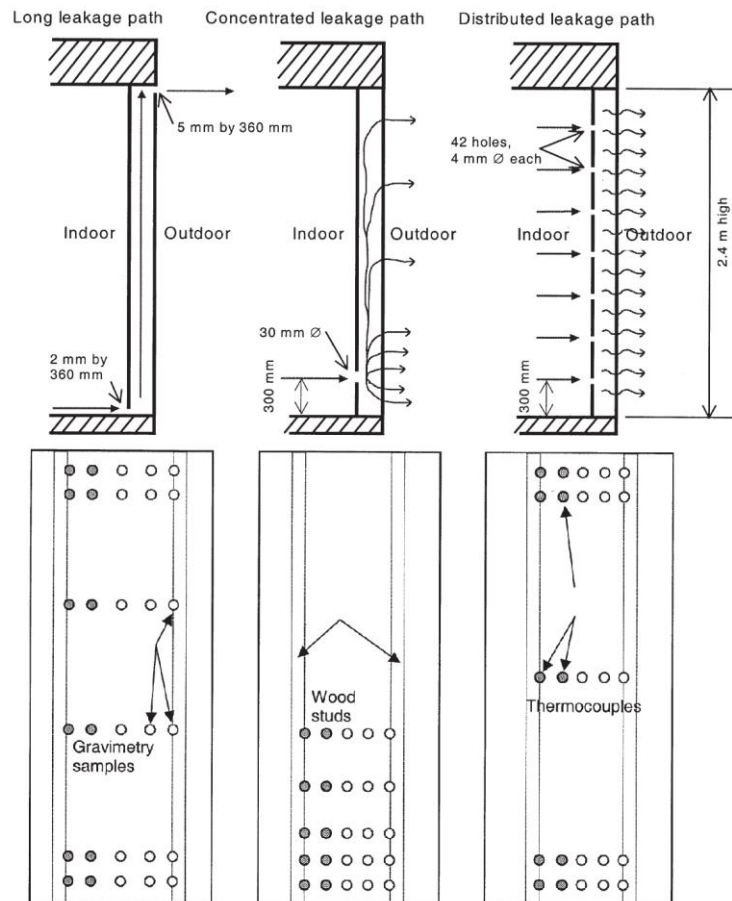


Figure 2.4 –Air leakage paths studied and corresponding monitoring grid implemented

A similar approach was used in 1995 by Ojanen and Simonson [68] to study the convective moisture accumulation in structures with additional inside insulation. Small wooden samples were placed at the interface between the old and new walls to measure the moisture content, and the temperature and moisture measurements enabled to determine the air flow direction. However, in this study the building envelope was airtight and there was therefore no air infiltration or exfiltration. The air flow was due to the temperature difference creating natural air convection of the indoor air at the interface between the old structure and new insulation layer.

### Holographic interferometry

Research about the visualization of the leakage flow has been carried out between 1986 and 1989 at the University of Joensuu in Finland ([69], [70] and [71]). In this region where each year temperatures can go down to  $-30^{\circ}\text{C}$  during several weeks, the issue of the air leakage understanding emerged well before the development of the passive house concept. The visualization was done by means of double exposure holographic interferometry. This technique enables to track changes in an object (air in this case) by comparing two states corresponding to the two exposures. The resulting fringes, called interferogram, are displacement iso-amplitude curves.

The laser optical path and the experimental set-up to visualize the leakage flow of a window are shown in Figure 2.5, as well as the resulting interferogram of a 3 mm wide and 8 mm high crack in the window sealing tape (at the bottom left of the photograph).

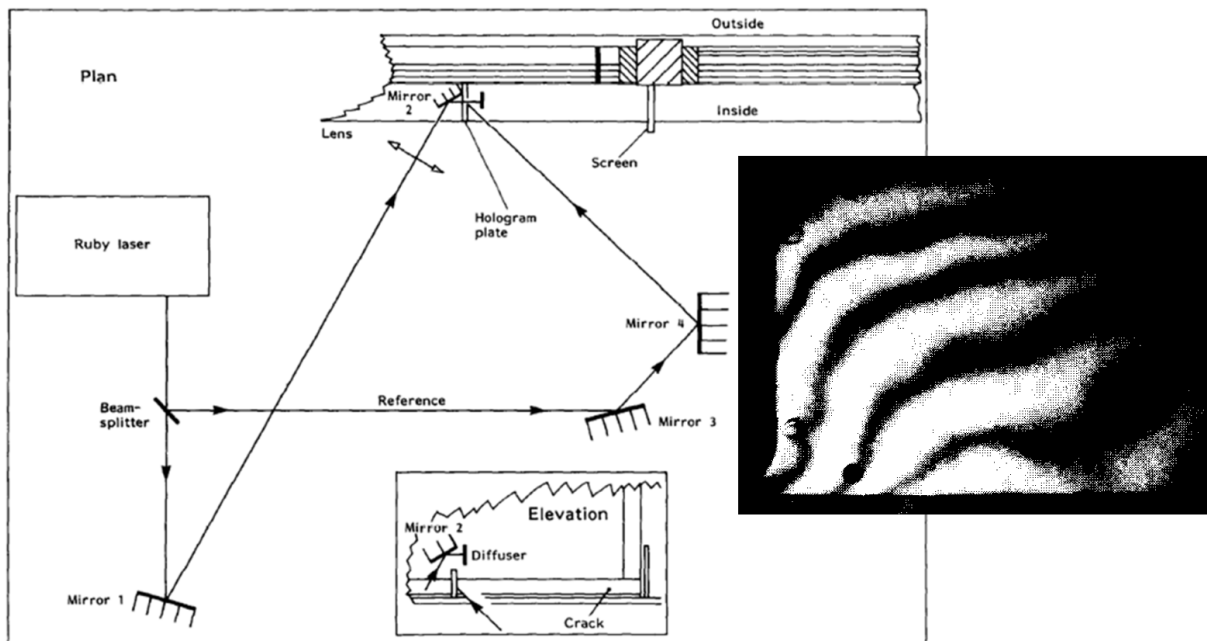


Figure 2.5 –Study of a flow induced by a crack by holographic interferometry: experimental set up and result [71]

#### 2.1.4. Synthesis

To conclude, various techniques have been used to identify and quantify the air leakage degrading the building airtightness. A summary is presented in Table 2.1.

For in-situ diagnostic the most widely used method to characterize the airtightness is the pressurization test usually carried out with a blower door, following a standard procedure such as EN ISO 9972 [72]. This allows an easy comparison between measurements on various buildings or with threshold values. However, while the significant pressure differential is necessary to decrease the impact of the weather conditions and the uncertainties in air flow measurement, it also artificially distorts the openings.

In order to get a more realistic measurement of the leakage air flow under natural pressure conditions, the tracer gas method is more appropriate. On the other hand the results obtained are more dependent on external conditions such as the wind speed that modifies the pressure field on the building's envelope. Moreover the gas has to be initially evenly mixed throughout the volume which can be difficult to achieve for big buildings.

The acoustic method is another alternative for in-situ measurements under natural conditions and has the advantage of its simplicity and of the low level of investment required. One can hardly use this technique to measure the leakage air flow of an entire building but it is appropriate to more local studies, for example on a room external wall or on the sealing of a window. It requires however preliminary work to obtain a reference value for the airtight configuration. The best is to carry out this measurement in laboratory but it is also possible to estimate the result using the theory of acoustic insulation of building elements.

To detect the leakage areas the infrared thermography and the smoke visualization can be implemented both for in-situ diagnostics and laboratory tests. The infrared thermography is the most widely-used technique since it does not need a pressurization of the building. It is easy to implement but one needs some experience when interpreting the results since the apparent temperatures given by the thermographs depend on the material emissivity and reflectivity. It requires a significant temperature difference between the inside and outside which can make summer measurements difficult without an additional heat source. The smoke visualization method enables to detect easily the leakages and can be a valuable complement of a pressurization test. However the information obtained is only qualitative.

Concerning the laboratory experiments on the airtightness issue, the previously mentioned methods are also used for more local studies on specific building components, in particular the pressurization test thanks to the construction of built-up boxes. The boundary conditions are controlled more easily and the aim is not necessarily to reproduce the natural ones. A large variety of tests is possible, such as the evaluation of a component resistance to very high pressure or the performance of various sealing methods.

In order to identify the air leakage path within a wall assembly separating two different atmospheres, it is possible to implement temperature and/or moisture sensors between the layers. This is however an intrusive method, complex to implement and giving local measurements only.

Finally, some studies have been carried out in the eighties on the air flow resulting from infiltrations by means of holographic interferometry. It can give valuable information in order to understand better the impact of the leakage on the indoor air circulation, but it is a complex technique to implement with results under the form of holograms which can be difficult to interpret.

To sum up, there is a number of experimental methods for different aspects of the building airtightness study, which all have advantages but also limits. The choice of the most appropriate one will therefore depend on the scope of the study. Moreover it has been pointed out that several methods enable to quantify the air leakage flow rate and detect the leakage location, but there has been until now only very few studies on the air path investigation within the wall assembly and there is a lack of technique developed to this end.

Several of these methods were used in this present study. As presented in Chapter 4 pressurization tests have been carried out for a global airtightness characterization of some construction details. Concerning the air path investigation, a new approach using tracer micro-particles is developed and tested in Chapter 5. Finally, in Chapter 6 this new technique is compared with the use of temperature and relative humidity sensors in a case study. The infrared thermography is also used for complementary results on the air dispersion at the inlet/outlet of the insulation material. It is compared with air flow velocity measurements by PIV (particle image velocimetry), a common laboratory technique but whose use for this application is also innovative.

These laboratory tests required the construction of test boxes, and the use of instrumentation to monitor the temperature, relative humidity, pressure difference, air flow rate and air velocity. Previous studies with the same needs are presented below to provide a background on these issues.

Table 2.1 –Summary of the experimental methods to study wall airtightness

Methods	In situ	Lab.	Occurr.	Objectives	Scale	Parameters	Advantages	Limits
Pressurization testing	x		++	Airtightness characterization	room / zone / building	- $\Delta P$ (usually set between 10 and 100 Pa) - Leakage flow rate	- Weather conditions independent - Widely used: required for standards	- Openings artificially distorted ( $\Delta P \neq$ natural conditions)
		x	+		wall assembly / component	- $\Delta P$ (potentially > 500 Pa) - Leakage flow rate	- Control of the boundary conditions - Possibility to reach the rupture - Possible modelisation of the airtightness defects	- Further from the natural conditions - Complex set-up (built-up boxes)
Acoustic approach	x	x	-		wall assembly / component	- Sound transmission loss leading to the leakage flow rate	- Air leakage rate calculated under real pressure conditions - Fast measurements - Economical: few instruments	- Upstream work required (laboratory measurements or theoretical study) - Little studied
Tracer gas	x		+	Air change rate measurement	room / zone / small building	- Gas concentration leading to the leakage flow rate	- Air leakage rate calculated under real pressure conditions	- Weather conditions dependent - Adapted for small volumes: good initial mixing of the gas required - Complex to implement
Temperature and moisture sensors		x	-	Mapping of air leakage in wall assemblies	wall assembly	- Temperature - Moisture	- Possibility to study the air leakage path within the wall assembly	- Intrusive method - Localized measurements - Complex to implement
Infrared thermography	x	x	++	Detection of the leakage location	Building façade / wall assembly / component	Infrared energy emitted from the surface leading to the apparent temperature	- Easy to implement - Widely used	- Experience needed for interpretation - Apparent temperature (dependent on the material emissivity) - Only the surface is studied - Significant indoor - outdoor $\Delta T$ required
Smoke visualization	x	x	+		room / zone / building	Visual diagnostic	- Easy to implement	- Qualitative information - Pressurization needed
Holographic interferometry	x	x	-	Study of the air flow pattern resulting from infiltrations	Airtightness defect	Visual diagnostic (interferogram)	- Non-intrusive	- Complex to implement - Difficult interpretation

## **2.2.Experimental research on HAM transfer using built-up boxes**

Heat air and moisture (HAM) transfer have been studied from the pore to the building scale with simulation tools for several decades. Their interactions induce complex equations difficult to solve.

As a result the studies and the models developed usually combine only two of the three transfer phenomena and focus on one specific scale. For example Künzel [73] focused on the heat and moisture transport in building components; Buchanan and Sherman [74] developed a mathematical model for infiltration heat recovery at the building scale; Hagentoft et al. [75] published a benchmark for 1D cases of HAM transfer in building components and lately Tariku et al. [76] developed a transient model for coupled HAM transfer through multilayered porous media and Belleudy et al. [77] proposed a 2D model for coupled HAM transfer through porous media in contact with air channels.

In all cases, experimental measurements are needed to both validate the developed models and to improve them. Several significant examples from the literature are described below.

### **2.2.1. Experimental setups review**

Experimental studies can carry out measurements either in-situ or in laboratories. Because of the necessity to implement sensors inside the wall assembly, in-situ tests can hardly be performed on inhabited buildings unless it was anticipated during the construction phase [78] and [79]. Alternatively, tests can be carried out in test buildings with the tested wall assemblies exposed to a controlled atmosphere on the indoor side and to naturally occurring weather conditions on the exterior side [80] and [81]. This enables to compare the performance of various wall assemblies at the same time thanks to larger test areas, and to investigate the behavior of the wall assemblies exposed to real external conditions.

On the other hand, laboratory tests enable to control the boundary conditions and to get a steady state solution which is of interest for model validations. Concerning the air transfer issue, they enable finer studies than a global envelope permeability measurement. It is indeed easier to test the airtightness of specific wall assemblies, building components or construction details, and to apply greater pressure differences to them. Concerning the heat and moisture transfer, laboratory studies are more commonly carried out since they enable to add, move or remove the sensors more easily.

They require however the construction of specific experimental setups. A non-exhaustive review of the existing ones is presented in Table 2.2, and was of use for the design of the new experimental facility, built for the present study and described in paragraph 4.1.2.

### **2.2.2. Instrumentation**

The experimental set-ups require a number of sensors to monitor physical variables such as the differential pressure between two sides of a tested wall, the flow rate induced or the temperature and moisture conditions inside the wall. A review of those chosen for the previously mentioned experimental studies is presented below.



Table 2.2 –Review of the built-up boxes for HAM transfer experimental research

Ref.	Study	Year	Cntry	Purpose	H	A	M
[67]	Desmarais et al.	2000	CA	Mapping of air leakage in exterior wall assemblies	x	x	x
[82]	Pavlik et al.	2002	CZ	Hygrothermal Performance of Multi-Layered Building Envelopes	x		x
[83]	Hall & Hauser	2003	GE	Quantification of leakage air flows for several airtightness defects		x	
[84]	Vinha	2007	FI	Hygrothermal performance of timber frame external walls	x	x	x
[85]	Talukdar et al.	2007	CA	Heat and moisture transfer in hygroscopic building materials (model validation)	x		x
[86]	Alturkistani et al.	2008	CA	Determination of the relative drying capacity of building envelope panels			x
[87]	Mao et al.	2009	CA	Comparison of the drying capacity of timber frame wall systems in evacuating water due to rain penetration in the stud cavities			x
[88]	David	2010	FR	Natural convection near walls with phase change materials	x		x
[89]	Kalamees & Kurnitski	2010	FI	Moisture convection performance of external walls and roofs	x	x	x
[90]	Van Belleghem et al.	2010	BE	HAM model validation	x	x	x
[44]	Inard et al.	2011	FR	Impact of the air path on the heat transfer	x	x	
[91]	Pinard	2012	FR	Multifunctional ventilated walls	x		
[92]	Rafidiarison	2012	FR	Heat and air transfer in timber frame buildings	x	x	
[14]	Langmans et al.	2013	BE	Feasibility of exterior air barriers in timber frame construction	x	x	x
[93]	Slimani	2015	FR	Hygrothermal behavior of highly hygroscopic walls	x	x	x

### Differential pressure

Pressure can be measured in various ways. The measurement instruments can be divided in two main groups: the mechanical manometer and the electronic sensors.

The mechanical manometers are suitable for continuous or slowly variable pressure measurements. They can either use a liquid [80] such as water or mercury or the deformation of a solid (diaphragm, capsule, bellows, Bourdon tube). In case of liquid use, they have to be calibrated after any change of

ambient temperature since the dilatation of the liquid could affect the accuracy. Pressure compensator can be used for the calibration: it is a piston-cylinder unit with the pressure to be measured imposed on the lower side and compensated on the upper side by weights until the equilibrium.

The electronic sensors and transmitters are also based on the measurement of a displacement but they enable to convert it into an electrically measurable parameter. This requires an external power source, unlike mechanical manometers. The main sensing elements are diaphragms, capsules and Bourdon tubes, but the displacements are smaller, of about  $10^{-6}$  m compared with about  $10^{-4}$  m for mechanical manometers. A wide variety of technologies are used to convert the displacement into an electrical signal, and it is not always specified in the products data sheets which one is used. As an example, potentiometric sensors use the sensing element to drive a wiper arm on a resistive element. There are also inductive pressure sensors such as the P26 used in [14] with a beryllium bronze membrane; capacitive sensors with usually a diaphragm on one plate of the capacitor that changes the capacitance when deflecting; strain gauge sensors; piezoresistive semiconductors using the change in conductivity as the sensor CP301 [93], etc.

As shown in Table 2.3, mostly electronic sensors are used in the field of HAM transfer investigation. They are indeed more suitable to measure and monitor differential pressures that may vary with time.

Table 2.3 – Review of the instrumentation for the HAM transfer in wall assemblies study – Pressure measurement

Type of sensor	Ref.	Product & characteristics
Differential pressure transmitter	[14]	P26 (Halstrup Walsher GmbH) ; Measurement range: 0-25 Pa; Accuracy: $\pm 4\%$
	[14] (small set-up)	4DG-700 (Energy conservatory); Measurement range: 0-1400 Pa; Accuracy: $\pm 1\%$
	[69]	Digital micromanometer
	[84]	FCO 16 (Furness Control LTD); Accuracy: $\pm 1$ Pa
	[85]	Accuracy: $\pm 15$ Pa
	[89]	FCO44; Measurement range: 0 - 50 Pa; Accuracy: $\pm 2.5\%$
	[93]	CP301-HOP (KIMO) Measurement range: 0-100 Pa ; Accuracy: $\pm 1$ Pa
Water manometer	[80]	Measurement range: 0-125 Pa; Accuracy: $\pm 1$ Pa

## Temperature

The various types of sensors used for temperature measurement are presented in Table 2.4. The temperature is commonly measured with thermocouples using the Seebeck effect: they respond to a difference of temperature by producing an electric current. If two conductive materials with different thermoelectric properties are in contact at one extremity, a voltage difference will be measurable between the two other extremities. For small temperature fluctuations the voltage is approximately

linear. They are not expensive, little intrusive (diameter > 0.2 mm), have a large measurement range and a rather good accuracy. Each couple of conductive materials is designated by a letter. For example thermocouples T correspond to copper/constantan, while thermocouples K are made of chromel and alumel.

RTD (resistance temperature detector) probes give the temperature by measuring the resistance of pure metals and require therefore a power source to operate. They can have greater stability, accuracy and repeatability than thermocouples but are more expensive, produce heat, and have a longer response time. They are also more intrusive (diameter > 1 mm) which can be a problem inside wall assemblies. This is the reason why they are mostly used to monitor the temperature in air volumes of for calibration purposes for this specific application. The most commonly used metal is platinum since it has a large measurement range, a good accuracy and stability, but copper and nickel are other options. Such platinum sensors usually have a nominal resistance of 100 Ω at 0°C and are therefore called PT100.

Thermistors are similar to RTD but they are made of sintered semiconductor materials (usually ceramic or polymer materials) whose resistance varies significantly for a small change of temperature (in the order of 200 Ω/°C). Their use is limited to temperatures under 200°C but they give high accuracy results. Both RTD probes and thermistors require a constant and accurate excitation source.

Temperature is usually also monitored by relative humidity sensors. In order to avoid the potentially intrusive addition of thermocouples, these sensors are also used for measurements inside wall assemblies, even if the accuracy is not as good.

Finally, as discussed in paragraph 2.1.3, the temperature at the surface can also be measured using an infrared radiation by infrared thermography.

Table 2.4 – Review of the instrumentation for the HAM transfer in wall assemblies study – Temperature measurement

Type of sensor	Ref.	Product & characteristics
Thermocouple T	[14], [67], [85], [91]	Accuracy: ± 0.3°C (at ambient temperature)
Thermocouple K	[88], [91], [90], [93]	Accuracy: ± 0.3°C (at ambient temperature)
RTD probes	[94](air cavity)	PT100 of 1/10 DIN class; Measurement range: -20°C : 70°C ; Accuracy: ± 0.1°C
	[93] (air volume) [91] (calibration)	PT100 Accuracy: ± 0.1°C
	[85] (air volume)	Accuracy: ± 0.1°C
Thermistors	[84] (air volume and surface)	LM 335 (National semiconductor Corporation)
T-RH sensors	[84], [85], [89], [93], [81]	cf Table 2.5
IR thermography	[71](surface temperature)	AGA Thermopoint 80
	[91] (surface temperature)	Camera Flir System

## Humidity and moisture content

As presented in Table 2.5, the bibliographic study has pointed out two main techniques for the humidity measurement in this field of application: the use of removable gravimetry samples to quantify the moisture content and the measure of the relative humidity by hygrometers.

Table 2.5 – Review of the instrumentation for the HAM transfer in wall assemblies study – Humidity measurement

Type of sensor	Ref.	Product & characteristics
Capacitive sensors	[14], [90]	HIH-4000 (Honeywell); Measurement range: 0-100%; Accuracy: $\pm 0.5\%$
	[84]	HMP233 (Vaisala); Measurement range: 0-100%; Accuracy: $\pm 0.1^\circ\text{C}$ ; 2% RH (<90%); 3% RH (>90%)
	[85]	Honeywell ( $\pm 1.3\%$ )
		TDK ( $\pm 1.2\%$ )
	[89]	HMP44L (Vaisala); Measurement range: $-20^\circ\text{C}$ - $60^\circ\text{C}$ ; Accuracy: $\pm 0.4^\circ\text{C}$
	[90]	TRANSMICOR T232 (Gefran); Accuracy: $\pm 2\%$
	[93]	Sensirion SHT75; Accuracy: $\pm 1.8\%$ HR and $\pm 0.5^\circ\text{C}$
Removable gravimetry samples	[14]	N/A
	[67]	38mm in diameter (144 samples)
	[84]	Balance LP62205 (Sartorius Ltd); Accuracy: $\pm 1.0$ wt%
	[86]	25 samples
	[87]	25 samples/ wall
	[89]	2 samples
Moisture pins	[81]	Moisture pins

The gravimetry samples are cut from the wall assembly and the measurement protocol consists in weighing the dry sample, putting it back in the wall assembly and weighing it again whenever the moisture needs to be measured. The difference between the two weighings leads to the moisture content. However it is a tedious and not always applicable method since it requires an easy access to the samples. It is not suitable to monitor rapid changes but it can be convenient to study for example the slow drying of a wall in the months after the construction [86].

As an alternative many types of hygrometers can be used [95]. Chilled mirror are known for being among the most accurate ones and are therefore commonly used for calibration. The temperature of the mirror is controlled and decreased until condensation is detected, which gives the dew point with an accuracy ranging from  $0.2^\circ\text{C}$  to  $0.5^\circ\text{C}$  (about 1% RH). They are however intrusive and small capacitive sensors are therefore preferred for the wall assembly instrumentation. They use a dielectric material made of high polymer membrane with an electrostatic capacity changing with the moisture content. Their main advantages are that they have the shortest response time (a few

seconds), a relatively good accuracy ranging from  $\pm 1\%$  to  $\pm 4\%$ , and they are not expensive. A temperature sensor is usually installed together with the humidity one to compensate its temperature dependency (about  $0.1\%/^{\circ}\text{C}$  at ambient temperatures). These sensors are usually a few millimeters thick which raises intrusiveness concerns when placed inside a wall assembly, but the cutting of gravimetry samples may also have an impact on the air leakage.

Finally, the moisture content inside wood studs may be measured using moisture pins [81]. These sensors measure the electrical resistance between two electrodes, which varies depending on the moisture content since the dryer the wood the less easily electricity flows. A calibration is required for each tested material.

### Air velocity

The local air velocity can be measured thanks to anemometers. For a measure at a precise point hot-wire anemometers are commonly used, as shown in Table 2.6. A very fine metal wire, of the order of several micrometers, is electrically heated up, and at the meantime cooled down by the air flow. The greater the air velocity, the cooler the wire gets. Since the electrical resistance of metals is dependent on its temperature, the flow speed can be obtained from the resistance measurement. This is however an intrusive technique that modifies the local flow field. It is therefore of use for local measurements in air cavities but not to get a mapping of the air leakage velocity inside the wall assembly.

There are other types of anemometers such as rotating vane and cups and differential pressure anemometers, but hot wire anemometers are the most appropriate to low air velocities measurements.

As an alternative to local measurement, the velocity field inside an air may be obtained with the PIV (particle image velocimetry) technique [91]. This method is based on the analysis of two images, taken shortly one after the other, of the flow seeded with particles. It is further described and implemented in paragraph 6.2.2.

Table 2.6 – Review of the instrumentation for the HAM transfer in wall assemblies study – Air velocity measurement

Type of sensor	Ref.	Product & characteristics
Hot wire anemometer (local measurement)	[14], [91]	8475 (TSI incorporated); Measurement range: 0.05-2.5 m/s; Accuracy: $\pm 3\%$
	[69]	N/A
	[84]	AFT-1D (Envic Ltd.); Measurement range: 0-10 m/s for outdoor air flow; 0-1 m/s for indoor air flow Accuracy: $\pm 0.1$ m/s + 3% of reading
	[93]	CTV210-HO150 (KIMO) Measurement range: 0-30 m/s ; Accuracy: $\pm 3\%$
PIV (air cavity)	[91]	Software: Dantec Dynamic Studio

## Air flow rate

There is a large variety of instruments to measure the flow such as pressure-based meters (Pitot tube, Venturi meter...) [84], thermal mass flow meters, magnetic flow meters... The bibliographic review shows that for this field of application with relatively low and stable flow rates, the mechanical ones are also an option. They use the fluid to drive a movable mechanical component such as a turbine [14], a piston or a wheel. The mechanical part can also be a float in a tapered tube that is pushed up by the fluid and down by gravity. This particular kind of flow meter is called variable area meter or rotameter ([14] and [80]). The viscous and pressure forces on the float increase with the flow rate and balance with gravity where the float stabilizes.

Table 2.7 – Review of the instrumentation for the HAM transfer in wall assemblies study – Air flow rate measurement

Type of sensor	Ref.	Product & characteristics
Variable area flowmeter	[14]	V-100 (Vögtlin) Measurement range: 0.02-0.9 m <sup>3</sup> /h; Accuracy: ±2%
	[80]	N/A
Turbine flow meter	[14]	Trigas FI; Measurement range: 3.4-36 m <sup>3</sup> /h; Accuracy: ±0.6%
Pitot	[84]	Accuracy: ± 0.1 l/min
Tapered orifice plate of specific diameter	[85]	Accuracy: ±6%
Electronic soap film calibrator (Bubble flow meter)	[89]	Measurement range: 100cc/min-30L/min; Accuracy: ±0.5%

## 2.3. Airtightness tests on timber frame wall assemblies

### 2.3.1. Tested wall assemblies

Timber frame buildings have a number of advantages as detailed in paragraph 1.1, including a lower environmental footprint, a higher energy efficiency for a given wall thickness and a much shorter build time on site. It is therefore a common method of construction around the world.

Many wall assemblies can be implemented in timber frame constructions. The simplest one consists of 3 layers (cf Figure 2.6):

- A thermal insulation incorporated in the spaces between the studs. There is a number of possible insulation materials such as glass wool, wood fiber, cellulose, EPS, straw... The studs carry the loads of the structure and are usually laid out every 40 to 60 cm.
- An exterior sheathing that provides resistance to lateral wind loads. It is usually made of particle boards such as OSB (oriented strand board) panels.
- An interior sheathing which is usually made of gypsum boards.

The vapor-barrier (VB) prevents moisture from entering the wall. This is an important membrane to protect the wall since the decrease of temperature through the wall assembly can lead to unwanted condensations between 2 layers in case of humid air exfiltration. A service cavity between the interior sheathing and the VB is recommended in order to avoid breaks in the membrane.

A cladding can be added on the exterior side in order to both increase the weather resistance and create the external appearance required by the client. A large variety of material is possible: stone, brick, wood, tile... An air cavity can separate the cladding from the exterior sheathing allowing water to drain down the back of the cladding and remaining moisture to dry through ventilation.

A WRB (water resistive barrier) stapled onto the external face of the exterior sheathing prevents moisture from entering during construction and protect the sheathing from wind-driven rain that gets past the cladding. It is usually not an air barrier and its vapor permeability should be chosen to minimize the risks of moisture damage. Vapor-permeable WRBs enable indeed the outward drying of the exterior sheathing but also allow inward-driven moisture.

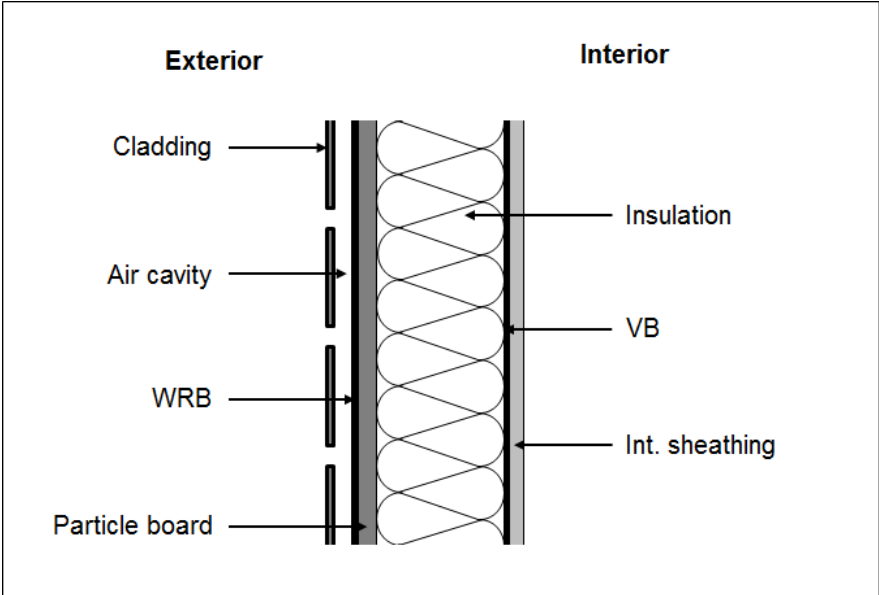


Figure 2.6 – Typical wall assembly in timber frame constructions

There is therefore a wide range of possible wall assemblies and choice of materials which means that there is no typical timber frame wall that could be representative of most envelopes. As a result, each experimental study on the HAM transfer listed in the previous paragraph uses a different wall assembly. A non-exhaustive review of them is presented in Table 2.8 in order to give an overview of the possibilities. The layers are separated by ";" and when several materials have been tested they are separated by "/".

Table 2.8 – Review of the wall assemblies studied

Ref	Study	Year	Cntry	Wall assembly		
				Ext. layer(s)	Insulation	Int. layer(s)
[80]	Tenwolde et al.	1995	USA	waferboard/ steel; -/air cavity (6mm); -/ foamcore (5mm)/ wood fiberboard)	Glass fiber	Gypsum board (8mm) with vinyl finish
[96]	Kalamees & Vinha	2003	ES-FI	Boarding (22mm); air cavity (25mm); wood-fiberboard (25mm)	Mineral wool/ Cellulose insulation/ Sawdust (173mm)	Plastic sheet/ Bitumen paper; Gypsum board (13mm)
[87]	Mao et al.	2009	CH - CA	-/ wood siding + air gap (19mm)/ Stucco; WRB; OSB/ Plywood/ Fiberboard/ EPS foam	Glass fiber (140mm)	-/vapor barrier; Gypsum board (13mm)
[81]	Maref et al.	2010	CA	Vinyl siding; -/ exterior insulation sheathing; sheathing membrane; OSB (11mm)	Glass fiber	Painted drywall
[43]	Desta et al.	2011	BE	Multiplex (18mm); air cavity (25mm); fiberboard (18mm)	Mineral wool (200mm)	-/air cavity (25mm); wooden board (12.5mm)/ gypsum board (12.5mm)
[97]	Leskovar & Premov	2012	SLI	Rough coating (6/9mm)	EPS (100mm)/ mineral wool (100mm)/ wood fiberboard(60mm); - /Gypsum fiberboard (15mm); mineral wool (160mm)+ VB/ cellulose fiber (360mm)+ OSB (15mm); -/timber substructure	Gypsum fiberboard (15+10mm)/ Gypsum plasterboard (12.5mm)
[98] [99]	Labat	2012	FR	Wooden cladding; air cavity (27mm); Particle board (10mm)	Glass wool/ wood fiber/ cellulose wadding (160mm)	-/ VB; OSB/ gypsum board
[14]	Langmans	2013	BE	Air barrier (several tested)	Mineral glass wool/ Cellulose (300mm)	OSB (15mm)
[100]	McClung et al.	2014	CA	Fibre cement (16mm); Air cavity (19mm)	Mineral wool/ EPS (76mm); NVP/VP WRB; CLTP (89 to 131mm)	-/polyethylene sheet; stud space (89 to 131mm); gypsum wallboard (9.5mm)



### 2.3.2. Tested airtightness defects

Because structurally more complicated than masonry walls, timber frame buildings require a high degree of accuracy by experienced workers during the construction to meet high airtightness levels. The multi-layer structure with control layers and many joints can indeed easily lead to assembly problems and defects in the moisture or airtightness protection. These defects combined with a pressure difference between the inside and the outside of the building induce air leakage which can lead to many issues such as an over-consumption of energy, moisture damage, poor indoor climate, etc [8]. Field measurements on 170 Finnish houses [101] gave an average leakage air flow for a pressure difference of 50 Pa of 2.3 ach. for the massive houses (concrete, brick, and lightweight block houses) while the averages of the timber frame and the log houses were 3.9 and 5.8 ach.

A few experimental studies have been carried out in laboratory for the characterization of specific airtightness defects in timber frame constructions. A review is presented in Table 2.9.

In 2003 Hall & Hauser [83] carried out pressurization tests (from 10 to 50Pa) for several airtightness defects on various components to reproduce the leaks they observed during an in-situ measurement campaign on 50 newly-built timber frame buildings. The experimental set-up consists simply of a small airtight chamber connected with a variable speed blower. Most of the tests were carried out on thin membranes with slits of various lengths (2 to 20 cm); overlaps (10 and 20 cm) with missing tape on various lengths (5-20 cm); holes of various diameters (5 to 25 mm); stapler holes; connection with a pipe (4 levels of sealing) and the passage of 1 to 5 electrical lines. A few tests were also carried out on plasterboard with a gap between two panels (0.5 to 2.5 cm) and circular holes (5 to 50 mm), as well as on several window profiles and roof battens. The pressurization laws established in this study are helpful to quantify the impact of individual airtightness defects encountered in timber frame buildings.

Relander et al. presented three experimental studies carried out in the Norwegian University of Science and Technology (NTNU) on several construction details. The first one [102] focused on the airtightness performance of various sealing methods for windows, testing a number of sealing materials, technique and craftsmanship with a pressure chamber testing rig. The conclusion was that there were significant differences (up to 11 m<sup>3</sup>/hm) between the tested sealing techniques, tape being the most airtight and self-expanding sealing strip the least airtight.

The second one [41] is a study in collaboration with the Catholic University of Leuven on the influence of structural floors on the airtightness of timber frame houses. Two air leakage paths were identified and the flow rate induced by each of them was measured for various sealing solutions. It was found in particular that a continuous vapor barrier reduces considerably the air leakage compared to a discontinuous one; the sealing between the beams on the interior side is essential; mineral wool wrapped in vapor barriers can reduce significantly the leakage. Rolled wind-barriers fastened with battens gave the highest airtightness. The results have shown that when sealed properly, structural floors can have a negligible influence on the total building airtightness, but it requires very conscious craftsmen.

The last one [42] presents the influence of the joint between the basement wall and the wood-frame wall on the airtightness of houses depending on the flatness of the basement wall, the sealing method used in the joint and the load. It was found that malleable sealing materials give generally

higher airtightness and unlike non-malleable ones they are almost non-sensitive both to load and flatness. The results show that it is also possible to have a negligible influence of the joint on the total airtightness, but the absence of sealing or the use of the least favorable sealing method can induce considerable air leakage.

Finally as explained in paragraph 2.1.2, the PREBAT project includes an experimental study of air leakage through 4 pairs of airtightness defects: wall/floor junction; wall/ceiling junction; wall/exterior joinery junction; electrical outlet and electrical panel. Each airtightness defect is modeled by a specific number of 2mm in diameter holes. The upstream one is located at the lower part of the wall and the downstream one at the upper part in order to maximize the air path length inside the wall assembly. It is found that the addition of an insulation layer (9 cm thick glass wool) between the two wall panels can decrease the air permeability of up to 40% at 50 Pa. The heat recovery is also investigated but it is off the topic of this section.

Table 2.9 – Review of the airtightness defects studied

Ref.	Study	Year	Country	Purpose
[83]	Hall & Hauser	2003	GE	Pressure - flow rate law for several airtightness defects on a vapor barrier (missing tape, holes, cuts, stapler holes, sealing of a tube, electrical wiring); on plasterboards (gap between panels; holes); on window profiles and on roof battens
[102]	Relander et al.	2008	NO	Airtightness of different sealing methods for windows (no sealing; mineral wool insulation; self-expanding strip; backer rod; tape)
[41]		2010	NO - BE	Influence of structural floors on the airtightness: test of various sealing solutions (for both vapor barriers and wind barriers)
[42]		2011	NO	Influence of the joint between the basement wall and the wood-frame wall depending on the flatness of the basement wall, the sealing method used and the load
[44]	Inard et al.	2011	FR	Pairs airtightness defects modeled by calibrated hole: impact of the addition of an insulation layer on the pressure – flow rate laws and investigation on the heat recovery

The pressure – flow rate laws found for circular holes in gypsum boards by both Hall and Hauser [83] and Inard et al. [44] are used as reference for the validation of the experimental set-up built for this study (paragraph 4.1.4).

## 2.4. Conclusion

This chapter serves as a background for the present study. A review of the experimental methods for the airtightness characterization was first presented. It showed that pressurization is the most

commonly used technique to test the permeability of a building envelope or smaller scale wall assemblies in laboratory. It will therefore be used in Chapter 4 to characterize a number of building components and construction details in timber frame wall assemblies.

Concerning the identification of air inlets and outlets in the wall, the infrared thermography is the most commonly used technique and unlike smoke visualization it enables a somehow quantitative characterization thanks to the thermographs. This method is therefore used in Chapter 6 and compared with the PIV technique. No studies were found in the literature using PIV for this specific application but it could be an alternative for laboratory tests since it enables to get the air flow velocity field.

This review also pointed out the lack of studies and therefore techniques for the air path investigation inside the wall assembly. The only previously tested method is the use of temperature and moisture monitoring grids, but the sensors are intrusive. As an alternative, a new method is developed and tested in Chapter 5 consisting in the innovative use of tracer micro-particles to track the air path inside the insulation. It is then compared with the previously mentioned use of temperature and humidity sensors in Chapter 6.

In a second part, a non-exhaustive review of the experimental set-ups for the HAM transfer investigation in laboratory was presented. Having a closer look at these built-up boxes was of use for the design and construction of a new experimental set-up (APIE box) presented in paragraph 4.1.2. A detailed study of the instrumentation implemented enabled to list the various sensor technologies and in some cases to point out the most appropriate one, such as the use of thermocouples for the temperature monitoring inside the wall assembly.

In the last section, a focus on the timber frame wall assemblies and airtightness defect tested revealed that the variety of possible configuration requires more experimentation on that field. It has been shown that there is no typical wall assembly representative of most timber frame constructions. Experimental tests are therefore required not only to improve the knowledge on the impact of specific construction details, but also to be able to validate numerical tools with which many more configurations can be tested. A few studies with this purpose that have been presented are used in paragraph 4.1.4 to validate basic results obtained with the newly-built experimental set-up.

# Chapter 3

## Inclusion of natural infiltration in building total ventilation rate calculations

Before going deeply into detailed study of wall assemblies, it is interesting to look at some of the impacts that air infiltration may have on overall buildings' performance. In this chapter the focus is on the ventilation in single-family detached homes. The airtightness is therefore characterized at the building scale through the air changes per hour at 50 Pa ( $ACH_{50}$ ). This envelope permeability induces naturally-driven infiltration. The aim of this study is to find models to predict how it combines with air flows from mechanical systems to determine the total ventilation rate. When there are balanced mechanical systems, the solution is simple additivity, because such mechanical systems do not impact the internal pressure. This is however not the case for unbalanced systems and the pressure changes can impact natural infiltration non-linearly and make it sub-additive.

Previous studies have selected several sub-additive approaches but they are not robust across the full spectrum from tight to leaky buildings. Unlike the work carried out at smaller scales presented in the next chapters, this study is only numerical. It was indeed necessary to cover a range of house airtightness and weather conditions as broad as possible. Moreover simulation allows the simultaneous calculation of the infiltration rate due only to the natural forces and the total ventilation rate with a mechanical system. This simultaneous data would not be available from field studies as one can only measure the total and mechanical air flow rates and not the co-incident infiltration.

The work presented in this chapter was carried out during a research stay at the Lawrence Berkeley National Laboratory in the Residential Building Systems group and detailed in a report [103]. Part of it was also published in *Building and Environment* in adapted form [104].

### 3.1. Superposition background

#### 3.1.1. Superposition issue

Most homes are ventilated by the form of natural ventilation known as “infiltration”, which is defined in ASHRAE Standard 62.2 [105] as the “uncontrolled inward leakage of air through cracks and interstices in any building element and around windows and doors of a building”. In order to

decrease energy consumption, house envelopes are getting tighter. Combined with potential increases in pollutant sources in indoor living environments, this raises concerns for indoor air quality (IAQ). People spend an average of 90% of their time inside. With the increased concern over IAQ, more houses are using a mechanical ventilation system to maintain a good air quality. As an example in France minimum ventilation rates are set by the law for each room, and a mechanical (often exhaust) ventilation system is installed in almost every dwelling.

In order to optimize the dual concerns of acceptable IAQ and minimum energy consumptions it is important to understand the total ventilation rate and that means it is important to understand how to combine natural ventilation such as infiltration with mechanical ventilation—i.e. fans. Detailed simulations models provide this capability, but often it is desirable to have simplified approaches that allow pre-calculation of certain quantities and then an after-the-fact superposition.

As illustrated in Figure 3.1, infiltration is caused by two driving forces, namely the wind and stack effects. The wind raises the pressure on the windward side of the building, and lowers the pressure on the other sides in proportion to the square of wind speed. The stack effect refers to density differences between indoor and outdoor air resulting from differences in temperature. In winter, the heated air inside the building is less dense than the cold air outside resulting in pressure differences across the envelope with higher inside pressure at the top of the building and lower inside pressure at the bottom of the building. The reverse happens in summer when the outside temperature is greater than the inside.

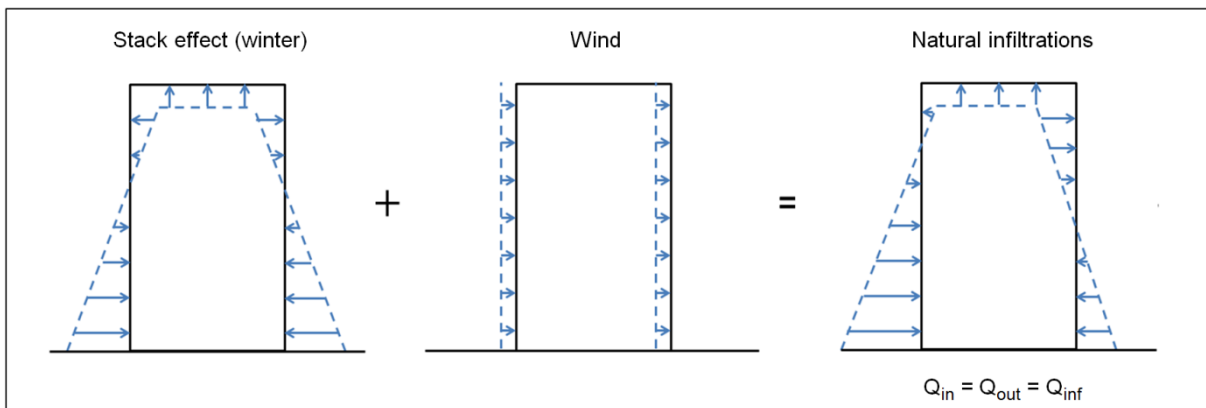


Figure 3.1 – Combination of the stack effect and the wind (infiltrations)

If a balanced ventilation system on room level (outdoor air introduced at the same rate that indoor air is exhausted) is installed, the impact on infiltration will not be significant, because the balanced system does not change the pressures across the building leaks. As a result, the total ventilation rate ( $Q_t$ ) is simply the addition of the fan flow ( $Q_f$ ) and the natural infiltration ( $Q_{inf}$ ).

The same does not apply, however, to unbalanced mechanical ventilation systems, as illustrated in Figure 3.2. They modify the indoor pressure of the building, which interacts with the wind and stack induced flows, making the combination of the flows sub-additive. Exhaust fans depressurize the building, which increases the air flow in through the building envelope. The greater the fan flow, the higher proportion of the building envelope experiences inflow. The opposite effect occurs with supply-only systems.

In order to avoid both excessive energy consumption and poor IAQ, it is necessary to predict the total flow rate resulting from the combined natural and mechanical ventilation. This can be done using mass balance physical and mathematical models to find the internal pressure that balances the incoming and outgoing mass flows. This approach is powerful, but requires many computational inputs and can be too time consuming for some purposes such as ventilation standards or simplified parametric modeling.

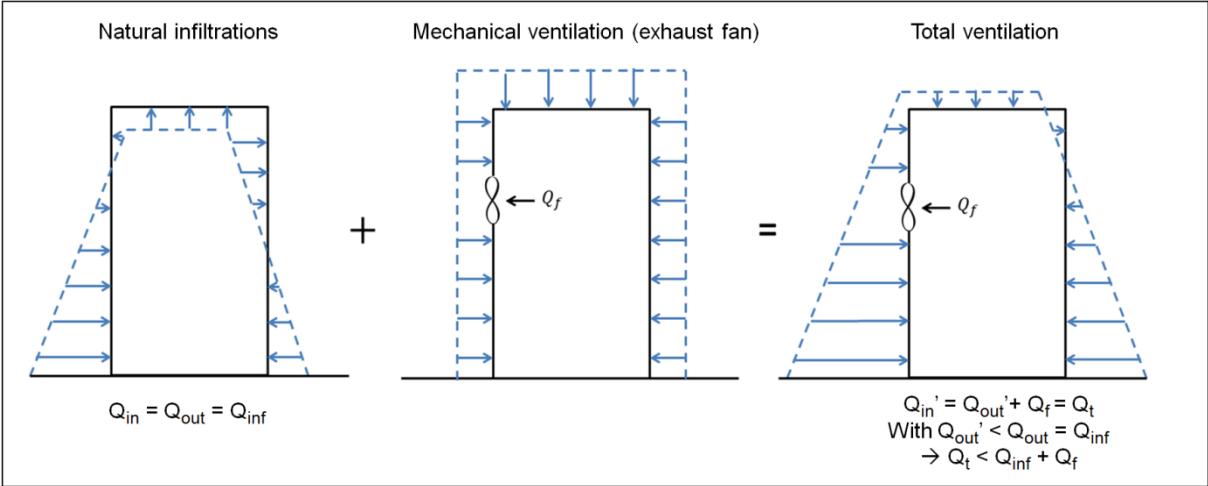


Figure 3.2 – Combination of the air flows due to the natural infiltrations and the mechanical ventilation

An alternative is to use a simple empirical model for estimating the total ventilation rate  $Q_t$  from  $Q_f$  and  $Q_{inf}$  (*forward models*). These models are generically called “superposition” models. A few models were suggested and tested a few decades ago, but the results were sometimes contradictory. There is to date no clear consensus on which model should be used, which is the reason why additional studies on this issue are required.

Another application is the one used in ASHRAE Standard 62.2, in which the total required flow is known ( $Q_t$ ) together with an estimate of natural infiltration ( $Q_{inf}$ ) and the aim is to determine the appropriate fan flow ( $Q_f$ ) to reach the total. Such models are called *inverse models* as illustrated in Figure 3.3.

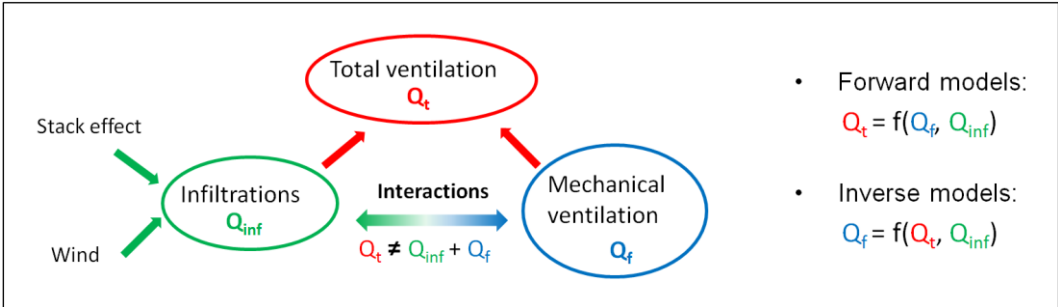


Figure 3.3 – Combination of infiltrations and mechanical ventilation flows: forward and inverse models

**3.1.2. Prior work**

In the eighties and early nineties a number of models for empirically combining the natural infiltration flow and unbalanced mechanical ventilation were suggested. A summary is presented in Table 2.1. Most of the models assume a linear addition of pressure differences:

$$\Delta P_t = \Delta P_{inf} + \Delta P_f \quad (3.1)$$

This is correct locally at the leakage scale, but is only an approximation at the building scale, since at some locations positive and negative pressures will cancel each other out.

Moreover, as mentioned in paragraph 2.1.2 the flow rate  $Q$  induced by a pressure difference  $\Delta P$  is given by:

$$Q = c\Delta P^n \quad (3.2)$$

Where  $c$  ( $\text{m}^3/(\text{hPa}^n)$ ) is the leakage coefficient characterizing the air permeability, and  $n$  (-) is the flow exponent, ranging from 0.5 to 1, which gives information on the flow regime (i.e., laminar versus turbulent). For a building envelope,  $n$  is normally found to be in the vicinity of 0.65.

By adapting equation (3.1) to the total ( $Q_t$ ), infiltration ( $Q_{inf}$ ) and fan flows ( $Q_f$ ), and by considering  $c$  as a constant, (3.2) becomes:

$$Q_t^{\frac{1}{n}} = Q_{inf}^{\frac{1}{n}} + Q_f^{\frac{1}{n}} \quad (3.3)$$

For  $n=1$  (laminar flow), this is the additivity model that will always over-predict the real total ventilation rate:

$$Q_t = Q_{inf} + Q_f \quad (3.4)$$

For  $n=0.5$  (orifice flow), this is the quadrature model which is the current model in ASHRAE Handbook of Fundamentals [106]:

$$Q_t = \sqrt{Q_{inf}^2 + Q_f^2} \quad (3.5)$$

If  $n$  is left as the real flow exponent, which differs slightly from one building to another:

$$Q_t = \left( Q_{inf}^{\frac{1}{n}} + Q_f^{\frac{1}{n}} \right)^n \quad (3.6)$$

There are many other methods for empirically combining the natural infiltration flow and mechanical ventilation (see the review by Li [107]). However, many of these are optimized for limited situations, such as the Palmiter and Bond [108] method, referred to here as the half-fan model, which was developed for stack-only natural infiltration.

Li tested ten models by comparing them with a flow model over a range of wind speeds (0 to 8 m/s) and temperature differences (-20 to 20°C) with open and closed exterior doors and two different exhaust fan speeds. His conclusion was that the quadrature combination of natural and mechanical ventilation worked best. This result is in agreement with the earlier work of Modera and Peterson [109], who also used a mass balance ventilation model.

Field tests with tracer gas measurements by Kiel and Wilson [110] found that for strong exhaust mechanical ventilation (four times the natural rate), simple linear addition was the most acceptable method, but that from a theoretical point of view, a half-pressure addition and half-linear addition model had more appeal with similar results to the linear addition. Continuing this work, Wilson and Walker [111] looked at a reduced fan flow rate that was approximately equal to the natural rate.

Table 3.1 –Summary of the suggested models and the results of the simulation/experimental comparison studies carried out on them

Name/Ref	Model	Range	Comparison		
			Ref.	Sim/Exp	Results
Additivity	$Q_t = Q_f + Q_{inf}$	All	Kiel & Wilson	Exp.	best agreement
			Wilson & Walker	Exp.	overpredicts $Q_t$ by 7%
			Li	Sim.	average error: 33%; max. error: 64%
Quadrature	$Q_t = \sqrt{Q_f^2 + Q_{inf}^2}$	All	Modera & Peterson	Sim.	good agreement: error on $Q_t < 10\%$
			Kiel & Wilson	Exp.	underpredicts $Q_t$ by 15-30%
			Wilson & Walker	Exp.	Underpredicts $Q_t$ by 20%
			Li	Sim.	good agreement: average error: 5%; max. error: 17%
			Palmiter & Bond	Exp.	underpredicts for $Q_{inf} < Q_f$ ; overpredicts for $Q_{inf} > Q_f$
Levins [112]	$Q_t = Q_{inf} + Q_f \cdot \exp\left(-\frac{Q_{inf}}{Q_f}\right)$	All	Kiel & Wilson	Exp.	underpredicts $Q_t$ by 15-30%
			Li	Sim.	good agreement: average error: 5%; max. error: 20%
Power Law	$Q_t = \left(Q_f^{\frac{1}{n}} + Q_{inf}^{\frac{1}{n}}\right)^n$	All	Modera & Peterson	Sim.	bigger errors on $Q_t$ than the quadrature model
			Kiel & Wilson	Exp.	underpredicts $Q_t$ by 10-25%
			Li	Sim.	average error: 11%; max. error: 30%
Shaw [113]	$Q_t = \begin{cases} Q_f & \text{for } h_0 > H \\ F \left( Q_{w-f}^{\frac{1}{n}} + Q_w^{\frac{1}{n}} \right)^n & \text{for } h_0 < H \end{cases}$		Shaw	Exp.	in general within 25% of the measured values
			Kiel & Wilson	Exp.	underpredicts $Q_t$ by 15-30%
Kiel	$Q_t = \sqrt{Q_f^2 + (2Q_{inf})^2}$	$Q_f \gg Q_{inf}$	Kiel & Wilson	Exp.	very spread data; overpredicts $Q_t$ when $Q_f < 0.7Q_t$ ; otherwise mostly underpredicts $Q_t$
			Li	Sim.	average error: 56%; max. error: 100%
Li	$Q_t = \left(Q_f^{\frac{1}{n}} + (2Q_{inf})^{\frac{1}{n}}\right)^n$	$Q_f \gg Q_{inf}$	Li	Sim.	average error: 98%; max. error: 160%
Kiel & Wilson	$Q_t = \sqrt{\left(\frac{Q_f}{2}\right)^2 + Q_{inf}^2} + \frac{Q_f}{2}$	All (Exhaust fan)	Kiel & Wilson	Exp.	underpredicts $Q_t$ by 10-30%
			Li	Sim.	average error: 12%; max. error: 35%
			Palmiter & Bond	Exp.	overpredicts the fan efficiency
Wilson & Walker	$Q_t = \left(\left(\frac{Q_f}{2}\right)^{\frac{1}{n}} + Q_{inf}^{\frac{1}{n}}\right)^n + \frac{Q_f}{2}$	All (Exhaust fan)	Wilson & Walker	Exp.	underpredicts $Q_t$ by 7%
			Li	Sim.	average error: 18%; max. error: 42%
Li	$Q_t = \frac{1}{2} \sqrt{Q_f^2 + (2Q_{inf})^2}$	$Q_f < Q_{inf}$	Li	Sim.	average error: 22%; max. error: 50%
Li	$Q_t = \frac{1}{2} \left(Q_f^{\frac{1}{n}} + (2Q_{inf})^{\frac{1}{n}}\right)^n$	$Q_f < Q_{inf}$	Li	Sim.	average error: 21%; max. error: 50%
Half-fan - Palmiter & Bond	$Q_t = \begin{cases} \frac{Q_f}{2} + Q_{inf} & \text{for } Q_f < 2Q_{inf} \\ Q_f & \text{for } Q_f \geq 2Q_{inf} \end{cases}$		Palmiter & Bond	Exp.	good agreement



The result was the same as Kiel and Wilson, where linear and half-linear/half-pressure addition were the closest to the measured and modeled combined rates.

The above two studies looked at exhaust fans only, but over a wide range of natural infiltration driven by both wind and stack effects. Unlike Li, these studies showed large underpredictions using quadrature. This could be due to different building envelope leakage, weather conditions, leakage distributions and strengths of mechanical ventilation, but it mainly underlines the necessity of additional study.

### 3.1.3. Cases of interest

Each simplified model can either be used for forward or inverse calculations. The forward model predicts the total ventilation air flow ( $Q_t$ ) as a function of the natural infiltration ( $Q_{inf}$ ) and the fan flow ( $Q_f$ ). The equivalent inverse model gives  $Q_f$  as a function of  $Q_t$  and  $Q_{inf}$ . They can be applied to hourly or annual calculations, which results in four different cases:

- (5) Hourly, Forward Case: for the hourly air change rate prediction; useful for estimating energy loads and needed for relative exposure calculations.
- (6) Annual, Forward Case: predicting the annual effective ventilation given the effective infiltration and a fixed (or effective) fan flow; for indoor air quality (IAQ) purposes.
- (7) Hourly, Inverse Case: when one wants to vary the fan size each hour to compensate for varying hourly infiltration in order to keep the total ventilation constant. This is not much used, but could be in future smart ventilation system controls.
- (8) Annual, Inverse Case: for finding the fixed fan size that will combine with effective infiltration to produce a desired total ventilation; useful for building codes/standards applications such as ASHRAE Standard 62.2.

## 3.2. Approach

### 3.2.1. REGCAP simulation

#### REGCAP Software

REGCAP is a two zone ventilation model combined with a heat transfer model and a simple moisture transfer model. The two zones are the house and the attic above it. The ventilation rate is found by determining for each zone the internal pressure required to balance the incoming and outgoing mass flows resulting from the natural and mechanical ventilation driving forces.

The model uses an envelope airtightness measurement and a description of the leakage distribution. The leakage for the home is split between walls, floor, ceiling and open flues/chimneys. In this study, the leakage distribution was varied with the number of storeys and the type of foundation. It is however not dependant on the global airtightness level whereas in reality infiltrations are usually for concentrated on the roof for very leaky buildings. Each leak is defined by its flow coefficient, pressure exponent, height above grade, wind shelter and wind pressure coefficient taken from wind tunnel

tests. An iterative numerical method is used to solve the non-linear mass balance equations. The attic temperature is not regulated and will therefore both be affected by the ventilation rate and affect the infiltration flow due to the stack effect. In addition, REGCAP includes models for the HVAC equipment in the home and operates on one-minute time steps. The ventilation and heat transfer models are coupled and the combined solution is also found iteratively.

The simulation tool REGCAP has been validated in previous studies as discussed by Turner and Walker [114] including a comparison with several years of hourly averaged tracer gas ventilation measurements for a wide range of house leakage distributions and weather conditions [115]. It has been found that the average differences between measured and simulated ventilation rates are approximately 5%. The results obtained with the previously described simulations are therefore considered as reliable and used to evaluate simplified combination models.

### Parameters description

The software REGCAP was used to create simulation data based on a wide range of weather and housing conditions. The range of inputs is presented in Table 3.2, with four different envelope leakage levels, two different ventilation systems; one two, and three stories single-zone buildings (that give different envelope leakage distributions); three different foundation types and weather data from eight different climates. This set of parameters results in 864 different building/climate configurations.

For simplicity a variety of assumptions were made. For example, no (other) exhaust devices (such as kitchen or bathroom exhausts) were used and the duct leakage was set to zero, since these kinds of factors would obscure the underlying impact. The number of stories changes, but the total floor area is constant at 1900 ft<sup>2</sup> (176 m<sup>2</sup>). The flow through the exhaust or supply fan ( $Q_f$ ) was calculated according to ASHRAE Standard 62.2, including the infiltration credit in the standard. For each set of inputs, the model was run for a full year using TMY3 data for the climates shown in Table 3.2. The output of the simulation was roughly 500 million minute-by-minute data points that were reduced to 7.5 million hourly averaged for the comparison with the superposition models.

Table 3.2 – Range of inputs for the REGCAP simulations

Parameters	Values
Envelope airtightness (ACH <sub>50</sub> )	0.6; 1.5; 3; 5; 7; 10
Mechanical ventilation type	Exhaust ; supply
Number of stories	1; 2; 3
Foundation type	Slab on-grade; crawlspace; basement
Climate zones	Miami; Houston; Memphis; Baltimore; Chicago; Burlington; Duluth; Fairbanks

For each combination of house inputs, two REGCAP simulations were performed. First, REGCAP was used to calculate the infiltration flow through the envelope ( $Q_{inf}$ ) due to the stack and wind effect,

with no mechanical ventilation operating. Then the simulations were repeated with supply or exhaust fans operating to obtain the total flow ( $Q_t$ ). This way it was possible to compare the  $Q_t / Q_f$  predicted by the superposition models to those achieved/used in the simulations.

For the annual calculations, the fan flow is still the same as it is a constant over the year (for a given simulation), but  $Q_{inf}$  and  $Q_t$  are effective annual average infiltration rates. The effective rates are the correct ones to use for indoor air quality applications (as shown by Sherman and Wilson [116] and subsequent work). While simply averaging ventilation rates can be easier to measure, they do not in fact correspond to anything physically useful. The effective values are almost always lower than the averaged ones. As defined in ASHRAE Standard 62.2, they correspond to “the constant air infiltration rate that would result in the same average indoor pollutant concentration over the annual period as actually occurs under varying conditions”. This annual approach can be particularly useful when one wants to size the fan to the total ventilation required by ventilation standards.

### 3.2.2. Simplified models

Superposition is not a new concept. Many researchers have tried in the past to come up with empirical or first principle models. Some of those models work in particular situations, but so far none of the models work well enough over a broad range of potential applications. In this paragraph eleven models are reviewed. Three of them are from the literature and the eight other have been developed for this study. The equations describing the forward and backward forms are presented in Table 3.3.

#### Models from the literature

The three first models come from the literature and were presented in paragraph 3.1.2. The *additivity* model, which is a simple addition of the flows, is in the current ASHRAE 62.2 Standard, and has been experimentally verified by Kiel and Wilson. *Simple quadrature* is the current model in the ASHRAE Handbook of Fundamentals [106], and has been verified by both Modera & Peterson and Li. The *Half Fan* model was used in earlier editions of ASHRAE Handbook of Fundamental and has been established experimentally by Palmiter and Bond. For each of these models the forward and inverse forms are equivalent. For all three models, verification was for a narrow range of conditions, and the current study aims to investigate their performance over a much wider range of homes and conditions. They are compared with eight new models described below.

#### Advanced quadrature

The advanced quadrature is similar to the quadrature model but with an additional correction term driven by the coefficient  $\beta$ :

$$Q_t = \sqrt{Q_f^2 + Q_{inf}^2 + \beta Q_f Q_{inf}} \quad (3.7)$$

If  $\beta=2$  this is the additivity model that will always overpredict  $Q_t$ . If  $\beta=0$  this is the simple quadrature model that tends to underpredict  $Q_t$ . So by taking intermediate values of  $\beta$  it is possible to improve the predictions of  $Q_t$ . Two values were studied:  $\beta=0.3$  and  $\beta=0.6$  which are minimizing respectively the error for the hourly and annual prediction. The way these two values were obtained is explained in Appendix A.

Table 3.3 – Forward and backward equations of the simplified models compared to the REGCAP results

Model	Forward	Inverse
Additivity ( $\beta=2$ )	$Q_t = Q_f + Q_{inf}$	$Q_f = Q_t - Q_{inf}$
Simple quadrature ( $\beta=0$ )	$Q_t = \sqrt{Q_f^2 + Q_{inf}^2}$	$Q_f = \sqrt{Q_t^2 - Q_{inf}^2}$
Advanced quadrature	$Q_t = \sqrt{Q_f^2 + Q_{inf}^2 + \beta Q_f Q_{inf}}$	$Q_f = \frac{\sqrt{\beta^2 Q_{inf}^2 + 4(Q_t^2 - Q_{inf}^2)} - \beta Q_{inf}}{2}$
Half-fan	$Q_t = \max\left(Q_f, Q_{inf} + \frac{Q_f}{2}\right)$	$Q_f = \min\left(Q_t, 2(Q_t - Q_{inf})\right)$
Half-smaller	$Q_t = \max\left(Q_f + \frac{Q_{inf}}{2}, Q_{inf} + \frac{Q_f}{2}\right)$	$Q_f = \min\left(Q_t - \frac{Q_{inf}}{2}, 2(Q_t - Q_{inf})\right)$
System coefficient ( $1/D=0.85$ )	$Q_t = \frac{1}{D} Q_f + Q_{inf}$	$Q_f = D(Q_t - Q_{inf})$
Simple forward sub-additivity (SFSA)	$Q_t = Q_f + \frac{Q_{inf}^2}{Q_{inf} + Q_f}$	$Q_f = \frac{(Q_t - Q_{inf}) + \sqrt{Q_t^2 + 2Q_t Q_{inf} - 3Q_{inf}^2}}{2}$
Simple inverse sub-additivity (SISA)	$Q_t = \frac{Q_f}{2} + \sqrt{\frac{Q_f^2}{4} + Q_{inf}^2}$	$Q_f = Q_t - \frac{Q_{inf}^2}{Q_t}$
Exponential forward sub-additivity (EFSA)	$Q_t = Q_f + \exp\left(-k_{fw} \frac{Q_f}{Q_{inf}}\right) Q_{inf}$	-
Exponential inverse sub-additivity (EISA)	-	$Q_f = Q_t - \exp\left(-k_{inv} \left(\frac{Q_t}{Q_{inf}} - 1\right)\right) Q_{inf}$
Modified Levins sub-additivity (MLSA)	$Q_t = \exp\left(-k'_{fw} \frac{Q_f}{Q_{inf}}\right) Q_f + Q_{inf}$	-

Table 3.4 – Values of the k coefficient for the exponential models

	Forward		Inverse
	EFSA	MLSA	EISA
Hourly	$k_{fw,h} = \frac{2}{3}$	$k'_{fw,h} = \frac{2}{3}$	$k_{inv,h} = 1$
Annual	$k_{fw,a} = \frac{4}{9}$	$k'_{fw,a} = \frac{1}{2}$	$k_{inv,a} = \frac{2}{3}$

### Half-fan and half-smaller

The half-fan model (equation 3.8) assumes stack-driven infiltration since the total ventilation equals to  $Q_f$  for strong mechanical ventilation.

$$Q_t = \max\left(Q_f, Q_{inf} + \frac{Q_f}{2}\right) \quad (3.8)$$

In the example of an exhaust fan, it corresponds to a situation where the neutral pressure level rises above the ceiling level. There is no exfiltration through the building envelope, and the infiltration is therefore only compensating for the exhaust fan flow. But the stronger the wind, the less likely this is to happen. As a result, when assuming a certain independence of the infiltration from the fan flow, a logical extension would be the following model:

$$Q_t = \max\left(Q_f + \frac{Q_{inf}}{2}, Q_{inf} + \frac{Q_f}{2}\right) \quad (3.9)$$

### System Coefficient

The ASHRAE 62.2 committee was investigating a new model as a replacement of the additivity one:

$$Q_t = \frac{1}{D} Q_f + Q_{inf} \quad (3.10)$$

D is the system coefficient, with a value suggested of 1/0.85 for not balanced ventilation systems.

### Sub-additivity models

The simulation results were used to approximate a sub-additivity coefficient ( $\Phi$ ) weighting the infiltration contribution to either the total ventilation (forward models) or the fan sizing (inverse models):

$$\begin{cases} Q_t = Q_f + \Phi Q_{inf} \\ Q_f = Q_t - \Phi Q_{inf} \end{cases} \quad (3.11)$$

$$\Phi = \frac{Q_t - Q_f}{Q_{inf}} \quad (3.12)$$

This equation form was chosen because infiltration is often viewed as a 'credit' towards the total ventilation. The sub-additivity coefficient enables to examine the results in a non-dimensional way and therefore to observe physical trends independently from the building specificities. This coefficient is plotted against the ratio of known flow rates in order to find simple models to approximate it. The infiltration fraction,  $\alpha$ , was used for the inverse model and a slightly different version for the forward one since  $Q_t$  is unknown:

$$\begin{cases} \alpha = \frac{Q_{inf}}{Q_t} \\ \alpha_{fw} = \frac{Q_{inf}}{Q_f + Q_{inf}} \end{cases} \quad (3.13)$$

As shown in Figure 3.4 the values of  $\Phi$  are following an almost linear trend except for very low infiltration rates. For  $\alpha$  and  $\alpha_{fw}$  below 0.15, the total ventilation flow seems to be equal to the fan flow, which means that infiltration has no significant effect. The half-fan model has this behavior qualitatively, but has a functional form overall.

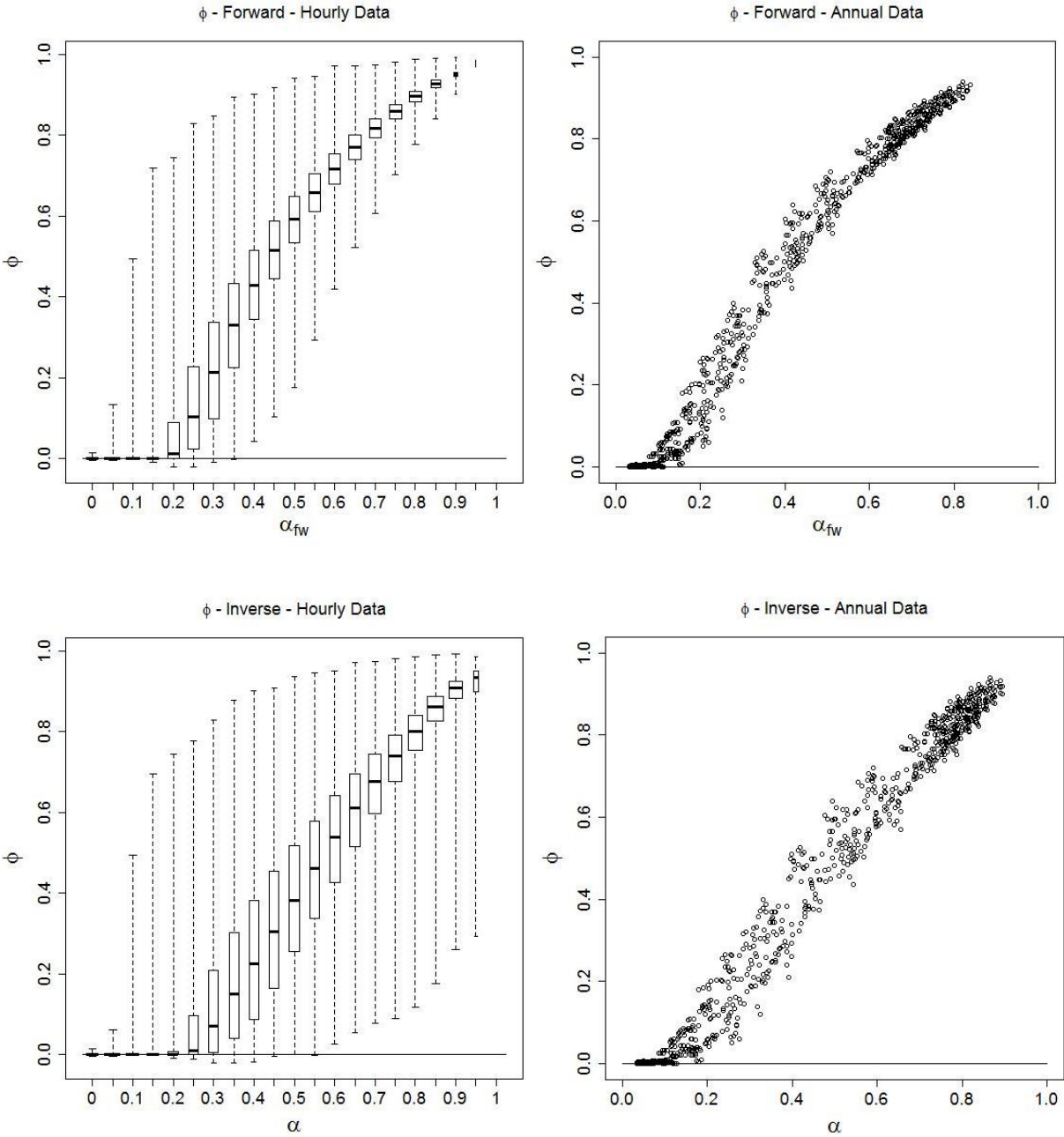


Figure 3.4 - Sub-additivity coefficient ( $\Phi$ ) from the REGCAP simulation

In the parameter study presented in Appendix C, one can see that the simulation points for which  $\Phi$  equals to 0 correspond mostly to houses with 0.6 ACH at 50Pa. Such very tight houses require indeed higher  $Q_f$  to ensure a good ventilation. As a result the fan induces a pressure difference between both sides of the envelope that is always bigger than the local dP induced by the stack and wind effect. Consequently, for exhaust ventilation there will be no exfiltration through the envelope, and for supply ventilation there will be no infiltration. When the airtightness level decreases, a smaller

fan flow is required and locally the wind and stack effects induce bigger pressure differences than the mechanical ventilation.

If, for simplicity, this effect is not taken into account,  $\Phi$  can be approximated by the infiltration fraction.

For the forward case this yields the *simple forward sub-additivity (SFSA)* model:

$$Q_t = Q_f + \frac{Q_{inf}^2}{Q_f + Q_{inf}} \quad (3.14)$$

For the inverse calculations it yields the *simple inverse sub-additivity (SISA)* model:

$$Q_f = Q_t - \frac{Q_{inf}^2}{Q_t} \quad (3.15)$$

On the other hand, a way to approximate this key parameter  $\Phi$  that reproduces this low infiltration behavior is to use the exponential form. However the use of this function makes it very complicated to have equivalent forward and inverse models. As a result it yields two different models respecting the same physical limits and the same trend:

- the *exponential forward sub-additivity (EFSA)*:

$$Q_t = Q_f + \exp\left(-k_{fw} \frac{Q_f}{Q_{inf}}\right) Q_{inf} \quad (3.16)$$

- the *exponential inverse sub-additivity (EISA)*:

$$Q_f = Q_t - \exp\left(-k_{inv} \left(\frac{Q_t}{Q_{inf}} - 1\right)\right) Q_{inf} \quad (3.17)$$

As explained in Appendix B, the coefficients  $k_{fw}$  and  $k_{inv}$  were optimized to best approximate the simulation results. Different values were found for the annual and hourly data, as presented in Table 3.4.

For the forward model, there is no obvious reason for choosing to apply the exponential form to  $Q_{inf}$  rather than  $Q_f$ . Another model is therefore tested:

$$Q_t = \exp\left(-k'_{fw} \frac{Q_{inf}}{Q_f}\right) Q_f + Q_{inf} \quad (3.18)$$

If  $k'_{fw}$  equals to 1, it is the Levins' model suggested in the early eighties and found to give very similar results than the quadrature model. But for this study, the coefficient is once again optimized to best approximate the simulation results (see Table 3.4). For this reason, this model is referred here as the *modified Levins sub-additivity (MLSA)*.

### 3.3. Model comparison

#### 3.3.1. Simulation results

The REGCAP simulations generate the values of  $Q_t$ ,  $Q_f$  and  $Q_{inf}$  over a wide range of conditions. The results are presented in Figure 3.5 with the air flow rates in air changes per hour plotted against the infiltration fraction ( $\alpha$ ). As mentioned in paragraph 3.2.1, the infiltration and total air flows are effective values for the annual simulations.

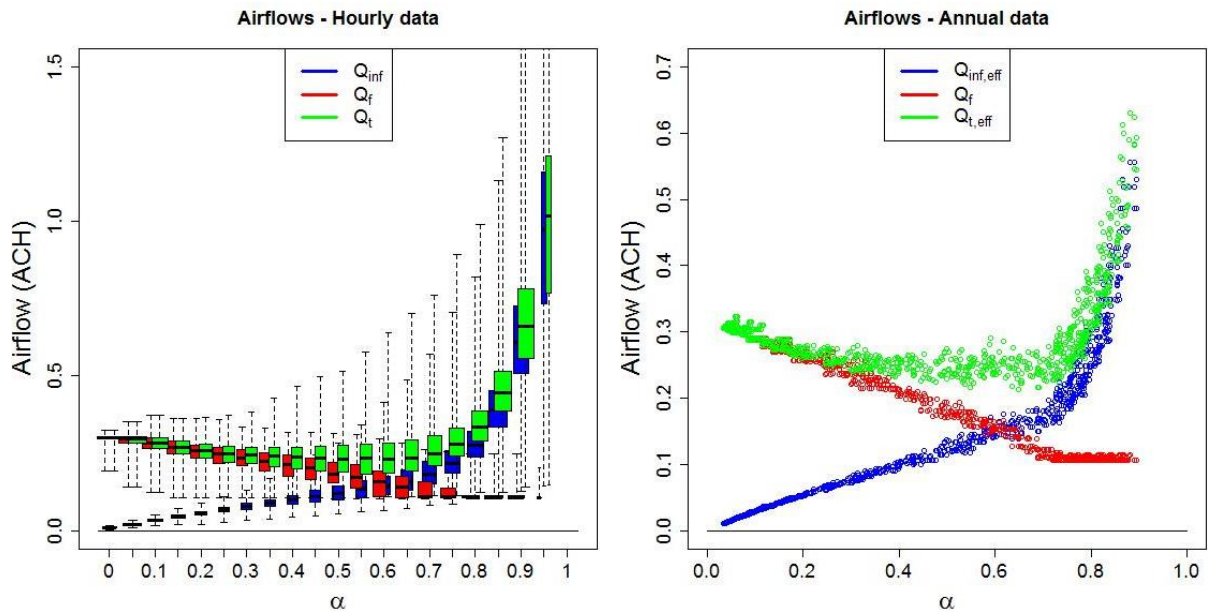


Figure 3.5 - Infiltration, fan and total ventilation flows from the REGCAP simulation

For the hourly data, the high number of points (over six million) requires the use of summary statistics, represented by box-and-whisker plots. The data was sorted into 20 bins by infiltration fraction and each bin is represented by a box. The box widths are proportional to the square-root of the number of observations in the bin. The bottom and top of the box are the first and third quartiles, and the black band inside is the median. The ends of the whiskers represent the minimum and maximum of the data. On average, a box represents more than 300,000 points, which explains the high variance. When several parameters are plotted, each of them is identified by a color and the horizontal offset in  $\alpha$  between them is only for the sake of clarity.

For the annual analysis, there is a single result for each of the parameter combinations presented in Table 3.2. This reduced number of points (864) allows all the individual results to be shown. Compared to the hourly data, there are less extreme values and no point with  $\alpha$  above 0.9.

A detailed parameter study is presented in Appendix C, with the impact of each input value on the sub-additivity coefficient.

#### 3.3.2. Simplified models errors

The models are evaluated by comparing the air flow prediction to the one obtained with the simulation. The forward model aims at predicting the total air flow so the error is given by:



$$E_{fw} = \frac{Q_{t,model} - Q_{t,sim}}{Q_{t,sim}} \quad (3.19)$$

In the same way, the error for the inverse model is the difference between the predicted and simulated fan flows. It is still divided by the total air flow since a division by a fan flow close to zero would give a significant error but the impact on the total ventilation would be very small.

$$E_{inv} = \frac{Q_{f,model} - Q_{f,sim}}{Q_{t,sim}} \quad (3.20)$$

As shown in Figure 3.6 and Figure 3.7, an over-prediction of the total ventilation ( $E_{fw}>0$ ) results in an under-prediction of the fan flow with the equivalent inverse model ( $E_{inv}<0$ ). This is not the case for the exponential model since the forward and inverse models are not equivalent. For the additivity model, the two errors have simply opposing values, but there is no such symmetry for the other models. The inverse error for the quadrature model reaches higher values than the forward error for high infiltration fractions. In the same way, the half-fan model gives a higher peak in the inverse error than the forward one.

The errors for the annual data are displayed in Figure 3.7. The trends are similar to those of the hourly errors. However since they are effective values,  $Q_t$  and  $Q_{inf}$  are smaller than a simple annual average, unlike  $Q_f$  which is constant over the year. As a result smaller over-predictions but greater under-predictions are observed for the forward models, and the opposite for the inverse models.

### 3.3.3. Discussion

The characteristics of the hourly and annual errors are presented respectively in Table 3.5 and Table 3.6. The various simulations give results covering a wide range of infiltration ratio ( $\alpha$ ) but not evenly dispersed. In order to compensate for this disparity, the bias and RMS of the errors are calculated for 20 bins of  $\alpha$  values, and then equally weighted. The bias is the error over the full range of house and weather parameters exercised in this study. The RMS is representative of the error for an individual home and is most useful for most applications – such as sizing fans for an individual home to meet a ventilation standard, such as ASHRAE 62.2. Because of the high number of points, the maximum error is not meaningful for the hourly error. The maximum median among the 20 groups of data was used instead, as well as the maximum of 90% of the data.

Each of the models have the same physical limits with  $Q_t$  equals to  $Q_f$  when  $\alpha$  tends towards 0 (no infiltration) and  $Q_t$  equals to  $Q_{inf}$  when  $\alpha$  tends towards 1 (no mechanical ventilation). That is the reason why the errors tend to 0 at the extreme values of  $\alpha$ . One can notice that some models, such as additivity and half-fan, have their maximum errors for  $\alpha$  close to 0.5 whereas the quadrature model has its maximum error around 0.7 for the forward calculation and 0.8 for the inverse one. This means that depending on the airtightness of the building, the ranking of the best models is different, and this could be one of the reasons why the previous studies did not agree on which model to recommend.

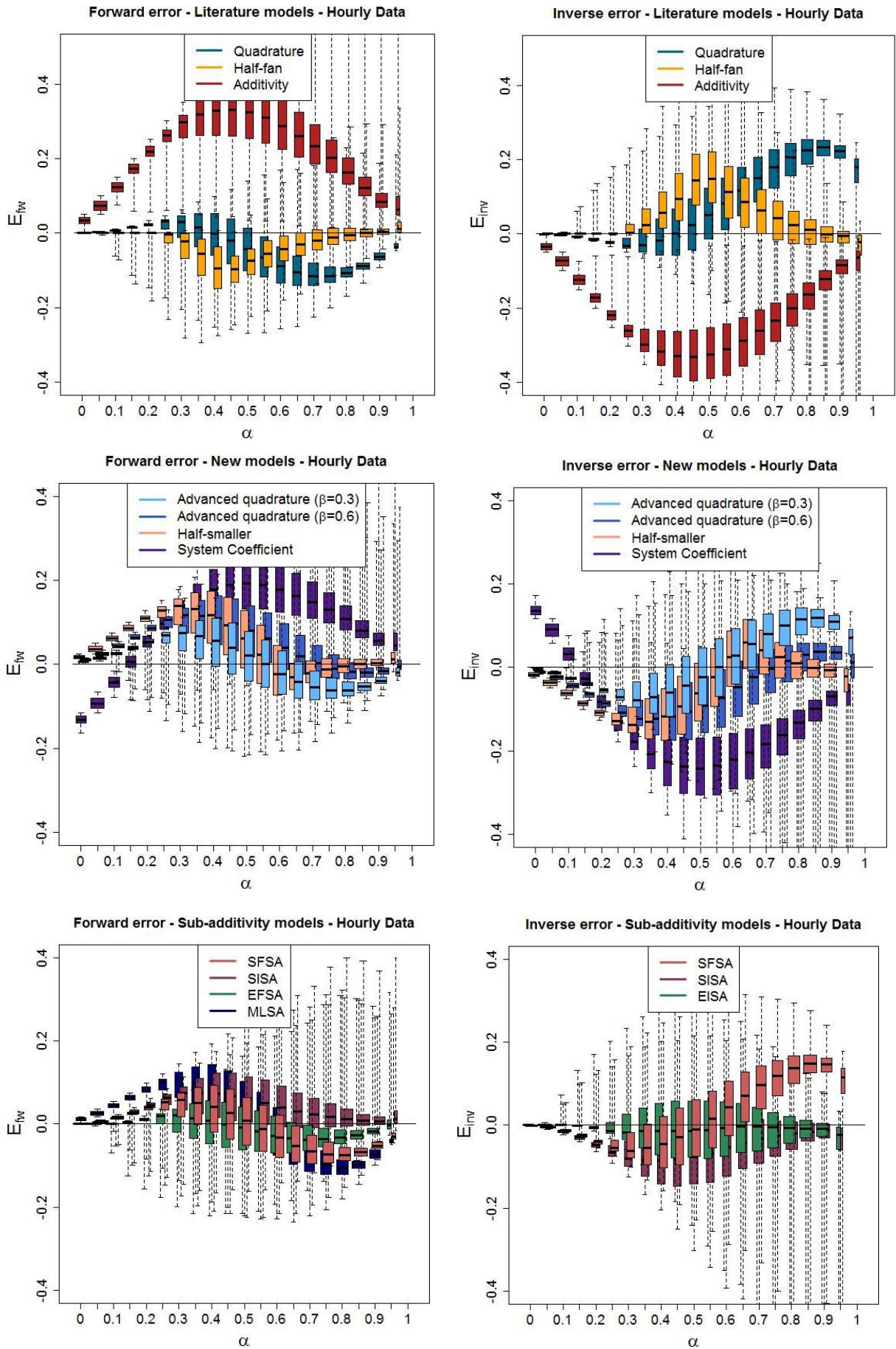


Figure 3.6 - Forward and Inverse errors of the superposition models compared with the hourly simulations

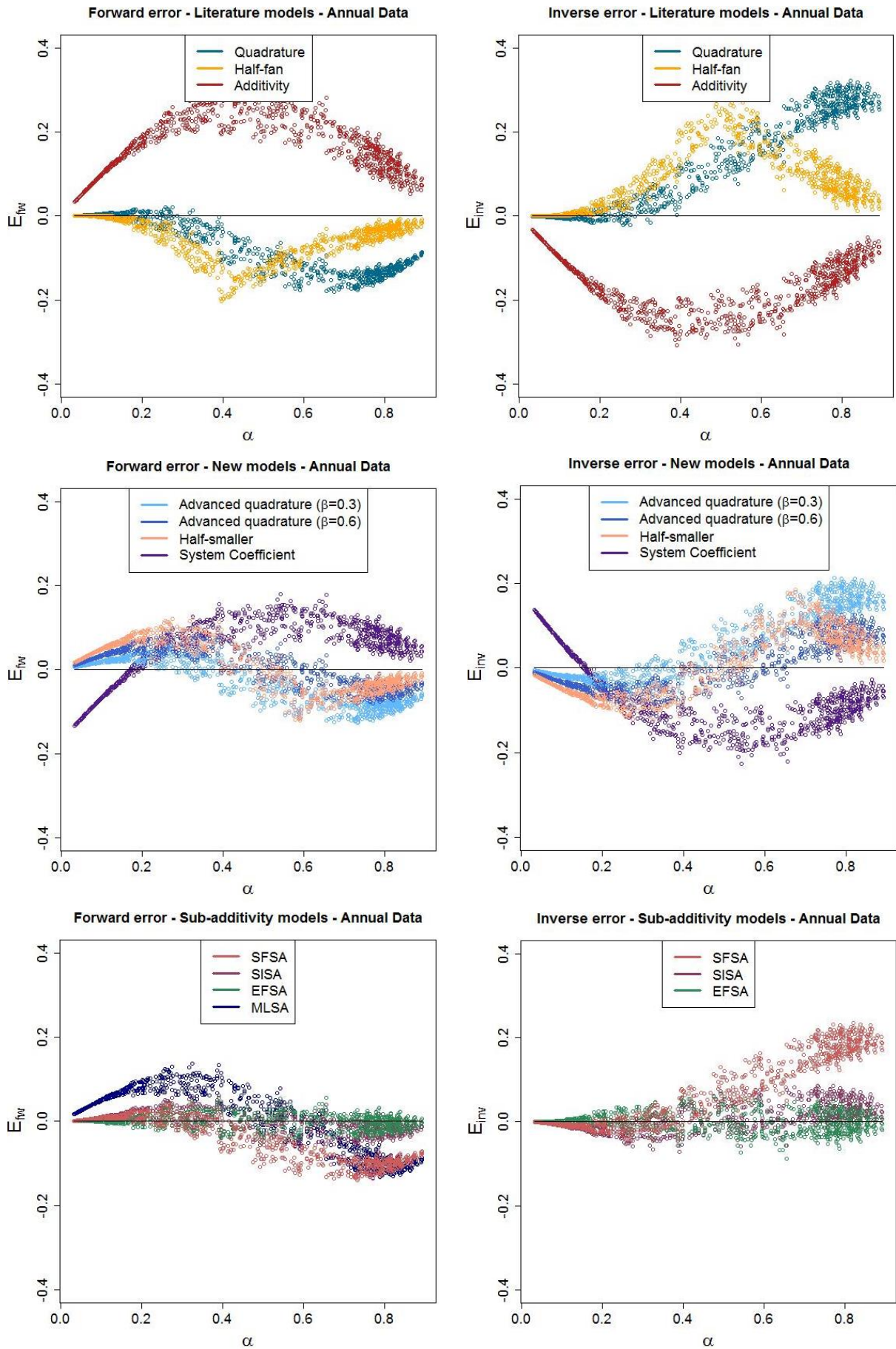


Figure 3.7 - Forward and Inverse errors of the superposition models compared with the annual simulations

Table 3.5 – Error on the model predictions for the hourly data

Model	Forward error				Inverse error				
	Bias	RMS	Max. Med.	Max. 90%	Bias	RMS	Max. Med.	Max. 90%	
Additivity	21.2%	22.1%	33.1%	34.4%	-21.2%	22.1%	33.1%	34.4%	
Simple quadrature	-3.67%	6.44%	11.6%	12.5%	7.67%	10.9%	23.3%	24.8%	
Advanced quadrature	$\beta=0.3$	0.53%	5.92%	7.45%	9.81%	0.88%	8.18%	11.9%	14.6%
	$\beta=0.6$	4.54%	7.20%	11.8%	12.1%	-4.68%	8.54%	12.3%	13.8%
Half-fan	-2.61%	4.60%	9.7%	8.72%	3.89%	7.41%	14.9%	14.7%	
Half-smaller	4.64%	7.62%	13.9%	13.1%	-4.45%	8.88%	13.9%	14.6%	
Constant system coefficient	9.34%	13.0%	19.3%	21.3%	-12.4%	16.1%	24.3%	26.6%	
SFSA	-0.75%	5.71%	7.57%	10.0%	2.69%	8.44%	14.9%	16.7%	
SISA	3.55%	5.59%	7.47%	9.64%	-4.44%	7.26%	8.51%	12.6%	
EFSA	-0.89%	4.02%	3.78%	7.72%			-		
EISA			-		-0.92%	5.60%	2.31%	10.8%	
MLSA	0.82%	8.15%	10.7%	12.9%			-		

Table 3.6 – Error on the model predictions for the annual data

Model	Forward error			Inverse error			
	Bias	RMS	Max.	Bias	RMS	Max.	
Additivity	17.6%	17.8%	30.9%	-17.6%	17.8%	30.9%	
Simple quadrature	-7.28%	7.70%	18.1%	11.5%	12.0%	32.2%	
Advanced quadrature	$\beta=0.3$	-3.06%	5.10%	12.7%	5.17%	7.32%	21.2%
	$\beta=0.6$	0.94%	4.22%	10.3%	-0.29%	5.18%	12.7%
Half-fan	-6.18%	6.38%	20.3%	9.60%	9.9%	31.6%	
Half-smaller	0.86%	5.49%	12.3%	0.42%	6.83%	18.6%	
Constant system coefficient	5.52%	8.77%	17.9%	-7.92%	11.0%	22.6%	
SFSA	-4.31%	5.35%	13.9%	6.73%	7.87%	23.4%	
SISA	0.11%	2.15%	6.18%	0.46%	2.81%	8.65%	
EFSA	-0.05%	1.60%	5.55%				
EISA				0.04%	2.14%	8.85%	
MLSA	1.08%	6.79%	13.6%				

The best models for each case are compared in Figure 3.8. For the four cases (hourly vs annual and forward vs. backward) the exponential models always give the best predictions, with biases around or below 1%, RMS ranging from 1.5% to 5.5% and maximums around or under 10%. As illustrated in Figure 3.9, the approximation of the sub-additivity coefficient captures indeed correctly the relation between  $\Phi$  and  $\alpha$ .

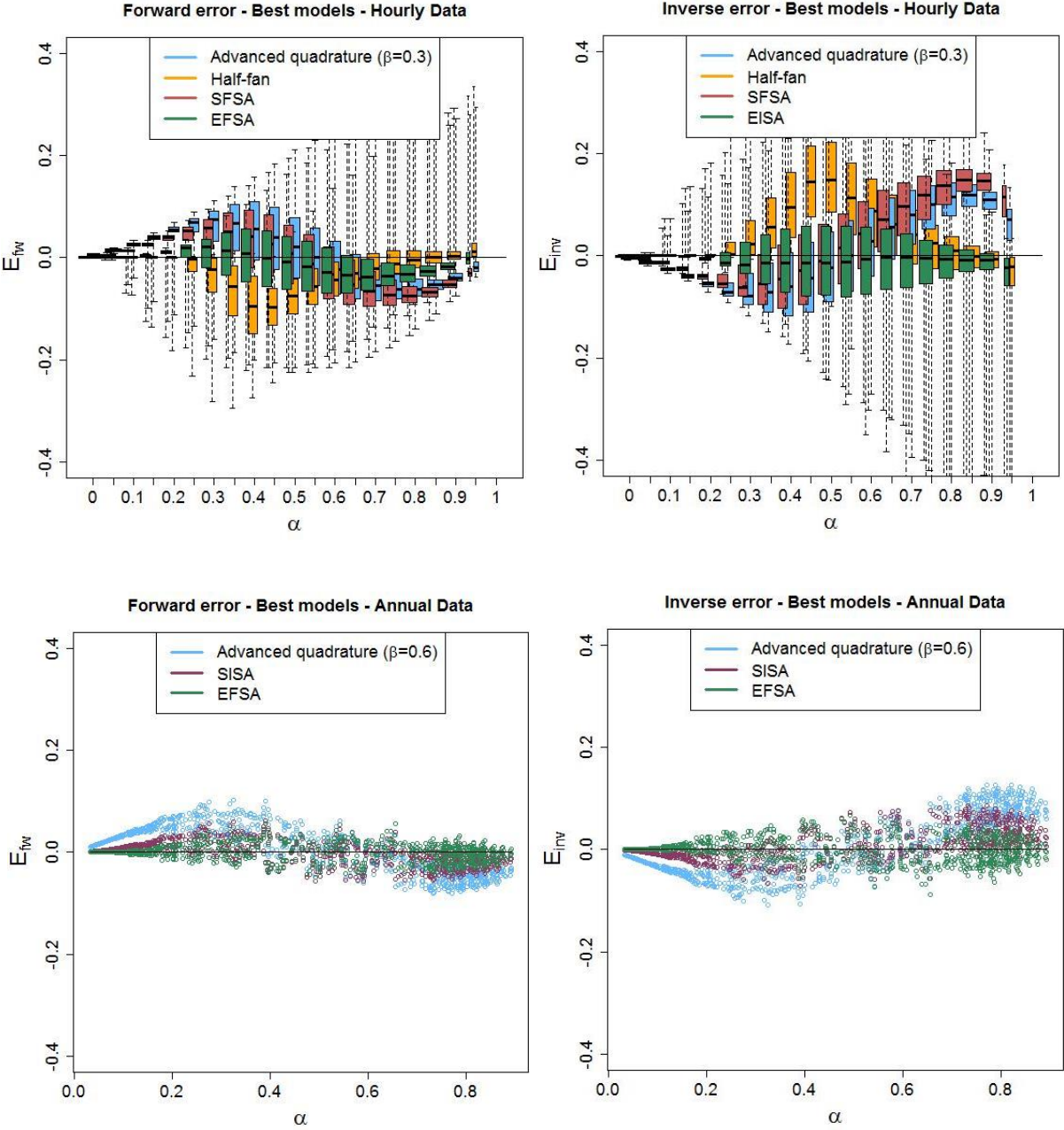


Figure 3.8 - Forward and Inverse errors of the superposition models compared with the annual simulations

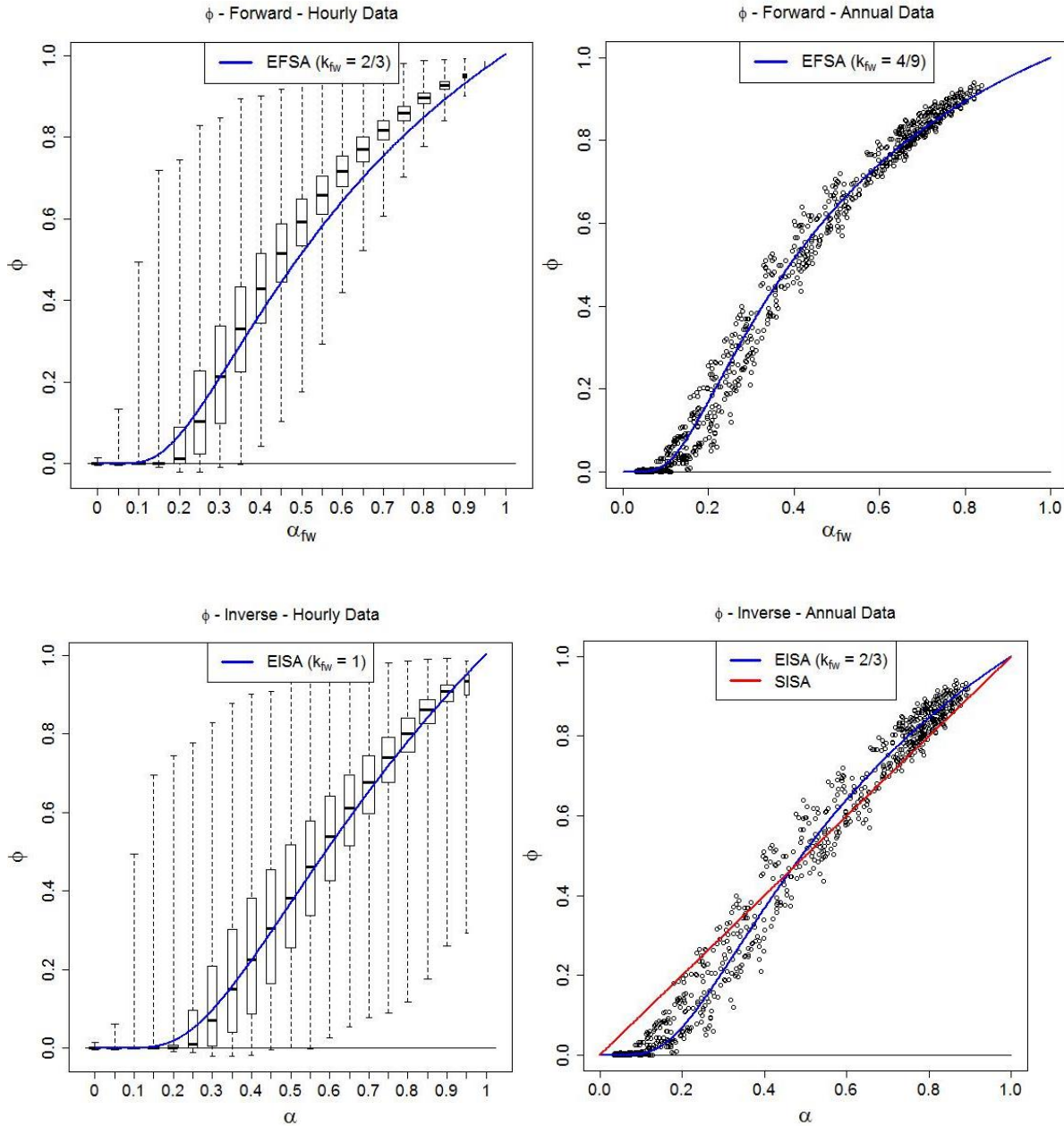


Figure 3.9 - Sub-additivity coefficient ( $\Phi$ ) from the REGCAP simulation with the best model(s) for each case

The simple additivity model has the largest errors, with bias and RMS errors of around 20% and maximums above 30%. It consistently overpredicts  $Q_t$  (and therefore underpredicts  $Q_f$ ), and the error has a parabolic shape with a maximum for an infiltration fraction  $\alpha$  close to 0.4.

The quadrature model gives good predictions for tight houses ( $\alpha < 0.4$ ), but it underpredicts  $Q_t$  for leakier houses. The maximum error is found in the vicinity of  $\alpha = 0.8$  and is almost doubled from the forward to the inverse model, reaching 32% for the annual data.

The use of advanced quadrature coefficients enables to have biases close to zero. These hourly and annual models overpredict  $Q_t$  for tight houses and underpredict for leaky houses with maximum errors of around 10% for  $\alpha = 0.25$  and  $\alpha = 0.75$ . The RMS errors around 5% are also smaller compared to the simple quadrature, and these two models are therefore a good improvement.

The half-fan model from the literature turns out to be good for extreme values of  $\alpha$ , but shows a peak error around  $\alpha=0.4$ , with a maximum error reaching 32% for the annual inverse case. The half-smaller model in comparison is better for the annual data, with errors very similar to the advanced quadrature, but is no improvement for the hourly data.

The constant system coefficient model is overall a slight improvement compared to simple additivity, but the biases and RMS errors are still significant, especially for the hourly data.

The error obtained with the SFSA model are very close to the advanced quadrature ones. The hourly cases have biases under 3% and RMS around 5% for the forward case and 8% for the inverse one. When applied to the annual data, the RMS is still as good, but the biases reach 6% and the maximum errors 23%.

The SISA model also gives very good results, and it is almost as good as the exponential for the annual data with biases below 1%, RMS around 2% and maximums at 6% and 8.7%. As shown in Figure 3.9, the approximation of the sub-additivity coefficient is not as good as the exponential one for very low  $\alpha$ . However for this range the coefficient applies to very small values of  $Q_{inf}$  and therefore does not result in large errors in the  $Q_t$  or  $Q_f$  predictions. There is no reason to prefer this model to the exponential one for the forward prediction, but it has a simpler expression for the inverse prediction. It also has the advantage of not having  $Q_t$  as a denominator, which, unlike  $Q_{inf}$ , can never equal to zero and may therefore be a good option for calculations determining fan size requirements to meet total ventilation rates.

### 3.4. Conclusion

The models from the literature that are currently used give significant errors when compared with the simulation. The simple quadrature and the half-fan models have a bias in their predictions on the order of 5-10% and an RMS error of approximately 10% for unbalanced systems. ASHRAE Standard 62.2's use of simple additivity is significantly worse, with a 20% bias and a 20% RMS error. Moreover these models have high maximum errors around 20-30% which means that they are not as accurate for the whole range of parameters. One can expect that these errors above 10% will result in measurable impacts on energy consumption or IAQ for an individual home.

A variety of other models were explored and several of them were found to be superior to simple quadrature in various ways. The model that is superior to all others is the exponential model. It takes different forms for the forward and inverse calculations, and it has different optimized coefficients for the hourly and annual forms:

Table 3.7 – Exponential sub-additivity model

	Forward	Inverse
Hourly	$Q_t = Q_f + \exp\left(-\frac{2}{3} \frac{Q_f}{Q_{inf}}\right) Q_{inf}$	$Q_f = Q_t - \exp\left(-\left(\frac{Q_t}{Q_{inf}} - 1\right)\right) Q_{inf}$
Annual	$Q_t = Q_f + \exp\left(-\frac{4}{9} \frac{Q_f}{Q_{inf}}\right) Q_{inf}$	$Q_f = Q_t - \exp\left(-\frac{2}{3} \left(\frac{Q_t}{Q_{inf}} - 1\right)\right) Q_{inf}$

While this model set is superior an even simpler application may be desired in some cases. When using annual data the following simple expression is almost as good as its exponential counterpart:

$$Q_f = Q_t - \frac{Q_{inf}^2}{Q_t} \quad (3.21)$$

For hourly data there is an advanced quadrature form that works reasonably well:

$$Q_t = \sqrt{Q_f^2 + Q_{inf}^2 + 0.3Q_fQ_{inf}} \quad (3.22)$$

A linear expression (in the forward direction) that works almost as well for hourly data may also be useful:

$$Q_t = Q_f + \frac{Q_{inf}^2}{Q_f + Q_{inf}} \quad (3.23)$$

These last three models have accuracy in both forward and backward directions, but their expressions become complicated quadratics when inverting from the way they are shown. Thus it may not be much more complicated to use the more accurate exponential forms.

To conclude, the work presented in this chapter has enabled the establishment of models to predict the combination of natural infiltration and unbalanced mechanical ventilation air flows. In the next chapters the focus will be on a more detailed investigation of the air infiltration in timber frame buildings. The study will be on a smaller scale with air permeability measurement on specific construction details followed by the investigation of the air path inside the wall assembly.





# Chapter 4

## Pressurization tests for airtightness characterization at the wall scale

In the previous chapter the air permeability was evaluated at the building scale, with a global envelope airtightness characterization. In this chapter, the focus is on individual airtightness defects, with three different scales of wall assembly pressurization tests.

This study is therefore a contribution to quantifying the impact of construction details on timber frame wall airtightness. Lightweight walls, such as timber-frame constructions with glass wool insulation, are indeed strongly exposed to air flow consequences. The three-scale approach proposed here required the development of two dedicated tests facilities to complement real scale measurements. Therefore, the first part of the chapter describes the experimental facilities and their validation. The measurements focused on wall assemblies, and more specifically on the junctions between different elements. For this purpose individual elements, and specifically the insulation types, are investigated first, followed by results for wall assemblies. Finally, the results are discussed and some conclusions are given.

This chapter was published in *Journal of Building Physics* in adapted form [117].

### 4.1. Experimental setups

#### 4.1.1. Small scale – SAPI box

The SAPI box (Small Air Path Investigation box) was constructed for the smallest scale study. As shown in Figure 4.1, it enables to characterize the permeability of insulation materials or very simple wall assemblies. The inside dimensions are 300 (length) x 150 x 150 mm. The air input is a 17 mm diameter centered hole and can be connected to the compressed air network. A first frame is placed 100 mm downstream to install the studied building component with a 150 mm square-section, and a width up to 200 mm. A second frame can be placed downstream to maintain the component at a constant compression. The box is airtight at the working pressures (under 5000 Pa). The airtightness between the tested component and the box walls is ensured by self-adhesive tape on the edges of its downstream side.

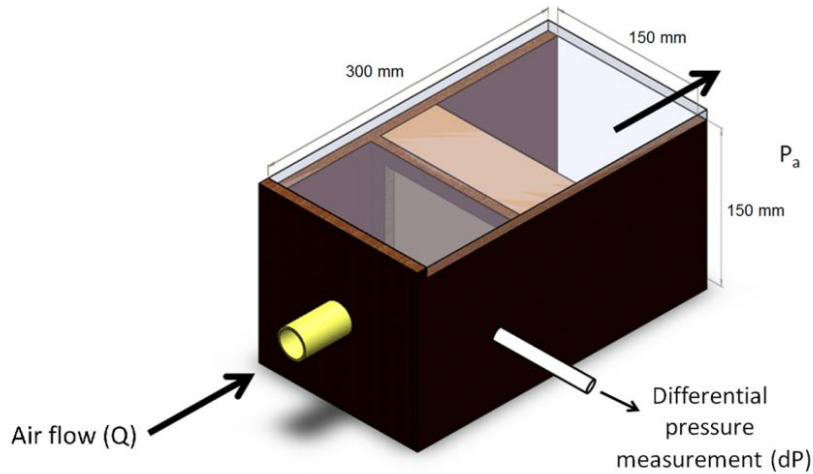


Figure 4.1 - Small scale set up – SAPI box

The flowrate is measured before entering the SAPI box with a mass flow meter (Brooks 5863S). The relative pressure is measured in the upstream part of the box with respect to atmospheric pressure by a piezoelectric pressure sensor (Kobold SEN-3231). For very low relative pressure there is an alternative differential pressure transmitters also based on piezoresistive pressure sensors (BTEL5002 – 0-200Pa). The detailed characteristics of the sensors are presented in Table 4.1. The temperature and relative humidity can be measured but not controlled.

Table 4.1 – Sensors characteristics

Type	Model	Range	Accuracy
Mass flow meter (thermal mass flow sensor)	Brooks 5863S	100 – 2500 NI/min (6 – 150 Nm <sup>3</sup> /h)	± 0.7% ± 0.2% FS (± 1% FS >1100 NI/min) (± 0.7% ± 0.3 Nm <sup>3</sup> /h)
Gas mass flow measurement (flow averaging tubes)	Eldridge Products 9724MPNH	3 – 300 Nm <sup>3</sup> /H	± 1% ± 0,5 % FS (± 1% ± 1.5 m <sup>3</sup> /h)
Differential pressure transmitter (piezoelectric pressure sensor)	Kobold SEN-3231	0-250 mbar	±0.1% FS (±0.25 mbar)
	BTEL 5002D	0-2 mbar	±0.25% FS (±0.005 mbar)

The objective of this box is to obtain quasi-instantaneous results for a comparison of different elements with good repeatability; however the absolute precision is limited. The small dimensions of the box compared to the potential high air velocity do not guarantee homogeneity of the pressure conditions along the upstream side of the tested building component. Moreover, the two frames reduce the inlet and outlet cross sectional area for the air flow to a 110 mm square-section. However, the air may flow through a larger section inside the building component (up to 150 x 150 mm), which makes absolute air permeability measurements somehow not very accurate using SAPI set-up.

#### 4.1.2. Intermediate scale – APIE box

The APIE box (Air Path In Envelopes box) was built to investigate the air path inside 2 m high and 0.7 m wide wall assemblies, to characterize the impact of the infiltrations on the temperature and humidity fields inside the wall, and to measure its air permeability [118]. The tested wall dimensions correspond to the regular spacing between two wood studs in timber frame buildings. Its design was inspired by the various experimental setups listed in paragraph 2.2.1. As shown in Figure 4.2, it is divided into three major parts: a fixed box in the center to install the studied wall assembly and two symmetrical movable boxes on each side with a 90 mm diameter air inlet and outlet, aimed at controlling boundary conditions on both sides of the wall. The inner dimensions of the two symmetrical boxes are 2 m (height) x 0.7 m x 0.7 m.

The APIE box is connected to an air supply ductwork with a variable speed blower enabling a large range of pressure difference (up to 200 Pa), varying depending on the tested building component). A micro-particle generator is also connected to the air circuit to seed the flow with fluorescein tracer micro-particles. This enables to investigate the air path inside the wall as described in Chapter 5.

For the same air path investigation purposes, the central box is partially made of PMMA for a possible use of the PIV technique (paragraph 6.2.2). The transparent surface on the top is for the laser sheet and the one on the side is to capture the upstream flow from outside with a CCD camera.

The experimental setup was sized with CFD simulations, using the PorousSimpleFoam solver of OpenFoam, and a  $k-\epsilon$  turbulence model. The aim was to identify the easiest geometry to implement that ensures a good homogeneity in the pressure field near the tested wall. This enables to consider identical flow characteristics near an airtightness defect on the tested wall regardless of its location. The results of the CFD simulation with straight enlargements of the air inlet and outlet and a location half-way up are shown in the Figure 4.3. It appears that the pressure field is homogeneous in cross-sections perpendicular to the flow direction. With a pressure difference between the inlet and the outlet of 200 Pa, in the vertical cross section in the middle of the porous insulation material the pressure values mostly range from 9.75 Pa to 10.5 Pa. This pressure homogeneity is linked with the velocity homogeneity. Apart from the regions near the wall boundaries where the velocity decreases to zero, the velocity values are also homogeneous in cross-sections perpendicular to the flow direction. This geometry is therefore implemented. More details about this simulation are presented in Appendix D.

For the permeability characterization the downstream box can be disassembled and the configuration is therefore similar to the SAPI box. The mass flow meter (Eldridge 9724MPNH) and the pressure sensor (BTEL5002) used are adapted for lower ranges. As for the SAPI box, the temperature and relative humidity can be measured but not controlled.

The sealing between the box walls and the building component is ensured by self-adhesive tape on the edges of each layer of the wall assembly. The airtightness of the box has been verified by substituting the tested building component with an airtight gypsum board. The flow meter didn't detect any leakage at a pressure of 200 Pa.



Figure 4.2 - Intermediate scale set-up: APiE box

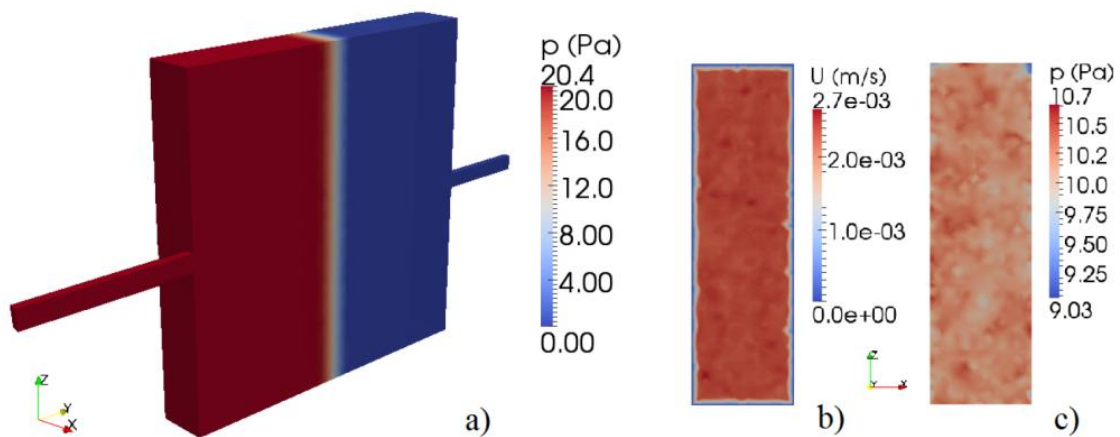


Figure 4.3 - Results of the CFD simulation: pressure field inside the box (a); velocity (b) and pressure (c) fields in a vertical cross-section in the middle of the insulation material

#### 4.1.3. Big scale – AEV test bench

In order to test wall assemblies at a bigger scale (up to 10 m x 5.5 m), the existing AEV (a French acronym standing for "Air, Water, Wind") test bench was used at the CSTB, Scientific and Technical Centre for Building, in Grenoble (Figure 4.4). It enables to test in accordance with EN 1026 the wind resistance, the air permeability and the waterproof performance of real-scale building components such as house gates, garage doors, claddings, or in our case a timber frame wall assembly.

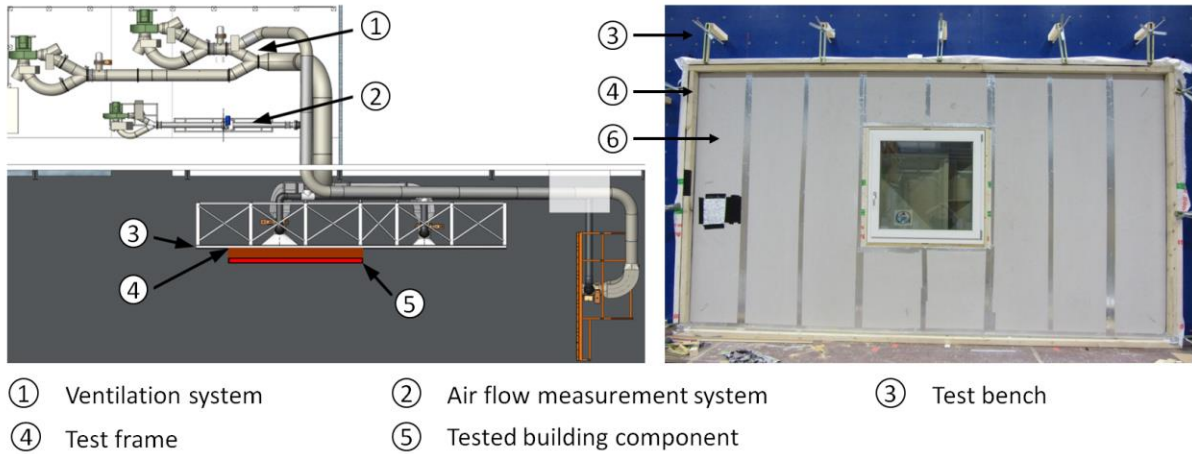


Figure 4.4 - Big scale set up - AEV test bench (left) and the real scale wall assembly tested (right)

When used for air permeability tests only, this bench has the same principle as the two smaller scale experimental set-ups presented above. A pressurizing/ depressurizing ventilation system is capable of generating up to 8 000 Pa of pressure difference between the two sides of the tested building component, and a flow meter measures the induced air leakage rate. A perfect sealing is required between the test frame and both the test bench and the tested building component.

#### 4.1.4. Verification of the experimental results reliability

The SAPI and APIE boxes were constructed for this study and further investigation on the air path in timber frame assemblies. In order to verify the reliability of the results, glass wool permeability tests were carried out similarly to the ones presented in the next section, and the results were compared with a reference value obtained with a permeameter ( $6.41 \cdot 10^{-10} \text{ m}^2$ ). The permeability measured with the APIE box is extremely close to the reference one, with a relative error of 0.43%. The SAPI box gives a higher relative error of 11%, but as mentioned before this box aims at producing relative results rather than very accurate absolute values.

Such pressurization tests were repeated four times, as shown in Figure 4.5. The even-numbered tests correspond to an increasing pressure whereas the odd-numbered tests correspond to a decreasing pressure, and the insulation material is disassembled and reassembled between the tests 2 and 3. The results enable to conclude that there is a good repeatability of the tests in the APIE box.

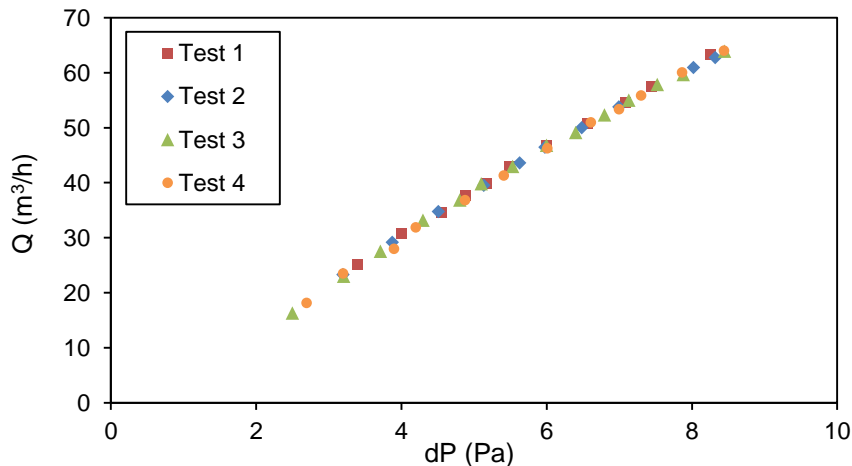


Figure 4.5 - Repeatability of APIE pressurization tests

Pressurization tests were also carried out on an airtight layer with a 20 mm diameter hole. As presented in paragraph 2.1.2, calibrated holes (2 mm in diameter) were used to model airtightness defects in the PREBAT study [119]. Each 2 mm diameter hole on a 10 mm thick PVC plate was characterized by:

$$Q_{PREBAT,2mm} = 0.0072 \cdot \Delta P^{0.5968} \quad (4.1)$$

This study was used as a comparison for the flow passing by a 20 mm diameter hole, which corresponds to our reference airtightness defect in the next tests. In order to have the same equivalent cross sectional area the leakage coefficient C is multiplied by 100.

The experimental results are also compared with the one obtained by Hall and Hauser [83] with a 20 mm in diameter hole in an airtight membrane. The comparison of the pressure - air flow laws is shown in Figure 4.6.

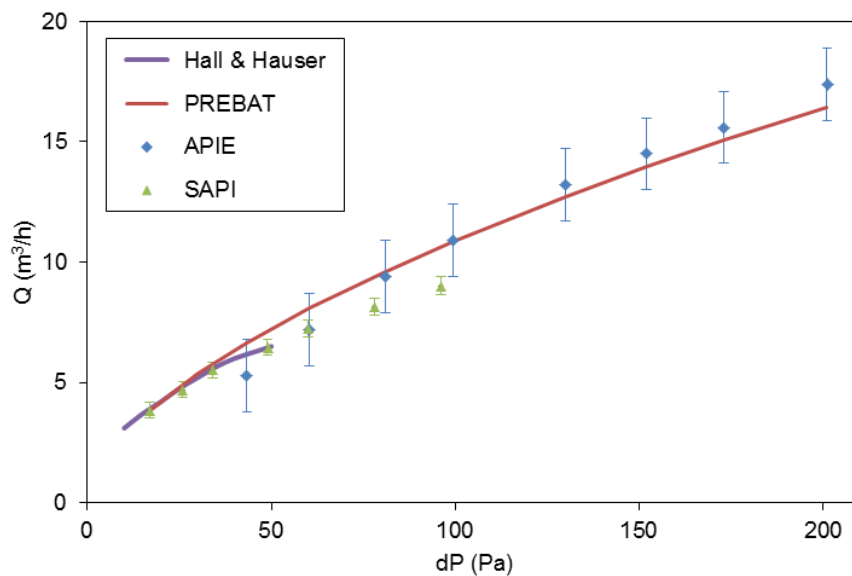


Figure 4.6 - Comparison of pressurization tests on airtight components with a calibrated hole

The results obtained with the APIE box are similar to the PREBAT ones since the differences are within the measurement uncertainties. One should note however that even if having the same order of magnitude is reassuring, the two experiments differ by the size of the holes, which has an impact on the flow behavior and can explain the systematic error observed. The range of pressure for the Hall & Hauser study (10-50 Pa) is too low for a proper comparison but around 50 Pa the differences are also within the measurement uncertainties.

The SAPI box also gives very similar results than the Hall & Hauser study and in the same order of magnitude than the PREBAT one. For pressures higher than 50 Pa the flow rate is smaller than the one measured with the other two experimental setups for. This can be due a thinner airtight layer (3 mm instead of 10 mm for the APIE box and the PREBAT project) which could induce higher turbulence near the hole and therefore lead to a smaller flow exponent. In the Hall & Hauser study the airtight layer was even thinner (<1 mm), and the same tendency seems to be observed from 50 Pa. Another possible explanation is the small cross sectional area for the SAPI box which can induce an edge effect. The dimensions of the test box used by Hall & Hauser were not given in the report but the cross-sectional area is also smaller than for the APIE box and the PREBAT study.

#### 4.1.5. Synthesis and overview of the tests

The dimensions of the tested building components and the pressure range are given in Table 4.2 for the three experimental set-ups described above. The SAPI box has the advantage of its ease of use: it requires small surfaces of material, and the sealing is simple to do. The box connection to the air ductwork enables relatively high pressurization, but the higher the pressure, the lower the accuracy.

Bigger components are tested in the APIE box which reduces the non-homogeneity issues. However the implementation and the sealing to prevent leakage between the tested component and the box walls are more time-consuming.

Finally, the AEV bench can be used to test a real timber frame wall assembly, with results easily applicable at the building scale. This experimental set-up is the most expensive and time-consuming one, which explains the relatively small number of tests. This is due to larger and heavier materials, the necessary technical staff to run the tests and the difficulty of the implementation. A specific test frame has to be built to fix the tested wall assembly on the test wall, and a perfect sealing between them is difficult to achieve.

Table 4.2 – Dimensions of the tested components and the pressure ranges for each set-up

Experimental set-up	Tested component dimensions (L x H)	Pressure range
SAPI	0.15 x 0.15 m	< 5000 Pa
APIE	0.7 x 2 m	< 200 Pa
AEV	5 x 2.5 m	20 – 150 Pa

As the objective of the study is to investigate the impact of different construction details, it was very important to test first the insulation material, as the most permeable wall assembly element.

The glass wool characterization was done using the SAPI and APIE boxes. Then wall assemblies were tested. Small details, such as conditions around a hole or the flow direction were tested in the SAPI box. Large scale construction details, such as sealing of window and vapor barrier were performed on the AEV test bench.

An overview of the tests carried out is presented in Table 4.3 and the results are presented in the next sections. The wall assemblies layers are given in order, starting from the upstream side, and separated by dashes.

Table 4.3 – Summary of the air permeability tests

Test	Material / wall assembly	SAPI	APIE	AEV
Glass wool characterization				
Glass wool (GW) permeability	Low-permeability glass wool (LPGW)		x	
	High-permeability glass wool (HPGW)	x	x	
Impact of the density	Several compression ratio of HPGW		x	



Simple wall assemblies				
Bond between the wall assembly materials	Plastic-coated cardboard (PCC) with a centered hole – HPGW	x		
Additivity of layers in a wall assembly	- PCC with a centered hole – HPGW - PCC with a not centered hole – HPGW	x		
Flow direction in wall assembly	PCC with a centered hole – HPGW	x		
Sealing of the gypsum boards (GB)	Timber frame wall assembly: GB – vapor barrier – wood fiber – MFP – weather resistant barrier			x
Sealing of the VB				
Sealing of a triple glazed window				x

## 4.2. Insulation characterization

### 4.2.1. Permeability measurements

As mentioned in Chapter 2, pressurization tests consist in generating incremental pressures between the interior and exterior sides of the tested wall or envelope  $\Delta P$  (Pa) in order to measure the induced volumetric flow rate  $Q$  (m<sup>3</sup>/h):

$$Q = c. \Delta P^n \quad (4.2)$$

Where  $c$  (m<sup>3</sup>/(hPa<sup>n</sup>)) is the leakage coefficient characterizing the air permeability and  $n$  (-) is the flow exponent ranging from 0.5 to 1 and giving an information on the flow regime. Values close to 0.5 correspond to turbulent flows obtained with large leaks such as orifices whereas values close to 1 indicate laminar flow conditions.

The Reynolds number in fibrous porous media is calculated using a representative glass fiber diameter as the characteristic dimension [120] [121] [122]:

$$Re = \frac{u. d_f}{\nu} = \frac{Q. d_f}{3600. S. \nu} \quad (4.3)$$

With:

$u$ : flow velocity (m/s)

$S$ : cross-sectional area to flow (m<sup>2</sup>)

$d_f$ : representative fiber diameter (m). For the HPGW it was estimated to be 5.7 μm (paragraph 5.3.1)

$\nu$ : kinematic viscosity (m<sup>2</sup>/s). The value for the air at 25°C is approximately 1.5e-5 m<sup>2</sup>/s

Flows with a Reynolds number below 1 are laminar. In that case (4.2) becomes a linear equation since the flow exponent  $n$  is equal to 1:

$$Q = c. \Delta P \quad (4.4)$$

The laminar flow in porous media is more precisely described by the Darcy's law:

$$Q = -\frac{k \cdot S}{\mu} \cdot \nabla P \quad (4.5)$$

With:

k: intrinsic permeability of the medium (m<sup>2</sup>)

μ: dynamic viscosity (Pa/s). The value for the air at 25°C is approximately 1.85e-5 Pa/s (μ = ν/ρ)

There is however no clear consensus on how to calculate the Reynolds number and the criterion to identify the beginning of non-Darcy flow [123]. The pore diameter can be taken as the characteristic linear dimension but it is not easily measurable for fibrous porous media. As an alternative, it is also possible to use the square root of the permeability:

$$Re = \frac{u \cdot \sqrt{k}}{\nu} \quad (4.6)$$

The air permeability of two types of glass wool with different densities but similar thermal conductivities were tested using the APIE box. The low-permeability glass wool (LPGW) is originally attached to a gypsum board (Calibel® panel), and its averaged density and porosity experimentally measured on 15 samples are respectively 63.8 kg/m<sup>3</sup> and 0.963. The high-permeability glass wool (HPGW) is lighter and usually used for the roofing insulation. Its averaged density and porosity measured on 10 samples are respectively 15.6 kg/m<sup>3</sup> and 0.994. One should note that the glass wool is relatively non-homogeneous and the standard deviation found on the density was for both materials equal to 5% of the averaged value.

The pressure – flow rate laws obtained are presented in Figure 4.7. The error bars on this graph and the following correspond to previously given accuracy of the differential pressure transmitter and the flow meter.

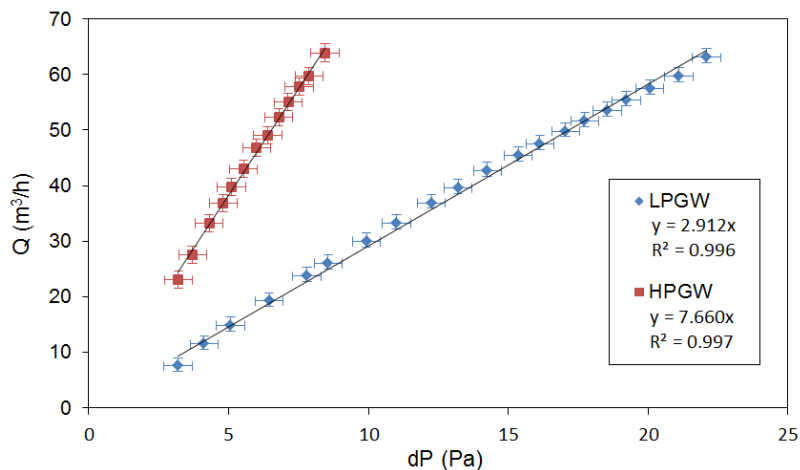


Figure 4.7 - Permeability of two glass wool materials (60 mm – APIE box)

The maximum air flow rate Q measured is less than 70 m<sup>3</sup>/h for our pressure ranges, and the cross-sectional area to flow S is 1.4 m<sup>2</sup> for this box which means that the maximum velocity u<sub>max</sub> is 0.0139 m/s. The Equation (4.3) using this maximum value of the air velocity gives a maximum Reynolds

number of  $5.3 \cdot 10^{-3}$ , which is two hundred times below the critical Reynolds number. The flow is therefore laminar in the porous media and can be described by the Darcy's law. This is confirmed by the experimental results with a linear relationship between the pressure and the air flow rate, which confirms that the flow exponent  $n$  equals to 1.

By combining (4.4) and (4.5) it is possible to calculate the permeability of the tested insulation material according to:

$$k = \frac{c \cdot \mu \cdot L}{S} \quad (4.7)$$

With  $L$  the length over which the pressure drop  $\Delta P$  takes place (m). In this first experiment the thickness of the glass wool layers was 60 mm.

The results are presented in Table 4.4 and show that for equivalent thermal properties, the permeability of the insulation material varies significantly. As expected the higher the density, the lower the permeability. The possible relationship will be investigated further in the next paragraph.

Table 4.4 – Measured density and air permeability of the two glass wool materials

	Thermal conductivity* W/(m.K)	Density (kg/m <sup>3</sup> )	Porosity (%)	Permeability (m <sup>2</sup> )	
				$k_{\perp}$	$k_{//}$
LPGW	0.034	63.8	0.963	6.41e-10	-
HPGW	0.035	15.6	0.994	1.69e-9	3.99e-9

\* manufacturers data

Furthermore, the anisotropic arrangement of fibers in the glass wool material leads to different permeability measurements depending on the air flow direction. Most of the air permeability values are given for a flow perpendicular to the fibers, but the permeability is usually significantly higher for parallel flow. As shown in Figure 4.8, both the perpendicular ( $k_{\perp}$ ) and the parallel ( $k_{//}$ ) permeability were measured for the HPGW in the SAPI box and a factor of 2.36 was obtained between them, which seems consistent with the literature [124].

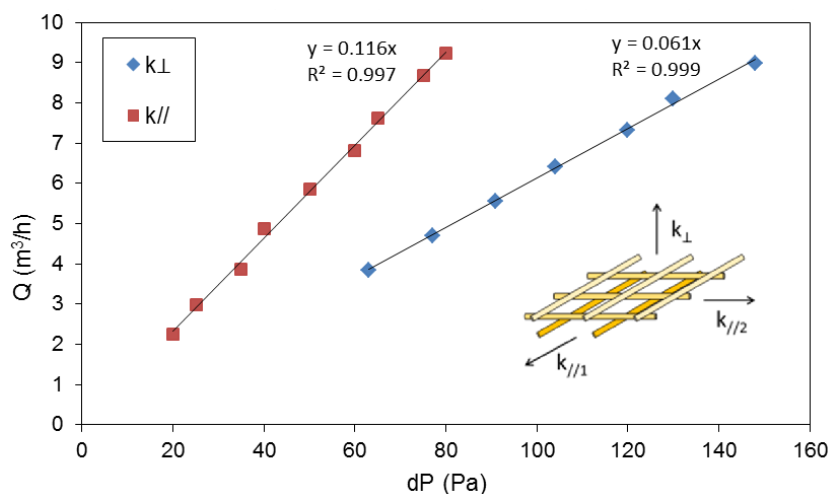


Figure 4.8 - Perpendicular and parallel permeability of the HPGW (SAPI box)

#### 4.2.2. Impact of the density

The density of the insulation material depends on the material but also on the workmanship since low-density fibrous insulation layers are very soft materials that can possibly be compressed inside the wall assembly. These two aspects are studied in this paragraph.

The influence of the compression on the air permeability was studied on the HPGW in the APIE box. For this purpose two 60 mm thick layers were assembled and a pressurization test was carried out for three compression levels. The results are presented in Figure 4.9. The cross-sectional area to flow is the same as for the density tests, and the flow rates remain under 70 m<sup>3</sup>/h, so the flow is still laminar in the porous media.

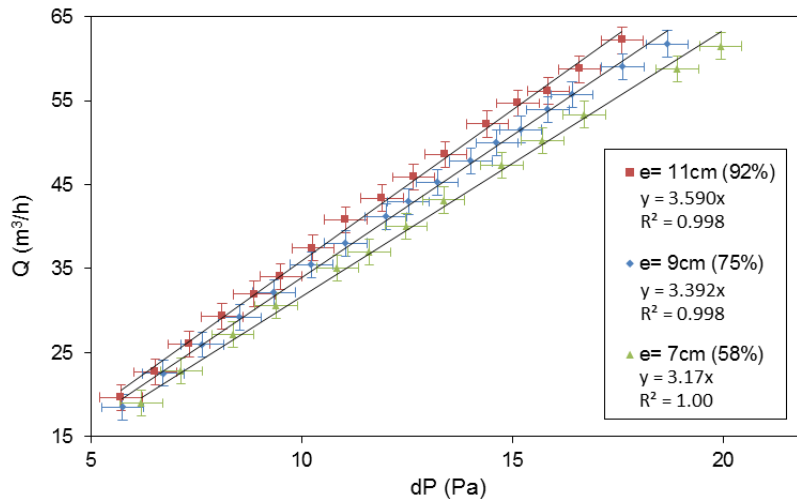


Figure 4.9 - Permeability of the HPGW depending on its compression (APIE box)

The equation (4.7) can be used to calculate the air permeability in each configuration and the results are shown in Table 4.5. The compression level is represented by the density ratio parameter:

$$DR = \frac{\rho_0}{\rho} = \frac{L_0}{L} \quad (4.8)$$

With:

$\rho_0$ : density of the material without compression (kg/m<sup>3</sup>)

$\rho$ : density of the compressed material (kg/m<sup>3</sup>)

$L_0$ : thickness of the material without compression (m). For the HPGW,  $L_0 = 6$  cm/layer

$L$ : thickness of the compressed material (m)

Table 4.5 – Density and air permeability of the HPGW at 3 compression levels

DR	Density (kg/m <sup>3</sup> )	k (m <sup>2</sup> )
92%	17.1	1.45e-9
75%	21.0	1.12e-9
58%	27.1	8.15e-10

It is clear from these tests that the air permeability of the material decreases with increasing density, which was directly related to compression rate in our case. In order to further investigate the impact

of density, the results of all permeability tests carried out on glass wool with up to three layers are presented in Table 4.6, together with values found in the literature for different mineral wools.

Table 4.6 – Summary of the pressurization tests on the glass wool

Glass wool	Nb. layers	Box	Thickness (cm)	Density (kg/m <sup>3</sup> )	k (m <sup>2</sup> )
HPGW	1	APIE	6	15.7	1.69e-9
		SAPI	4	23.4	1.04e-9
	2	APIE	11	17.1	1.45e-9
			9	21.0	1.12e-9
			7	27.1	8.15e-10
	3		15	18.9	1.19e-9
LPGW	1	APIE	8	63.8	6.41e-10
Kronvall [125]	-	-	-	20	2.20e-9
Kumaran [126]- I				20	1.45e-9
Kumaran [126]- II				17.9	1.15e-9
Økland [127]				18.3	1.9e-9
Marmoret [128] - I				79	2.69e-10
Marmoret [128] - II				119	3.36e-10
Langmans [124]				21.3	17e-9

These results collected together confirm that there is a relation between the density and the air permeability of the glass wool, but it does not seem to be linear. An empirical relation is therefore established, as shown in Figure 4.10:

$$k = 1.94 \cdot 10^{-8} \times \rho^{-0.89} \tag{4.9}$$

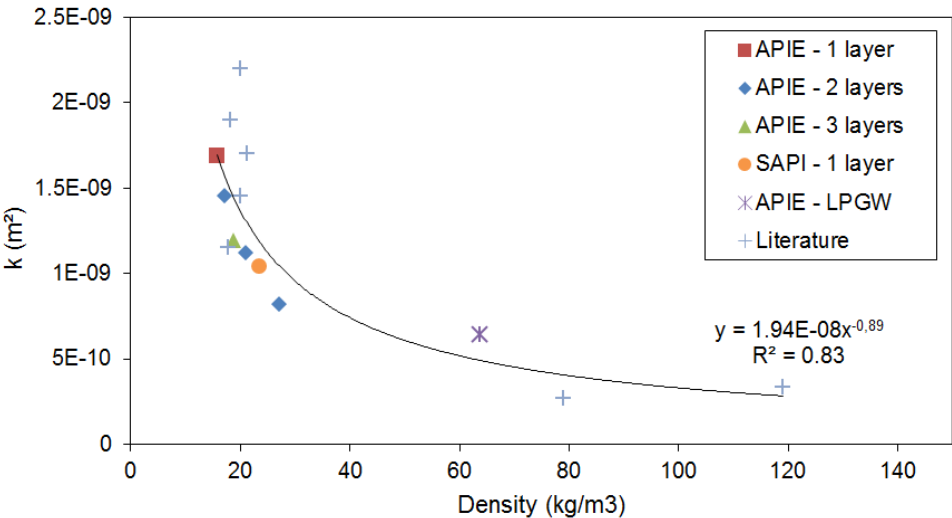


Figure 4.10 - Permeability of the glass wool in function of the density ratio

The correlation coefficient  $R^2$  is only 0.83 which means that there are significant relative errors. This is due to the fact that there are other parameters impacting on the air permeability that were not considered here, such as the fibers diameter, the porosity or the tortuosity. Detailed models have been suggested in the literature ([129], [130] and [131]). However relation (7) may be useful as a first approximation since the density is one of the most available glass wool characteristics.

### 4.3. Simple wall assemblies

In this section simple wall assemblies are tested in the SAPI box with much lower air permeability than a porous medium as the glass wool. In order to maintain a good accuracy on the flow rate measurement, higher relative pressures are reached. They are not representative of normal conditions in a building, but the pressurization laws obtained below can be interpolated to predict the air flow rate at a lower pressure.

#### 4.3.1. Bond between the wall assembly materials

The bounding between the layers may also significantly impact air permeability of a wall assembly. A simple wall assembly has been implemented in the SAPI box to quantify the impact of this parameter. The first layer is a plastic-coated cardboard (PCC) with a 20 mm diameter centered hole, and the second layer is the HPGW material. As mentioned above, the pressure difference ranges in this study are much higher than those encountered in-situ, but this was necessary to maintain good air flow measurement accuracy despite the low permeability. The various configurations studied are presented in Figure 4.11 and the results in Figure 4.12.

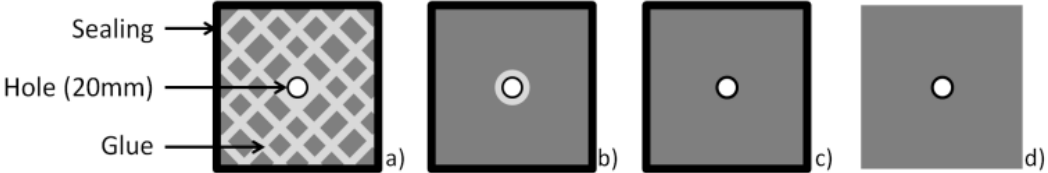


Figure 4.11 - Studied PCC-HPGW interfaces: sealed – glued (a); sealed – circle of glue (b); sealed – no glue (c); no sealing – no glue (d)

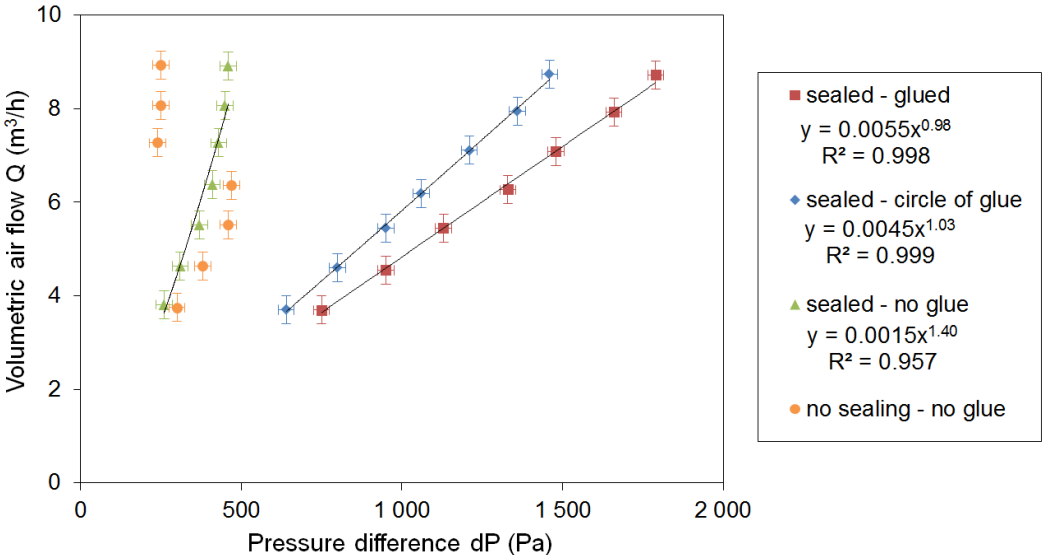


Figure 4.12 - Impact of the sealing and the bond between a plastic-coated cardboard with a 20 mm diameter centered hole and a 4 cm layer of HPGW

One test is carried out with a sealing (adhesive tape and 2<sup>nd</sup> frame) preventing the air to pass between the glass wool and the box walls, and the two materials glued on their whole interface surface (Figure 4.11.a). This results in an almost linear trendline with a flow exponent  $n$  that equals to 0.982. The fact that it is slightly under 1 can be due to uncertainties or explained by the fact that locally, where the air goes through the hole in the PCC, the section is reduced so the air velocity is higher. Using (4.3) at this air inlet, with an air flow  $Q$  of 9 m<sup>3</sup>/h, and a fiber diameter of 5.7 μm gives a Reynolds number of 3.0. The use of the alternative equation (4.6) leads to a Reynolds of 5.3, which is in the same order of magnitude. This means that, even if the increase of the cross sectional area in the insulation layer will rapidly guarantee a laminar flow, the critical Reynolds number of 1 can be locally overpassed.

The same test with only a circle of glue around the air inlet (Figure 4.11.b) gives slightly different results. The leakage coefficient  $C$  is lower, which means there is probably a small air gap between the two layers: even if the air enters the insulation by a 20 mm diameter section, it can partially exit it after the glue circle and disperse in the air gap to re-enter with a larger cross-sectional area. This phenomenon reduces the risk of local high velocity and therefore the flow exponent reflects a laminar flow. The fact that it is slightly above 1 can be due to the uncertainties or to a small displacement of the glass wool with the pressure.

When there is no glue between the PCC and the HPGW (Figure 4.11.c), there is naturally an air gap appearing between the two components. The flow exponent is above 1 ( $n=1.40$ ), which is not physically possible. As explained in the introduction, this parameter varies from 1 for a completely laminar flow to 0.5 for a completely turbulent flow. The only explanation is therefore that the wall assembly has been transformed during the pressurization test due to the impact of air pressure, with probably an increasing thickness of the air gap between the two materials.

Finally the same wall assembly without sealing (Figure 4.11.d) is tested and it results in a non-continuous curve. First the increase of flow rate increases the pressure inside the box, with a flow exponent clearly above 1 reflecting again an increasing air gap thickness. The HPGW was cut with slightly bigger dimensions than the inner box section, and the fact that these points are close to the one from the test with a sealing means that for this air flow range no air is passing along the box walls rather than through the insulation material. However around 7 m<sup>3</sup>/h the relative pressure decreases suddenly from 470 to 240 Pa, which is below the initial pressure of 300 Pa measured for an air flow of 3.7 m<sup>3</sup>/h. This means that the HPGW has been moved under the pressure to allow a more direct air path along the box walls.

As a conclusion, the bond between the wall assembly layers has a significant impact on its air permeability, and to ensure no air gap the whole surface should be glued. Moreover the absence of sealing is not always significant since for example larger insulation materials can prevent leakage along the test box walls, but if the components are not fixed correctly there is a risk for them to move with the increasing pressure.

#### **4.3.2. Additivity of layers in a wall assembly**

Measuring the air permeability of each wall element taken alone gives an indication about the wall assembly. However each layer has a more or less well defined air inlet and outlet areas, and

therefore impacts the air path in the other layers. Consequently additional investigations are needed in order to assess the behavior of assembled elements. For this purpose the air permeability of a simple wall assembly on the SAPI box was studied by adding the layers successively: a plastic-coated cardboard (PCC) with a 20 mm diameter centered hole (CeH); 1 and then 2 layers of high permeability glass wool (HPGW); another PCC with a 20 mm diameter CeH. The bond between the PCC and the HPGW was a circle of glue around the centered hole. The results are presented in Figure 4.13.

The first layer made of an airtight PCC with a 20 mm diameter centered hole does not create much pressure losses: an air flow rate of 9 m<sup>3</sup>/h leads to a relative pressure inside the box of only 30 Pa. The flow exponent n equals to 0.6 which means the flow is almost turbulent. This is verified by the calculation of the Reynolds number with the diameter of 20 mm as a characteristic length and a flow of 9 m<sup>3</sup>/h giving 2650. This is in the vicinity of the critical Reynolds number since the transition between a laminar and turbulent flow usually occurs between 2300 and 3000, depending on factors such as the flow uniformity and the roughness.

The addition of the first layer of glass wool has a significant impact on the air permeability since pressures are going up to 1500 Pa for the same flow range. The insulation material alone has a high permeability with only 5 Pa induced by a 9 m<sup>3</sup>/h air flow rate. As discussed in the previous paragraph, the PCC alone generates also very few pressure losses. This is an example of the non-additivity of the pressure losses: the first layer reduces the air inlet area in the HPGW from an 11 cm square section to a 2 cm diameter hole, which significantly decreases its air permeability. This is an expected result since in theory the pressure losses could be additive only with an air gap between the layers big enough to have an established flow.

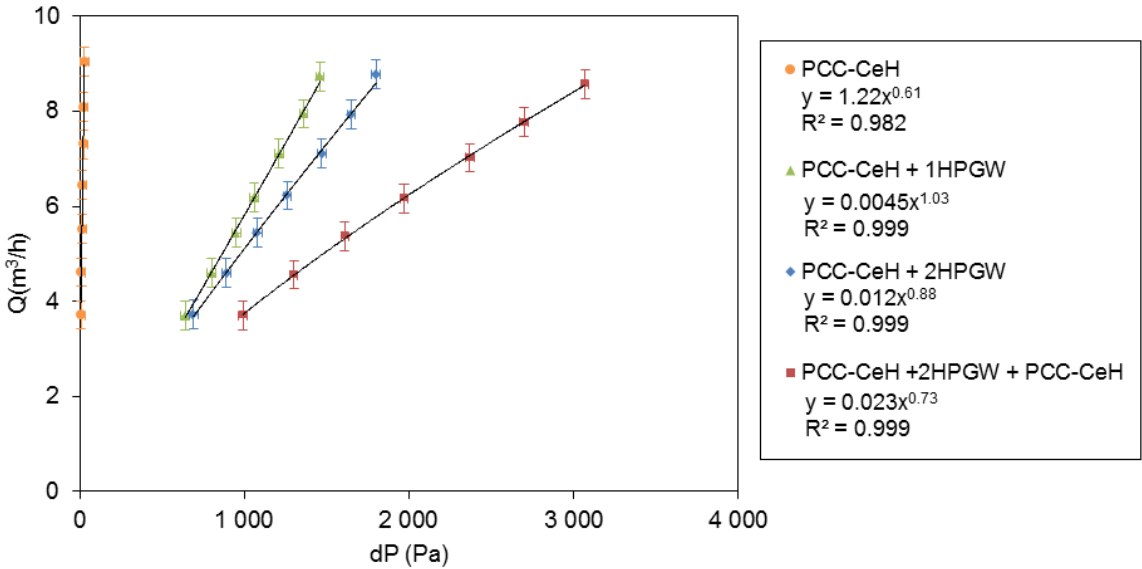


Figure 4.13 - Successive addition of layers: plastic-coated cardboard (PCC) with a 20 mm diameter centered hole (CeH) and high permeability glass wool (HPGW)

A second layer of HPGW decreases the air permeability as expected. The relative pressure reaches 1800 Pa at 9 m<sup>3</sup>/h, which corresponds to an increase of 20% compared to the 1 layer configuration. The addition of another insulation layer causes a non-linear decrease of total air permeability. The pressure difference is indeed not doubled since the second layer has a larger air inlet area as a result



of the air dispersion in the first layer. On the other hand, the fact that the increase is significant compared to the pressure losses induced by the HPGW alone means that the air did not disperse in the whole cross-sectional area before entering the second layer.

Finally, the addition of a second PPC with a centered hole reduces the air outlet area and therefore the global air permeability of the assembly. This reduction of the air dispersion inside the insulation material also generates higher velocities for the same flow rate, which explains a flow exponent under 1.

The same study is carried out with a 20 mm diameter hole located in the corner rather than in the middle of the PCC, with the center at 40 mm from the two adjacent sides. The results are presented in Figure 4.14. This first layer alone creates a lower flow rate than when the hole is centered and aligned with the air inlet inside the SAPI box. The dimensions of the box are indeed too small to guarantee homogeneity of pressure along the wall assembly. The flow exponent is however still equal to 0.5 which is characteristic of turbulent flows through large opening.

The successive addition of one and then two layers of HPGW has a similar effect as the one observed in the previous configuration, but the air permeability is reduced almost by half. This is due to the fact that the location of the hole in the corner reduces even more the air dispersion inside the insulation materials. The flow exponents are slightly above one, which can once again be explained only by a slight displacement of the HPGW under the pressure despite the circle of glue.

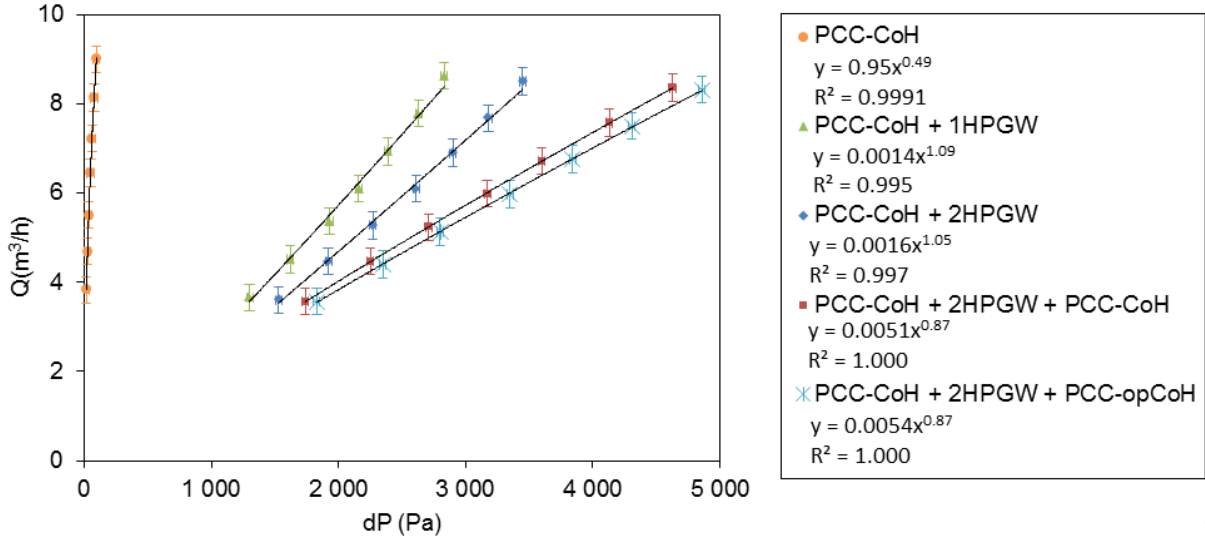


Figure 4.14 - Successive addition of layers: plastic-coated cardboard (PCC) with a 20 mm diameter hole in the bottom – right corner (CoH) or bottom -left (opCoH) and high permeability glass wool (HPGW)

A second PPC is added reducing the air outlet area, with the location of the hole aligned with the first one (bottom-right corner) the air permeability decreases in the same way than in the previous configuration. One can notice that when the hole is located on the opposite corner, the longer air path inside the wall assembly induces 5% lower air flow rates.

**4.3.3. Flow direction**

The order in which the air flow meets the layers may also have an impact on non-symmetrical wall assemblies. This phenomena is studied with a simple wall assembly made of a PCC with a 20 mm

centered hole glued with a 4 cm HPGW layer. As shown in Figure 4.15, for pressure difference below 300 Pa the two resulting pressure-flow laws seems to coincide, but above 300 Pa the higher the pressure the more the air permeability differs depending on the direction of the air flow. This difference is therefore due to the second order terms of the laws which become more significant at high pressures. The flow exponent is indeed higher when the air is diverging inside the insulation material (0.85 compared to 0.72), which means that the porous media make the flow more laminar. Therefore, when testing the airtightness of a wall assembly at high pressure, one should be aware that the result can change depending if the air is converging or diverging inside the insulation material.

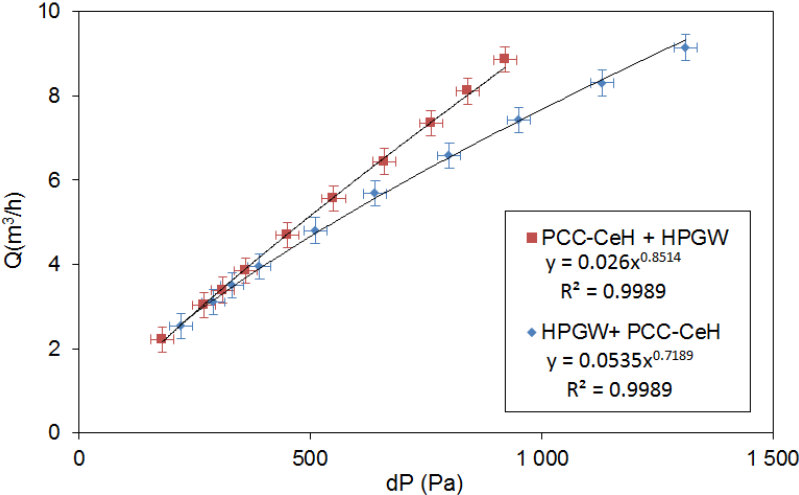


Figure 4.15 - Impact of the flow direction for a plastic-coated cardboard (PCC) with a 20 mm diameter centered hole (CeH) and high permeability glass wool (HPGW)

### 4.4. Tests on a real timber frame wall assembly

The air permeability of a real timber frame wall assembly was measured on the AEV test bench. As shown in Figure 4.16, the wall is 5 m long and 2.6 m high, and is a copy of the southern side of an experimental test house described in [132] and [37]. From the interior to the exterior side it is made of a 15 mm thick gypsum board (GB), a vapor barrier (VB), two 80 mm thick wood fiber layers and a 10 mm thick multifunctional plate (MFP).

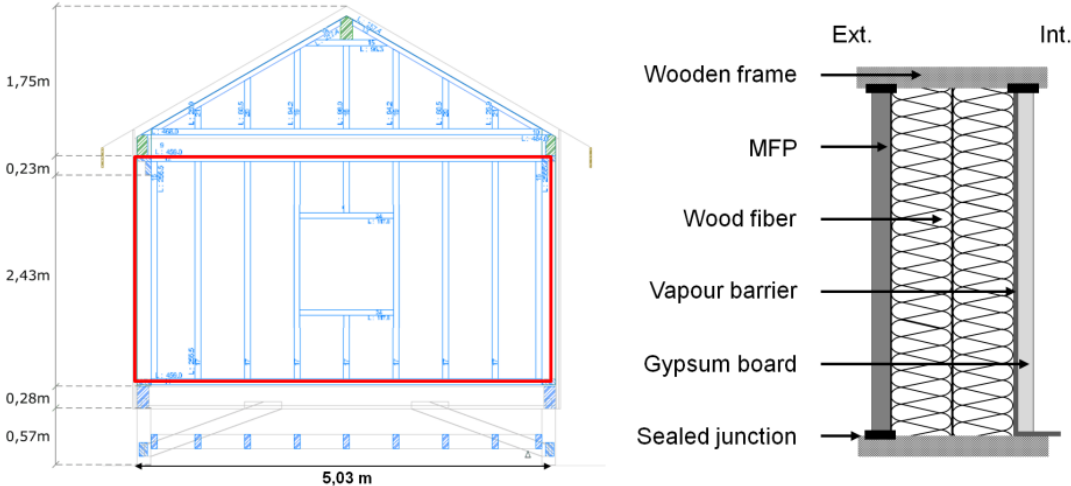


Figure 4.16 - Composition of the timber frame wall assembly tested on the AEV bench

There are 8 gypsum boards (GB) placed next to each other corresponding to the 8 stud interspaces, consequently each extremity of the GB can be tightened against the framework. The tested wall was built to ensure the possibility of adding a window, with a squared timber frame already mounted. However at first the wall assembly is the same at that location than elsewhere, with no discontinuity of the VB and the same building components.

First the wall assembly is tested with no sealing between the GB, no sealing of the VB against the bottom wall plate, and no window (Figure 4.17.a ). Then aluminum foil tape was used to seal the GB and several VB sealing with the bottom wall plate were tested (Figure 4.17.b). Finally, a triple glazed window was added to study the impact on the air permeability depending on its sealing (Figure 4.17.c).

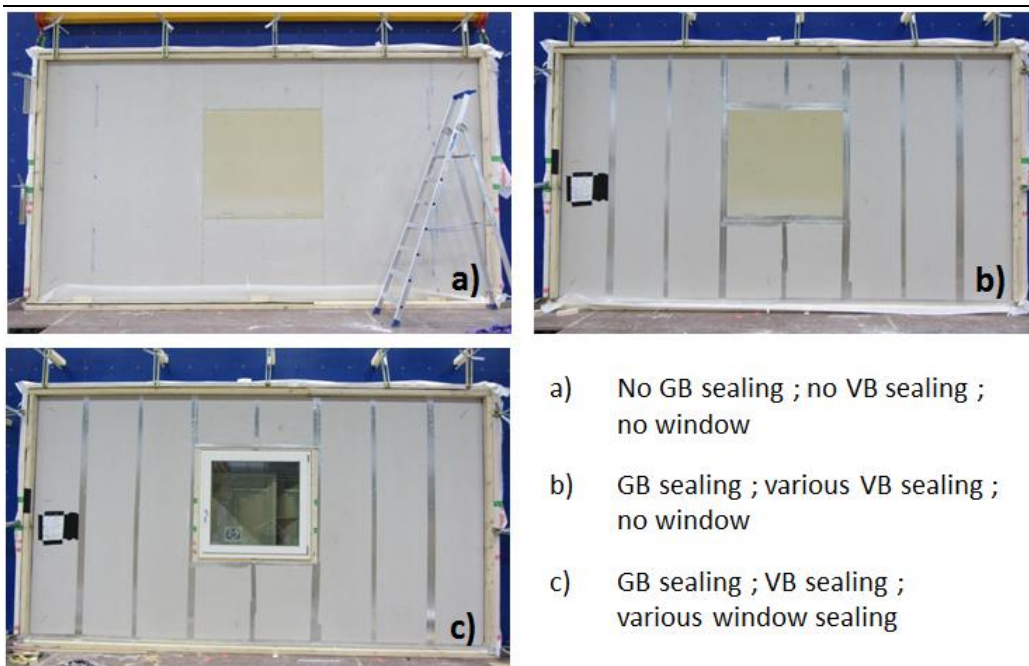


Figure 4.17 - Steps of the timber frame wall assembly air permeability tests on the AEV bench

For each configuration the air permeability was measured for both pressurization and depressurization at 10 pressure differences values: 20-30-40-50-60-70-80-90-100 and 150 Pa. The results presented in the next sections are averaged values between the pressurization and depressurization tests. As discussed previously the values can differ, but with this relatively symmetrical test wall the differences in the measured air flow values were not very significant (5% on average).

The uncertainties are calculated considering that the resulting pressure – flow law is a power law (equation (4.2)), and using the deviation from this model.

#### 4.4.1. Sealing between the gypsum boards

The impact of the sealing between the GB is presented in Figure 4.18. The aluminum foil tape on the boards' junctions reduces the air permeability of the wall assembly, but the difference between the two configurations is under 10% at 150 Pa. This is not very significant compared to the slot length covered, which is about 19 m. It can be explained by the fact that the air permeability on the exterior side (upstream side) is low since the MFP is airtight and the junctions between the panels are sealed with polyurethane sealant. As a result, even a leaky interior side does not generate much air flow.

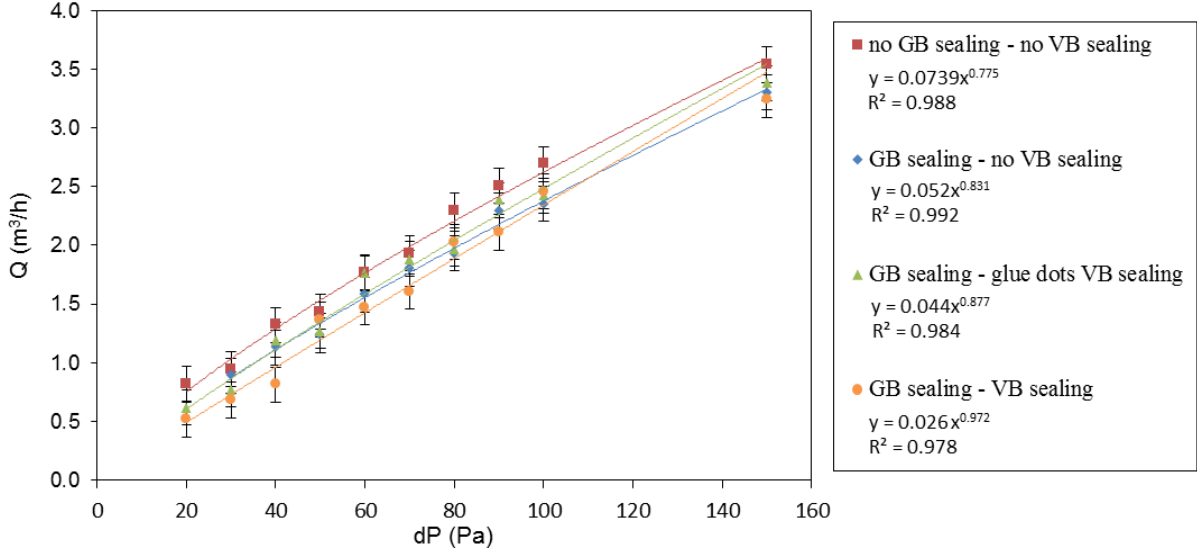


Figure 4.18 - Impact of the GB sealing and the VB sealing against the bottom wall plate

#### 4.4.2. Sealing of the vapor barrier

Another construction detail studied is the sealing of the VB against the bottom wall plate. The wall assembly is delivered with no sealing at this junction, and a VB projecting passing under the gypsum boards (Figure 4.19.a). A glue dot between the VB and the bottom plate was then added every 20 cm (Figure 4.19.b) to prevent the VB to move up. Finally this junction was sealed completely with polyurethane, as it is the case for the other horizontal-vertical components junctions (Figure 4.19.c).

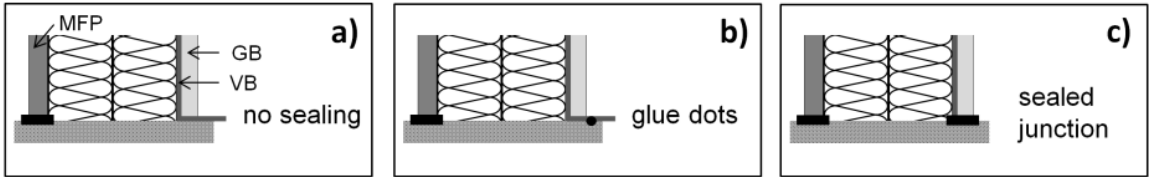


Figure 4.19 - Steps of the VB sealing against the bottom wall plate

The air permeability tests results are presented in Figure 4.18. The first conclusion that can be drawn is that the sealing of the VB has not a very significant impact on the total air permeability of the wall assembly. The air leakage flow is reduced on average by 7% despite a 5 m slot length covered. The explanation for this is the same than for the sealing between the GB: the good sealing on the exterior (upstream) side of the wall is efficient and prevents high leakage regardless of the sealing on the interior side.

In this highly airtight configuration, the two tests with and without the glue dots enable to conclude that the glue dots do not improve the airtightness of the wall assembly, or in a way not significant enough compared to the measurements uncertainties.

#### 4.4.3. Sealing of a window

For a second configuration, a triple-glazed window was installed by a professional constructor of timber-frame houses.

The window is first sealed from the exterior side with polyurethane sealant, and in a second step it is also sealed from the interior side with SIGA<sup>®</sup> adhesive tape. The results of the air permeability tests are presented in Figure 4.20.

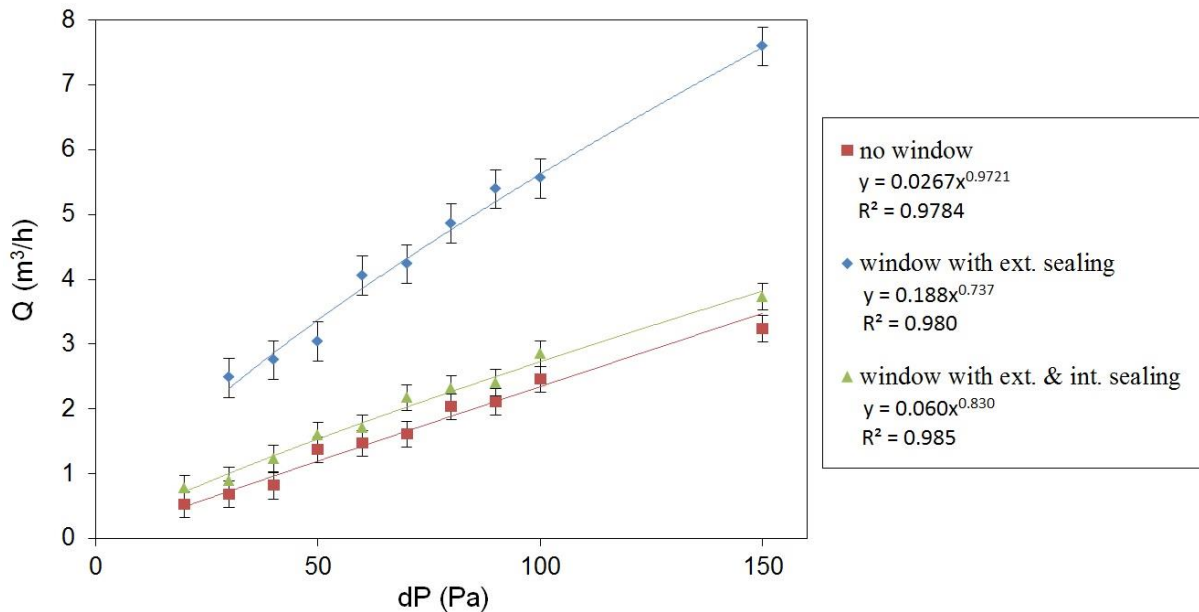


Figure 4.20 - Impact of the window sealing

It appears that when sealed only from the exterior side, the window doubles the air leakage for this airtight wall assembly: for example at 150 Pa, with an air flow of 7.6 m<sup>3</sup>/h is measured instead of 3.2 m<sup>3</sup>/h without the window. The flow exponent without a window equals to 0.97, reflecting a mostly laminar flow, passing through porous media or very small openings. On the other hand, when the window is added and sealed only from the exterior side, the flow exponent decreases to 0.74, which means that the air is passing through larger openings. Even if there is a good sealing between the MFP and the window, once the air managed to infiltrate after the MFP it has a direct path to exit the wall assembly along the window. When sealed on both sides, the impact of the window on the air permeability is much less significant, with an air flow of 3.7 m<sup>3</sup>/h at 150 Pa compared to 3.3 m<sup>3</sup>/h without window.

#### 4.4.4. Use of the results for building scale simulations

In order to facilitate the use of these results for building scale simulations, a summary of the pressurization law coefficients is presented in Table 4.7. The leakage rate is given at 50 Pa which

enable to draw the following conclusion on the additional air leakage induced by our construction details at this pressure:

- The impact of an unsealed junction between two gypsum boards is 0.012 m<sup>3</sup>/h/m
- The impact of an unsealed junction between the vapor barrier and the bottom plate is 0.036 m<sup>3</sup>/h/m
- The impact of a window is 2.16 m<sup>3</sup>/h (0.52 m<sup>3</sup>/h/m) when sealed on one side only; 0.35 m<sup>3</sup>/h (0.08 m<sup>3</sup>/h/m) when sealed on both sides

One should note that unlike the previous tests made on a significant airtightness defect (20 mm in diameter hole), these test results are of interest mostly for low-energy constructions. The tested wall was built to meet passive standards, and for every test the exterior side was properly sealed which explains the relatively low leakage rates measured in comparison with the literature. Relander et al. [102] have indeed compared different sealing methods for windows in timber-frame buildings and they found that the least airtight one (self-expanding sealing strip) could lead to leakages of 11 m<sup>3</sup>/h/m.

Table 4.7 – Summary of the results for the real timber frame wall assembly tests

Sealing GB (19 m)	Sealing VB – bottom plate (5 m)	Sealing window (4.8 m)	C	n	Leakage rate at 50 Pa (m <sup>3</sup> /h)
no	no	no window	0.074	0.73	1.56
yes			glue dots	0.052	0.83
	0.044			0.88	1.38
	0.027			0.97	1.20
	ext. side			0.188	0.74
	ext. & int. sides		0.060	0.83	1.54

## 4.5. Conclusions

The building airtightness is a rising concern to meet the regulation requirements tightened by the development of low-energy and passive houses. That challenge needs to be addressed by academic studies, including laboratory experiments on the building components air permeability, on the performance of simple wall assemblies and on the impact of the workmanship.

For this purpose two original experimental setups were built and a third existing one was used. Each of them enables to carry out pressurization tests at a different scale. The SAPI box is convenient to get quickly relative results on 15 cm x 15 cm building materials and elementary components. The APIE box has bigger dimensions (2 m x 0.7 m) which decrease the error sources and enables to test simple wall assemblies. The reliability of these new set-ups was verified by comparison with a permeameter test and a literature study. In addition normalized tests on the AEV bench were used.

The tests carried out on these three experimental setups contribute to quantifying the impact of workmanship on timber-frame wall airtightness. It has been found that the choice of the insulation

material can have a significant impact since the tested soft glass wool had a three times higher air permeability than a rigid one with the same thermal performances. Even if many other parameters are involved, an empirical formula was established for the relation between the density and the permeability that can be used as first approximation. Moreover it has been pointed out that whether or not the gypsum board and the insulation are glued together has a significant impact on the resulting pressure-flow law, and to ensure no air gap the whole surface should be glued. The direction of the air flow through the wall layers also influences air flow values for high pressure differences.

Finally, the tests carried out on a real timber-frame wall assembly showed that when the sealing is properly achieved on one side of the wall, the impact of an airtightness defect on the other side is not very significant on the air flow through the wall. The addition of aluminum foil tape to seal the gypsum boards and the sealing of the vapor barrier against the bottom wall plate were found to have both an impact on the air leakage flow under 10%. On the other hand it has been shown that a proper sealing on both sides of a window is required. In our configuration the addition of a window with only the exterior sealing has more than doubled the air leakage, whereas a both side sealed window had an impact under 20%. This brings to the conclusion that when air gaps are involved, providing a direct path for the air, a good sealing on both sides of the wall is required, but otherwise an airtight defect on one side has not a very significant impact on the global wall assembly air permeability. These experimental results obtained at a real scale can be used in models by expressing the permeability reduction by meter of sealed gap. However the relative decrease in permeability is dependent on the pressure difference since the flow exponent is also impacted by the change of air path.

These wall-scale tests enable a finer characterization than global building envelopes air permeability measurements. However, in order to better understand the impact of the airtightness defects on the wall assembly performances an even finer analysis is required. Air leakage induces indeed thermal losses that vary depending on the heat recovery factor which is itself linked with the air path inside the wall assembly. Sherman and Walker [133] have found that taking into account the heat transfer between the infiltrating air and walls can reduce by up to 95% the predicted infiltration energy load compared to a more traditional calculation considering only the product of the infiltration flow and the enthalpy difference between inside and outside.

Moreover, in case of humid air leakage, a good knowledge of the air path is required to evaluate properly the moisture risks. The impact is indeed different if the humid air is only flowing through a non-hygroscopic material such as the glass wool or in contact with hygroscopic materials such as a wood stud where water may more easily accumulate and lead to long-term damage.

In the next two chapters the focus is therefore on the experimental study of the air path inside the timber frame wall assemblies. A new approach using fluorescein tracer micro-particles is presented and tested in Chapter 5, and compared with four other techniques in Chapter 6.

# Chapter 5

## Experimental investigations of the air path through an airtightness defect using a tracer technique

This chapter focuses on a non-intrusive experimental study presenting an innovative use of tracer to track the air path inside simple timber frame wall assemblies. Such measurements are of interest to measure the air dispersion and for instance the implication on moisture risks, as well as for validation of detailed air flow models. Moreover, Gao and Zhang [134] underlined in a recent study that analytical methods are effective for calculating particle penetration through simple geometries such as tubes but the complex geometry of wall assemblies requires a numerical approach such as CFD to study the particle transport. They were the first to model the penetration of particles through fiberglass insulation as part of the assembly and the use of tracer particles could contribute to validate such models.

First the choice of the tracer and the insulation material is explained. The experimental protocol implemented is then presented as well as the results of preliminary tests carried out to validate the relevance of this method. In a second part a model is studied for the micro-particles collection by the fibers and validated by a comparison with experimental results. Finally a case study is carried out on air channels in contact with a porous medium. 2D mappings of the fluorescein concentration are analyzed to identify the air path and a comparison is made with numerical results of a CFD simulation coupled with the micro-particles collection model.

### 5.1. Methodology

#### 5.1.1. Tracer selection

Solid particles, liquid droplets of adapted gases may be used to track streamline within an air flow. A colored gas would be appropriate to an immediate visual diagnostic. However such gases ( $\text{Cl}_2$ ,  $\text{Br}_2$ ,  $\text{NO}_2$ ) are highly toxic so this possibility was dismissed here. Another option would be to use a gas reacting with the porous media on his way through it, but insulation materials are inherently chemically inert materials. There is a number of tracer gas commonly used with air such as  $\text{CO}_2$ ,  $\text{SF}_6$  or  $\text{N}_2\text{O}$  [135] but unlike the previously mentioned gases, they are not colored and don't color the porous



media on their way by chemical reaction. Their use requires therefore sensors to measure their concentration at different locations, which would make this technique intrusive.

Solid micro-particles are an alternative to using a tracer gas. Fluorescein is an organic molecule with one of the most intense fluorescence and high water solubility, which makes it easily detectable at very low concentration levels [136]. It also has the advantage of having rather low costs and low toxicity which makes it the best option for this study among other tracers as rhodamine or zinc sulfide. Fluorescein is most commonly used as a hydrological tracer to determine the flow pathways but it has other applications including being used as artificial aerosol to study the particle deposition in pipes [137], in ventilation ducts [138] or on building facades [139].

It is proposed here to use the fluorescein as a tracer particle to follow the air path through porous media being a part of a timber frame wall assembly. The particles are captured by the insulation fibers along the air pathway, and then the amount of fluorescein in a sample is measured by immersing it into water and measuring the absorbance of the solution. The presence of particles in a sample indicates an air flow and the relative concentration gives information on its significance. The particles diameter is a determining parameter in that case. There is an optimum size, usually in the range of 0.1 and 0.2  $\mu\text{m}$ , for which the filtration efficiency of the porous media will be the lowest [140]. Smaller particles are more easily captured because of the Brownian motion, and the effect of the other filtration mechanisms (sieving, gravitational sedimentation, interception and impaction) increases with the particle diameter. Since the objective is to track the air on a distance as long as possible, the particles should be in this range of low collection efficiency.

### **5.1.2. Fluorescein micro-particles generator**

The generator SETRA GP92 was used for to generate the tracer particles. As illustrated in Figure 5.1, a water solution of fluorescein with a concentration of 10 g/L is placed in a container. Pressurized air is introduced through a spread head creating little drops of liquid fluorescein suspended in the air. The fluorescein-laden air is then passing through two separation nozzles to keep only the smallest drops, and the flow is mixed with another pressurized air flow to dry the liquid drops. According to a previous study [141], the generator is producing fluorescein solid micro-particles (about 30 mg/h) with a theoretical mass median diameter of 0.18  $\mu\text{m}$  (50% of the particles by mass are larger and 50% are smaller).

### **5.1.3. Fluorescein concentration measurement**

The mass of fluorescein in a water solution corresponds to the amount of particles stopped by the piece of insulation immersed in it. As shown in Figure 5.2 the color of the fluorescein solution depends on its concentration ( $C_{\text{fluo}}$ ).

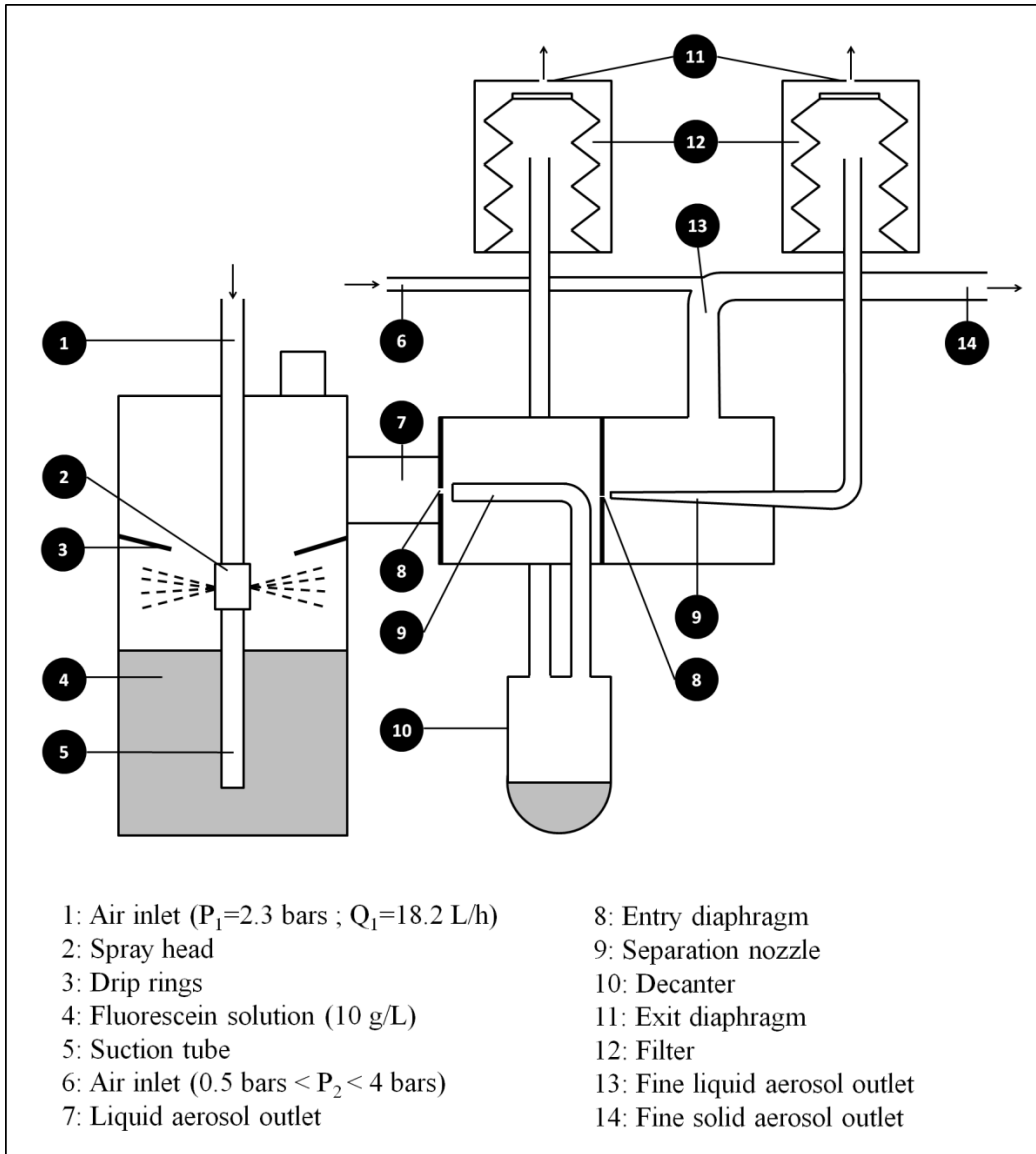


Figure 5.1 - Aerosol generator SETRA GP92 for the fluorescein micro-particles generation

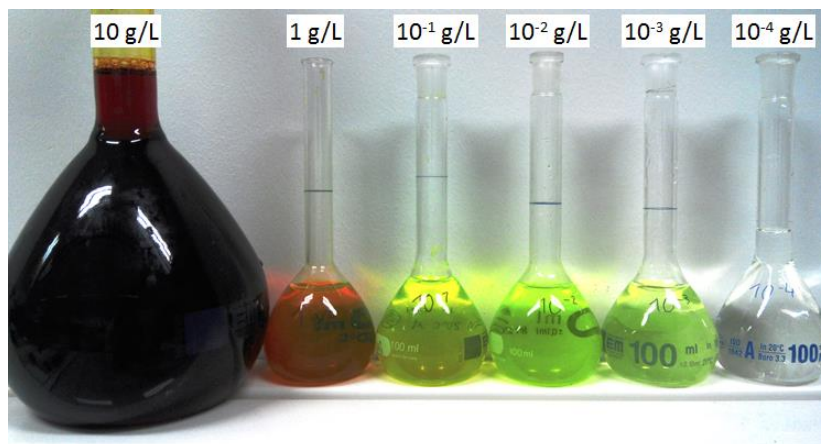


Figure 5.2 - Fluorescein solutions ranging from 10 g/L to  $10^{-4}$  g/L

## Absorbance measurement

The amount of fluorescein in a solution can be quantified by measuring either its fluorescence (emission) or absorbance. The fluorescence can be measured by a fluorometer. This instrument generates a wavelength of light to excite the electrons in the fluorescein molecules and measures the intensity of the nearly instantaneous re-emission at another wavelength.

Alternatively, the absorbance can be measured by spectroscopy. The intensity of a beam of light after passing through the solution ( $I$ ) is compared to a reference value with no fluorescein in the solution ( $I_0$ ). The absorbance ( $A$ ) is then calculated as follow:

$$A = \log\left(\frac{I_0}{I}\right) \quad (5.1)$$

It can be directly related to the attenuating species concentration according to the Beer-Lambert-Bouguer law, generally called the Beer-Lambert law:

$$A = \varepsilon c L \quad (5.2)$$

With  $\varepsilon$  the molar absorption coefficient (L/mol.m),  $c$  the molar concentration of the solution (mol/L) and  $L$  the path length traveled by light through the solution (m). This law tends to break down at very high concentrations.

Both methods are commonly used and considered accurate [142]. The fluorescence measurement presents the advantage of having a higher sensitivity leading to greater limits of detection, and a better specificity since only molecules that fluoresce are detected. The instrument is however more expensive and since an absorption visible spectrometer was available, absorbance measurements were performed in this study. As discussed in paragraph 5.1.5, the accuracy and repeatability were found to be satisfactory for this application.

For the fluorescein solutions, the maximum of the absorbance spectrum is usually measured for a wavelength in the vicinity of 489 nm ([142] and [143]) which was confirmed experimentally as shown in Figure 5.3.

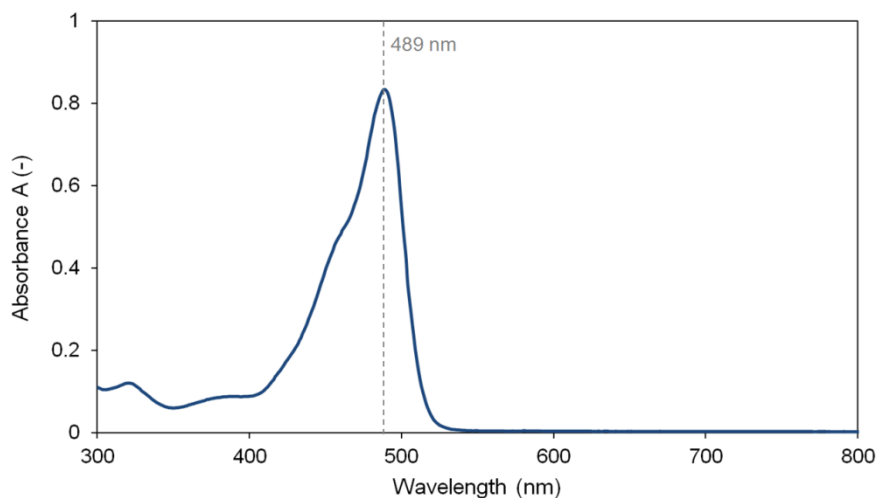


Figure 5.3 – Absorbance spectrum of the fluorescein solution at  $C_{\text{fluo}} = 10^{-2}$  g/L

## Calibration law

In order to determine the absorption coefficient an experimental calibration law has to be established. For this purpose, the absorbance of solutions with various fluorescein concentrations was measured. The results are presented in Table 5.1. They show that the minimum detectable level is  $1.10^{-4}$  g/L and the maximum reliable measurement is obtained for  $10^{-2}$  g/L, after which the solution is not transparent enough. A saturation point is indeed reached after  $10^{-2}$  g/L: the increase of concentration has then almost no impact on the absorbance measurement with values almost stable around 2. The volume of water  $V_{\text{water}}$  in which the sample is immersed should therefore be chosen to be in this range of concentration. It is accurately measured with a volumetric flask.

Table 5.1 – Absorbance measurements for fluorescein solutions at various concentrations

$C_{\text{fluo}}$ (g/L)	$1.10^{-1}$	$5.10^{-2}$	$2.5.10^{-2}$	$1.7.10^{-2}$	$1.10^{-2}$	$5.10^{-3}$	$2.10^{-3}$	$1.10^{-3}$	$1.10^{-4}$
Absorbance (A)	2.19	2.11	2.02	1.74	0.838	0.412	0.122	0.076	0.004

The calibration curve is plotted in Figure 5.4 in the range of concentration previously specified. Unlike stated by the Beer-Lambert law, the measured relation between the absorbance and the concentration is often not perfectly linear. This can be explained in particular by the instrumental deviation due to polychromatic radiations, the presence of stray radiation (from the instrument), and/or unequal optical characteristics between the cells of the analyte and the blank solutions. As a result, logarithmic values of A and  $C_{\text{fluo}}$  are used to take into account this non-linearity. The slope obtained is the exponent of the calibration law:

$$C_{\text{fluo}} = 1.077.10^{-2} \times A^{0.8537} \quad (5.3)$$

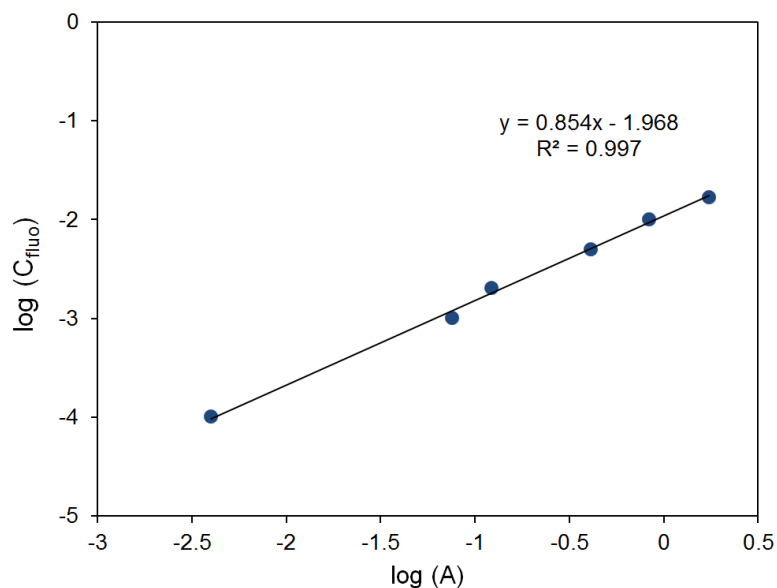


Figure 5.4 - Fluorometry calibration graph

#### 5.1.4. Insulation material

Practical application of fluorescein measurements imposes some limitations on the porous media. Certainly, one important criterion is to have an insulation material not interfering with this calibration law, e.g. neutral at wavelength of 489 nm. Some insulation materials tend indeed to colour the water when immersed, which modifies the absorbance of the fluorescein solution. As shown in Figure 5.5, it is particularly the case for wood fiber (absorbance equal to 0,195) which is therefore not suitable for this experiment. The glass wool (GW) chosen for this study is suitable because of its very light coloration (absorbance equal to 0,008) but rock wool is almost as good. An absorbance measurement for a 5cm x 5cm x 6cm GW sample immersed in 50mL of water gives an equivalent fluorescein concentration of  $1.10^{-4}$ g/L which is not significant.

There are many GW types available, the high-permeability one (HPGW) was selected to minimize the fluorescein collection efficiency.



Figure 5.5 – Water coloring and absorbance measurements after immersing insulation materials

#### 5.1.5. Experimental protocol

The outlet of the fluorescein generator is connected to the inlet of the test box so that the air seeded with fluorescein micro-particles goes through the tested wall (with a flow rate of up to  $10 \text{ Nm}^3/\text{h}$ ). The air flow rate should be adapted to the tested configuration and its minimum cross sectional area to avoid high air velocities. It has been found experimentally that above 3m/s the particles have difficulties to follow the air streamlines and are all captured by impaction in the first millimetres of the GW. As illustrated in Figure 5.6, the experimental protocol is as follows:

- (1) The tested 'wall' is exposed to the fluorescein particle-laden air for a few hours. The duration is chosen depending on the size of the air dispersion area to have significant fluorescein concentrations and therefore improve the accuracy. When various tests are compared with each other, a constant exposition time may be preferable for additional information on the relative global infiltrating air flow rate.
- (2) The insulation layer is cut into small samples (5 x 5 cm).
- (3) Each sample is immersed in a measured distilled water volume  $V_{\text{water}}$  and mixed until all the fluorescein is dissolved. The mixing consists in compressing several times the insulation in the water to evacuate the air and therefore force the contact between the fluorescein molecules and water. This action is more determining than the immersion time, and it was found by absorbance measurements that after 30s of mixing, no additional fluorescein is dissolving.

- (4) The colored solution is poured into a little plastic flask and is put in a centrifuge at 22000 rpm for 5 minutes so that GW fibers residues settle at the bottom.
- (5) The absorbance of the solution is measured with a spectrometer at 489 nm.
- (6) The fluorescein concentration ( $C_{fluo}$ ) is calculated for each sample (i) according to equation (5.3).
- (7) The mass percentage ( $MP_{fluo}$ ) of the total amount of fluorescein in the layer is calculated for each sample (i) with (5.4). The resulting 2D (or 3D for multi layers tests) mapping is a good indicator of the air dispersion inside the insulation.

$$(MP_{fluo})_i = \frac{(C_{fluo} \times V_{water})_i}{\sum_{i,layer} (C_{fluo} \times V_{water})_i} \times 100 \quad (5.4)$$

In order to check the repeatability, the absorbance of 10 samples from the same solution were measured and for one of samples the absorbance was also measured 10 times. The relative errors between the minimum and maximum values were respectively 4.2% and 0.8% which is not very significant. The tests are time consuming and have the inconvenient of being destructive, but the method is non-intrusive.

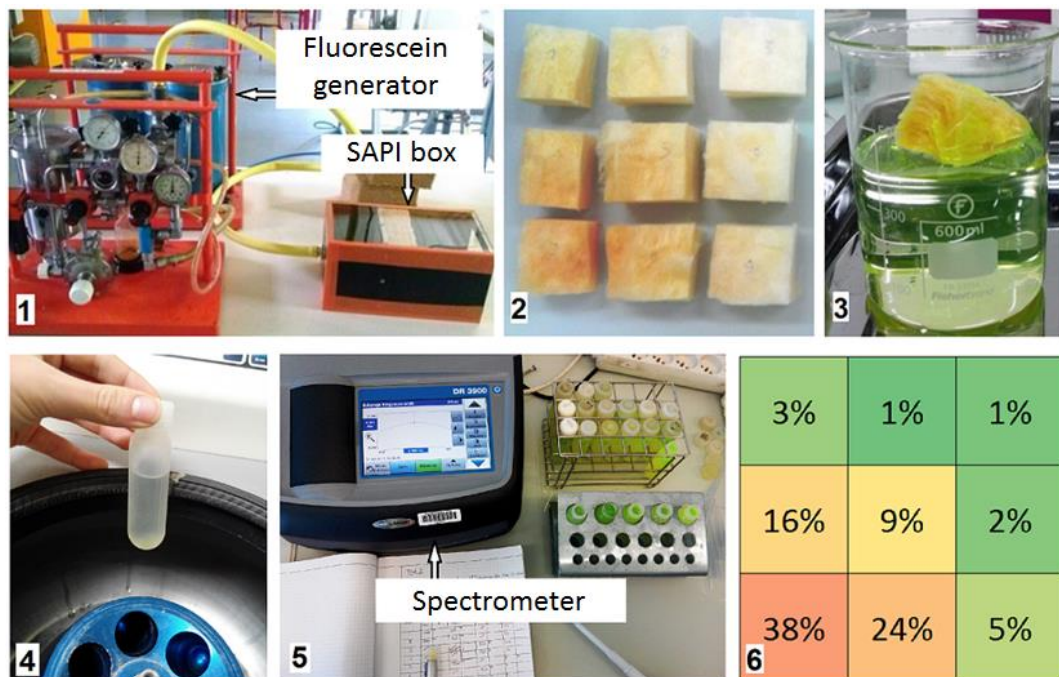


Figure 5.6 – Steps of the experimental protocol for the fluorescein tests

## 5.2. Preliminary tests

A number of preliminary tests have been carried out at a small scale on the SAPI box to validate the use of fluorescein micro-particles to track the air path in wall assemblies. The experimental set-up is presented in Figure 5.7 and the different tests and results in Figure 5.8. The exposition time to the

fluorescein-laden air was 3 hours and the flow rate was around  $2.5 \text{ m}^3/\text{h}$  ( $v_{\text{max}} = 2.2 \text{ m/s}$ ). Two types of components were used: an airtight layer (represented in black) with a 2 cm diameter hole located either in the centre or in a corner; and the HPGW (represented in grey) with an original thickness of 60 mm but compressed to 40 mm. A circle of glue around the hole holds the two components together and tape is used to seal the junctions with the SAPI box. The composition of each tested “wall assembly” is given streamwise, and the dimensions are 15 cm x 15 cm.

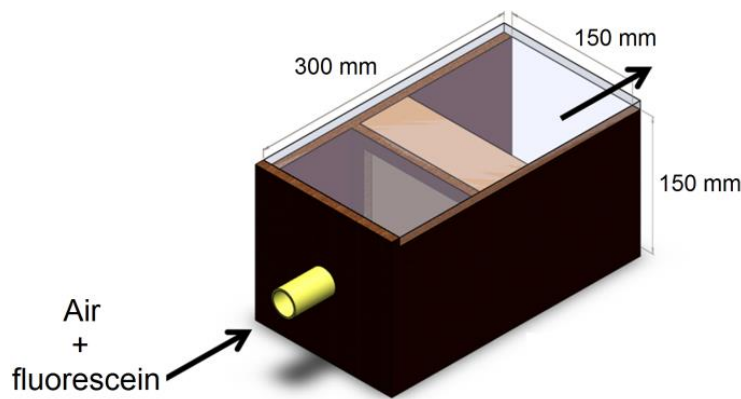


Figure 5.7 – Fluorescein tests on the SAPI box as a preliminary study

With the exception of test 2, for concentration analyses the first GW layer was cut at half of its thickness. One should note that the mapping given for the whole layer ( $A_{\text{tot}}$ ) is not an average of the  $A_1$  and  $A_2$  values, but is calculated using again equation (5.4), but, this time, applied to the whole layer. Since the concentration of fluorescein in the air decreases as the particles are captured along the air path, the mass measured in the first sub-layer  $A_1$  is greater than in  $A_2$  which explains why the MP is closer to the  $A_1$  value.

The tests 1 and 1' were carried out on the same configuration. The aim was to test the repeatability of the method. The results are very close for  $A_{\text{tot}}$  but some differences can be observed when one looks at the  $A_1$  and  $A_2$  results. It could be explained by a lack of precision in dividing the GW into two identical 3 cm thick sub-layers since the fibre plane is not exactly parallel to the GW surface plane. For these two tests as for the following one, the symmetry of the geometry is relatively well respected in the results. The disparities cannot be explained by the fluorescein measurements uncertainties, and are therefore due to the GW non-homogeneity and/or a not perfectly symmetrical placing of the tested wall assembly in the SAPI box.

Test 2 shows that the addition of a second insulation layer does not impact much the air dispersion in the first one. However, we can observe that the air continues its dispersion, with 29% of the fluorescein mass found in the middle compared with 34% for  $A_1$ . On the other hand, the restriction of the air outlet on the test 3 has a significant effect with more than half of the flow passing through the very centre.

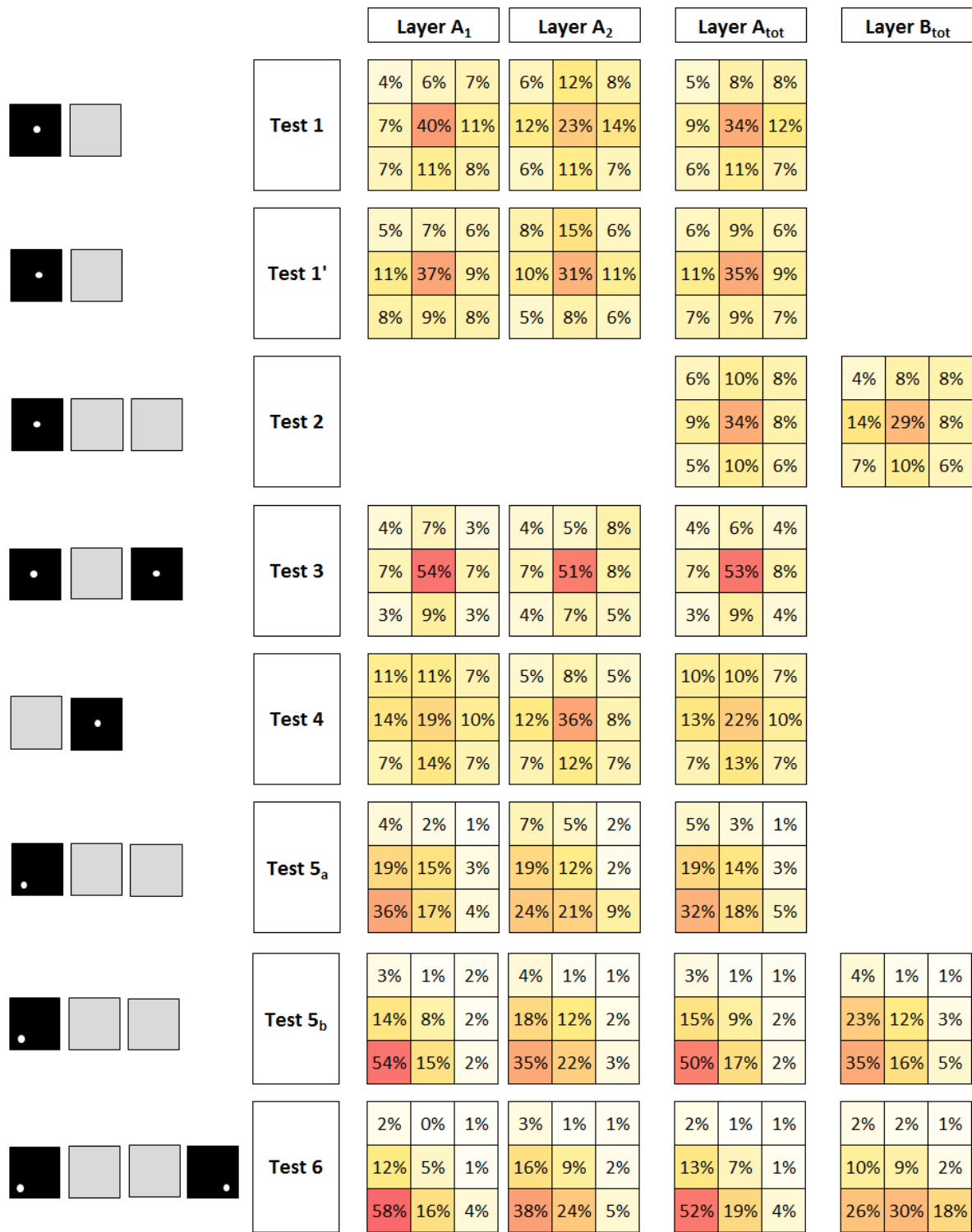


Figure 5.8 – Results of the preliminary tests with fluorescein as micro-particle tracer

Test 4 is the same configuration as test 1 but with the reverse order of the layers. This enables to point out the filtration effect on the results. In the same way as the values in A<sub>tot</sub> are not averages of A<sub>1</sub> and A<sub>2</sub>, the MP calculated for each sub-layer are not an average over the thickness, they are more



representative of the air dispersion in their upstream part. As a result, inverting the order gives indication on the flow behavior on the other side of the layer.

The difference between the tests 5<sub>a</sub> and 5<sub>b</sub> is that in 5<sub>a</sub> unlike every other test, there is no glue between the airtight layer and the GW. With the pressure, a local air gap is created between the two components and the air can disperse before entering the insulation layer. As a result, in A<sub>1</sub> 36% of the fluorescein is found in the sample facing the hole against 54% with the glue. One can note that for this configuration with an air inlet in a corner, the opposite corner receives no more than 1 or 2% of the total fluorescein, even on the second layer (B<sub>tot</sub>). This seems to indicate that for this thickness of GW, almost no air is passing 15 cm away from a local airtightness defect, but it can also be due to a total filtration of the particles before the air flow reaches the opposite corner.

The last test, with the air outlet on the other side than the inlet, enables to follow the air path along the bottom of the GW. As explained previously, the values in each layer are representative to the flow on their upstream side. That is the reason why the MP values in B<sub>tot</sub> are higher in the bottom center than near the air outlet.

These eight preliminary tests validate the relevance of using fluorescein particles to track the air path through the porous media. It has been shown that this method gives consistent results and enables to investigate the flow behavior inside the insulation, with however the limitation of the filtration effect. The two phenomena involved in the fluorescein particles transport are indeed the advection and the collection by the insulation fibers. The advection is directly correlated with the air flow velocity and is therefore of interest for the air path study. However the measured fluorescein concentrations on the insulation samples are also highly dependent on the collection efficiency and as mentioned before an absence of fluorescein can also be explained by a total filtration on the upstream air path. In order to facilitate the interpretation of the experimental results the filtration effect must therefore be further investigated.

### **5.3. Fluorescein micro-particles filtration model**

The filtration of solid aerosols by porous media is particularly of interest for public health reasons when the aerosol is a contaminant and for the recovery of valuable products ([144] and [145]). For these two fields of application, the main objective is to optimize the collection efficiency of the aerosols and a large number of models have been suggested to this end. In this study the objective sought is the opposite one: the fluorescein micro-particles should penetrate as far as possible in the glass wool to track long air path lengths. The same models are however applied, as presented in the next paragraphs.

#### **5.3.1. Theoretical study of the collection efficiency**

##### **Collection efficiency of a single fiber**

The collection efficiency of a single fiber is defined as:

$$\eta = \frac{\text{amount of particles collected by the fiber}}{\text{amount of particles approaching the fiber}} \quad (5.5)$$

For solid or liquid aerosols with a diameter under 1  $\mu\text{m}$ , it is possible to consider that every particle touching a fiber is collected, without substantial re-entrainment [121]. This global coefficient is

obtained by adding the collection efficiencies of several physical mechanisms listed below and illustrated in Figure 5.9:

- Interception: when a particle has its center of gravity following the air streamline coming closer to a fiber than its radius, it touches the fiber and gets captured by it.
- Impaction: it is due to the inertia of the particle that prevents it from following the abrupt change of the streamline direction near a fiber. This effect increases with the mass, the size and the velocity of the particles.
- Diffusion: micro-particles are subject to the Brownian motion: when the average particle trajectory comes close enough to a fiber it happens that this motion makes the particle touch and be collected by the fiber.
- Sieving: this is the simplest mechanism in filtration. Particles larger than the space between the fibers are blocked. However given the high porosity of the HPGW and the small size of the fluorescein micro-particles, it is not taken into account for this study.
- Gravitational sedimentation: at low velocities the trajectory of large particles can be deviated from the streamline because of the gravity. However given the very small mass of the particles, this mechanism is also not taken into consideration for this study.

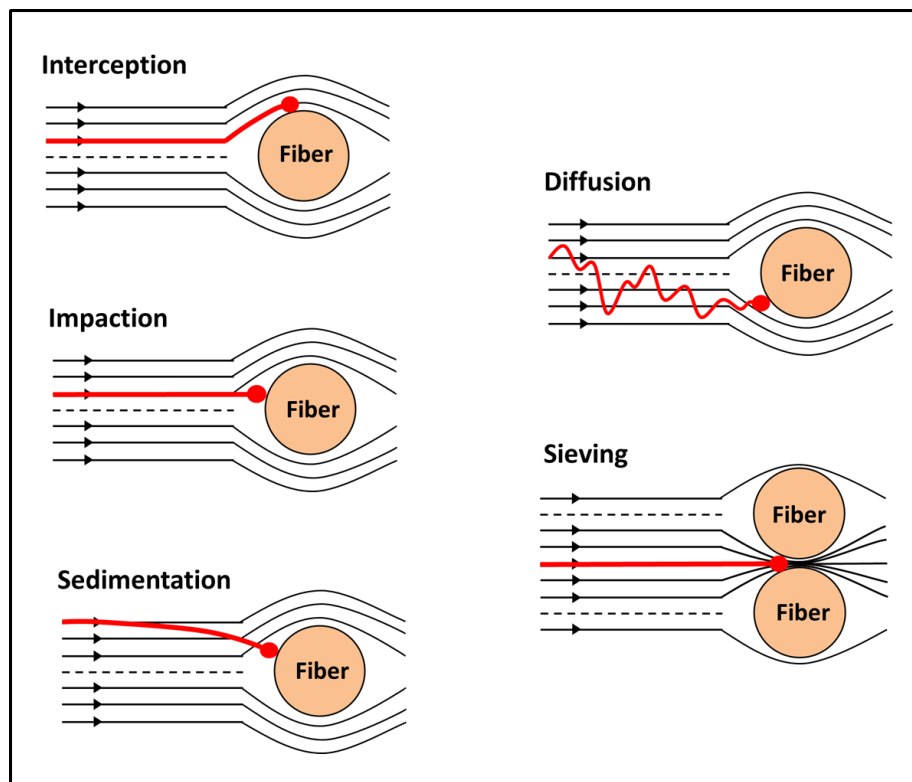


Figure 5.9 – Mechanisms of particles collection by a fiber

Many methods have been proposed for estimating the component collection efficiencies [146]. The Miecret and Gustavsson model [147] is commonly used for fibrous filters [121] and was therefore chosen for this study. The collection efficiency of a fiber is expressed as the sum of the efficiencies due to each collection mechanism ( $\eta_j$ ), with an additional term ( $\eta_{dr}$ ) to account for the interaction between the diffusion and the interception:

$$\eta = \Sigma\eta_j + \eta_{dr} \quad (5.6)$$

The collection efficiencies due to the interception ( $\eta_i$ ), the diffusion ( $\eta_d$ ) and the impaction ( $\eta_r$ ) combined for this model are defined below.

- For the interception, the Cai model [147] is used:

$$\eta_i = 2.4 (1 - \varphi)^{1/3} R^{1.75} \quad (5.7)$$

With  $\varphi$  the porosity and R defined as the ration between the particles diameter ( $d_p$ ) and the fiber diameter ( $d_f$ ):

$$R = \frac{d_p}{d_f} \quad (5.8)$$

- The Davies model [148] is used to express the collection efficiency due the diffusion mechanism:

$$\eta_d = 1.5 Pe^{-\frac{2}{3}} \quad (5.9)$$

With Pe the dimensionless Peclet number comparing the particle transport by advection and diffusion:

$$Pe = \frac{d_f v}{D} \quad (5.10)$$

With v the flow velocity (m/s) and D the particle diffusion coefficient (m<sup>2</sup>/s).

- The collection efficiency due to the impaction is described by the Suneja and Lee model [120]:

$$\eta_r = \frac{1}{\left(1 + \frac{1.53 - 0.23 \ln(Re_f) + 0.0167(\ln Re_f)^2}{Stk}\right)^2} \quad (5.11)$$

With  $Re_f$  the dimensionless Reynolds number calculated with  $d_f$  as the characteristic dimension,

$$Re_f = \frac{d_f \cdot v \cdot \rho_f}{\nu} \quad (5.12)$$

And Stk the dimensionless Stokes number defined as:

$$Stk = \frac{\rho_p d_p^2 C_c v}{9\mu \cdot d_f} \quad (5.13)$$

With  $C_c$  the Cunningham correction factor taking into account the discontinuities when the particles diameter is close to the mean free path  $\lambda$  [149]:

$$C_c = 1 + \frac{2\lambda}{d_p} \left( 1.246 + 0.42 \cdot \exp\left(-0.435 \frac{d_p}{\lambda}\right) \right) \quad (5.14)$$

- Finally, the interaction between the diffusion and the interception mechanisms is given by Stechkina and Kirsch [150]:

$$\eta_{dr} = 1.24Ku^{-0.5} \cdot R^{2/3} \cdot Pe^{-0.5} \quad (5.15)$$

With  $Ku$  the dimensionless Kuwabara hydrodynamic factor [151]:

$$Ku = (1 - \varphi) - \frac{1}{2} \ln(1 - \varphi) - \frac{1}{4} (1 - \varphi)^2 - \frac{3}{4} \quad (5.16)$$

### Collection efficiency of a fibrous filter

The total collection efficiency  $CE$  of a fibrous filter is defined as follow:

$$CE = \frac{\text{particle concentration on the filter upstream side}}{\text{particle concentration on the filter downstream side}} \quad (5.17)$$

It varies between 1 (no filtering effect) and  $+\infty$  (perfect filtration). In order to express its value as a function of the  $\eta$ , a filter with a thickness  $dz$  and a surface  $\Omega$  is considered. The volume of the fibers  $V_f$  is given by:

$$V_f = (1 - \varphi)\Omega dz \quad (5.18)$$

This volume of fiber is linked with the total length of the fibers  $L_{f,t}$  in this volume:

$$V_f = \frac{\pi d_f^2}{4} L_{f,t} \quad (5.19)$$

From equations (5.18) and (5.19)  $L_{f,t}$  can be expressed as:

$$L_{f,t} = \frac{4(1 - \varphi)\Omega}{\pi d_f^2} dz \quad (5.20)$$

By considering that the fibers are perpendicular to the flow, the total projected area of the fibers  $A_{f,t}$  is given by:

$$A_{f,t} = d_f L_{f,t} = \frac{4(1 - \varphi)\Omega}{\pi d_f} dz \quad (5.21)$$

The definition of the collection efficiency of a single fiber  $\eta$  given in equation (5.5) leads to the following equation expressing the number of collected particles  $N_p$  in this filter of a thickness  $dz$ :

$$\frac{dN_p}{dt} = \eta \frac{v C_p A_{f,t}}{\varphi} \quad (5.22)$$

With  $C_p$  the concentration of particles. By developing using equation (5.21):

$$\frac{dN_p}{dt} = 4 \eta \frac{(1 - \varphi)}{\varphi} \frac{v \Omega}{\pi d_f} C_p dz \quad (5.23)$$

Moreover, the material balance applied in the volume considered leads to the following equation:

$$\frac{dN_p}{dt} = -v \Omega dC_p \quad (5.24)$$

By combining equations (5.23) and (5.24) a first order differential equation is obtained:

$$\frac{dC_p}{dz} + \left( 4 \eta \frac{(1 - \varphi)}{\varphi \pi d_f} \right) C_p = 0 \quad (5.25)$$

As a result:

$$C_p(z) = C_0 \exp\left(-4 \eta \frac{(1 - \varphi)}{\varphi \pi d_f} z\right) \quad (5.26)$$

By combining equations (5.17) and (5.26) the total collection efficiency of a filter with a thickness  $t_{filter}$  can be expressed as [121]:

$$CE = \exp\left(-4 \eta \frac{(1 - \varphi) t_{filter}}{\varphi \pi d_f}\right) \quad (5.27)$$

With  $\eta$  the sum of the collection efficiencies due to each mechanism given in equations (5.7), (5.9), (5.11) and (5.15).

### Model parameters

When fluorescein-laden air is infiltrating the wall assembly, the glass wool performs as a fibrous filter and its collection efficiency can be estimated with the equation (5.27). Several parameters are needed to use this model they are listed together with the inputs in Table 5.2. The compression of the HPGW is taken into account with the porosity parameter as discussed later. The impact of the key parameters will be discussed in the following paragraphs.

The resulting collection efficiency for a 10 cm thick HPGW is plotted against the flow velocity ranging from 0.01 m/s to 1 m/s in Figure 5.10. As expected the main mechanism of collection is the diffusion for air velocities below 1 m/s, and impaction for greater velocities. The collection efficiency due to the interception does not depend on the velocity and is equal to 1.3 which is not significant. The effect of the interaction between the diffusion and the interception remains also very low (under 4.6 for this velocity range), but is significant at small velocities.

Table 5.2 –Parameters and inputs of the filtration model

	Unit	Value	Source	Parametric study
<b>Parameters</b>				
Particle diameter ( $d_p$ )	$\mu\text{m}$	0.18	[141], [152]	[0.05 ; 1.5]
Fiber diameter ( $d_f$ )	$\mu\text{m}$	5.7	exp.	[2 ; 20]
HPGW porosity ( $\varphi$ )	-	0.99	exp.	[0.900 ; 0.999]
Mean free path - air ( $\lambda$ )	m	$6.59 \cdot 10^{-8}$	theory	-
Dynamic viscosity - air ( $\mu_a$ )	Pa.s	$1.82 \cdot 10^{-5}$	theory	-
Particles density ( $\rho_p$ )	$\text{kg/m}^3$	1602	manufacturer data	-
<b>Inputs</b>				
Filter thickness ( $t_{\text{filter}}$ )	m	-	-	-
Air flow velocity ( $v$ )	m/s	-	-	[0.01 ; 10]

One can note that the global collection efficiency is the lowest (<16) between 0.1 m/s and 1.5 m/s and reaches its minimum at 0.6 m/s with a collection efficiency of 3.6 for this 10 cm thick HPGW. It is therefore the ideal velocity range to track the air path on a longer distance. Moreover these results confirm the experimental observation that the collection efficiency was too high for the fluorescein particles to penetrate the HPGW above 3 m/s. This model estimates indeed that the concentration would be almost 3000 times lower after 10 cm of HPGW at this critical velocity against 53 times for a velocity of 2 m/s and  $4 \cdot 10^5$  times at 4 m/s.

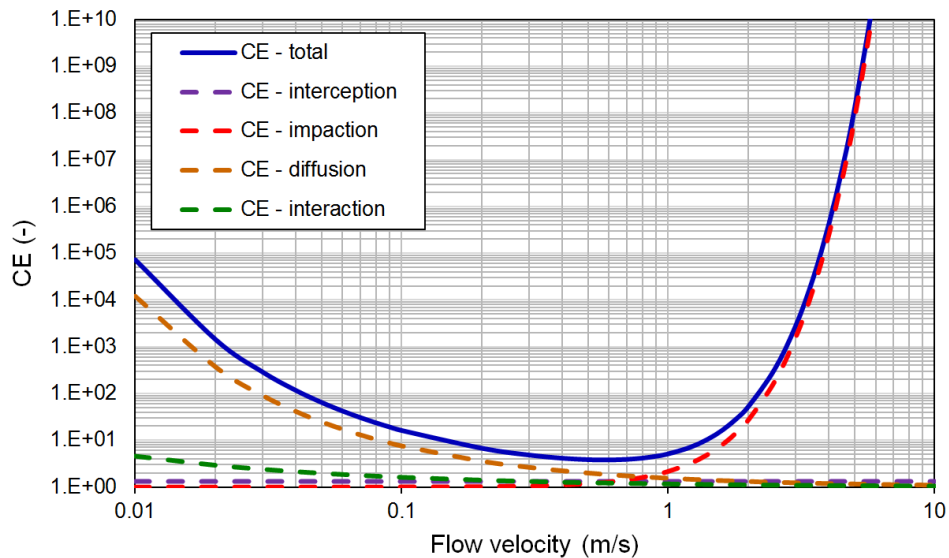


Figure 5.10 – Collection efficiency of a 10 cm thick HPGW calculated with the Miecret and Gustavsson model

As mentioned in paragraph 5.1.2, previous studies with the same fluorescein generator have found an average particle diameter of  $0.18 \mu\text{m}$ . This is however only an average and there are both smaller and bigger particles in the flow. This was confirmed by using a scanning electron microscope (SEM) to visualize the fluorescein particles collected on the glass wool fibers. As shown in Figure 5.11, there

are indeed many particles with a diameter in the vicinity of 0.18  $\mu\text{m}$  but there are also some with a diameter close to 1  $\mu\text{m}$ .

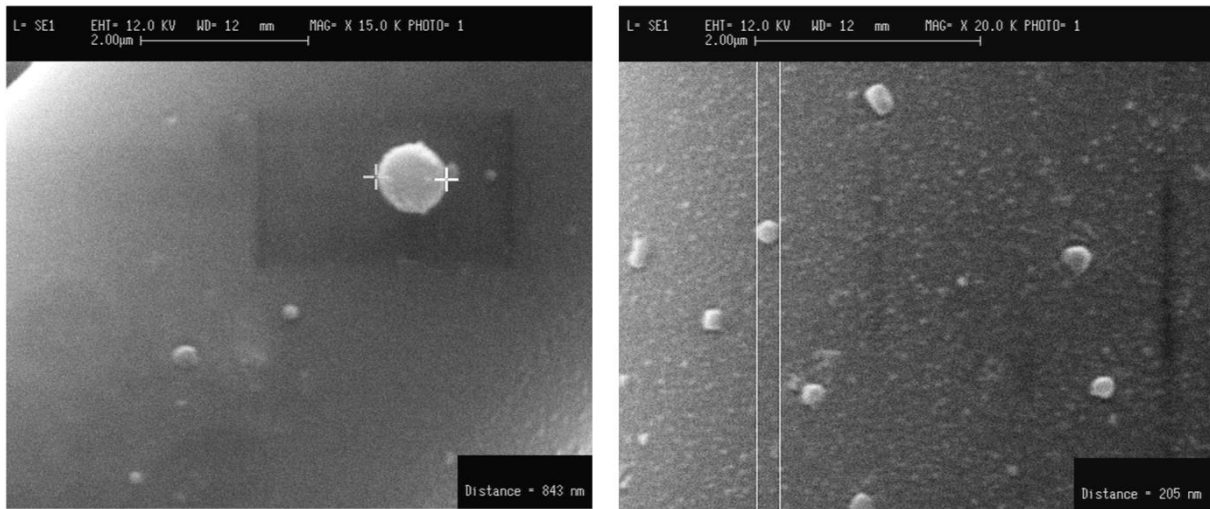


Figure 5.11 – Fluorescein particles collected on glass wool fibers (SEM)

Similarly, the fiber diameter  $d_f$  is not a constant over a glass wool volume, as shown on the SEM picture in Figure 5.12.a. In order to estimate the most representative value, the optical microscope was used to measure 119 fiber diameters, as shown in Figure 5.12.b. The results are presented in Figure 5.13. The software Origin was used to get the Gaussian curve fitting best the measurements:

$$y = 1,567 + \frac{88.53}{4.561\sqrt{\frac{\pi}{2}}}\exp\left(-2\left(\frac{d_f - 5.756}{4.561}\right)^2\right) \quad (5.28)$$

This curve has a maximum for  $d_f = 5.7 \mu\text{m}$  which is therefore used as an input in the model.

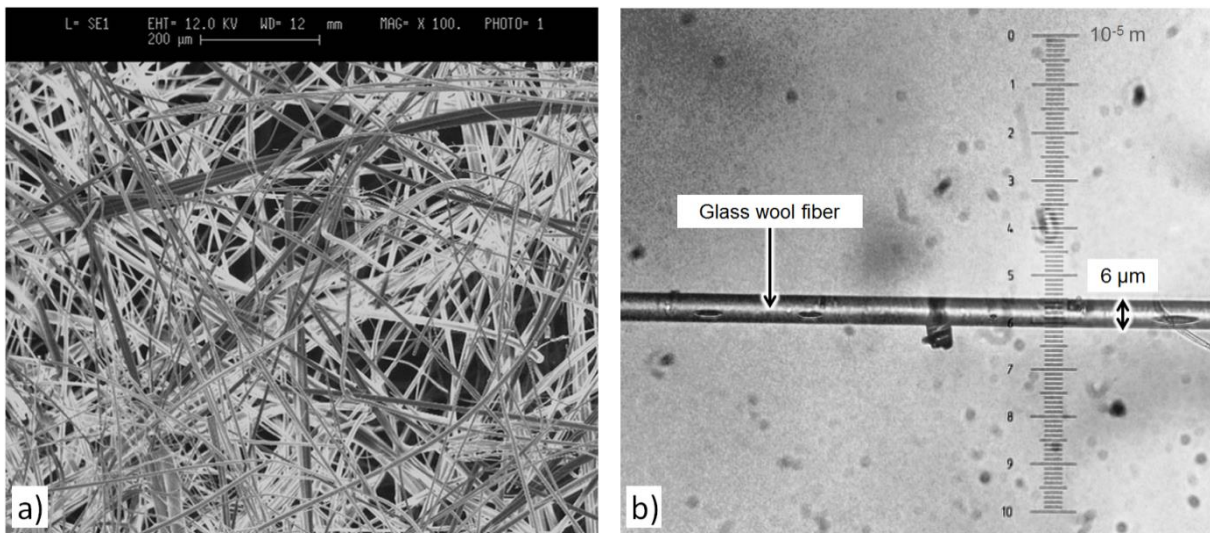


Figure 5.12 – Glass wool fibers visualized with a SEM (a) and an optical microscope (b)

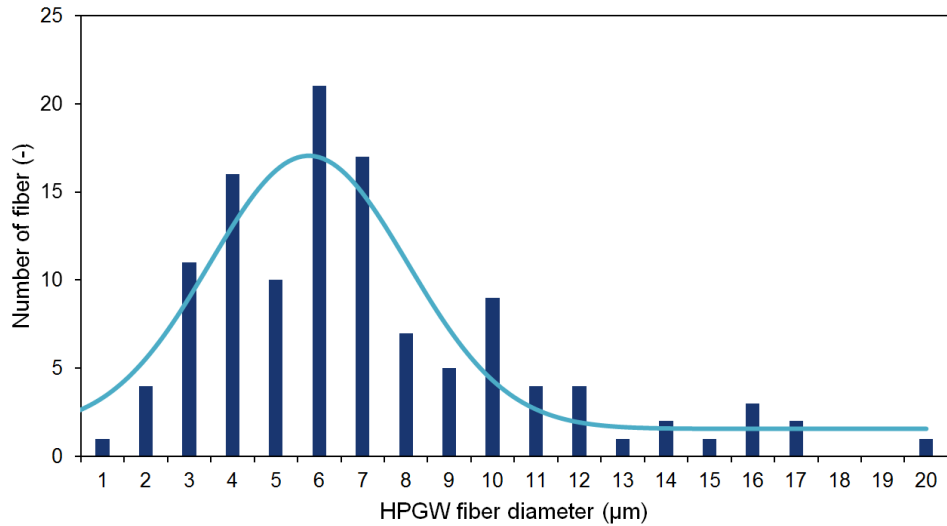


Figure 5.13 – Measurement of 119 HPGW fibers diameter with the optical microscope

The other uncertainty is on the HPGW porosity. As mentioned in paragraph 4.2.1, it has been estimated at 0.994 without compression, which corresponds to a value of 0.990 when compressed from 60 mm to 40 mm (67%).

A sensitivity analysis is carried out on these three input parameters. The collection efficiency of a 10 cm thick HPGW layer is plot against the flow velocity from 0.01 m/s to 10 m/s, with the other input parameters set as presented in Table 5.2. The impact of the fibers diameter ( $d_f$ ), the particles diameter ( $d_p$ ) and the porosity ( $\varphi$ ) are illustrated respectively in Figure 5.14, Figure 5.15 and Figure 5.16.

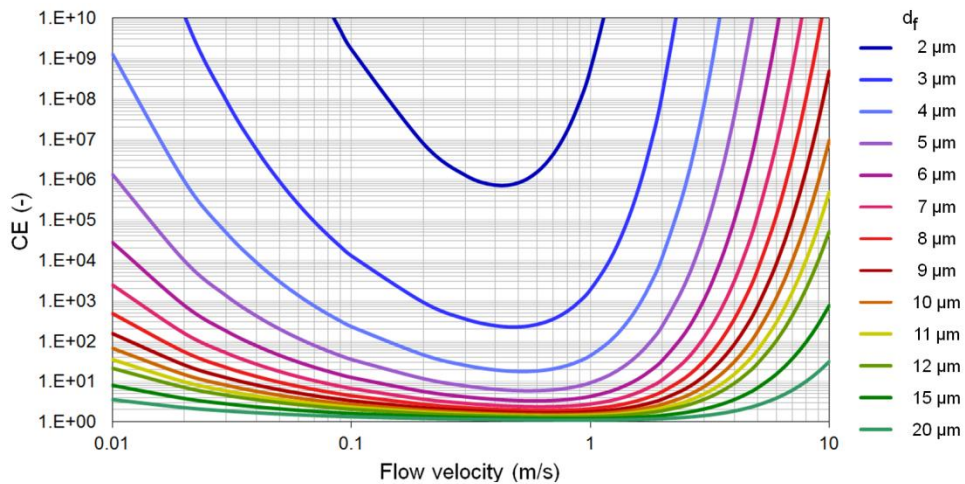


Figure 5.14 – Impact of the fibers diameter ( $d_f$ ) on the filter collection efficiency (CE)



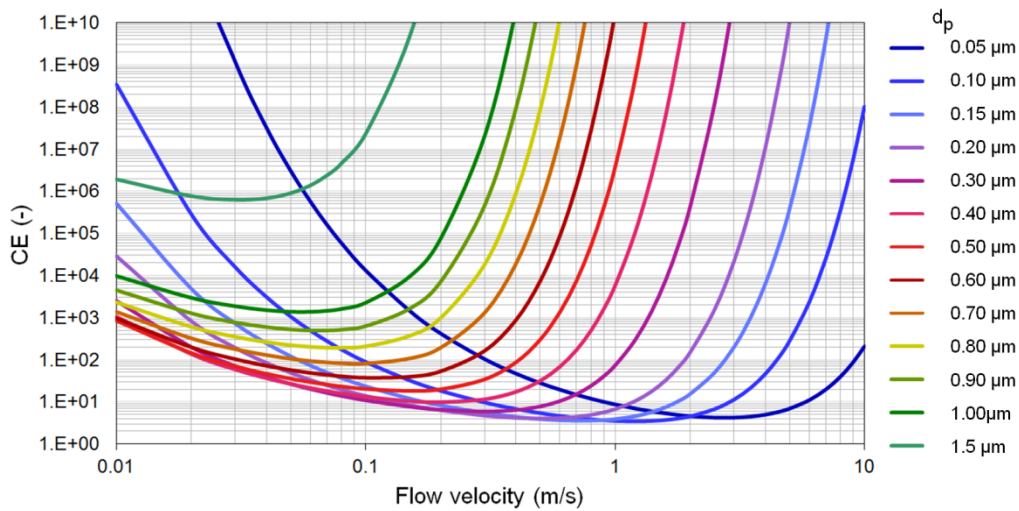


Figure 5.15 – Impact of the particles diameter ( $d_p$ ) on the filter collection efficiency (CE)

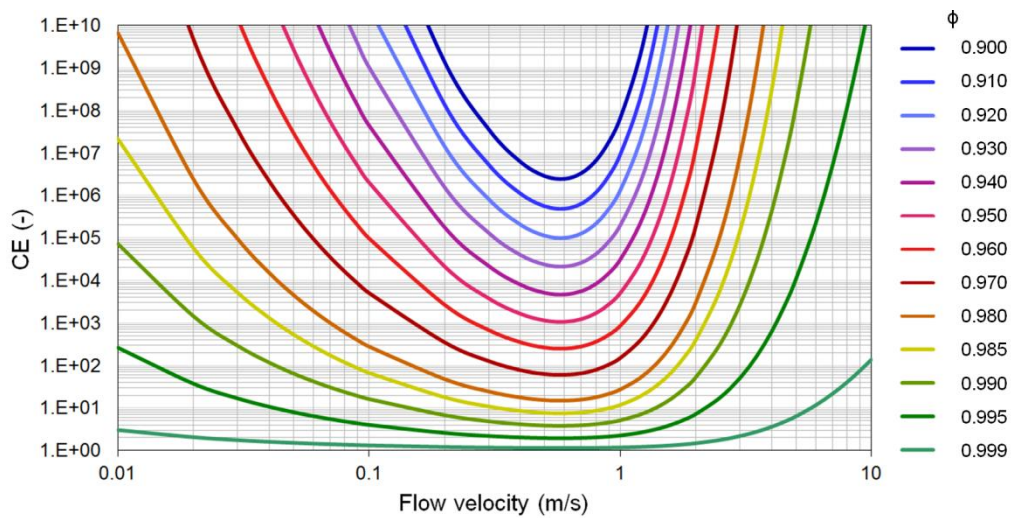


Figure 5.16 – Impact of the HPGW porosity ( $\phi$ ) on the filter collection efficiency (CE)

For a given porosity, the larger the fibers, the lower the collection efficiency. It means indeed that there are bigger gaps between the fibers where the particles-laden flow is not disrupted. The impact of the particles diameter is a bit more complex. At low velocities there is an optimum particle size ( $\sim 40 \mu\text{m}$ ) for which the collection efficiency is the lowest. Smallest particles have indeed higher chances to be collected by diffusion, and bigger ones by interception. However, as mentioned before, the diffusion is no longer significant at higher velocities. As a result above 1 m/s, the smaller the particles, the lower the collection efficiency.

Finally as expected the decrease of porosity is increasing the global collection efficiency since there are more obstacles for the fluorescein-laden air flow. From this theoretical model it seems that only very porous insulation materials can be analyzed with this fluorescein technique, since a porosity of 0.95 gives a minimum collection efficiency of about 1000 for this glass wool thickness. However one should not forget that lower porosity can also come with larger fibers, as it is the case for the LPGW, and for the same porosity of 0.95 the collection efficiency goes down to 14 for  $d_f = 10 \mu\text{m}$  instead of  $5.7 \mu\text{m}$ .

To conclude the model is rather sensitive to these three parameters, so they have to be evaluated with the best possible accuracy. Yet, as mentioned before, both the particles and fibers diameters do not have a constant value but follow a distribution which is a possible cause of inaccuracy. This is also the case for the porosity, but to a lesser extent since the experimental measurements on 15 samples show an uncertainty of only +/- 0.2%.

### 5.3.2. Coupled air flow-filtration model

In order to represent more precisely the experiments using fluorescein as an airflow tracer, the presented Miecret and Gustavsson filtration model is implemented on the software COMSOL Multiphysics® and coupled with a CFD module for porous media flows. This software was chosen because it allows both using conventional physics-based user interface and entering differential equations for coupled phenomena or multiphysics. The fluorescein concentration  $C_{fluo}$  (kg/m<sup>3</sup>) is calculated with an advection-diffusion equation where the last term accounts for irreversible particle deposition [153]:

$$\frac{dC_{fluo}}{dt} = D\nabla^2 C_{fluo} - \vec{v}\nabla C_{fluo} - k_d C_{fluo} \quad (5.29)$$

With  $k_d$  the deposition factor (s<sup>-1</sup>).

The Stokes-Einstein equation [154] was used to estimate the particle diffusion coefficient:

$$D = \frac{k_B T}{3\pi\mu_a d_p} = 1.31 \times 10^{-10} \text{ m}^2/\text{s} \quad (5.30)$$

With  $k_B$  the Boltzmann constant (1.38 x 10<sup>-23</sup> J/K) and T the temperature (K) taken at 293 K. This very low value of D implies that diffusion term is hardly significant compared to the advection one. However for numerical stability purposes, it is necessary to keep it in the equation. It is indeed well known that pure advection model present serious numerical difficulties due to shock discontinuities [155]. As observed in paragraph 5.4.3, this does however not fully solve the problem since advection-dominated models are still subject to moving steep fronts.

#### Determination of the deposition factor $k_d$

The collection efficiency given by the Miecret and Gustavsson model depends on the filter thickness unlike the deposition factor  $k_d$ . In order to establish a relation between these two parameters, the unit collection efficiency  $CE_1$  corresponding to a 1 m thick porous medium is introduced:

$$CE_1 = \frac{C_{fluo,0}}{C_{fluo,1}} \quad (5.31)$$

With  $C_{fluo,i}$  the fluorescein concentration in the porous medium at x=i (m), with  $\vec{x}$  the direction of the flow. The fluorescein concentration can then be expressed as:

$$C_{fluo,x} = C_{fluo,0} e^{-\ln(CE_1)x} \quad (5.32)$$

In this study the diffusion term is very small compared to the advection one. By neglecting it, the equation (5.29) is written for the steady-state as:

$$-\vec{v} \nabla C_{flu0} - k_d C_{flu0} = 0 \quad (5.33)$$

By solving this equation for one-dimensional flow we get:

$$-\frac{\vec{v}}{k_d} \int_{C_{flu0,0}}^{C_{flu0,x}} \frac{dC_{flu0}}{C_{flu0}} = \int_0^x dx \quad (5.34)$$

$$-\frac{\vec{v}}{k_d} \ln \left( \frac{C_{flu0,z}}{C_{flu0,0}} \right) = x \quad (5.35)$$

$$C_{flu0,z} = C_{flu0,0} e^{-\frac{k_d}{\vec{v}} x} \quad (5.36)$$

Then, by comparing equation (5.32) and (5.36), we can deduce the following relation:

$$k_d = \ln(CE_1) \vec{v} \quad (5.37)$$

### Model implementation

As mentioned before, the model was implemented in COMSOL Multiphysics simulation environment. The filtration model was specified as a partial differential equation (PDE) and coupled with already existing equation describing airflow. The general form of the equation is as follow:

$$e_a \frac{\partial^2 C}{\partial t^2} + d_a \frac{\partial C}{\partial t} + \nabla \cdot (-c \nabla C - \alpha C + \gamma) + \beta \cdot \nabla C + a C = f \quad (5.38)$$

By identification we have for the filtration model:

$$\left\{ \begin{array}{l} e_a = \alpha = \gamma = f = 0 \\ d_a = 1 \\ c = D \\ \beta = \vec{v} \\ a = k_d \end{array} \right.$$

This PDE is coupled with the air flow equations through the flow velocity  $\vec{v}$ . As further detailed in paragraph 5.4.3, an initial fluorescein concentration  $C_0$  is defined at the inlet (1<sup>st</sup> order boundary condition) and a zero gradient is set at the outlet and along the wall (2<sup>nd</sup> order boundary condition).

### 5.3.3. Experimental collection efficiency of the HPGW

In order to verify the theoretical collection efficiency obtained with the Miecret and Gustavsson model, simple experimental tests have been carried out at various flow velocities.

#### Experimental set-up

An additional experimental setup CETT (Collection Efficiency Test Tube) was built to determine the filtration properties of the HPGW depending on the fluorescein-laden air velocity. As illustrated in Figure 5.17 it has the shape of a tube with a 150 mm long PVC part to let the air flow disperse

followed by five removable little cylinders. Each of them is a location for a 70 mm in diameter and 40 mm thick GW layer. In order to prevent the GW to move with the pressure of the flow, there are 3 mm thick separators between two successive layers with a reduced interior section of 60 mm.

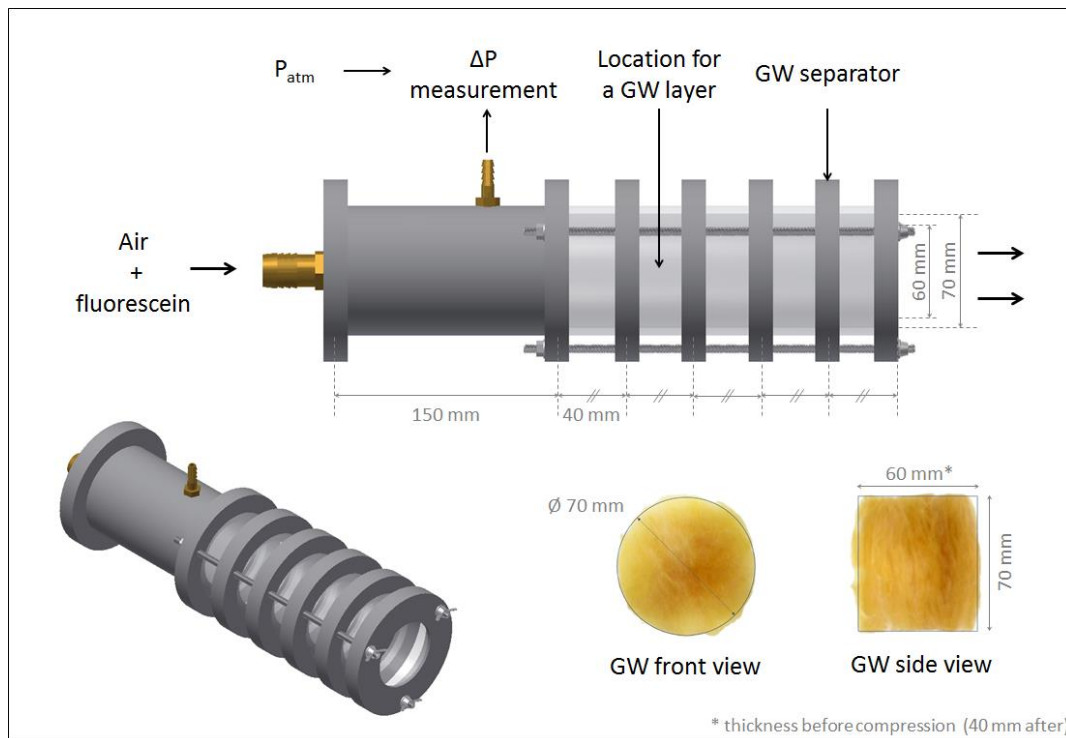


Figure 5.17 – Collection efficiency test tube (CETT) and HPGW cutting

The small dimensions of the separators prevent from disrupting too much the air flow, but they limit the relative pressure to 7000 Pa, after which the glass wool is pushed away from the CETT. Moreover, the separators and the small cylinders dimensions impose a GW thickness of 40 mm. The 60 mm thick HPGW is therefore compressed during the test, which minimizes the likelihood of air gaps appearance between the GW layers.

### Description of the tests

The aim of these tests is to determine the collection efficiency of the HPGW as a function of the air flow velocity. As a result seven tests are carried out with each time a different air flow rate. The relative pressure ( $\Delta P$ ), the air flow rate ( $Q$ ) and the air flow velocity ( $v$ ) are given for each test in Figure 5.18.a.

The velocity range covered by the first 6 tests is from 0.2 m/s to 0.7 m/s and corresponds to experimental limitations due to the compressed air supply. However, it has been possible to carry out a seventh test at the maximum pressure of 7000 Pa to get a higher velocity point at 1.5 m/s. It was done by conveying compressed air from another laboratory, and mixing it with the fluorescein-laden air before the CETT inlet. This implied however a complex and cumbersome set-up, which explains why there is only one measuring point above 0.7 m/s.

It is necessary to have a precise measurement of the air flow rate but it is not possible to insert a flow meter before the CETT entrance since the fluorescein particles could damage it. A pressurization

test was therefore carried out each time before starting the fluorescein generation. The velocity during the actual test could then be simply deduced from the relative pressure measurement.

The comparison of all the pressurization tests is presented in Figure 5.18.b. Apart from the test 3 which seems to have slightly higher flow rates for a given  $\Delta P$ , all the pressurization laws are very similar. This means that the glass wool layers were assembled the same way each time. Moreover the flow exponent equals to 1 which characterizes a laminar flow and confirm that there was no obvious air gap between the GW and the CETT walls.

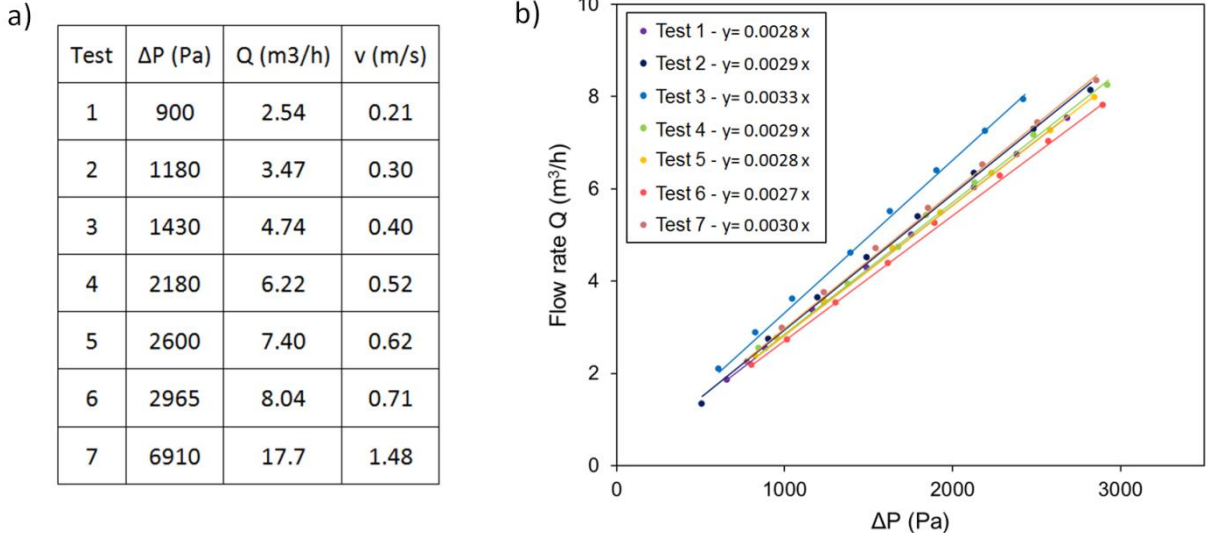


Figure 5.18 – Collection efficiency tests description (a) and corresponding pressurization tests (b)

For each test, the CETT is connected to the outlet of the fluorescein generator similarly to the preliminary test on the SAPI box described in paragraph 5.2. After a generation time of 4 hours, each GW layer is cut at half of its thickness as illustrated in Figure 5.19. There are therefore a total of 10 GW samples each time, which are analyzed as described in paragraph 5.1.5 to measure the mass of fluorescein collected in them.

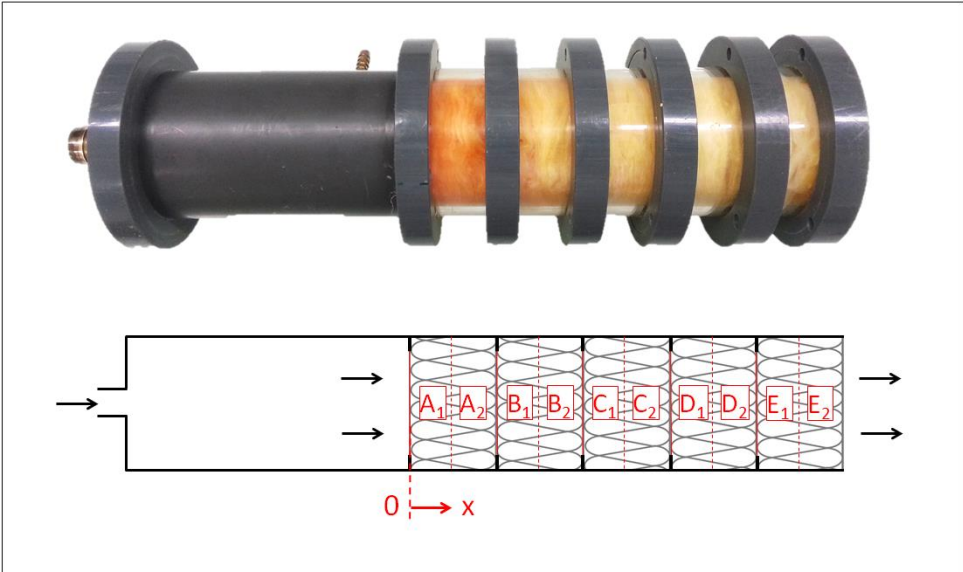


Figure 5.19 – Example of the GW coloration at the end of a test and GW cutting for the analysis

## Results

The result for the test 1 with a flow velocity of 0.2 m/s is presented in Figure 5.20.a. The mass of fluorescein of each sample is plotted against the distance  $x$  between the air inlet in the GW and the middle of the sample. The fluorescein concentration is directly proportional to the mass of fluorescein since each sample has the same volume. As a result the exponential trend line enables to directly get the coefficient  $\ln(CE_1)$  by comparison with the equation (5.32). These coefficients obtained for the seven tests are presented in Figure 5.20.b and compared with the model for various particle diameters in Figure 5.21. The experimental and numerical results for  $d_p = 0.18 \mu\text{m}$  are in rather good agreement and show a fairly stable minimum of collection efficiency in this range of velocity. The average relative error is 19% but this is not very significant in comparison with the rapid changes of  $\ln(CE_1)$  with the velocity (+148% between 1 m/s and 2 m/s).

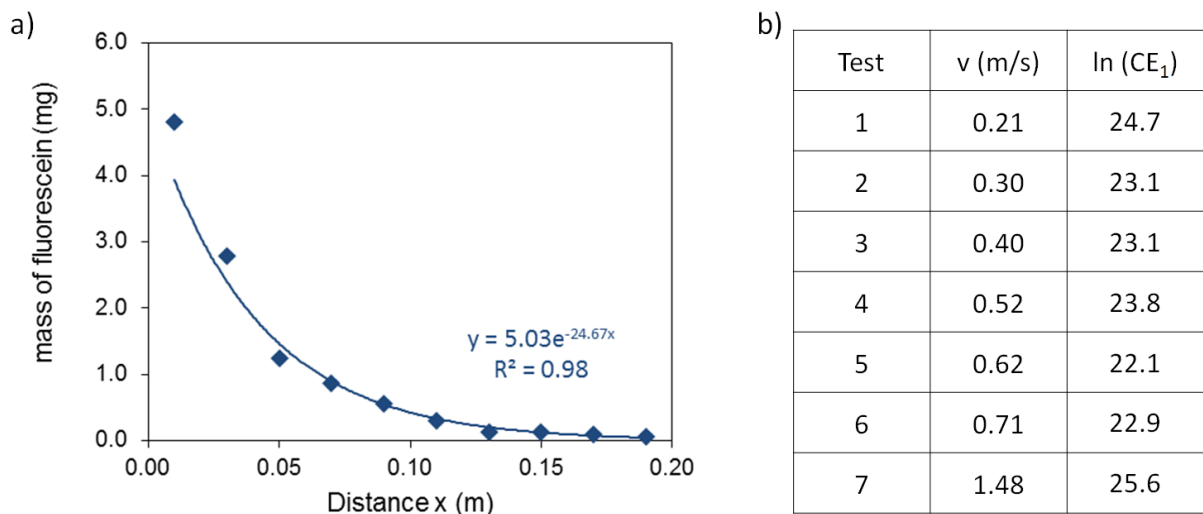


Figure 5.20 – Result of the fluorescein measurement for the test 1 (a) and deduced collection efficiencies for every test (b)

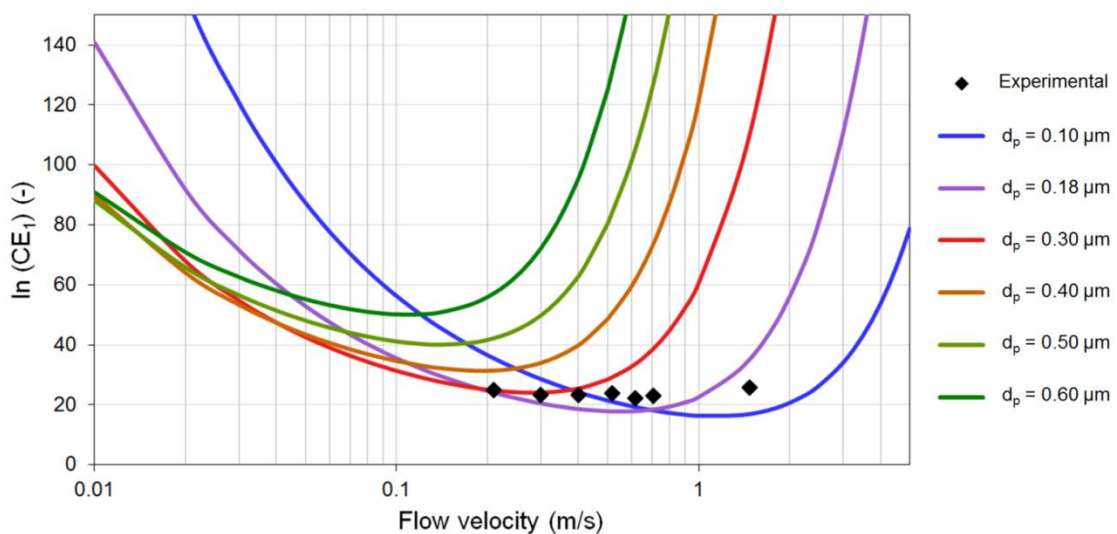


Figure 5.21 – Comparison between the experimental and numerical collection efficiencies

## Conclusion

The experimental tests have validated the consistency of the Miecret and Gustavsson model applied to the fluorescein-laden air flow through the HPGW for velocities ranging from 0.2 to 1.5 m/s. This model is therefore implemented in COMSOL Multiphysics® as described in paragraph 5.3.2, with the parameters presented in Table 5.2 used to calculate the collection efficiency ( $CE_1$ ) as a function of air flow velocity  $v$ . This coupled equations air-fluorescein enables a better comparison between the experimental and the numerical results, as discussed below with the example of an air channel in contact with the glass wool.

### 5.4. Air channel in contact with a porous medium

The use of fluorescein as tracer gas enables qualitative experimental studies of air flow through complex wall assemblies. Actual challenge is to investigate configurations where porous media is in contact with an air channel. Indeed, to the best of our knowledge such studies are still lacking in the literature even if they are representatives of an important number of real configurations [156]. For example this type of flow is frequently found when air infiltrates timber frame wall assemblies with porous insulation materials [119]. An example of a typical envelope leakage was numerically studied by Belleudy et al. [77]. As illustrated in Figure 5.22, a missing flexible sealing is creating a 2 mm air channel between the wood bottom wall plate and the foundation wall, and a part of this air channel is in contact with the porous wood fiberboard insulation.

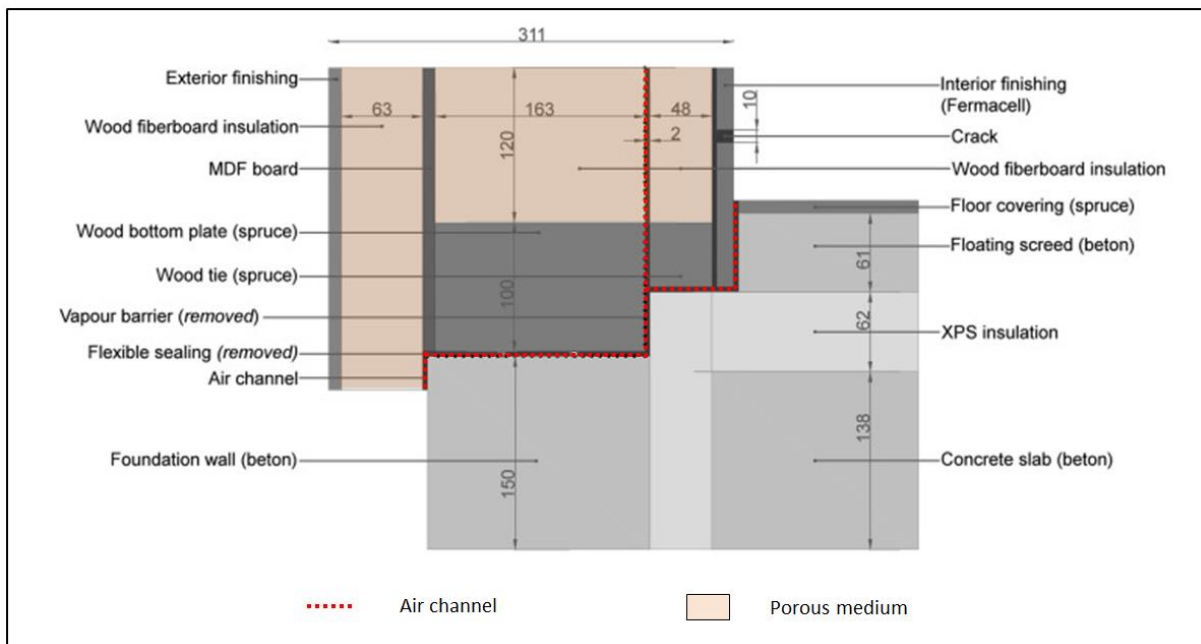


Figure 5.22 – Example of air channels in contact with porous media numerically studied by Belleudy et al. [77]

#### 5.4.1. Tests description

Three configurations, inspired by the wall assembly presented in Figure 5.22, were elaborated for experimental tests in the SAPI box. They are shown in Figure 5.23. In all three configurations a narrow air channel is in contact with a porous media (glass wool), located in between two airtight

wooden plates. The cross-sectional area of the air channel has a thickness  $t_{AC}$  of either 3 or 6 mm and has the same height as the SAPI box: 150 mm.

The first one consists in an angled air channel with a wooden panel on the inlet side so that the air can enter the wall assembly only through the air channel. On the angle channel outer side, the air flow is in contact with first the SAPI box wooden wall and then a wooden panel which are both airtight. On the inner side, the air flow is in contact with a porous medium, the glass wool, and can therefore infiltrate.

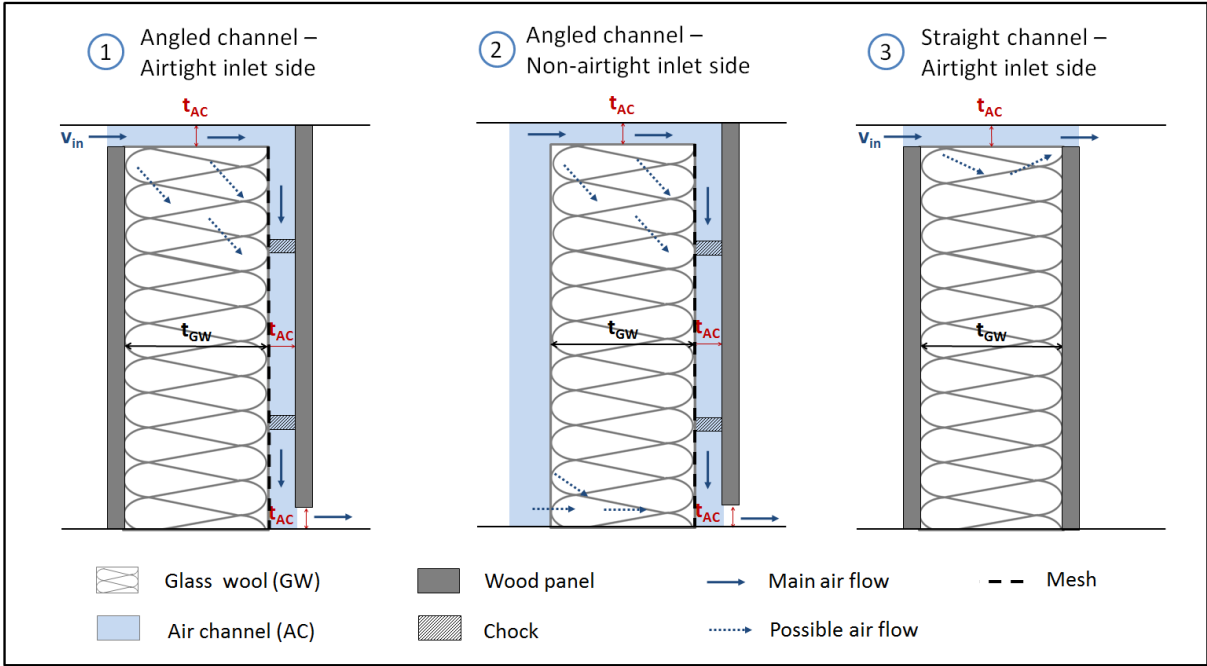


Figure 5.23 – Top view of the air channel configurations (SAPI box)

In the second configuration there is no wooden panel on the inlet side. The air can infiltrate the glass wool over its entire surface, in particular near the channel angle and on the opposite side facing the channel outlet. For these two configurations, there is a rigid mesh as well as small chocks to maintain a constant air channel thickness despite the pressure of the flow. The chocks are only 5 mm high and are placed on the top and on the bottom so that the air can flow normally in between.

For the third configuration the wooden plates touch the porous media on both sides; there is only one straight air channel, with the outlet facing the inlet. The air can still possibly infiltrate the glass wool but unlike for configurations 1 and 2 this does not shorten the air path length.

In addition of comparing these three configurations, the impact of different parameters, such as the thickness of the air channel, of the insulation layer, as well as the air velocity and air permeability of the porous media, is also studied. An overview of all the tests carried out is presented in Table 5.3. For the first configuration, the test 1.a is taken as a reference. The glass wool used is the HPGW, with an original thickness of 60 mm but compressed to 40 mm; an air channel thickness of 3 mm and an air flow velocity of about 2.5 m/s. This test is done twice (1.a') to check the repeatability, and then a number of parameters are changed one by one for a comparison with the reference: the HPGW is replaced by the LPGW (1.b), a second layer of HPGW is added (1.c), and finally the thickness of the air channel  $t_{AC}$  is doubled (1.d), which divides the inlet velocity  $v_{in}$  by two.



Similarly, for the third configuration, the test 3.a is taken as a reference. The glass wool used is still the HPGW but there are two layers to have an 80 mm long straight air channel. They are first placed perpendicularly to the air flow, as for the configurations 1 and 2, and then in parallel (3.b) as illustrated in Figure 5.24. The same tests are also carried out with a 6 mm air channel thickness (3.c and 3.d).

Table 5.3 – Overview of the air channel fluorescein tests

Test	Specificity	$t_{GW}$ (mm)	$t_{AC}$ (mm)	Q (m <sup>3</sup> /h)	$v_{in}$ (m/s)
1.a	Reference 1	40	3	4.00	2.52
1.a'	Repeatability			3.67	2.31
1.b	LPGW	60		3.84	2.42
1.c	2 layers of GW	80		3.37	2.12
1.d	Larger air channel	40	6	3.07	0.97
2	Reference 2	40	3	3.86	-
3.a	Reference 3	80	3	3.96	2.49
3.b	GW // to the flow			3.92	2.47
3.c	Larger air channel		6	2.99	0.94
3.d	Larger air channel + GW // to the flow			4.12	1.30

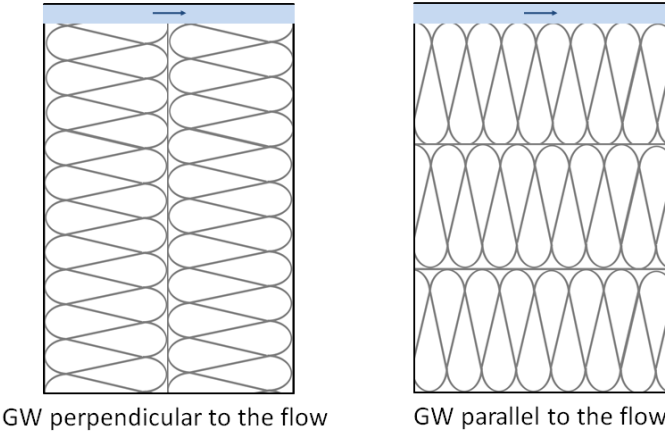


Figure 5.24 – Glass wool orientation for the configuration 3

One challenge for these tests is to ensure that there is no other air gap between the components than the air channel. For this purpose each junction between a wall assembly component and the SAPI box walls is sealed with tape. In addition, the interface between the upstream wood panel and the GW is covered by double-sided tape for the configurations 1 and 3.

The inlet of the SAPI box is connected to the fluorescein generator as for the preliminary tests. The exposition time during which the fluorescein-laden air is passing in the air channel is 2 hours for each test.

## Tests analysis

At the end of the test, the wall assembly is dismantled and the glass wool is cut into small pieces to be analyzed as described in paragraph 5.1.5. The cutting of the glass wool is detailed in Figure 5.25 for the test 1.a but is similar for the other tests.

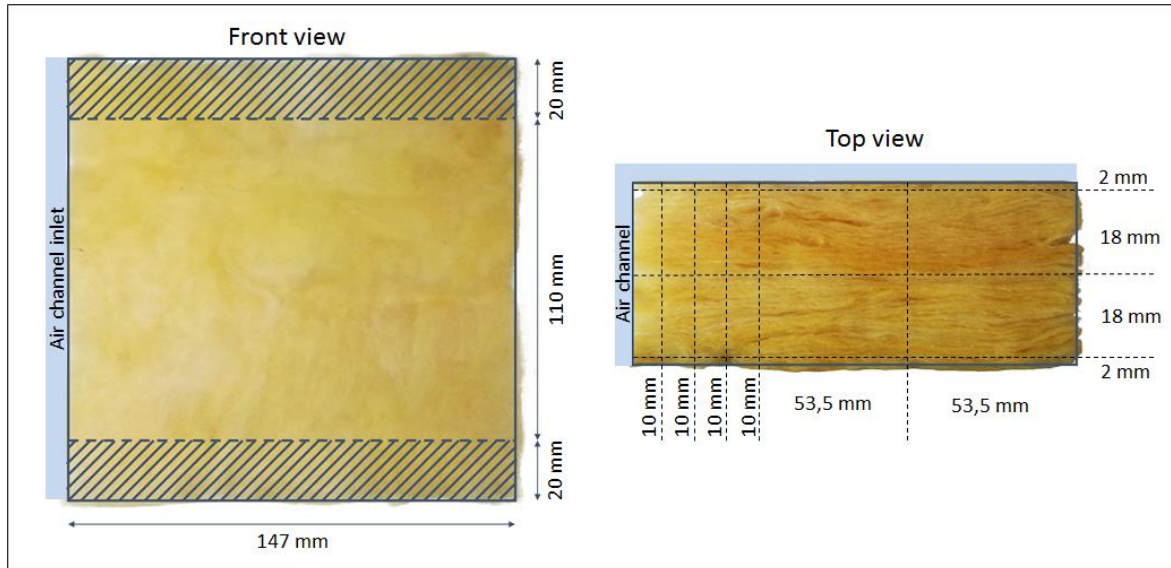


Figure 5.25 – Glass wool cutting for the fluorescein analysis - example of the test 1.a

For each sample, the uppermost and lowermost 20 mm are removed. This aims at preventing the edge effect due to possible air leakage along the SAPI box walls despite the tape. The remaining GW is then cut as follow:

- The front surface (2 mm thick) is removed to check if there is some air flow infiltrating between the upstream wood panel and the GW
- Similarly the back surface (2mm thick) is also removed since it is in contact with the air channel and fluorescein particles can therefore deposit on it.
- The GW is cut at half of its thickness for a 2-D analysis. It could possibly be divided into more layers for a better spatial accuracy but this would also make the analysis time longer and the uncertainties due to the cutting accuracy higher.
- Four 10 mm thick strips are cut on the corner side, where air infiltration into the glass wool is expected. The size of 10 mm was selected as a good compromise between spatial resolution of the results and the non-homogeneity of the material and related difficulty of the manual cutting.
- On the opposite side where air is not expected to pass, two bigger pieces (53.5 mm thick) are cut.

The mass of fluorescein  $m_{flu0}$  is quantified in each sample using absorbance measurements. Unlike for the preliminary tests, the samples do not have all the same dimensions so the mass is divided by the volume to obtain the concentration. Moreover, for a better comparison between the tests, it was decided to divide this number by the maximum concentration found among all the samples of all the tests. As a result the relative concentration of each sample  $i$  ( $C_{r,i}$ ) is defined as follow:

$$C_{r,i} = \frac{m_{flu0,i}}{V_i \times \max(C_{r,i})} \quad (5.39)$$

The maximum concentration  $\max(C_{r,i})$ , was found in the test 3.a and equals  $63.43 \text{ g/m}^3$ .

## 5.4.2. Results

### Angled channel – airtight inlet side

The results of the angled air channel tests (configuration 1 and 2) are presented in Figure 5.26. For the reference test 1.a, the highest fluorescein relative concentration (0.28) is found as expected in the corner of the channel angle. The two adjacent samples have also a significant fluorescein concentration. The air seems to infiltrate the glass wool on the whole length of the first part of the channel, before the angle.

The relative concentration on this air infiltration side (0.17) is higher than in the location of air exit in the glass wool (0.09). This is mainly due to the filtration effect that reduces the fluorescein concentration in the air along the air path. An additional explanation is the fact that fluorescein particles can deposit on this first part of the channel by just flowing along the GW. Unlike for the second part of the channel, it was too difficult to remove the surface 2 mm (due to the direction of the GW fibres). Consequently in this location the effect of surface deposit may impact the results. However for all these tests, the concentration along the 2<sup>nd</sup> part of the channel was very low, and the finer cutting analysis of the tests 1.d in Figure 5.26 shows that the fluorescein is mostly found next to the corner. The surface deposit due to the contact with the fluorescein-laden air flow is therefore not significant.

The second test 1.a' shows a good repeatability of the measurements even if the total amount of fluorescein is slightly lower (0.94 mg instead of 1.14 mg). There are a few sources of potential differences when repeating a test. The main one is the difficulty of having a very accurate cutting with a fibrous and soft material as the HPGW. This leads to a small uncertainty about the thickness of the air channel  $t_{AC}$  as well as in the cutting of the samples of the analysis, especially for the small ones. Moreover, the HPGW is a non-homogeneous material with a density that may vary locally and therefore modify slightly the air flow behavior. Comparing the results of the tests 1.a and 1.a' is however reassuring on the limited impact of these potential differences.

In the test 1.b the HPGW is replaced by the LPGW which has an air permeability about 2.6 times lower as mentioned in paragraph 4.2.1. Because of its rigidity the LPGW cannot be compressed and the thickness of the layer is therefore 60 mm for this test. This lower air permeability has a significant impact on the air flow since fluorescein is found almost only along the first part of the air channel. One should note that because of its higher density, the LPGW has also probably greater collection efficiency. This means that for the same air flow pattern, there would be a greater difference between the fluorescein concentration near the air inlet in the glass wool and near the air outlet. However, in this case the concentration along the first part of the air channel is half the concentration found for the reference case: there is indeed a smaller air flow rate infiltrating the GW.

In the test 1.c a second layer of HPGW is added. The same compression rate is applied to avoid air gaps between the wall assembly components so the total GW thickness  $t_{GW}$  is 80 mm. It is however clear from the results that there is air passing between these two layers despite the GW compression.

1.a -  $m_{\text{fluo,tot}} = 1,14 \text{ mg}$

Air channel		
0.17	0.28	
0.05	0.09	
0.02	0.02	
0.01	0.01	
0.00	0.00	
0.00	0.01	
0.01		0.08

1.a' -  $m_{\text{fluo,tot}} = 0,94 \text{ mg}$

Air channel		
0.14	0.22	
0.06	0.10	
0.03	0.03	
0.02	0.02	
0.00	0.01	
0.00	0.01	
0.02		0.01

1.b -  $m_{\text{fluo,tot}} = 0.84 \text{ mg}$

Air channel		
0.07	0.10	
0.02	0.02	
0.00	0.00	
0.00	0.00	
0.00	0.01	
0.01	0.01	
0.01		0.05

1. c -  $m_{\text{fluo,tot}} = 0.91 \text{ mg}$

Air channel				
0.04	0.05	0.11	0.07	0.08
0.02	0.02	0.08	0.03	0.03
0.01	0.01	0.05	0.01	0.01
0.01	0.01	0.05	0.01	0.01
0.00	0.00	0.00	0.00	0.00
0.00	0.00	0.00	0.00	0.00
0.19		0.13		0.14
0.00		0.01		0.02

1.d -  $m_{\text{fluo,tot}} = 0.55 \text{ mg}$

Air channel		
0.06	0.11	0.20
0.05	0.06	0.16
0.02	0.02	0.07
0.01	0.02	0.11
0.01	0.02	0.11
0.00	0.00	0.01
0.00	0.00	0.01
0.01		0.02
0.01		0.01

2 -  $m_{\text{fluo,tot}} = 1.14 \text{ mg}$

Air channel	
0.04	0.12
0.04	0.04
0.02	0.02
0.02	0.01
0.02	0.01
0.02	0.01
0.02	0.01
0.03	0.01
0.03	0.01
0.04	0.01
0.09	0.06
0.08	
0.14	
0.03	
0.01	

Figure 5.26 – Angled air channel – Results of the experimental fluorescein tests

For the test with a larger air channel of 6 mm (1.d), the total air flow rate is about the same as the reference case, so it is the air velocity at the inlet  $v_{in}$  that is divided by two (1 m/s). The GW cutting for the analysis is finer since the air flow is expected to less penetrate the porous medium. This assumption is confirmed by the results since almost no fluorescein is found more than 10 mm from the air channel. Moreover, the total mass of fluorescein is half the one obtained with the reference case. It means that not only the air flow infiltrates a smaller part of the GW but also with about half of the air flow rate.

#### **Angled channel – non-airtight inlet side**

The last test with an angled channel corresponds to the configuration 2 with no airtight wood panel on the upstream side of the wall assembly. The highest fluorescein concentration is still found in the corner in contact with the channel angle, but the global air flow pattern is very different. The opposite corner also presents a significant amount of fluorescein. It is indeed facing the channel outlet so the air path length through the GW is the shortest at this location. Moreover, unlike for any other test, some fluorescein is detected in each part of the sample. It shows that air is passing through the whole GW, even if it is at low flow rates. The air seems however to flow mostly on the two extremities of the GW, near the air channel inlet and outlet, and not much in the middle.

#### **Straight channel– airtight inlet side**

For the third configuration, the air channel outlet is facing the inlet, so there is no more an angle to be cut by the air flow through the glass wool. The impact of two parameters is studied: the thickness of the air channel  $t_{AC}$  and the orientation of the glass wool. The results are presented in Figure 5.27. As for the configuration 2, the GW cutting is finer near the air channel, with layers of 5 mm instead of 10 mm. For the tests with the glass wool layers parallel to the flow (3.b and 3.d), the front and back layers are 5 mm thick instead of 2 mm since it is difficult to cut a very thin layer perpendicularly to the GW fibers.

The reference case 3.a is similar to the test 1.c (double HPGW layer), with the exception of the air outlet location. The results show a difference of air penetration between the first and the second GW layers. On the first one, there is a significant relative concentration of fluorescein in the first 10 mm (between 0.09 and 0.19). At the interface between the two layers, the highest fluorescein concentration is reached, and despite the GW compression there is clearly an air path between the two layers. On the second GW layer the relative concentrations do not exceed 0.04, which is more surprising. This decrease in concentrations is indeed much more rapid than observed before, it may be partially due to higher air velocities which can have an impact on the collection efficiency as mentioned before. Another possible explanation is that once the air infiltrates between the two layers, it goes up and/or down to pass between the GW and the SAPI box walls to reach the channel outlet. Since the uppermost and lowermost 20 mm are removed, this air flow does not appear on the results.

The second test 3.b has the glass wool layers parallel to the air flow, which removes the issue of the GW interface at the middle of the channel. However when placed in that direction it is more difficult to ensure a good contact between wood panels and the glass wool. The GW fibers are indeed perpendicular to these interfaces so the tape is less efficient. As a result, there is probably a small air gap between the glass wool and wooden panel layers on both the upstream and downstream side.

3.a -  $m_{\text{fluo,tot}} = 1,23 \text{ mg}$

Air channel						
0.10	0.19	0.17	0.09	0.01	0.04	0.09
	0.12	0.09	1.0	0.03	0.02	
	0.09	0.04	0.2	0.01	0.01	
	0.05	0.03	0.2	0.01	0.01	
0.02	0.02	0.01	0.00	0.00	0.00	0.01
	0.01	0.00	0.00	0.00	0.00	
	0.00	0.00	0.00	0.00	0.00	

3.b -  $m_{\text{fluo,tot}} = 1.56 \text{ mg}$

Air channel						
0.33	0.07	0.14	0.18	0.26	0.06	0.02
	0.02	0.02	0.07	0.11	0.02	
	0.02	0.01	0.03	0.07	0.02	
	0.01	0.02	0.03	0.07	0.02	
0.17	0.00	0.01	0.02	0.04	0.00	0.01
	0.02	0.01	0.00	0.00	0.00	
0.05	0.00	0.00	0.00	0.00	0.01	0.01
	0.00	0.00	0.00	0.00	0.01	

3.c -  $m_{\text{fluo,tot}} = 0.91 \text{ mg}$

Air channel						
0.10	0.04	0.10	0.08	0.09	0.11	0.25
	0.01	0.04	0.1	0.03	0.03	
	0.01	0.03	0.0	0.02	0.02	
	0.00	0.02	0.1	0.01	0.01	
0.01	0.00	0.01	0.00	0.00	0.00	0.01
	0.00	0.00	0.01	0.00	0.00	
	0.00	0.00	0.00	0.00	0.00	

3.d -  $m_{\text{fluo,tot}} = 0.45 \text{ mg}$

Air channel						
0.11	0.02	0.03	0.03	0.05	0.01	0.01
	0.01	0.01	0.01	0.02	0.01	
	0.01	0.01	0.01	0.01	0.01	
	0.01	0.01	0.00	0.01	0.01	
0.01	0.00	0.00	0.00	0.00	0.01	0.01
	0.01	0.00	0.00	0.00	0.01	
0.00	0.00	0.00	0.00	0.00	0.01	0.01
	0.00	0.00	0.00	0.00	0.01	

Figure 5.27 – Straight air channel – Results of the experimental fluorescein tests

The tests 3.c and 3.d are the same as 3.a and 3.b but with a 6 mm thick air channel. The air flow rate is similar but the velocities are lower, around 1 m/s. This reduces significantly the air infiltrations in the glass wool. There is almost no fluorescein found after 5 mm (relative concentration below 0.04), except at the interface between the two GW for the test 3.c. The pressure drop decreases due to this larger air channel, which reduces the issue of air gap apparition between components.

## Conclusion

Seeding the air flow with fluorescein micro-particles is helpful for a qualitative air infiltration diagnostic. These various experimental tests have shown each time an air infiltration inside the glass wool despite the air channel. In comparison, the numerical simulation predicted an air infiltration for angled air channel but not for the straight channel configurations.

The simple comparative fluorescein concentration analysis has given evidence of lower air infiltration in the glass wool for lower velocities or less porous insulation materials. It has also demonstrated a preferential air path between two layers of glass wool despite an apparent good contact between them. However, because of the filtration effect the fluorescein concentration mapping cannot be directly compared with an air flow pattern obtained by simulation. For a better comparison between the numerical and experimental results, the micro-particles collection model presented in paragraph 5.3 is coupled with a CFD module, as detailed below.

### 5.4.3. Comparison with the simulation

In this paragraph the experimental tests from 1a to 3d are compared with a numerical simulation with the software COMSOL Multiphysics®, except the test 1.b with the LPGW since the collection efficiency of this porous material has not been determined. The simulation parameters and boundary conditions are illustrated in Figure 5.28, and detailed respectively in

Table 5.4 and Table 5.5. The model used to solve the air flow is *Free and Porous Media Flow*. The flow is described by the Navier-Stokes equation in the air channel and the Brinkman's extension of Darcy's Law in the porous region with an additional term to obtain consistent boundary conditions [157]. The fluorescein micro-particles transport is simulated with the Miecret and Gustavsson model presented in paragraph 5.3.2. The results discussed below represent the stationary solution. It facilitates indeed the convergence of the calculations and since only relative concentrations are presented, the quantification of the amount of particles collected after a given time is not of interest here.

Thanks to a 2-D geometry and relatively simple equations in the models, the computational time is very short. The mesh is therefore taken "extremely fine" with a minimum element size of  $8 \cdot 10^{-7}$  m and a maximum element size of  $3 \cdot 10^{-4}$  m which leads to over 200 000 elements for the configuration with the smallest simulated area (1 layer of GW), and a computational time of about 1 min. A refinement is also done with boundary layers at the interface between the glass wool and the air flow to facilitate calculations on this discontinuity. It has been verified that twice finer meshes had no significant impact on the results.

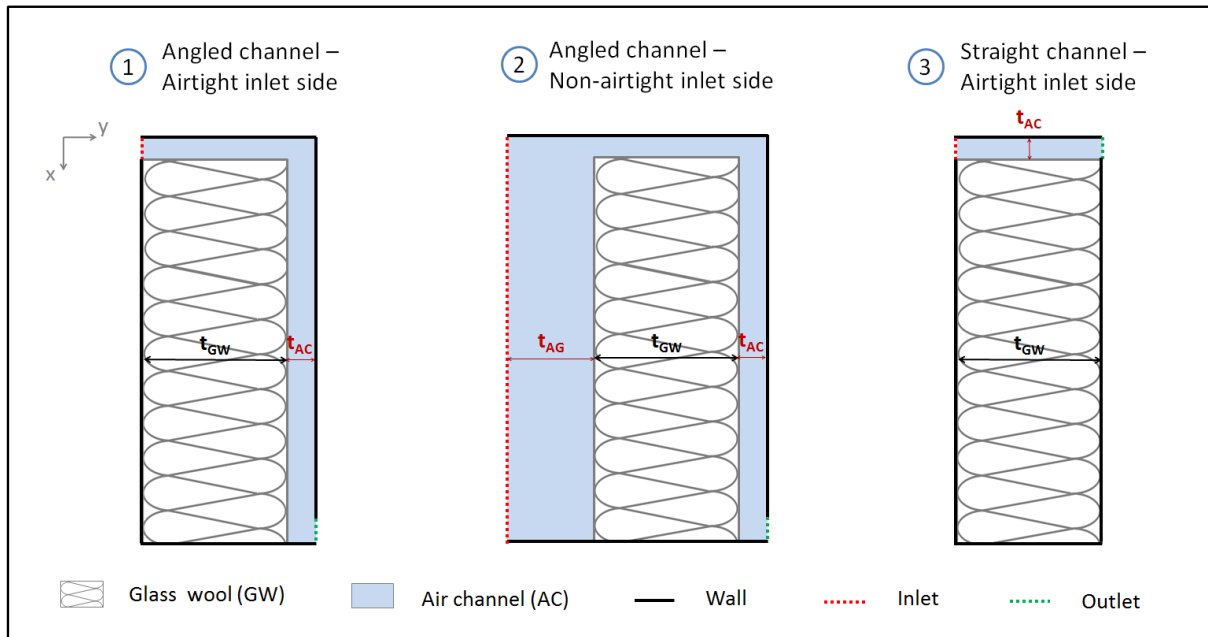


Figure 5.28 – 2-D geometries for the air channel simulation study

Table 5.4 – Numerical study parameters

COMSOL models	Free and Porous Media Flow ; Miecret and Gustavsson
Glass wool	Compressed HPGW (67%): - Porosity: 0.99 - Air permeability: $1.09 \cdot 10^{-9} \text{ m}^2 (\perp)$ ; $2.57 \cdot 10^{-9} \text{ m}^2 (//)$
Air	Properties taken at 20°C: - Density: $1.20 \text{ kg/m}^3$ - Dynamic viscosity: $1.83 \cdot 10^{-5} \text{ kg/m/s}$

Table 5.5 – Numerical study boundary conditions

Boundary	Air flow	Fluorescein concentration
Inlet	$v = v_{in}$	$C = C_0$
Outlet	$P = P_{ext} = 1 \text{ atm}$	$-\vec{n} \cdot \left( \frac{\partial C}{\partial x}, \frac{\partial C}{\partial y} \right) = 0$
Wall	Zero velocity (no slip) : $v = 0$	Zero flux: $-\vec{n} \cdot \left( \frac{\partial C}{\partial x}, \frac{\partial C}{\partial y} \right) = 0$

The geometry implemented is two-dimensional and corresponds to a cross-section of the glass wool half-way up. The air channel thickness  $t_{AC}$  and the GW thickness  $t_{GW}$  depend on the tested configuration ( $t_{AC} = 3$  or  $6 \text{ mm}$ ,  $t_{GW} = 40$  or  $80 \text{ mm}$ ). For the configuration with no airtight layer on the inlet side, an air gap with a thickness  $t_{AG}$  of  $40 \text{ mm}$  is added. The HPGW is modeled by a



homogeneous porous medium characterized by its porosity and air permeability. The density and the dynamic viscosity of the air are taken at 20°C.

At the inlet, first order (Dirichlet) boundary conditions are imposed on the air velocity and the fluorescein concentration. The inlet velocity  $v_{in}$  is set at the corresponding experimental value. As an improvement of this model, it would be possible to model the upstream air flow, before entering the channel. The value of the fluorescein concentration at the inlet  $C_0$  is not relevant since only relative concentrations are presented in this chapter, and the results are from the stationary solution.

For the air flow there are also first order boundary conditions at the outlet and along the wall. At the outlet the condition is on the pressure that equals to 1 atm, and along the walls the velocity is set to zero (no slip condition). Concerning the fluorescein transport, the concentration at the outlet of the wall assembly is not known a priori, a second order boundary condition (Neumann) is therefore imposing a zero gradient for the diffusive term. The same condition applies for the walls, but since there is no velocity at this boundary, the advection term will also equal to zero which leads to the particles conservation within the simulation domain.

The results of these simulations are presented in different forms:

- The streamlines to evaluate the air flow penetration in the HPGW. They represent the path of 50 equidistant points taken on the inlet boundary.
- The velocity field which complements the streamline representation. It enables to see that for each test the air velocity inside the porous medium is much smaller than in the air channel.
- The fluorescein concentration field which differs from the velocity one since the particles get collected only in the porous medium: the maximum concentration in the GW is therefore the same than in the air channel. As mentioned in paragraph 5.3.2, the advection-dominated particle transport models are subject to numerical difficulties, which explains the discontinuities in the solutions. Decreasing the convergence from  $10^{-3}$  to  $10^{-6}$  didn't change the results. There are other avenues for reflection to decrease this risk of discontinuity such as using a velocity profile at the inlet rather than a constant velocity or implementing a turbulence model since velocities are locally in the vicinity of the critical Reynolds number. Such developments were however beyond the scope of this study.
- The surface-averaged fluorescein concentrations with the same cutting than the experiment for a direct comparison. The values given are relative concentrations which were calculated to have an identical experimental and numerical total mass of fluorescein for the reference test 1.a.

### **Angled channel – Reference case**

The experimental and numerical results for the angled channel reference case (Test 1.a) are compared in Table 5.6. The velocity field shows no obvious air penetration into the HPGW with high velocities only in the air channel. However 30% of the 50 streamlines drawn are crossing the porous medium from the whole channel length but with a greater density near the angle. As a result there is a significant part of the air flow that bypasses the angle to shorten the path length, even if the velocities are smaller due to a larger cross-sectional area. The numerical fluorescein concentration field reflects the streamlines representation, with high values at the interface between the first part

of the air channel and the glass wool. Because of the particles collection along the air path, the fluorescein concentration is no longer significant near the flow outlet. This is the main limitation of using this experimental method for the air path investigation: the infiltration area is easily identified but the longer the air path, the fewer particles remain to track the flow.

The experimental volume-averaged and the numerical surface averaged fluorescein relative concentrations  $C_{fluo,r}$  can be directly compared since the same cutting is applied. As mentioned before, the total masses of fluorescein are equivalent for this test. The distribution is however slightly different. The experimental mapping shows a greater relative concentration in the corner (0.28) than on the upstream adjacent volumes (0.17). In the numerical mapping the two GW pieces near the first part of the air channel have very similar relative fluorescein concentration (0.21 and 0.22). These results enable to conclude that during the experiment the flow infiltrating the GW was probably more concentrated around the corner than predicted by the numerical model.

**Angled channel – Addition of a 2<sup>nd</sup> GW layer**

In the simulation the two layers of GW are modeled as if the contact was perfect between them, ensuring continuity in the flow. Consequently, the results presented in Table 5.7 show continuity in the streamlines at this interface. This is however not what is observed experimentally. As discussed in paragraph 5.4.2, the experimental fluorescein results for the test 1.c showed an air path between the two GW layers. Moreover one can note that the relative concentrations are lower for the experimental results than for the numerical ones. This can also be explained by the experimental evidence of an air gap between the GW layers that decreases the pressure and the flow velocities in the air channel.

Table 5.6 – Experimental and numerical results of the air channel Test 1.a

Exp. results	Numerical results			
Volume av. $C_{fluo,r}$	Velocity field	Streamlines	$C_{fluo}$ field	Surface av. $C_{fluo,r}$



was indeed the one with the highest fluorescein concentration measured experimentally whereas the model shows a smaller concentration than at the opposite side of the GW.

Table 5.8 – Experimental and numerical results of the air channel Test 1.d

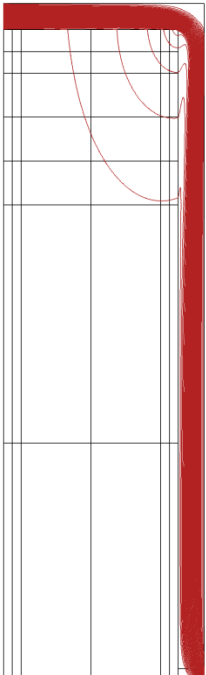
Exp. results	Numerical results																																																																																					
Volume av. $C_{fluor}$	Streamlines	Surface av. $C_{fluor}$																																																																																				
<table border="1"> <thead> <tr> <th colspan="4">Air channel</th> </tr> </thead> <tbody> <tr> <td>0.11</td> <td>0.06</td> <td>0.11</td> <td>0.20</td> </tr> <tr> <td>0.07</td> <td>0.05</td> <td>0.06</td> <td>0.16</td> </tr> <tr> <td></td> <td>0.02</td> <td>0.02</td> <td></td> </tr> <tr> <td></td> <td>0.01</td> <td>0.02</td> <td></td> </tr> <tr> <td></td> <td>0.01</td> <td>0.02</td> <td></td> </tr> <tr> <td></td> <td>0.00</td> <td>0.00</td> <td></td> </tr> <tr> <td>0.01</td> <td></td> <td></td> <td>0.02</td> </tr> <tr> <td>0.01</td> <td></td> <td></td> <td>0.01</td> </tr> <tr> <td></td> <td></td> <td></td> <td>0.01</td> </tr> <tr> <td></td> <td>0.00</td> <td>0.00</td> <td></td> </tr> </tbody> </table>	Air channel				0.11	0.06	0.11	0.20	0.07	0.05	0.06	0.16		0.02	0.02			0.01	0.02			0.01	0.02			0.00	0.00		0.01			0.02	0.01			0.01				0.01		0.00	0.00			<table border="1"> <thead> <tr> <th colspan="4">Air channel</th> </tr> </thead> <tbody> <tr> <td>0.12</td> <td>0.17</td> <td>0.21</td> <td>0.14</td> </tr> <tr> <td>0.08</td> <td>0.06</td> <td>0.10</td> <td>0.14</td> </tr> <tr> <td></td> <td>0.02</td> <td>0.03</td> <td></td> </tr> <tr> <td></td> <td>0.00</td> <td>0.00</td> <td></td> </tr> <tr> <td></td> <td>0.00</td> <td>0.00</td> <td></td> </tr> <tr> <td>0.00</td> <td></td> <td></td> <td>0.01</td> </tr> <tr> <td>0.00</td> <td></td> <td></td> <td>0.00</td> </tr> <tr> <td></td> <td></td> <td></td> <td>0.00</td> </tr> <tr> <td></td> <td>0.00</td> <td>0.00</td> <td></td> </tr> </tbody> </table>	Air channel				0.12	0.17	0.21	0.14	0.08	0.06	0.10	0.14		0.02	0.03			0.00	0.00			0.00	0.00		0.00			0.01	0.00			0.00				0.00		0.00	0.00	
Air channel																																																																																						
0.11	0.06	0.11	0.20																																																																																			
0.07	0.05	0.06	0.16																																																																																			
	0.02	0.02																																																																																				
	0.01	0.02																																																																																				
	0.01	0.02																																																																																				
	0.00	0.00																																																																																				
0.01			0.02																																																																																			
0.01			0.01																																																																																			
			0.01																																																																																			
	0.00	0.00																																																																																				
Air channel																																																																																						
0.12	0.17	0.21	0.14																																																																																			
0.08	0.06	0.10	0.14																																																																																			
	0.02	0.03																																																																																				
	0.00	0.00																																																																																				
	0.00	0.00																																																																																				
0.00			0.01																																																																																			
0.00			0.00																																																																																			
			0.00																																																																																			
	0.00	0.00																																																																																				

Table 5.9 – Experimental and numerical results of the air channel Test 2

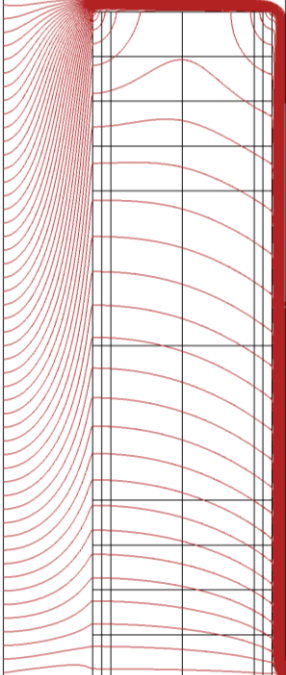
Exp. results	Numerical results																																																																																																													
Volume av. $C_{fluor}$	Streamlines	Surface av. $C_{fluor}$																																																																																																												
<table border="1"> <thead> <tr> <th colspan="4">Air channel</th> </tr> </thead> <tbody> <tr> <td>0.14</td> <td>0.04</td> <td>0.12</td> <td>0.03</td> </tr> <tr> <td>0.08</td> <td>0.04</td> <td>0.04</td> <td>0.01</td> </tr> <tr> <td></td> <td>0.02</td> <td>0.02</td> <td></td> </tr> <tr> <td></td> <td>0.02</td> <td>0.01</td> <td></td> </tr> <tr> <td></td> <td>0.02</td> <td>0.01</td> <td></td> </tr> <tr> <td>0.01</td> <td></td> <td></td> <td>0.03</td> </tr> <tr> <td>0.01</td> <td></td> <td></td> <td>0.01</td> </tr> <tr> <td></td> <td>0.02</td> <td>0.01</td> <td></td> </tr> <tr> <td></td> <td>0.02</td> <td>0.01</td> <td></td> </tr> <tr> <td></td> <td>0.03</td> <td>0.01</td> <td></td> </tr> <tr> <td></td> <td>0.03</td> <td>0.01</td> <td></td> </tr> <tr> <td></td> <td>0.04</td> <td>0.01</td> <td></td> </tr> <tr> <td></td> <td>0.09</td> <td>0.06</td> <td></td> </tr> </tbody> </table>	Air channel				0.14	0.04	0.12	0.03	0.08	0.04	0.04	0.01		0.02	0.02			0.02	0.01			0.02	0.01		0.01			0.03	0.01			0.01		0.02	0.01			0.02	0.01			0.03	0.01			0.03	0.01			0.04	0.01			0.09	0.06			<table border="1"> <thead> <tr> <th colspan="4">Air channel</th> </tr> </thead> <tbody> <tr> <td>0.16</td> <td>0.08</td> <td>0.03</td> <td>0.01</td> </tr> <tr> <td>0.19</td> <td>0.09</td> <td>0.01</td> <td>0.01</td> </tr> <tr> <td></td> <td>0.09</td> <td>0.01</td> <td></td> </tr> <tr> <td></td> <td>0.09</td> <td>0.01</td> <td></td> </tr> <tr> <td></td> <td>0.10</td> <td>0.02</td> <td></td> </tr> <tr> <td>0.01</td> <td></td> <td></td> <td>0.01</td> </tr> <tr> <td>0.01</td> <td></td> <td></td> <td>0.01</td> </tr> <tr> <td></td> <td>0.11</td> <td>0.03</td> <td></td> </tr> <tr> <td></td> <td>0.12</td> <td>0.03</td> <td></td> </tr> <tr> <td></td> <td>0.12</td> <td>0.04</td> <td></td> </tr> <tr> <td></td> <td>0.12</td> <td>0.04</td> <td></td> </tr> <tr> <td></td> <td>0.13</td> <td>0.04</td> <td></td> </tr> </tbody> </table>	Air channel				0.16	0.08	0.03	0.01	0.19	0.09	0.01	0.01		0.09	0.01			0.09	0.01			0.10	0.02		0.01			0.01	0.01			0.01		0.11	0.03			0.12	0.03			0.12	0.04			0.12	0.04			0.13	0.04	
Air channel																																																																																																														
0.14	0.04	0.12	0.03																																																																																																											
0.08	0.04	0.04	0.01																																																																																																											
	0.02	0.02																																																																																																												
	0.02	0.01																																																																																																												
	0.02	0.01																																																																																																												
0.01			0.03																																																																																																											
0.01			0.01																																																																																																											
	0.02	0.01																																																																																																												
	0.02	0.01																																																																																																												
	0.03	0.01																																																																																																												
	0.03	0.01																																																																																																												
	0.04	0.01																																																																																																												
	0.09	0.06																																																																																																												
Air channel																																																																																																														
0.16	0.08	0.03	0.01																																																																																																											
0.19	0.09	0.01	0.01																																																																																																											
	0.09	0.01																																																																																																												
	0.09	0.01																																																																																																												
	0.10	0.02																																																																																																												
0.01			0.01																																																																																																											
0.01			0.01																																																																																																											
	0.11	0.03																																																																																																												
	0.12	0.03																																																																																																												
	0.12	0.04																																																																																																												
	0.12	0.04																																																																																																												
	0.13	0.04																																																																																																												

Table 5.10 – Experimental and numerical results of the air channel Test 3.a

Exp. results						Numerical results								
Volume av. $C_{fluo,r}$						Streamlines			Surface av. $C_{fluo,r}$					
Air channel						[Empty Streamlines Grid]			Air channel					
0.19	0.17	0.16	0.01	0.04	0.01				0.07	0.04	0.00	0.00	0.00	0.00
0.12	0.09	0.04	0.03	0.02	0.03				0.02	0.00	0.00	0.00	0.00	0.00
0.09	0.04	0.02	0.01	0.01	0.01				0.00	0.00	0.00	0.00	0.00	0.00
0.05	0.03	0.02	0.01	0.01	0.01				0.00	0.00	0.00	0.00	0.00	0.00
0.02	0.01	0.00	0.00	0.00	0.00				0.00	0.00	0.00	0.00	0.00	0.00
0.01	0.00	0.00	0.00	0.00	0.00				0.00	0.00	0.00	0.00	0.00	0.00
0.00	0.00	0.00	0.00	0.00	0.00				0.00	0.00	0.00	0.00	0.00	0.00
0.00	0.00	0.00	0.00	0.00	0.00				0.00	0.00	0.00	0.00	0.00	0.00

There is therefore a significant difference between the experimental and numerical flow patterns. It has been checked that it was not due to a small air gap thickness ( $t_{AG} = 20$  mm) by repeating the simulation with  $t_{AG} = 100$  mm. The results presented in the Appendix E show no significant difference for both the streamlines and the surface-averaged fluorescein relative concentrations.

**Straight channel**

As shown in Table 5.10, the simulation of a straight channel shows no streamlines through the porous media for the reference case 3.a. The simulation with the opposite direction of the GW (3.b, 3.d) and with a larger air channel (3.c, 3.d) give the same result as presented in Appendix F. The fluorescein concentration does not equal to zero at the inlet of the air channel but this is probably due to numerical instabilities at the inlet boundary. The fluorescein particle transport is indeed highly advection-dominated, which presents numerical difficulties as mentioned in paragraph 5.3.2. On the downstream part of the air channel there is a zero fluorescein concentration in the GW, which is consistent with the absence of air flow.

Complementary results of the simulation for each configuration are presented in Appendix F.

**5.5. Conclusions**

Experimental investigations of the path of an infiltrating air within a timber wall assembly are complex to perform, but can be necessary for numerical models validation. A new method was developed for this purpose, consisting of seeding the air with fluorescein micro-particles. The particles are collected by the fibers of the porous insulation material along the air flow, the insulation

is then cut into small volumes and the fluorescein concentration is measured in each of them by spectrometry. The main advantage of this technique is that it is non-intrusive. The fluorescein was chosen among other the possible tracers mainly because it is easily detectable at very low concentration levels.

A number of preliminary tests on simple configurations have validated the consistency and the repeatability of this method for experimental analyses of the air dispersion inside the insulation material. The rather high filtration efficiency has however been pointed out as a limitation to this technique. An absence of fluorescein deposition should reflect the absence of air flow but it can result as well from the total filtration of particles before reaching that point.

In order to avoid this confusion for the results interpretation, a better understanding of the micro-particles collection mechanisms was necessary. The Miecret and Gustavsson model gave a good agreement with simple experimental tests on the HPGW collection efficiency. It was also confirmed that the filtration is low in the velocity range of 0.1 – 1.5 m/s for this association of insulation material and size of particles. However a sensitivity analysis pointed out that this collection efficiency was strongly dependent on the micro-particles and fibers diameters, two parameters that are not constant, and with a distribution somehow difficult to assess.

This fluorescein method was then applied to a specific case study: the air flow in channel in contact with porous media. A simple analysis of the resulting fluorescein concentration mappings was first presented. It enabled to already draw conclusions on the impact of parameters such as the flow velocity or the insulation material on the air infiltration in the glass wool. It has also given evidences of phenomena such as the appearance of thin air gaps between the components of the wall assembly.

The link is however not direct between the fluorescein concentration and the velocity field inside the insulation. For a better comparison between these two parameters and between the experimental results and the numerical predictions, the tests were simulated using a CFD model coupled with the particles collection model implemented in Comsol software. This enabled to point out significant differences in the air flow patterns. For angled air channels, the measured air infiltration was more concentrated in the corner than predicted by the simulation. The air dispersion inside the GW was also much smaller for the case without an airtight layer on the inlet side. And concerning straight channels, some fluorescein was found experimentally in the GW whereas the simulation does not predict an air infiltration.

Overall this study has shown that the use of fluorescein to track the air path in timber frame wall assemblies is of interest and enables to point out differences with CFD models. In case the insulation material is hygroscopic (wood fibers), such differences can have a significant impact on the moisture transfer and the mold risk identification. In the next chapter this technique is compared with the main existing experimental approaches.



# Chapter 6

## Assessing the performance of different experimental methods to evaluate air dispersion in wall assemblies

In this chapter, five different experimental techniques are tested for the air path study in timber frame wall assemblies. The air inlets and outlets are first determined by infrared thermography and particle image velocimetry. The air path inside the wall assembly is then investigated. Three-dimensional grids of thermocouples and relative humidity sensors were implemented inside the wall to track respectively the warm and the humid air infiltrating. Finally fluorescein micro-particles were used as tracer inside the insulation material. These experimental methods are compared with each other and with a numerical model, to identify their respective benefits and limitations.

There are each time two possible levels of analysis. The temperature, humidity and fluorescein concentration mappings obtained experimentally may be directly used for a qualitative or even quantitative air path study. For further investigation it is also possible to couple the air flow model to include additional physical phenomena impacting the measurements: heat transfer, moisture transfer or fluorescein transport. Consequently, the experimental results can be linked with the numerical velocity fields and it enables to validate numerical models that can later be applied to any particular configuration. In the present study, this coupling is done only for the fluorescein technique because of its innovative use for the air path investigation. There are however coupled heat air and moisture models in the literature that would enable a finer analysis for the other approaches.

### 6.1. Description of the tested configurations

#### 6.1.1. Experimental study

In order to compare the experimental methods with each other, three test configurations were constructed in the APIE box. They are described in Figure 6.1. One should note however that some experimental techniques (thermography and PIV) have required the modification and/or addition of configurations.



In each configuration there are two layers of glass wool placed between two gypsum boards. The glass wool is the HPGW characterized in paragraph 1004.2. Each layer is originally 60 mm thick, but in order to guarantee a good surface contact between the layers, the material was compressed when possible, until reaching 40 mm thick. The gypsum boards are 10 mm thick, and a 20 mm diameter calibrated hole is made on each of them at the same location. Unless specified otherwise (for PIV tests), the junction between each building component and the APIE box walls is sealed with tape on both sides of the layer. This ensures that the air is only passing through the calibrated hole and not around the wall assembly. On the downstream side, the glass wool and the gypsum board are glued together with two concentric circles of glue (around the hole) of respectively 25 mm and 130 mm in diameter. The difference between these three configurations lies in the upstream junction between the gypsum board and the glass wool.

The first test configuration represents the case where there is a service cavity usually for routing electrical cables and sometimes also for the plumbing and ductwork. It is usually only a few centimeters thick, but in order to simplify the implementation, for that case there is simply no GB on the upstream side. This is equivalent to a 1 m thick air gap, since it is the distance between the air inlet in the APIE box and the tested wall. We have verified with a numerical simulation on COMSOL that after 2 cm, the air gap thickness does not have an impact on the flow behavior inside the glass wool.

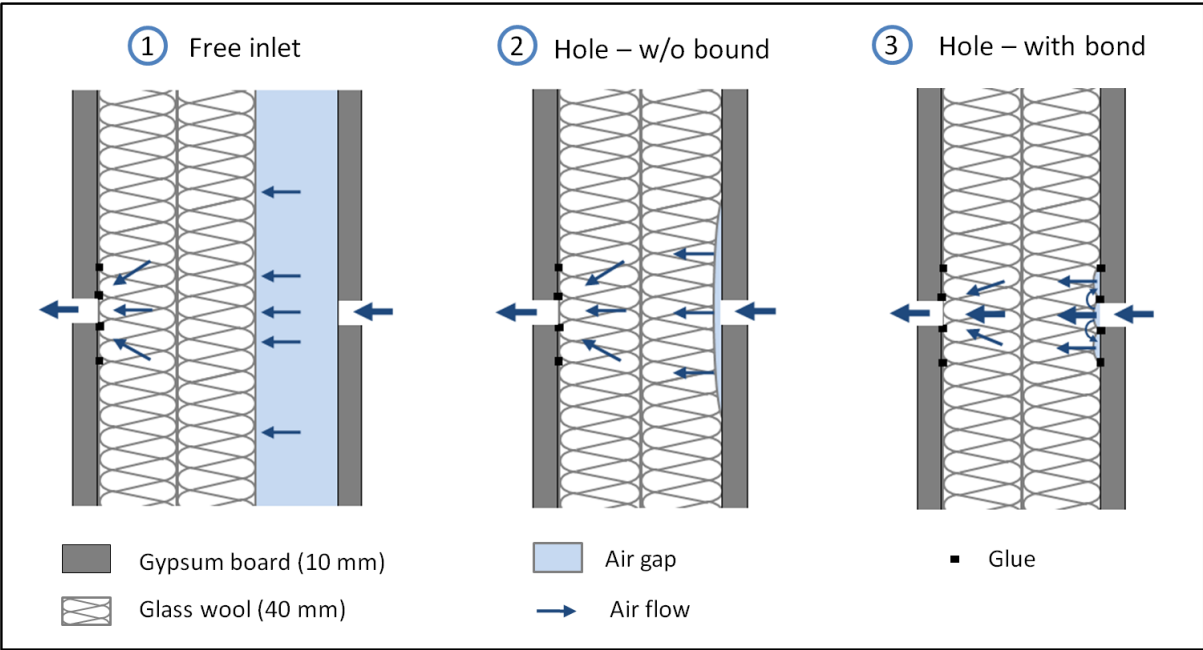


Figure 6.1 - Reference test configurations

On the second test configuration, the gypsum board is placed along the glass wool. As discussed in paragraph 4.3.1, the pressure induces a non-intentional air gap around the calibrated hole. It is however not possible to observe the shape and the size of this air gap, and difficult to predict it.

On the third configuration, the upstream junction is similar to the downstream one, with two circles of glue to maintain the glass wool against the gypsum board. One should note however that it is difficult to guarantee the absence of air gap. As shown in Figure 6.1, the air can pass over the circles of glue, at least the first one and enter the glass wool through a larger surface area. Even gluing the

whole junction surface wouldn't prevent the appearance of a small air gap between the first glass wool fibers glued to the gypsum board and the rest of the glass wool. This is mostly a problem for the upstream junction where the air flow is pushing the glass wool away from the gypsum board, unlike the downstream junction where the glass wool is pressed against it.

Although they are fairly realistic, these configurations do not aim at representing real wall assemblies. They have been chosen to ensure good conditions for the experimental investigation and differ from a usual timber frame wall assembly in several points:

- The airtightness defect, a 2 cm diameter hole, is not commonly found in real buildings. There are through holes on airtight layers of timber frame walls, such as the one induced by an electrical outlet, but the equivalent leakage area is usually smaller. This dimension was chosen for practical reasons: the flow rate is higher for a given pressure, which improves the accuracy of its measure; the air velocity near the hole is smaller, which decreases the turbulence chances and prevents the fluorescein micro-particles to be all filtrated by the glass wool in this critical area; and for the optical diagnostic by PIV (Particle Image Velocimetry) a larger inlet also enables to have several velocity vectors calculated along it. The round shape was chosen to ensure an axial symmetry.
- Gypsum boards are usually used only on the interior side of the building since it is not weather resistant. Particle boards such as OSB are often used for the exterior side, but for this study focused on the air transfer, any airtight layer has the same behavior, and it was easier to use a single material.
- The wall assembly is usually more complex, as described in paragraph 2.3.1, with very often at least a vapor barrier between the gypsum board and the insulation material. For this study, any air barrier would have stopped the air transfer, unless it is pierced as well. However, as mentioned above, the gypsum boards represent any airtight layer including an air barrier.

The infinite number of different existing wall assemblies and airtightness defects would anyway prevent from getting results directly applicable to any building. As mentioned above, the aim of this study is to provide and compare experimental techniques to validate numerical models that can later be applied to any particular configuration.

### **6.1.2. Numerical study**

In this chapter, each experimental technique is compared with the results of a numerical study carried out on COMSOL Multiphysics®. The simulation parameters and boundary conditions are illustrated in Figure 6.2, and detailed respectively in Table 6.1 and Table 6.2. The model used for the configurations 1 and 2 is *Free and Porous Media Flow*. The flow is described by the Navier-Stokes equation in the air gap region and the Brinkman equations in the porous region which is similar to the Darcy law but with an additional term to account for transitional flow between boundaries. For the 3<sup>rd</sup> configuration the flow is only flowing through the porous medium and the model *Darcy's Law* is therefore adequate [77].

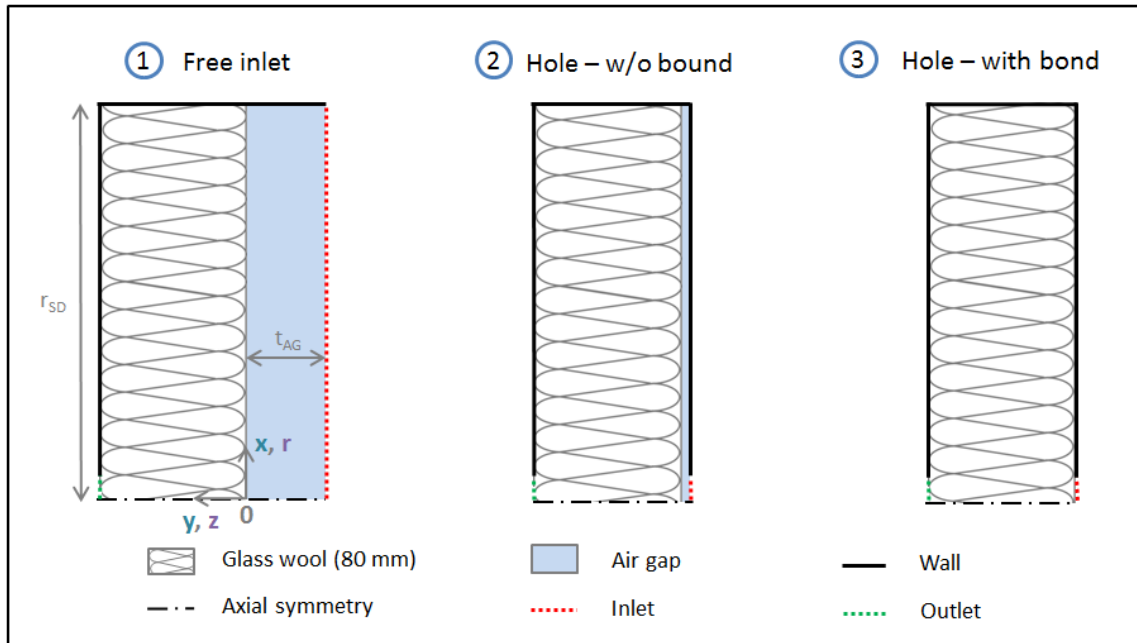


Figure 6.2 - Reference test configurations for the numerical study

Table 6.1 – Numerical study parameters

Parameters	Free inlet	Without bond	With bond
COMSOL model	Free and Porous Media Flow		Darcy's Law
Glass wool	Compressed HPGW (density ratio of 67%): - Porosity: 0.99 - Air permeability: $1.09 \cdot 10^{-9} \text{ m}^2 (\perp)$ ; $2.57 \cdot 10^{-9} \text{ m}^2 (/ /)$		
Air	Properties taken at 20°C: - Density: $1.20 \text{ kg/m}^3$ - Dynamic viscosity: $1.83 \cdot 10^{-5} \text{ kg/m/s}$		
Radius of the simulated domain ( $r_{SD}$ )	0.67 m	0.35 m	
Air gap thickness ( $t_{AG}$ )	100 mm	1 mm	-
Inlet velocity ( $v_{in}$ )	$6.0 \cdot 10^{-4} \text{ m/s}$ ( $3.0 \text{ m}^3/\text{h}$ )	$2.21 \cdot 10^{-4} \text{ m/s}$ ( $2.5 \text{ m}^3/\text{h}$ )	$2.47 \cdot 10^{-4} \text{ m/s}$ ( $2.8 \text{ m}^3/\text{h}$ )
Inlet fluorescein concentration ( $C_0$ )	30 mg/h		

Table 6.2 – Numerical study boundary conditions

Boundary	Air flow	Fluorescein concentration
Inlet	$v = v_{in}$	$C = C_0$
Outlet	$P = P_{ext} = 1 \text{ atm}$	$-\vec{n} \cdot \left( \frac{\partial C}{\partial r}, \frac{\partial C}{\partial z} \right) = 0$
Wall	Zero velocity (no slip) : $v = 0$	Zero flux: $-\vec{n} \cdot \left( \frac{\partial C}{\partial r}, \frac{\partial C}{\partial z} \right) = 0$

The implemented geometry is 2-D axisymmetric, with the axis of symmetry being the line between the inlet and the outlet holes. The radius of the simulated domain  $r_{SD}$  is 0.67 m for the free inlet configuration, which enables to have an inlet area equivalent to the experimental one (2 m x 0.7 m). For the configuration 2 and 3 the inlet is local (through the hole) so this dimension has no required value, as long as it does not restrain the air flow dispersion. It is set at 0.35 m, which is the distance between the hole and the closest APIE box wall for the experiment.

The diameter of the hole is the same as for the experiment: 20 mm in diameter. For the first configuration, the air gap thickness  $t_{AG}$  is 10 cm. As mentioned previously and demonstrated in paragraph 6.2.3, this dimension has no impact on the results as long as it is greater than 2 cm. The configuration 2 is the most difficult to model since the glass wool behavior under the pressure is not well known. As a first approximation the absence of glue is translated into a 1 mm thick air gap. The glass wool is modeled by a homogeneous porous medium characterized by its porosity and air permeability. Since only the air and fluorescein transfer are simulated, the gypsum boards are not modeled: they are equivalent to a 'wall' boundary condition. The density and the dynamic viscosity of the air are taken at 20°C.

At the inlet Dirichlet (first order) boundary conditions are imposed. The inlet velocity  $v_{in}$  has no impact on the air dispersion and therefore on the normalized velocity profiles presented in the next paragraphs. It is however a parameter of the filtration model for the fluorescein tests and is therefore set at the experimental values measured for this technique. The inlet fluorescein concentration  $C_0$  is set at 30 mg/h which is the theoretical production from the fluorescein generator. This value has however not been experimentally checked and there is a deposition of particles in the pipes and the APIE box walls difficult to quantify. As a result, only relative concentrations are presented in this chapter, and the value of  $C_0$  is therefore not relevant.

For the air flow, Dirichlet boundary conditions are imposed at the outlet and along the wall. At the outlet the pressure is set to 1 atm, and along the walls the velocity is set to zero (no-slip condition). Concerning the fluorescein transport, the concentration at the outlet of the wall assembly is not known a priori, a Neumann (second order) condition is therefore imposing a zero gradient for the diffusive term. The same condition applies for the walls, but since there is no velocity at this boundary, the convective term will also be equal to zero which leads to the particles conservation within the simulation domain.

Some detailed results of these simulations are presented in Appendix G with both the streamlines to visualize the air dispersion and the relative fluorescein concentration fields. In the next paragraphs they are compared with the various experimental results.

## **6.2. Air inlet and outlet identification with IRT and PIV**

For the investigation of the air path inside a wall assembly, a first step is to identify the air inlets and outlets. Regarding to the three configurations previously presented, only the first one is of interest to this end since the configuration 2 and 3 have well defined inlets and outlets. In this paragraph two experimental approaches are presented. The first one is the infrared thermography that is commonly used on-site to detect, inter alia, air leakage in the building envelope. The second one is the particle image velocimetry which is a laboratory technique to obtain a flow velocity field.

### 6.2.1. Infrared thermography

#### Measurement principle

Infrared thermography (IRT) is a common tool for building envelope diagnostics. A camera detects infrared energy emitted and reflected by the envelope and converts it into temperature to produce images called thermographs. It has the advantage of being non-destructive, non-intrusive and is popular for a large range of applications even within the building sector, including the detection of air leakage but also thermal bridges, the settling or lack of insulation materials, excessive heat loss areas or problems with the electrical and mechanical installations. IR cameras started to be commercialized in the late 1960s and several approaches for thermographic inspections have been developed since then. A state-of-art for the building application was proposed by Balaras et al. [64] and more recently by Kylili et al. [63].

One limitation of this technique is the fact that it only gives the surface temperature of the studied object. It means that in this study it can only be applied to detect the air inlets and outlets of the wall assembly. As a result, configurations 2 and 3 are not relevant to study, since the air is entering and exiting the wall through the calibrated holes.

#### Description of the tests

We have therefore carried out tests on the first configuration, with however the opposite flow direction. As discussed in paragraph 4.3.3, the flow direction does not have a significant impact on the air dispersion for pressure below 300 Pa. The warm air infiltrates through the hole and the dispersion at the outlet of the glass wool is visualized. As shown in Figure 6.3 the case with only one glass wool layer was first studied, and then with two layers at two different compression levels (67% and 50%). A grid is placed on the downstream side of the glass wool to avoid a displacement of the building components and to maintain a glass wool compression level. The metal grid has however a different emissivity than the glass wool and is therefore visible on the thermographs.

The downstream part of the APIE box is not assembled so that the camera can be positioned far enough from the wall to capture a 70 cm square (width of the tested wall). The model of the infrared camera is FLIR E60bx with a resolution of 320 x 240 pixels, a thermal sensitivity inferior to 0.045°C and an accuracy of  $\pm 2^\circ\text{C}$ .

A convection heater is placed in the upstream side of the box, and heats in a few seconds the air volume up to 45°C and then automatically stops. This increase in temperature has an impact on the pressure inside the box. At a constant volume of 1.4 m<sup>3</sup>, a 20°C step of temperature (from 20°C to 40°C) induces an additional pressure of almost 7000 Pa. In order to not destroy the sealing between the wall assembly and the APIE box, an opening is manually controlled during the test to stay below 300 Pa of relative pressure with the ambient air. However after reaching 45°C the warm air infiltrating the wall is slowly replaced by colder compressed air and since there is no way to turn the heater up again without opening the box, the temperature inside the upstream box is decreasing during the test.

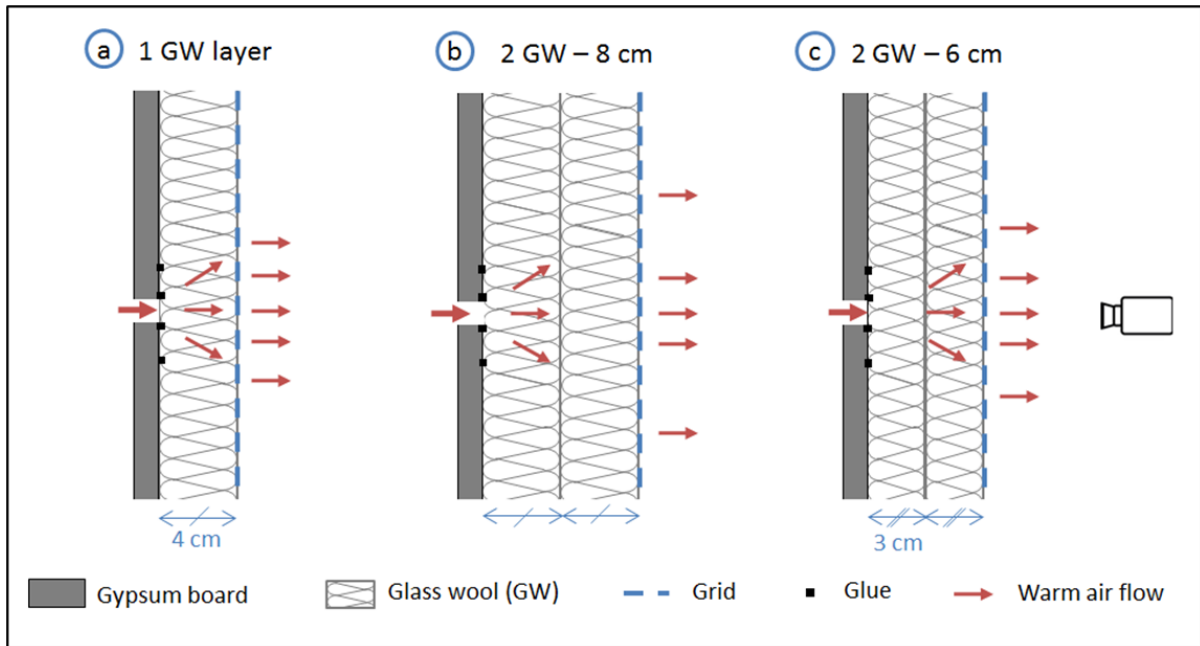


Figure 6.3 – Tested cases for the infrared thermography study

## Results

One difficulty of this experimental approach is that the temperature pattern is constantly evolving, and in a way that depends on the wall assembly, as illustrated in Figure 6.4. It raises the question of how to compare two different tests. As a matter of fact, from the moment the heater is tuned on ( $t_0$ ), it takes some time for the air flow to warm up the building components. A warm area (WA) is visible after  $t_1=15$  seconds for the 1 layer test, but about 40 seconds are necessary for the 2 layers cases before the external surface of the glass wool starts to heat up. The WA is then growing since the lower warm air flow rates far from the center of the hole take more time to warm up the glass wool. In the meantime, the temperature in the center reaches a maximum at  $t_2$  before decreasing since the air flow itself gets colder. In the same way as for the heating process, the lower flow rates away from the center take more time to cool down the glass wool which results in higher temperatures at the extremities of the WA.

This phenomenon as well as the conduction transfer explain why there is no real stabilization possible for the temperature patterns but after a certain time ( $t_3$ ) the size of the WA is increasing much more slowly. The measurements are made on the last images of the tests ( $t_{end}$ ) but the results would be similar for  $t=t_3$ .

The values of these specific times characterizing each test are presented in Table 6.3, the corresponding images for the test a) are shown in Figure 6.5 and the results of the three tests at  $t=t_{end}$  in Figure 6.6. A circle is drawn around each WA to measure its size. The accuracy is not very high since WA are not perfectly circular and the temperature has no spatial discontinuity. One can however clearly see that the addition of a second GW with the same compression (4 cm/layer) is increasing the air dispersion. The measured WA diameter increases from 26 cm to 34 cm, which multiplies the surface by 1.7.

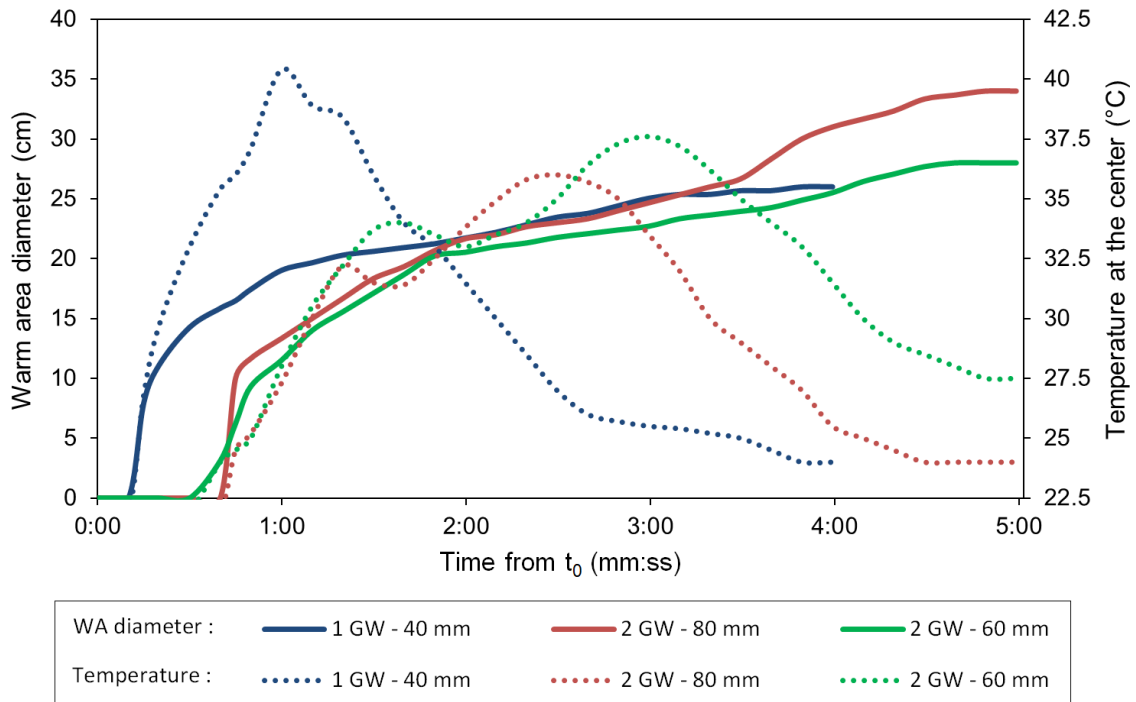


Figure 6.4 – Warm area diameter and temperature at the center plotted against time for the three tests

Table 6.3 – Characteristic times of the IRT tests

Test	$t_0$ (start of heating)	$t_1 - t_0$ (WA appearance)	$t_2 - t_0$ (max. temperature)	$t_3 - t_0$	$t_{end} - t_0$ (end of test)
1 GW	1 min	15 s	58 s (40°C)	3 min	4 min
2 GW – 80 mm	1 min 30	45 s	2 min 30 (36°C)	4 min 30	5 min
2 GW – 60 mm	30 s	40 s	3 min (38°C)	4 min 30	5 min

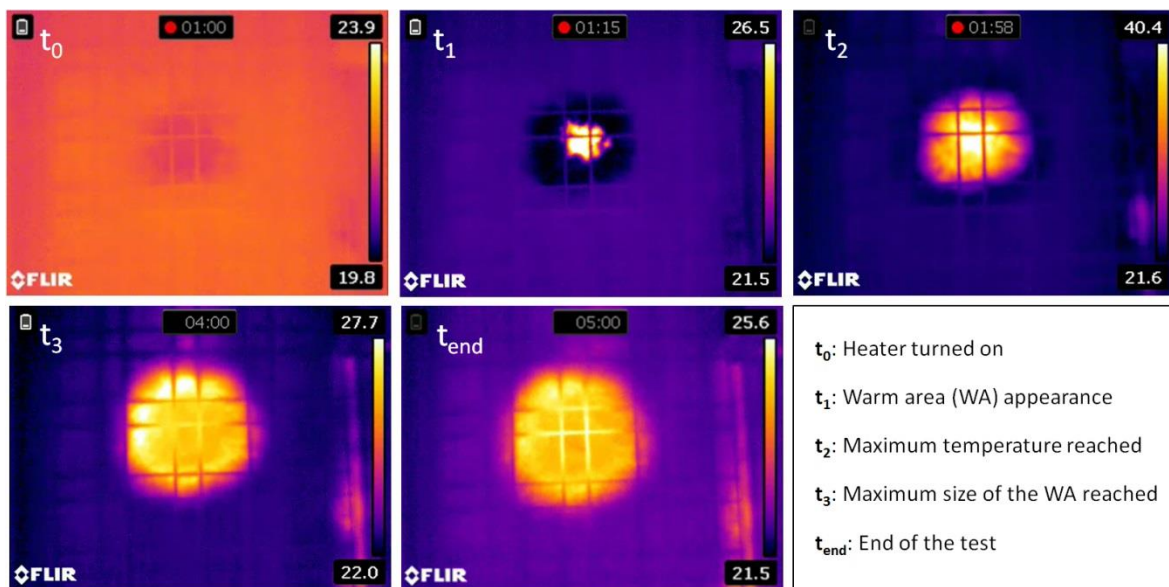


Figure 6.5 – Results of the test a) at the characteristic times

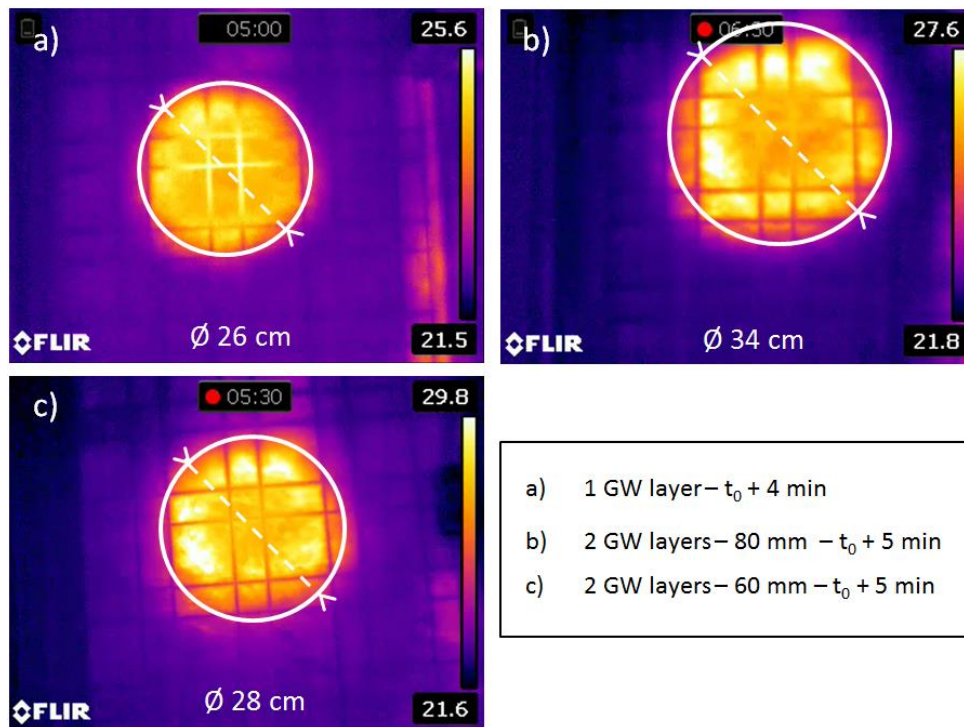


Figure 6.6 – Results of the IRT tests at  $t=t_{end}$

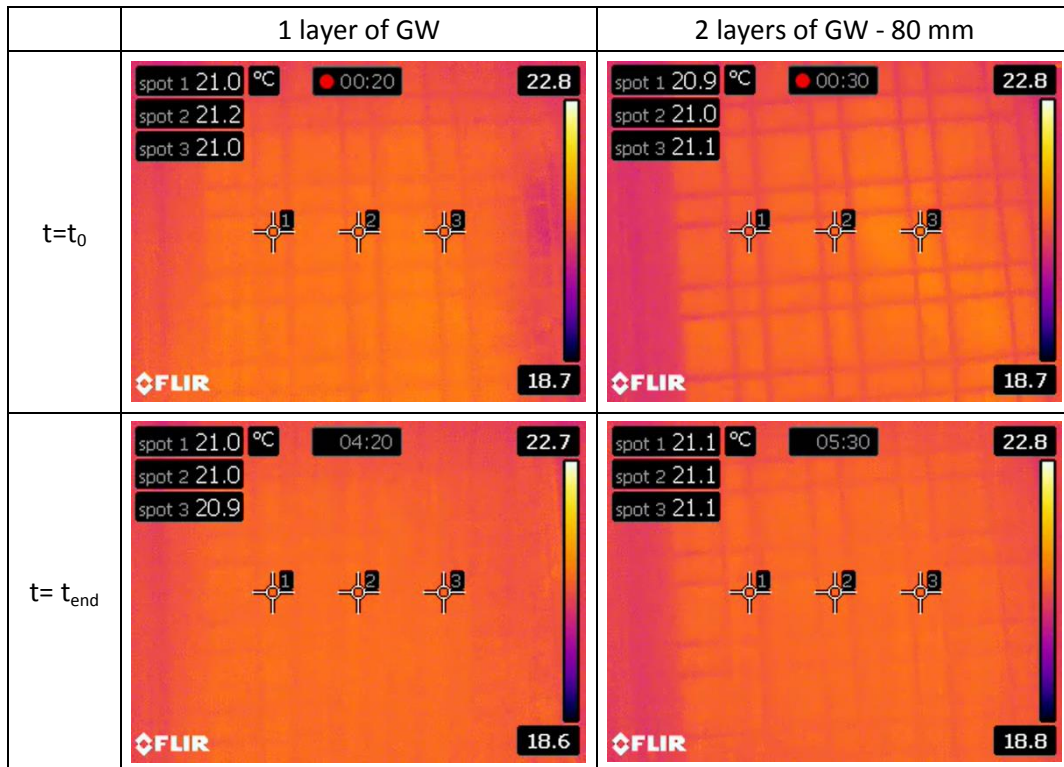
The compression of these two GW layers is significantly reducing this difference since the WA diameter equals to 28 cm. This can be partly explained by the reduction of the total GW thickness, but not only since a 60 mm thickness is in the middle between case a) (40 mm) and case b) (80 mm), whereas the resulting WA diameter is closer to case a). The reason may be that the high compression reduces the possibility of an air gap induced by the pressure between the two GW layers but also between the gypsum board and the GW. It has indeed been mentioned in paragraph 5.1 that the glue between these two components does not guarantee a perfect surface contact under high pressure.

In order to verify that the temperature measurements are due to the convection flow and not the conduction through the wall assembly layers, two additional tests are carried out with the calibrated hole sealed with tape. The results are presented in Table 6.4. One can see that for the two configurations with respectively one and two layers of glass wool, the surface temperature at the three monitored points remain the same at  $t_0$  as at  $t_{end}$ . It means that during this time the heat transfer by conduction from the warm upstream side of the box to the ambient air is not significant compared to the convection induced by the infiltrating air flow. However this does not guarantee that there is no significant conduction between the WA and the surrounding glass wool at the ambient temperature. This is a potential limitation of this method for direct conclusions on the air dispersion, but it can be taken into account in coupled heat and mass transfer simulations.

The full results of the three IRT tests are presented in Appendix H with one image every 30 seconds.



Table 6.4 – Results of conduction tests on the wall assemblies with a sealed hole



### Conclusion

Infrared thermography tests are easy to implement, quick to perform and give conclusive results for the airtightness defects detection. IRT is therefore a good tool for a global characterization, but as mentioned before there are some limitations for a precise air infiltration area measurement. The air transfer is studied through the heat transfer which raises two main concerns: the thermal inertia and the conduction. Because of thermal inertia it takes time for the warm infiltrating air flow to heat up the glass wool so the longer one waits for the measurement the better. But on the other hand the longer one waits, the more conduction transfer may become significant.

These issues also apply for the air path study inside the wall assembly with three-dimensional grids of thermocouples presented in paragraph 6.3.

### 6.2.2. PIV

#### Measurement principle of PIV

The PIV (Particle Image Velocimetry) is a non-intrusive technique that enables to get the velocity field of the flow. As explained in Figure 6.7, a double-pulsed laser is illuminating the flow seeded with micron-sized particles. Two pulses at a small time interval  $\Delta t_p$  are required for each measure, and a CCD camera placed perpendicularly to the laser sheet is capturing each light pulse in separate image frames. The images are then divided into small rectangles called interrogation areas, and in each of them the most likely average displacement of the tracer particles is calculated by cross-correlation. By dividing this displacement by  $\Delta t_p$ , a velocity vector is calculated for each interrogation area, which results in a velocity vector map.

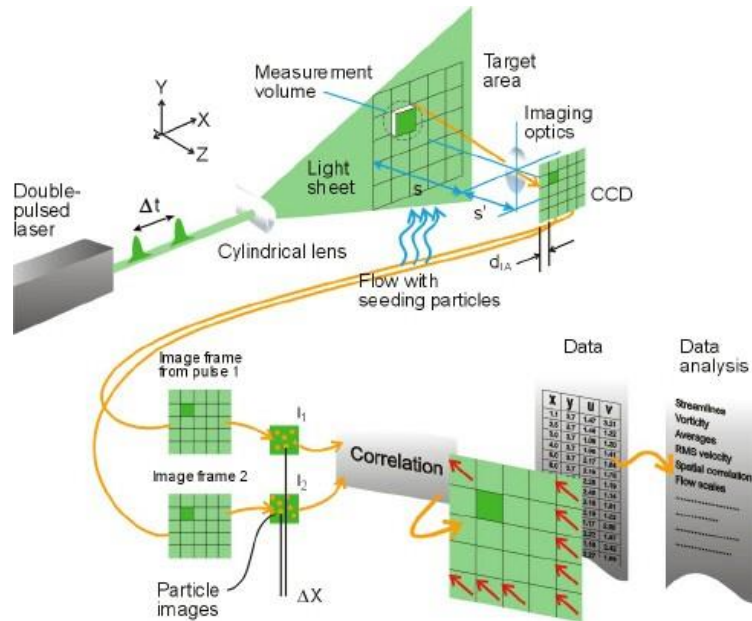


Figure 6.7 - Measurement principles of PIV (Source: DantecDynamics)

There are more complex PIV setups enabling for example to produce three-dimensional vector fields [158], or to measure simultaneously the velocity and the temperature of the flow [159]. However, for our rather simple configuration with an axial symmetry, a two-dimensional study as described above is appropriate.

In order to guarantee the success of the technique, a number of parameters have to be chosen carefully, such as the tracer. The particles have indeed to be small enough to follow the flow but big enough to reflect the laser light, have a density similar to the fluid to avoid sedimentation, not react with the fluid and the surrounding materials, be easy and cheap to produce, etc. For this study we have chosen olive oil particles produced by the Liquid Droplet Seeding Generator (10F03), with a droplet size range of 1-3  $\mu\text{m}$ . This is an usual tracer for PIV applied to air flows [160]. The density of olive oil is between 800 and 920  $\text{kg/m}^3$  which is much higher than the air, but since particles can hardly be as light as air, it is the small size of the particles that prevents from sedimentation.

The camera was placed at a distance of about 1 meter so that the particles were about 2 pixels large. During the acquisition, the time between two pulses  $\Delta t_p$  was also adjusted so that the particles had a displacement between the two frames under 4 pixels which corresponds to 25% of the interrogation area size (16 x 16 pixels, 25% of overlap).

### Description of the tests

The PIV is therefore an alternative to infrared thermography since it also enables to visualize the air inlets and outlets of a wall assembly. It has been used in the building sector such as for the identification of air flow patterns in rooms ([161], [162] and [163]), or ventilated façades studies [164], but to our knowledge there hasn't been studies for the air path in wall assemblies application yet.

Unlike IRT, only the upstream side of the wall can be studied with PIV. The particles are indeed too big to go through a few centimeters of porous insulation without being filtrated, which means that the flow would not be seeded properly for a visualization of the downstream flow.

The various tests are described in Figure 6.8, with two main cases: a free air inlet and a restricted one through calibrated hole(s). There are two 20 mm diameter holes on each gypsum board ( $I_1$  and  $I_2$  for the air inlets,  $O_1$  and  $O_2$  for the air outlets), with a distance of 150 mm between them. They can be open or sealed with tape depending on the test. A list of every test carried out is presented in Table 6.5 with the corresponding acquisition parameters.

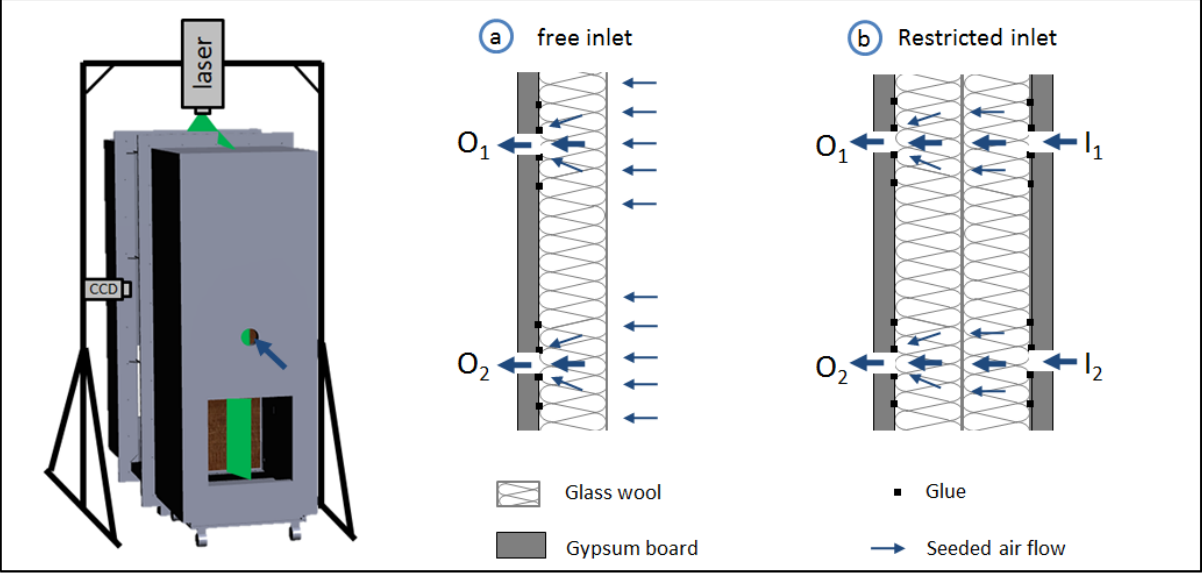


Figure 6.8 - Tested cases for the PIV study

Table 6.5 – Air inlets out outlets for the PIV tests

	Test	Inlet	Outlet	$n_{ppi}$	$f_{acq} (s^{-1})$	$t_{acq}$
Free inlet	$a_1$	-	$O_2$	500	2	4 min 10
	$a_1'$			200	3	1 min 07
	$a_2$		$O_1$	500	2	4 min 10
	$a_3$		$O_1, O_2$	600	2	5 min
	$a_3'$			500	2	4 min 10
	$a_3''$			200	3	1 min 07
Restricted inlet	$b_1$	$I_2$	$O_2$	200	3	1 min 07
	$b_2$	$I_1$				

For each test, the oil particles are first introduced in the upstream side of the APIE box. Once they are well mixed with the air with a homogeneous spatial concentration, an air flow is introduced to maintain a pressure difference of 300 Pa between the two sides of the tested wall and the acquisition starts. A certain number of pairs of particle images  $n_{ppi}$  are captured at the frequency  $f_{acq}$  (pairs of particle images per second), which corresponds to an acquisition time  $t_{acq}$  before the air flow is turned off.

The tests  $a_1$  and  $a_3$  are carried out respectively twice and three times for a repeatability study, with various acquisition times. Two tests ( $a_1'$  and  $a_3''$ ) had smaller number of images and higher

acquisition frequency to prevent the particles to agglomerate on the first millimeter of the glass wool, which could modify the flow behavior. The other tests were then carried out on a longer time to get more proper results, and as discussed below there was no visible change in the flow behavior near the wall assembly.

An example of a particle image from test  $a_1$  is shown in Figure 6.9. The focus of the camera is made on the center between the two holes. The extremities of the image are a somehow fuzzy which makes the particle tracking difficult. The cross-correlation analysis is therefore carried out on a smaller 405 mm x 130 mm rectangle, with the left hand side corresponding to the contact between the air and the wall assembly. Each pair of images gives an instantaneous velocity field, and an average between the  $n_{ppi}$  images is then calculated. Each vector represents the velocity in a 4.3 mm x 4.3 mm interrogation area. From this average, profiles of the y component of the velocity vector ( $U_y$ ) are plotted for several distances from the glass wool. The planes  $p_1$ ,  $p_2$ ,  $p_3$  and  $p_4$  are respectively 7 mm, 11.3 mm, 15.6 mm and 20 mm away from the wall assembly.

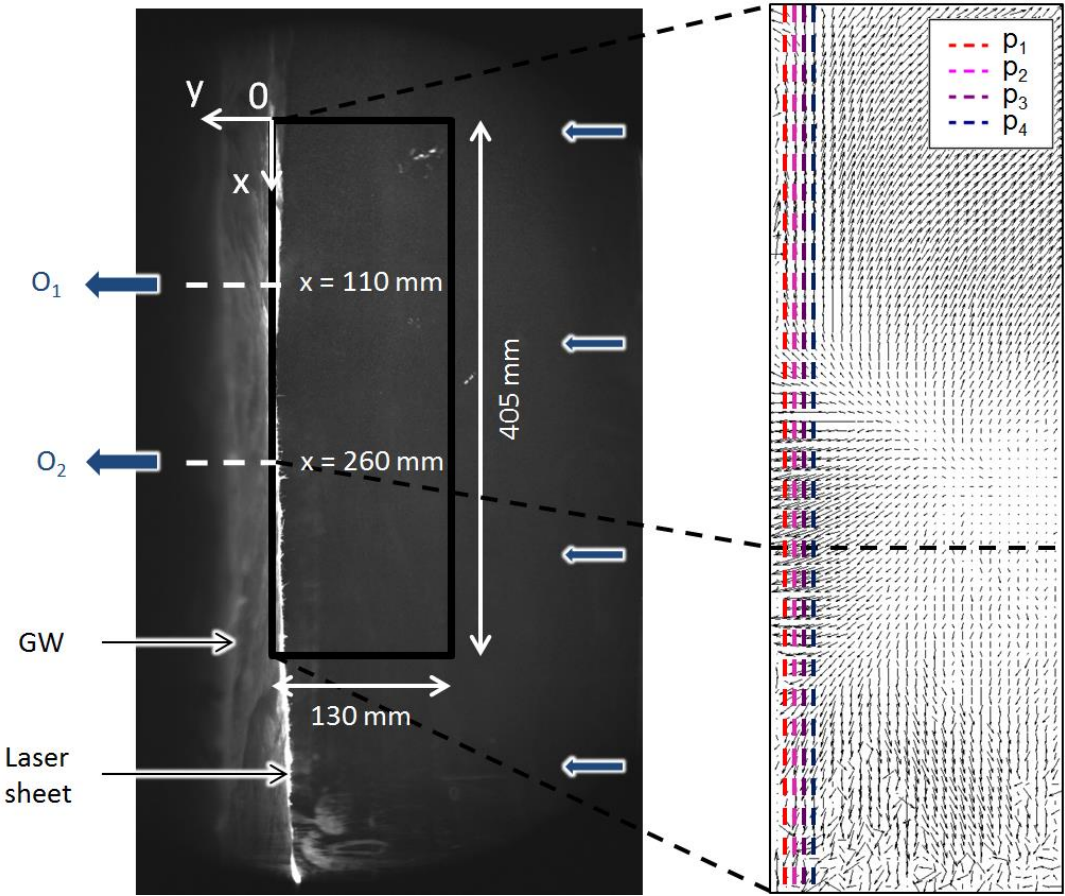


Figure 6.9 – Analysis of PIV results: from the row image to the velocity vector field (test  $a_1$ )

The studied section of the wall assembly is located on its lower part to avoid confusion with the air flow entering in the APIE box halfway up. Preliminary tests have shown that the straight air flow was impacting the wall assembly and was then moving along it with high velocities, which was a problem to visualize the infiltrating flow. In order to break this air jet, a 15 cm x 15 cm airtight cardboard was placed right after the inlet so that the air was impacting on it before flowing around it. However the

inconvenient is that this discontinuity is creating turbulence in the upstream side of the APIE box. As a consequence the instantaneous vector fields taken one by one do not always give clear tendencies. Results averaged on a large number of images are more interesting to analyze, but one can see that the velocity profiles presented below are not very smooth because of this turbulence.

**Free inlet results**

The first tests carried out correspond to the configuration 1 (free inlet) described in paragraph 5.1. There is no gypsum board on the upstream side of the wall assembly, but there is one on the downstream side with two 2 holes ( $O_1$  and  $O_2$ ) 150 mm away from each other. The laser sheet is aligned with the center of these two 20 mm diameter holes so that the infiltrating air flow can be visualized. The results are presented in Figure 6.10. One should note that given the large area studied, it is difficult to have a proper focus of the camera on the whole x range. For the tests  $a_2$  and  $a_3$ , the area far from the hole ( $x > 350$  mm) was out of focus and is therefore not displayed here but it is shown in Appendix I.

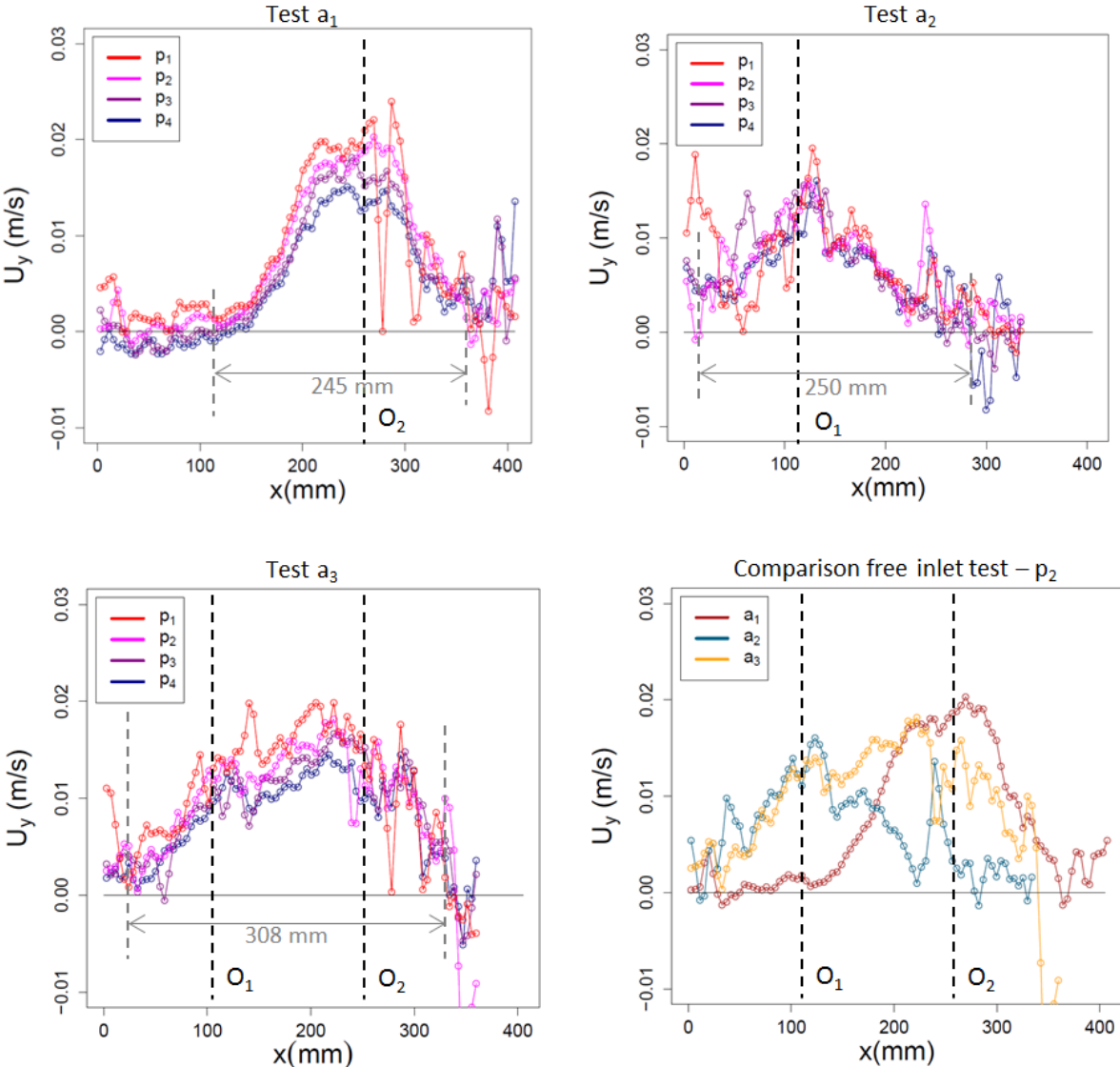


Figure 6.10 – Results of the free inlet PIV tests with various air outlets

One difficulty of these tests with a free inlet is that it is hard to have a perfectly straight and flat glass wool in the vertical direction. As shown in Figure 6.9, the first line of velocity vectors is not plotted because it corresponds to points that are mostly on the glass wool where oil particles cannot be tracked. Even the line corresponding to  $p_1$ , 7 mm away from the border of the analyzed area, presents many discontinuities that may be due to the presence of glass wool fibers. This is the reason why the results are compared for  $p_2$  in the last graph.

On the first test  $a_1$  with only the hole  $O_2$  open, the velocity profiles are Gaussian shaped and centered at the height of  $O_2$  with the velocity  $U_y$  reaching 2.5 cm/s. Near the hole ( $x \in [100 ; 350]$ ), the closer to the glass wool, the higher the velocities. On the other hand, at the extremities of the Gaussian, the velocities are close to zero for  $p_1$  and  $p_2$  but tend to be negative further from the glass wool which characterizes an impinging area with no (or few) infiltration. This is more easily visible on the upper part corresponding to the left-hand side of the graph ( $x < 100$ ). The right-hand side ( $x > 350$ ) is indeed smaller due to the decentered position of  $O_2$ , and the extremity was already slightly out of focus which induces higher uncertainties.

The second test  $a_2$  is similar but with the upper hole  $O_1$  open. The maximum velocity in the  $y$  direction is also slightly above 2 cm/s but the Gaussian is not as clearly visible which can be due to vortices near the area of interest during the acquisition. The right-hand side of the hole on the graph ( $x > 110$  mm) shows however a clear decrease of the velocity until oscillating around zero.

The test  $a_3$  with both holes open seems to be roughly equivalent to the addition of the two previous tests  $a_1$  and  $a_2$ . This is visible on the last graph comparing the velocity profiles along the plane  $p_2$ . For  $x < 120$  mm the velocity  $U_y$  was close to zero for the test  $a_1$  and the values are very similar for  $a_2$  and  $a_3$ . In the area impacted by the opening of both holes, between 120 and 260 mm, the velocity for  $a_3$  is higher than both  $a_1$  and  $a_2$  but is however under an addition of them. Finally for  $x > 260$  mm, the velocity for  $a_2$  is close to 0 and the two other profiles are close to each other, even though  $a_3$  has more oscillations and is slightly under  $a_1$ . This is an expected result since the tests are carried out at the same pressure of 300 Pa: if the holes were distant enough from each other, the air flow rates due to each hole separately could be added. However since there is an interaction area ( $x \in [120, 260]$ ) the flow rate in this area is lower than the addition of the individual ones.

For each test the size of the air infiltrating area is evaluated by marking where the velocity profiles at  $p_2$  crosses  $x=0$  on both sides of the Gaussian curves. This is a good indication of where most of the air flow is infiltrating but one should note that it does not mean no air is infiltrating outside of this area. The accuracy of the PIV velocity measurements is very hard to quantify but the discontinuities and oscillations in the profiles due mainly to the flow turbulence and the slightly out-of-focus areas make it difficult to differentiate a zero velocity from low ones. It seems therefore possible that the air is entering through a larger area at low velocities.

The repeatability of these measurements is investigated for test  $a_1$  and  $a_3$  with respectively one and two additional tests under the same boundary conditions. The aim is two-fold: to evaluate if repeating the exactly same test changes the results but also to check if there is an agglomeration of oil particles with time on the glass wool that could modify the air flow. The results are presented in Figure 6.11 for  $p_2$ . The velocity profiles of  $a_1$  and  $a_1'$  are very similar even though  $a_1'$  has more discontinuities due to a shorter acquisition time (1'07 instead of 4'10). Similarly the three  $a_3$  tests give roughly the same results with also more discontinuities for shorter acquisition times. This means

there is a good repeatability and the flow is not impacted by the potential agglomeration of oil particles over a short time.

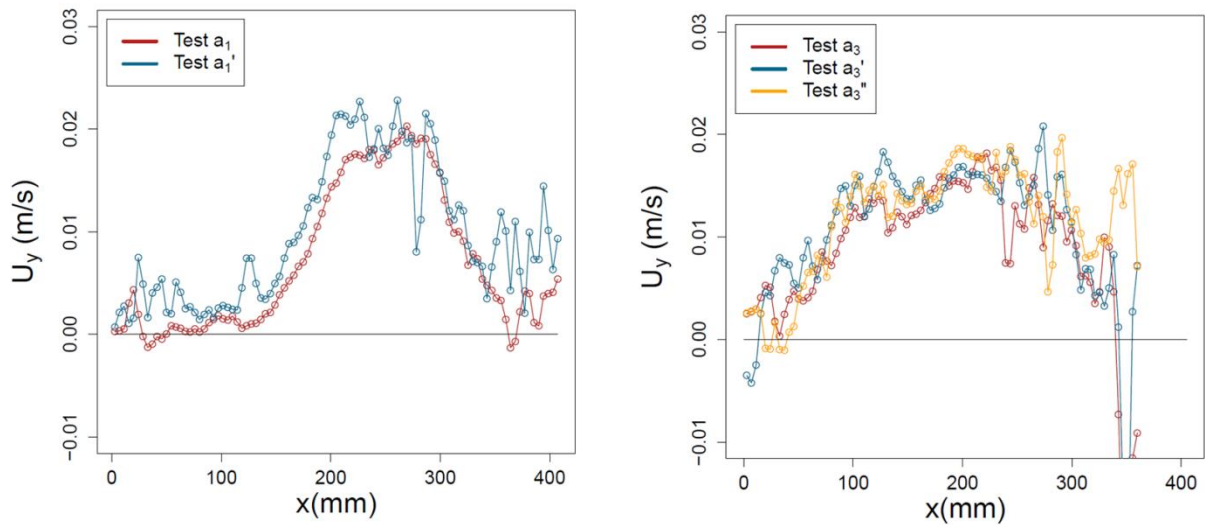


Figure 6.11 – Repeatability study on the free inlet tests a1 and a3 for various acquisition times ( $p_2$ )

### Restricted inlet results

In this second part of the PIV study, the air inlet is restricted with a second gypsum board on the upstream side of the wall assembly, as illustrated in Figure 6.12. This corresponds to the configuration 3 described in paragraph 5.1. Unlike the previous tests, the area of infiltrating air is known and controlled through the opening of  $I_1$  or  $I_2$ . The objective of this second part is two-fold:

- (1) To check the results consistency with well-defined air inlets
- (2) To test the feasibility of applying PIV to higher velocities inducing higher chances of oil particles agglomeration

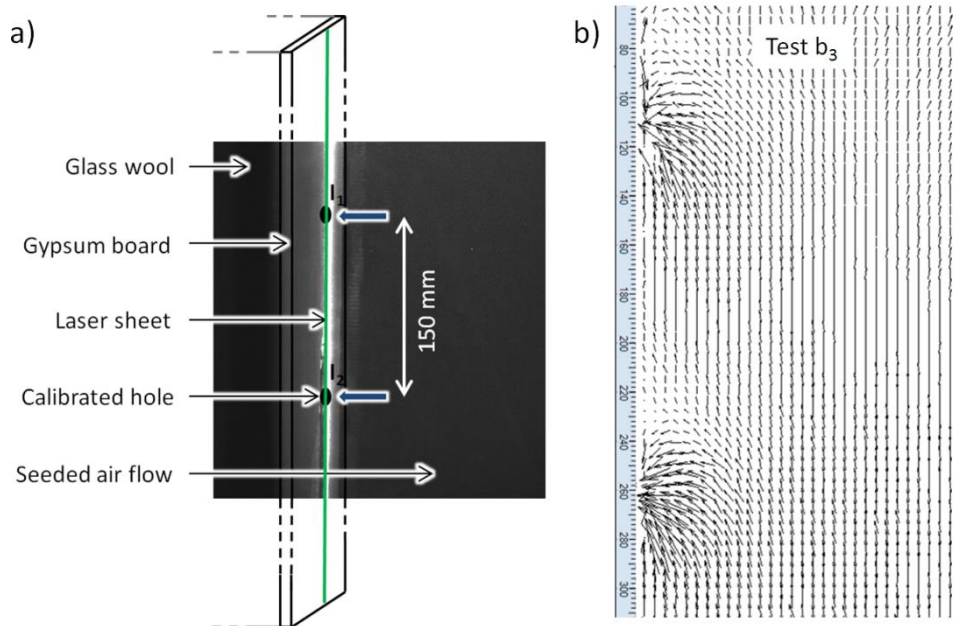


Figure 6.12 – Restricted inlet configuration (a) and vector field obtained for the test  $b_3$  (b)

The two tests are carried out with only the outlet  $O_2$  open and the inlets  $I_1$  and  $I_2$  open one after the other. The analysis is performed in the same way as for the free inlet tests, with the velocity field obtained for a 130 mm x 405 mm window, and the velocity in the y direction plotted for several distances from the wall. As one can note from the picture in Figure 6.12, the first line of vector is not relevant since it corresponds to an area too bright because of the laser sheet reflection on the gypsum board. The velocity profiles for these tests presented in Figure 6.13 are therefore also starting at the plane  $p_1$ , which is 7 mm away from the border of the analyzed area.

Concerning the objectives mentioned above, we can draw the following conclusions:

- (1) The results are consistent in the way that there is a clear peak of velocity near the inlets.  $U_y$  reaches 0.12 m/s close to the wall for the test b1 with the inlet ( $I_2$ ) in line with the outlet ( $O_2$ ) and 0.10 m/s for the test b2 with the inlet ( $I_1$ ) 15 cm higher than the outlet ( $O_2$ ). However, the peaks are larger than the diameter of the holes (20 mm). This is probably because of the distance to the inlet (7 mm for  $p_1$ ). As mentioned above, the reflection of laser light on the gypsum board prevents indeed from measurements closer to the wall assembly.
- (2) The three tests have been carried out with short acquisition times (1'07) and from the results described above, it seems that there was no particle agglomeration significant enough to modify the flow behavior. This proves the feasibility of this technique with high infiltration velocities (0.15 m/s).

Complementary results for both the free and restricted inlet tests are presented in Appendix I.

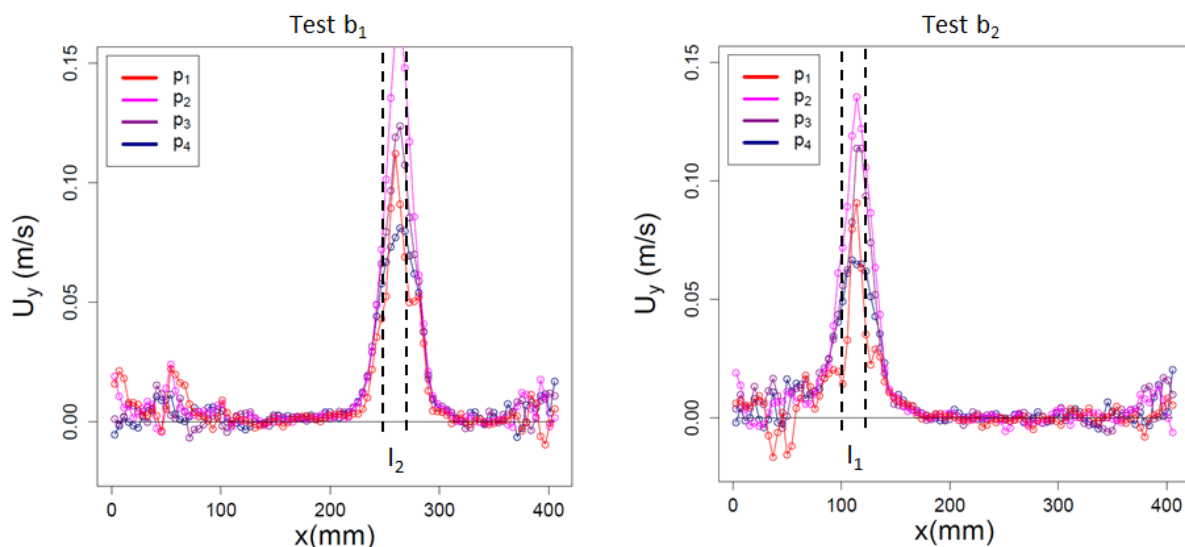


Figure 6.13 – Results of the restricted inlet PIV tests

## Conclusion

These tests carried out on two distinctive configurations show that the PIV produces conclusive results on the air inlet in timber frame wall assemblies study. It turned out to be a useful tool to identify infiltration areas and investigate the accumulation of several airtight defects. It is conceivable to implement this technique in-situ but unlike the IRT, the complex set-up makes it more appropriate to laboratory studies.



There are however several possible limitations to this technique. As mentioned before high velocities and long acquisition time increase the risk of particle agglomeration on the glass wool near the air inlet. Moreover only significant velocities compared to the surrounding flow can be measured, which can be an issue to determine the dimensions of the air infiltration area. This is also the reason why the free inlet test was performed on a single layer of glass wool: the addition of a second one was increasing the size of the air infiltration area and the velocities were getting too small to be properly measured.

It has also been mentioned that it is complicated to obtain the velocity profile in immediate vicinity of wall surface. This is a common PIV problem but it may be reduced by painting this interface in black to decrease the reflection of the laser light. However for insulation materials such as glass wool, the surface is not flat enough to prevent little fibers from obstructing partially the air flow.

Finally, it would be possible to measure the induced flow rate by integrating the velocity near the air inlet in the wall. However in this study it would not have been possible to compare it with the flow rate entering the APIE box. This is because the PIV requires an absence of sealing between the tested wall and the APIE box walls in some parts to avoid obstruction for both the camera on the side and the laser sheet on the top.

**6.2.3. Comparison with the numerical simulation**

The numerical simulation described in paragraph 6.1.2 is used for a comparison with IRT and PIV results. The ‘free inlet configuration’ with free entrance into porous insulation is chosen. Normalized velocity profiles (divided by  $v_{max}$ ) are plot at the outlet of the GW for both one and two layers compressed at 67% (4cm). The results are shown in Figure 6.14.

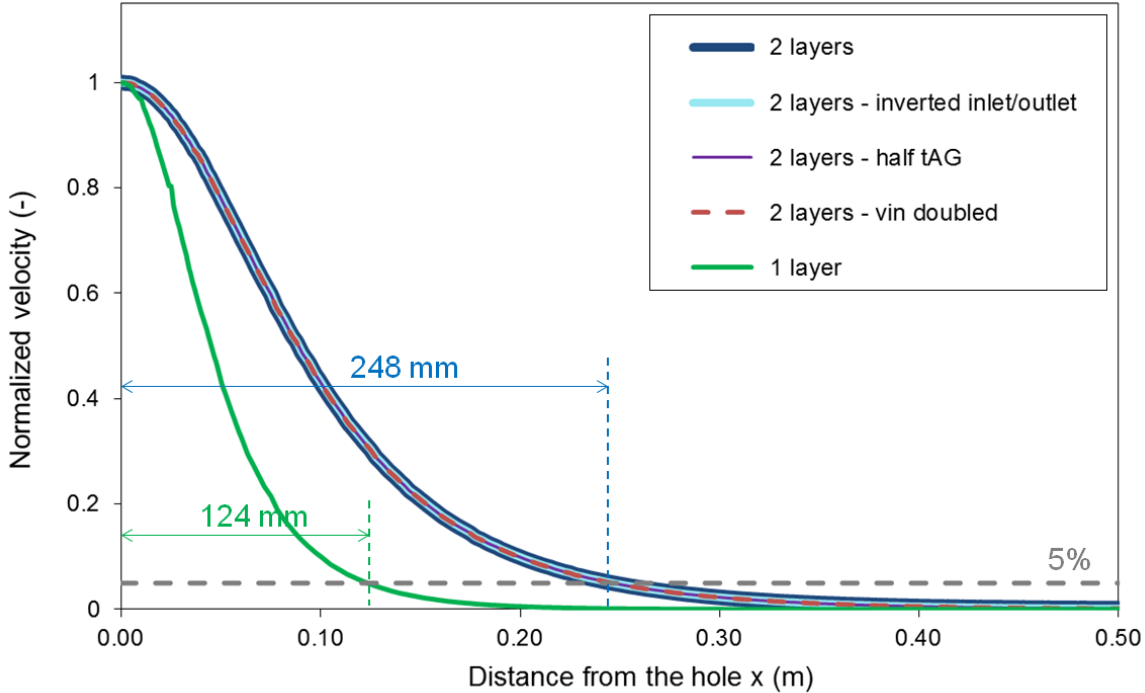


Figure 6.14 – Results of the restricted inlet PIV tests

For the two-layer case, it can be concluded that:

- (1) The direction of the flow has no impact on the simulation results, even if experimentally a difference was noted at high pressure (cf paragraph 4.3.3). This means that the same numerical results apply as a comparison for both the IRT and PIV tests with opposite flow directions.
- (2) The thickness of the air gap is taken large enough to not impact the flow behavior: reducing by half this value (half  $t_{AG}$ ) does not change the simulation results.
- (3) The inlet velocity  $v_{in}$  has also no impact on the normalized velocity profiles: doubling its value does not change the simulation results.

For a comparison with the experimental air dispersions, the distance is measured between the center of the hole and the point where the velocity drops below 10%, 5% and 1% of its maximum value  $v_{max}$ . The results are presented in Table 6.6. The experimental and numerical results for 5% of  $v_{max}$  are in good agreement for the one-layer case. However for the two-layer case the air dispersion is lower according to the IRT results than for the simulation, by 15% for 10%  $v_{max}$  and by 31% for 5% of  $v_{max}$ . As expected the dispersion is indeed twice larger for the simulation when doubling the HPGW thickness, whereas the IRT technique shows an increase of only 30%. A possible explanation is that the addition of a GW layer increases the air dispersion and therefore decreases the outlet velocities. As a result it takes longer for the low flow rates to warm up the surrounding glass wool, and if velocities are in the same order of magnitude as the one induced by natural convection around the wall, the GW is at the meantime cooled down by the ambient air.

Table 6.6 – Air dispersion diameters for 1 and 2 layers of HPGW compressed at 67%

		1 layer	2 layers
IR thermography		260 mm	340 mm
PIV		245 , 250 mm	-
Simulation	10% $v_{max}$	200 mm	400 mm
	5% $v_{max}$	248 mm	496 mm
	1% $v_{max}$	364 mm	720 mm

These results also highlight the complexity in defining the air dispersion, even in a 2D axisymmetric configuration, with a diameter strongly depending on the percentage of  $v_{max}$  taken as a limit. The simulation results show indeed that the air dispersion diameter almost doubles between 10% and 1% of  $v_{max}$ . Finally, it seems that for the PIV technique that is not based on heat transfer, the air dispersion measured corresponds approximately to the area where the velocity is higher than 5% of  $v_{max}$ . This is however not a generality since it depends on the flow pattern on the upstream air volume, as discussed in paragraph 6.2.2. The addition of a second HPGW layer was indeed reducing too much  $v_{max}$  to visualize clearly the infiltration area.

### 6.3. 3-D grid temperature monitoring

In this paragraph and the two following ones, the focus is no longer on the air inlets/outlets of the wall, but on the air path inside the wall assembly and through the insulation material. As mentioned in Chapter 2, this has been previously attempted by implementing temperature and/or humidity sensors inside the wall and study the air transfer through respectively the heat and the moisture

transfer [67]. A similar approach is followed in this study for comparison purposes. First temperature measurements within the insulation layer were performed using a three-dimensional grid, as described below.

**6.3.1. Preliminary tests**

The temperature is monitored with type K thermocouples consisting of chromel and alumel. Thermocouples are chosen over other temperature sensors because of their small intrusiveness (<1 mm in diameter). Due to its reliability, accuracy and inexpensiveness, type K is the most commonly used thermocouple. In order to verify these properties a few preliminary tests have been carried out.

**Thermocouples characterization**

60 thermocouples are placed inside a temperature-controlled bath and temperature steps of one hour are made at T=5°C, 25°C and finally 45°C, which is the maximum of the tests temperature range. Three conclusions have been drawn:

- (1) The 60 thermocouples have a good accuracy with an error below ± 0.2°C, which is not significant compared to the temperatures differences obtained in the tests described below.
- (2) The temperature measurement is stable with time: no significant variations were observed during each one-hour step, and in particular no sensor drift.
- (3) The thermocouple measurement inertia is almost inexistent: when the thermocouples are moved from ambient air to 20°C colder or warmer water, the response time was inferior to the 3 seconds acquisition time steps. This reactivity is important for the air path study with temperature steps.

**Intrusiveness study on the SAPIE box**

In addition to a good accuracy and responsiveness, a low intrusiveness is essential for the air path investigation. The sensor should indeed not disturb the flow by creating preferential air paths around it. It is difficult to quantify this parameter but as a preliminary test, 12 thermocouples were implemented in a simple wall assembly made of an airtight layer with a 20 mm hole followed by two layers of glass wool. The test was carried out in the SAPI box with an air flow passing through the wall assembly and pressurizing the upstream side of the box. The pressure was monitored while the thermocouples were pulled out one by one. The result is presented in Table 6.7.

Table 6.7 – Intrusiveness test on the thermocouples

Nb thermocouples	12	11	10	9	8	7	6	5	4	3	2	1	0
ΔP (Pa)	530	530	530	530	530	530	530	520	520	520	520	520	510

The pressure is almost constant with a decrease of 20 Pa (3.7%) over the removal process. This can be due to the thermocouple leaving a hole when removed or to the wall assembly slightly moved during the process. The best would be to be able to compare the pressure before and after the implementation of the thermocouples but there would be no guarantee that the instrumented wall assembly is positioned exactly as the not-instrumented one. However, this preliminary test with a pressure almost constant is reassuring on the low intrusiveness of the thermocouples.

### 6.3.2. Description of the tests

#### Wall assembly instrumentation

All three configurations presented in paragraph 6.1 are tested with a 3-D grid of thermocouples implemented as described in Figure 6.15. The 60 thermocouples are placed at the junction between the building components, with a distance of 5 cm between each of them. The first one (T1) is inside the upstream air volume, then respectively 21 (T2 to T22), 20 (T23 to T42) and 18 (T43 to T60) thermocouples are implemented at the junction  $J_1$ ,  $J_2$  and  $J_3$ . For a given junction, the larger the thermocouple index number, the further from the hole. In the schematic representation, the sensors are placed at the middle of the 5 cm x 5 cm square in which its number is written.

The axial symmetry around the hole is used to avoid an excessive number of thermocouples that would disturb more the air flow: the measurements are concentrated next to the hole and on its upper right side.

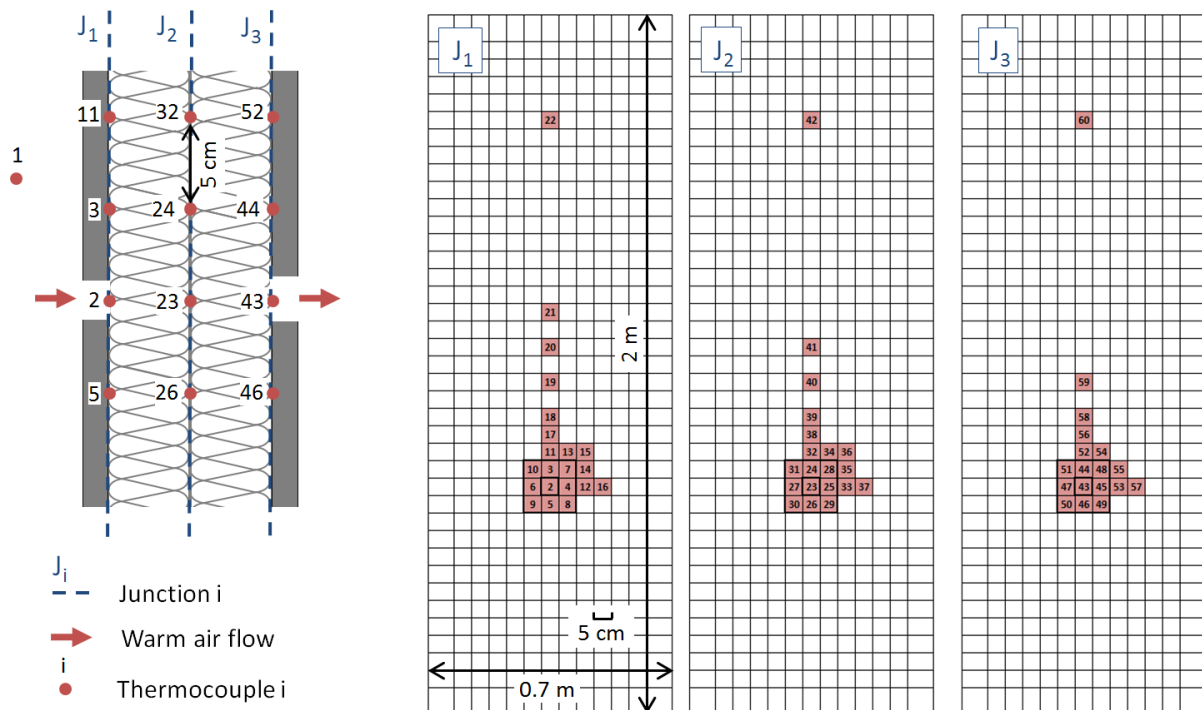


Figure 6.15 – Position of the 60 thermocouples

For  $J_1$  and  $J_3$ , the junctions between the gypsum boards and the glass wool, the thermocouples are placed against the gypsum board with tape. For the  $J_2$  junction between the two layers of glass wool, the thermocouples are attached on 0.5 mm thick straight wires inserted in the porous media as illustrated in Figure 6.16.

#### Acquisition

The 60 thermocouples are connected to a data acquisition unit Keysight 34972A which is able to read all the temperatures within 3 seconds. A LabView program was used to visualize in real time and save all the values in a text file.

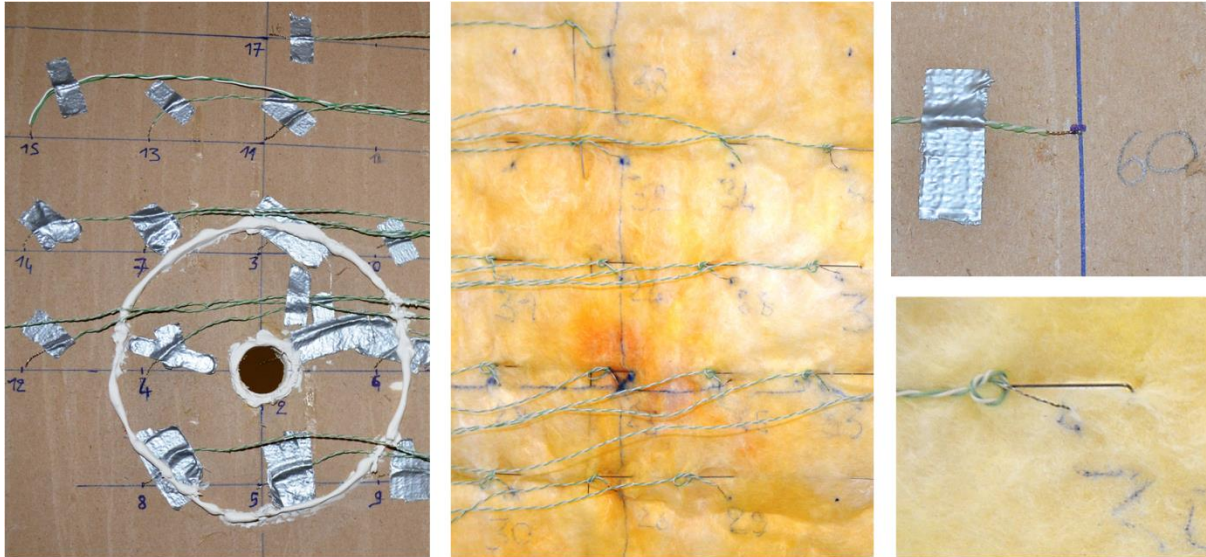


Figure 6.16 – Thermocouples fixing on the building components

An air flow rate of  $7.5 \text{ m}^3/\text{h}$  pressurizes the upstream side of the APIE box and a convection heater placed in it is turned on after the acquisition starts ( $t=t_0$ ). The heating process is the same as the one for the infrared thermography tests described in paragraph 6.2.1: the upstream air volume is heated up to  $45^\circ\text{C}$  in a few seconds and then the heater turns off by itself.

Pressurization tests on the three configurations are also carried out to characterize each wall assembly's airtightness. The results are presented in Figure 6.17, with higher air permeability for the free inlet configuration but also a significant difference between the "without bond" and "with bond" ones. A  $7.5 \text{ m}^3/\text{h}$  air flow rate is imposing a  $\Delta P$  of respectively 160, 250 and 270 Pa, but once the heater is turned on, the pressure is rising. The opening of a hole on the APIE box is manually controlled to maintain a relative pressure close to the initial one.

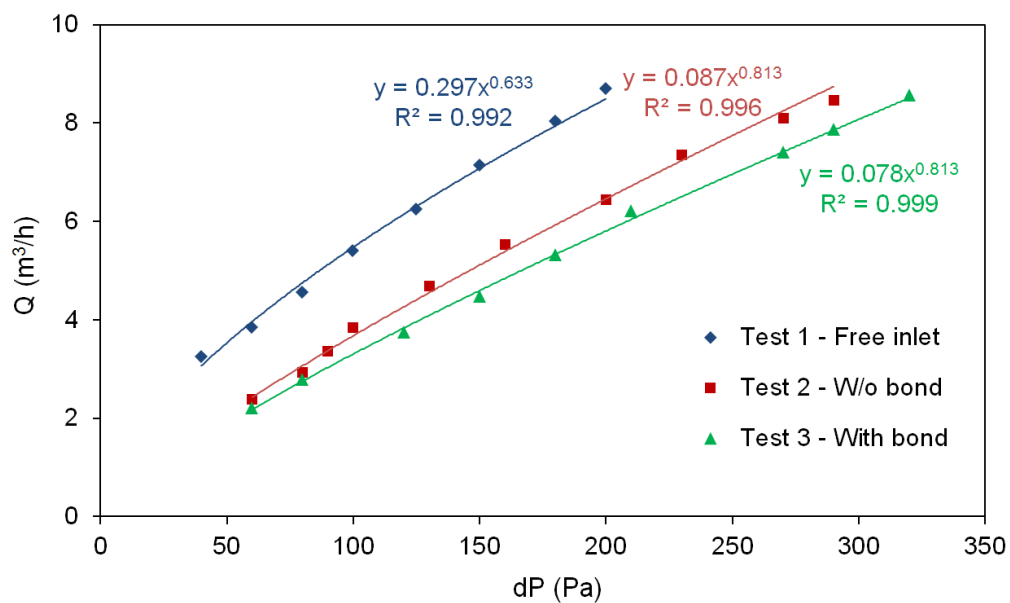


Figure 6.17 – Pressurization tests on the three configurations with 60 thermocouples

## Data analysis

The air path study through the heat transfer raises the same issues as the infrared thermography study: the thermal inertia and the conduction make the process dynamic and complicate the interpretation of the results.

The temperature values for the analysis are taken at time  $t=t_m$  corresponding to the peak recorded by the thermocouple T1 in the upstream air volume. This occurs about two minutes after the heater is turned on. This relatively short time has the advantage of reducing the impact of the heat transfer by conduction as further explained in paragraph 6.3.3. For each test, the temperature difference between  $t_0$  and  $t_m$  recorded by the thermocouple 43 at the outlet of the hole was between 5°C (configuration 1) and 15°C (configuration 3).

In order to obtain a mapping of the warm air leakage in the wall assembly, the parameter  $\Delta T_r$  (relative temperature difference) is calculated for each thermocouple  $i$  at the junction  $J_j$  as follow:

$$\Delta T_{r,i,J_j} = \frac{T_{i,t_m} - T_{i,t_0}}{\max (T_{i,t_m} - T_{i,t_0})} \quad (3)$$

With  $T_{i,t_k}$  the temperature of the thermocouple  $i$  at the time  $t=t_k$ . The maximum temperature difference (calculated for a given junction  $J_j$ ) by which each  $\Delta T$  is divided does not include the thermocouple  $T_1$  that is located in the air volume. It is usually the one obtained by the thermocouple  $T_2$  for  $J_1$ ,  $T_{23}$  for  $J_2$  and  $T_{43}$  for  $J_3$  since there are on the line between the inlet and the outlet holes.

### 6.3.3. Results

Each test is done twice to verify the repeatability, the full results of the tests are presented in Appendix J. The raw results at each junction are given for each test as well as the “averaged results” with the  $\Delta T_r$  averaged between thermocouples equidistant from the hole (considering the axial symmetry). The results for the junction  $J_3$  are not presented below since only the thermocouple facing the outlet hole (T43) was detecting a significant temperature change.

#### Free inlet

The configuration 1 with an air gap is the only one that has no acquisition at the junction  $J_1$  since there is no upstream gypsum board. The results are presented in Figure 6.18 with a dotted line representing  $\Delta T_{r,23}$  (corresponding to the thermocouple facing the outlet hole). As shown on the graph the analysis is made at  $t_m = 2 \text{ min } 15\text{s}$ , just before the temperature decreases in the upstream air volume (T1) which depressurizes this side of the APIE box and inverse temporarily the air flow direction. This can be clearly seen with T43 decreasing to the ambient air temperature for a few seconds.

It appears from the raw results that the symmetry is not perfect, with a left hand side colder than the right hand side of the hole. This is an inconvenient of having local measurements: they are subject to the flow local variations and to the small-scale non-homogeneity of the porous glass wool. Moreover the way each thermocouple is placed also has an impact. The better the contact with the building component; the more the measurement reflects its temperature impacted by the thermal inertia rather than the air flow temperature.

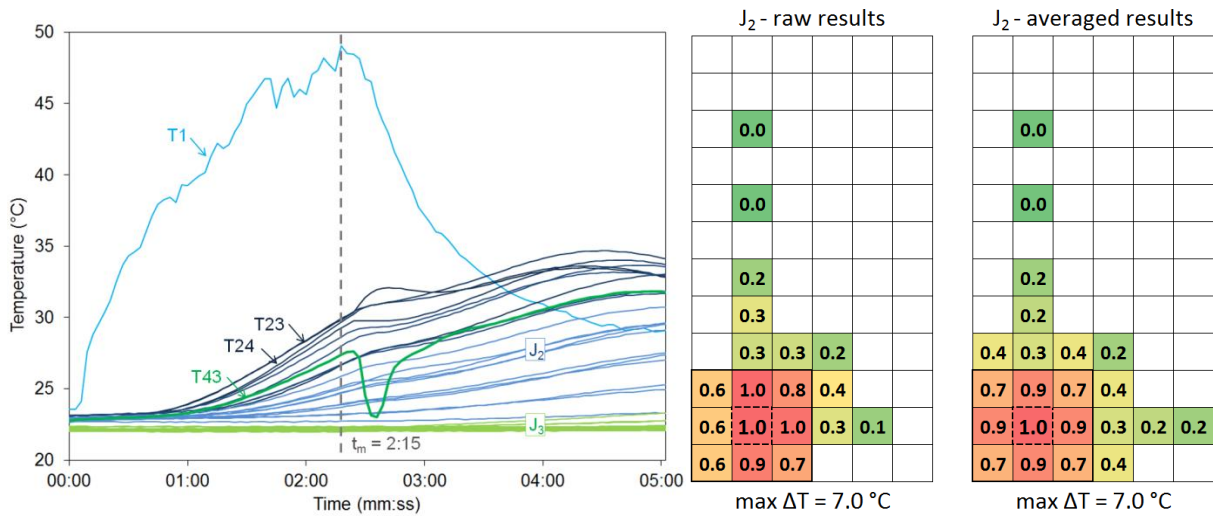


Figure 6.18 – Thermocouples measurements and  $\Delta T_r$  mapping for the configuration 1 (free inlet)

However the averaged results seem to be consistent: the relative temperature difference is the biggest for T23, and decreases away from this central point. At 20 cm there is still a significant temperature increase of about 1.5°C, but at 30 cm no significant  $\Delta T$  is detected.

### Without bond

A gypsum board is added on the upstream side of the wall assembly without glue at the interface. This reduces the air inlet even if a small air gap can possibly appear between these two components because of the pressure. The results of the heating test are presented in Figure 6.19, with t<sub>m</sub>=1 min 30.

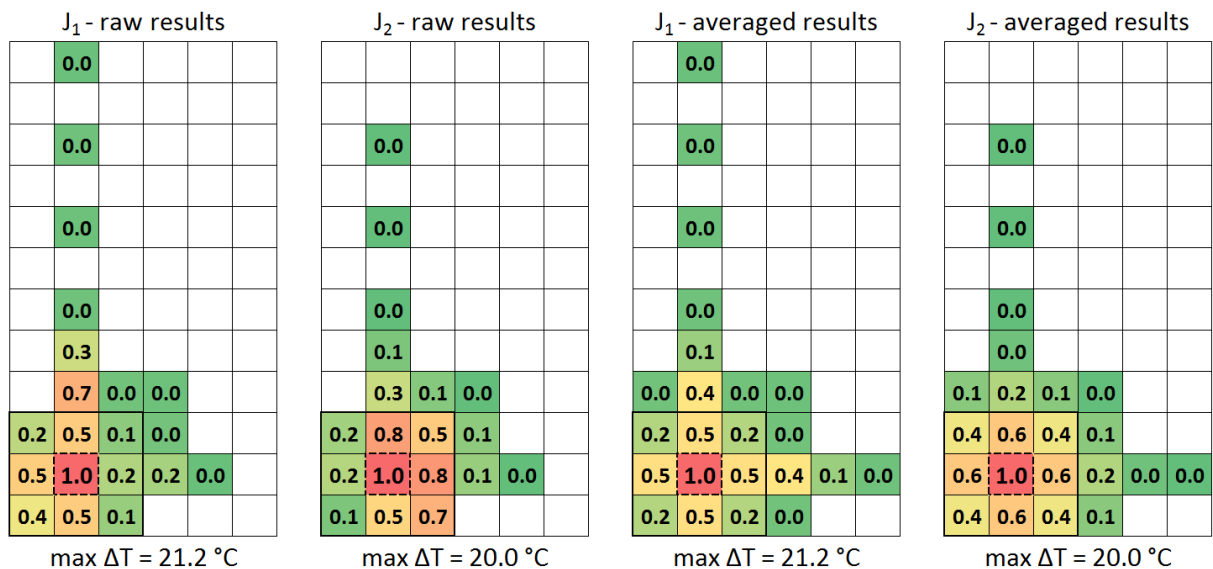


Figure 6.19 –  $\Delta T_r$  mapping for the configuration 2 (without bond)

As for the previous configuration, the raw results show an asymmetry but trends can be observed from the averaged ones. At the first interface J<sub>1</sub> the air is entering through a rather small area. The thermocouple T11 located 10 cm above the hole has a high  $\Delta T_r$  (0.7) which seems to not be

consistent with the other measurements. When the wall assembly was disassembled it was noticed that T11 was slightly spaced from the gypsum boards. It was therefore maybe less impacted by the wall inertia than the other thermocouples which could explain a higher  $\Delta T_r$ . By leaving aside this abnormal measurement, it seems that the limit of the warm air infiltration area is smaller than 10 cm. The air dispersion seems to be a bit wider between the two layers of glass wool ( $J_2$ ) with a temperature difference of about 4°C 10 cm away from the hole.

One can note that the maximum  $\Delta T$  for  $J_2$  is 20°C which is much higher than the 7°C obtained for the first configuration. The air flow rate is constant for each test (7.5 m<sup>3</sup>/h) but for the first test the air inlet area is wider and therefore the velocities are smaller. As a result the local air flow at the center is lower which means it takes longer for the glass wool to warm up.

**With bond**

For the third and last configuration, the gypsum board on the upstream side is glued to the glass wool with two co-centric circles, as described in paragraph 6.1 and shown in Figure 6.16. This does not guarantee a perfect contact between the two components with the pressure of the flow but because of the thermocouples it was not possible to glue the whole interface. The results of the heating tests are presented in Figure 6.20, with  $t_m = 1$  min 33. The air inlet at  $J_1$  seems to be slightly smaller compared to the configuration without the glue but the results are very similar. This might be partly due to the presence of the thermocouples creating inevitably a small air gap by their thickness.

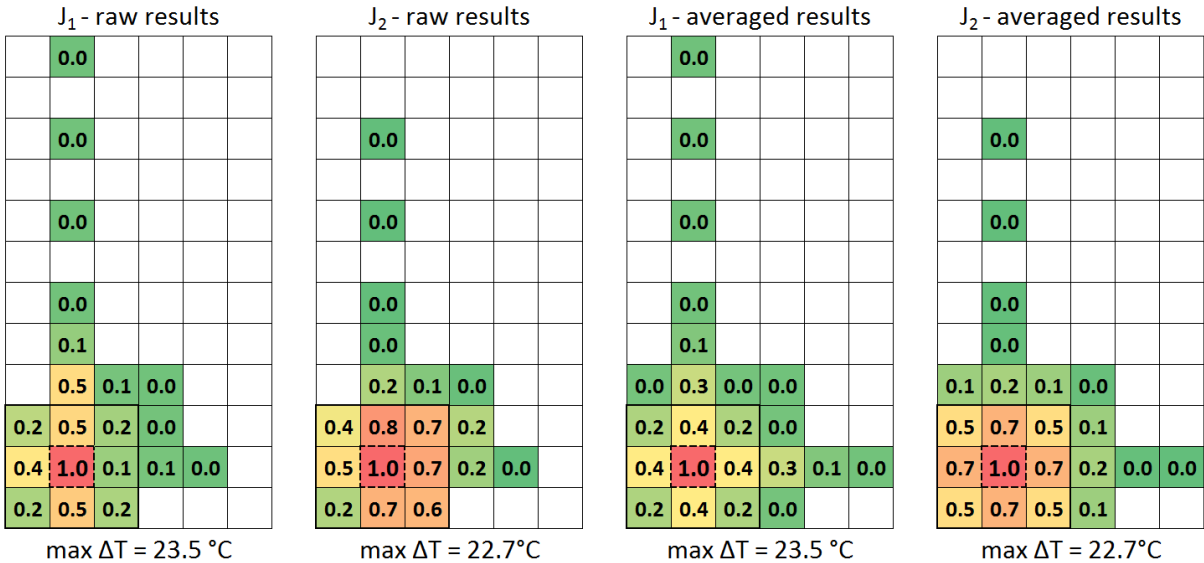


Figure 6.20 – $\Delta T_r$  mapping for the configuration 3 (with bond)

For this configuration another test is carried out with the inlet hole sealed with tape in order to evaluate the heat transfer by conduction. The temperature course measured by the 60 thermocouples is presented in Figure 6.21.

The first plane of thermocouples  $J_1$  does not measure an increase of temperature before 1 min 30 s, which is the value of  $t_m$  for the configurations 2 and 3. Only T2 which is right behind the tape is about 0.5°C warmer at that time, which is not significant compared to the 20°C measured with an open hole.



Similarly, at  $t = 2 \text{ min } 15 \text{ s}$ , the value of  $t_m$  for the first configuration, the thermocouples of  $J_2$  have not detected a temperature rise yet. Even if for this configuration there is no gypsum board, which reduces a bit the thermal resistance of the wall assembly, the  $J_2$  thermocouples measure an increase of temperature about 5 minutes after the  $J_1$  ones. It means that for each test presented above the  $\Delta T$  measured is not due to the conduction from the warm upstream air volume to the ambient air. Given that 4 cm separate  $J_1$  from  $J_2$ , it also means that the glass wool warmed up by the flow probably does not impact much the surrounding cold glass wool by conduction.

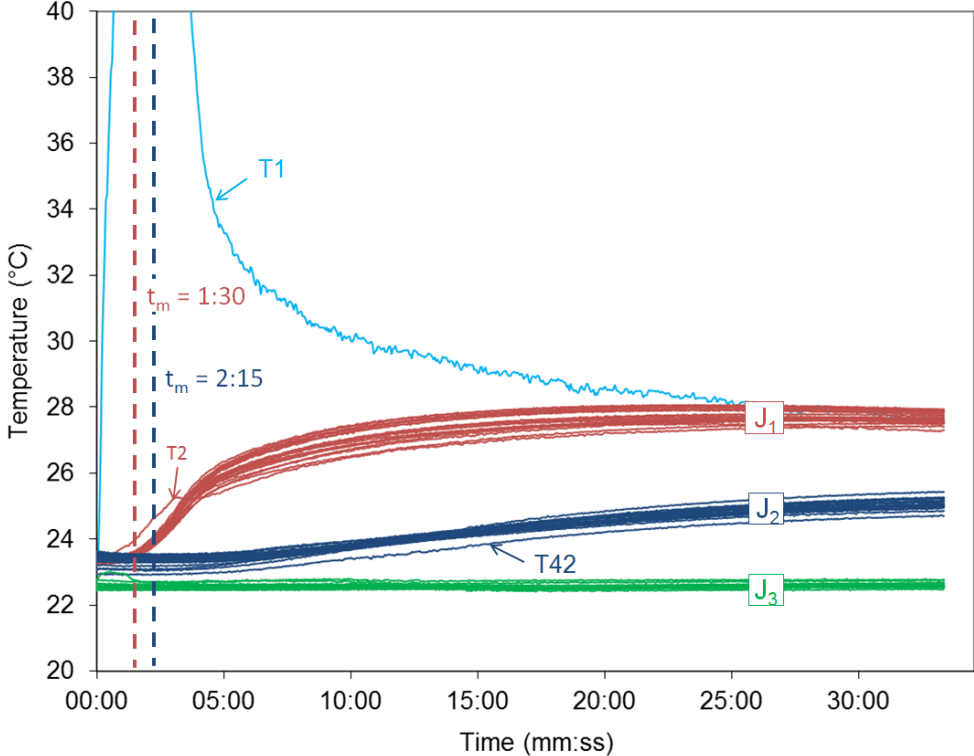


Figure 6.21 – Conduction test for the configuration 3 (inlet hole sealed with tape)

**6.3.4. Comparison with the numerical study**

The simulations described in paragraph 6.1.2 are used for a comparison with the thermocouples (TC) study results. Normalized numerical velocity profiles are plot at the inlet ( $J_1$ ), outlet ( $J_3$ ) and in the middle of the two GW layers ( $J_2$ ) and are compared with the averaged  $\Delta T_r$  experimental values in Figure 6.22. Unlike for the PIV results presented in paragraph 6.2.2, the origin of the x axis is located at the center of the hole(s).

At the inlet, there is a much greater air dispersion measured with the TC than numerically predicted. This could be due to the presence of a large amount of sensors. Even if the intrusiveness is very low, inside a highly porous media, the thickness of the wires can become significant along solid and flat surfaces. As a result, the presence of thermocouples between the two glass wool layers ( $J_2$ ) has probably a very low impact on the flow behavior but this might not be the case for  $J_1$  and  $J_3$  with the sensors taped on the gypsum board. The same problem accounts for the sealing between the tested wall assembly and the APIE box walls. The 60 thermocouples connected to the data acquisition unit make it difficult to prevent the appearance of small air paths around them at this interface. A

possible additional explanation is that the pressure of the air flow is pushing the glass wool away from the gypsum board despite the glue and the insulation compression.

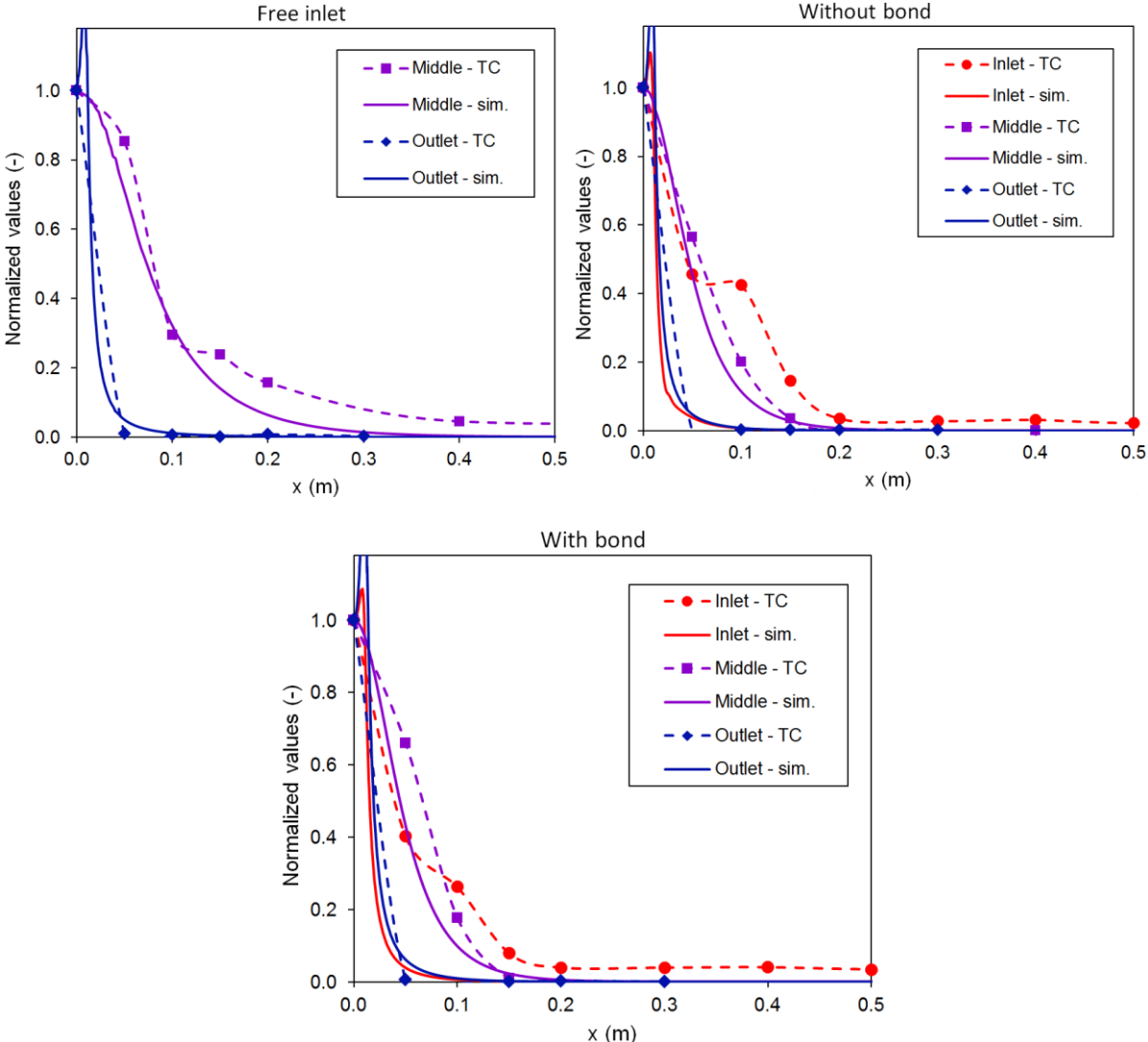


Figure 6.22 – Comparison of the thermocouples and the numerical results for the three tested configurations

In the middle, the air dispersion measured with the TC is also greater than numerically predicted but the difference is not as significant. This is a normal consequence assuming that the air entered through a larger surface than predicted by the simulation.

Finally at the outlet there is a good agreement between the experimental and numerical results: the low velocities 5 cm away from the hole confirm that only the thermocouple T43 facing the hole could detect a significant temperature increase. Although at this junction the thermocouples are also taped on the GB, the intrusiveness is less of a problem for several reasons. First, the pressure of the air flow is pressing the GW against the GB which helps to prevent the appearance of air gaps. Then, as illustrated in Figure 6.23, at the junction with the APIE box walls, the TC wires are exiting the wall assembly on the upstream side, along the 2 GW layers that are softer than the GB and therefore decrease the air infiltration risk. There are also less TC wires at this junction: 17 compared to 59 at the junction between J1 and the APIE box.

For a more accurate comparison, the mass transfer could be coupled with heat transfer in the simulation if the thermal properties of each building component are known, as well as the boundary temperature conditions. This would enable to compare the experimental temperature differences with the numerical ones rather than with flow velocities. Such models with coupled heat and mass transfer already exist [77] but implementing them was out of this study scope.

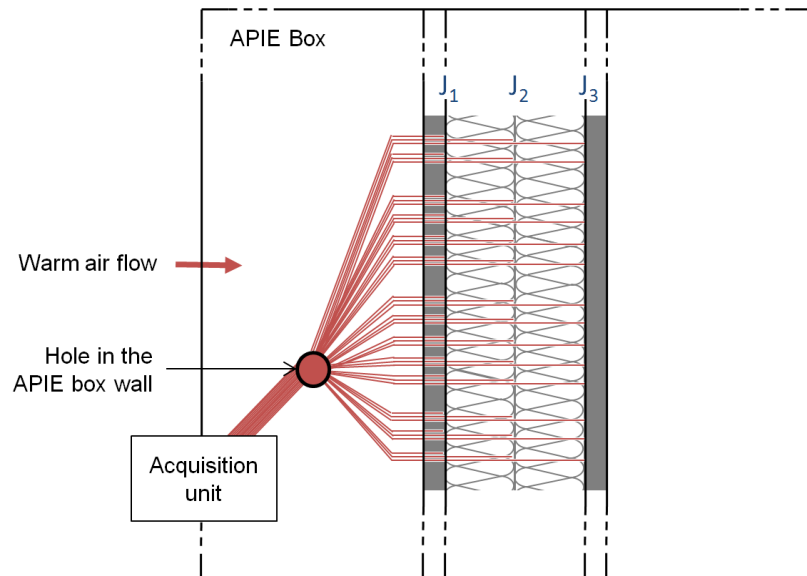


Figure 6.23 – Thermocouples wires at the junction between the APIE box walls and the tested wall assembly

### 6.3.5. Conclusion

These tests confirm the possible use of thermocouples for the air path study, with a good accuracy and responsiveness. The second tests carried out for each configuration presented in Appendix J show also a good repeatability.

There is however a number of limits to this approach. As discussed previously, a large amount of thermocouple wires can create small air paths along them at the interface with solid and flat surfaces. In order to decrease the risks of modifying the air path by monitoring it, a lower number of thermocouples would be necessary, but that goes against the second limit of this technique: the local nature of the measurement. The fact that the temperature is measured at a given position increases uncertainties due to the temporal and spatial flow fluctuations, as well as the small-scale non-homogeneity of the porous material. One should also note that the implementation of sensors inside the wall assembly restricts the application of this technique to laboratory studies.

Finally, as discussed for the infrared thermography technique, investigating the air path through the heat transfer study presents difficulties. The thermal inertia of the building components may result in an underestimation of the air dispersion. The further from the direct path, the smaller the air flow and the longer the path is, so the cooler it can get before reaching the sensor. On the other hand the conduction transfer may result in an overestimation of the air dispersion, with a risk increasing with the duration of the test. It has also been mentioned that the sensors should be strictly placed in the same way since the surface temperature of a building component differs from the flow temperature.

## 6.4. 3-D grid relative humidity monitoring

Another possibility for the air path investigation is to study it through the moisture transfer in the wall assembly. This approach is very similar to the previously described one, with a three-dimensional grid of sensors monitoring the changes in relative humidity (RH) as air with high moisture content infiltrating into the wall.

### 6.4.1. Preliminary tests

#### RH sensors characterization

The sensors chosen for this study are the Sensirion SHT 75, with a capacitive sensor element used for measuring relative humidity while temperature is measured by a band-gap sensor. The temperature measurement is used by the sensor to calculate the relative humidity but is not of interest for this study.

A previous study [165] had selected this RH sensor among nine other for the moisture transfer study in wall assemblies. They had pointed out a good accuracy with a maximum error of 2% with a chilled mirror. This is consistent with the datasheet provided by the manufacturer indicating an error of  $\pm 1.8\%$  RH and  $\pm 0.5^\circ\text{C}$  in a RH range of 0 to 90% and a temperature range between 5 and  $45^\circ\text{C}$ . These sensors also had a better responsiveness than the other tested ones and a small size limiting the intrusiveness. The relatively small dimensions of the sensor (3.1 mm x 5.08 x 19.5 mm) are indeed an important criterion to minimize the impact of the flow monitoring on its behavior. Another advantage is the fact that each sensor is calibrated by the manufacturer and the coefficients are already integrated into the chip which in theory avoids the necessity of a calibration by the user.

In order to verify the performance of the SHT 75 sensors, both a stationary and a dynamic test are carried out. Two RH boxes are used with salt solutions maintaining an inside relative humidity of respectively 70% (high RH) and 35% (low RH), and a chilled mirror is used as a reference to monitor the actual instantaneous humidity. The sensors are connected to a specific data acquisition system SHT DaqBox with 12 channels, so the 24 tested sensors are separated into two groups. For each of them the sensors are placed successively in the high RH box and the low RH box together with the chilled mirror and the measurements are taken after 15 minutes to ensure a good stabilization.

The results are presented in Figure 6.24. At low humidity the accuracy seems rather good, with a maximum error of -2.1% RH for the sensor 13. However at high humidity, the accuracy is not as good as expected with a maximum error of -5.6% for the sensor 3. This test has been used to adjust the calibration coefficients but a second and a third similar test showed only a small improvement on the resulting errors (maximum error of 4% at high humidity). This leads to the conclusion that the uncertainty is due to the sensor technology itself and can't be decreased with calibration. Moreover, out of 24 sensors, 4 turned out to be defective. This might be due to welding problems rather than the sensor technology but it highlights their fragility.

In order to evaluate their responsiveness, a dynamic test on nine SHT 75 is also carried out. The sensors are taken out of the high RH boxes and placed at ambient RH around 25%. The resulting RH course is presented in Figure 6.25. One minute is necessary before the sensors reach 80% of the RH

change, and about 4 minutes to reach the real RH value. It is also visible from this test that the accuracy is better at low RH.

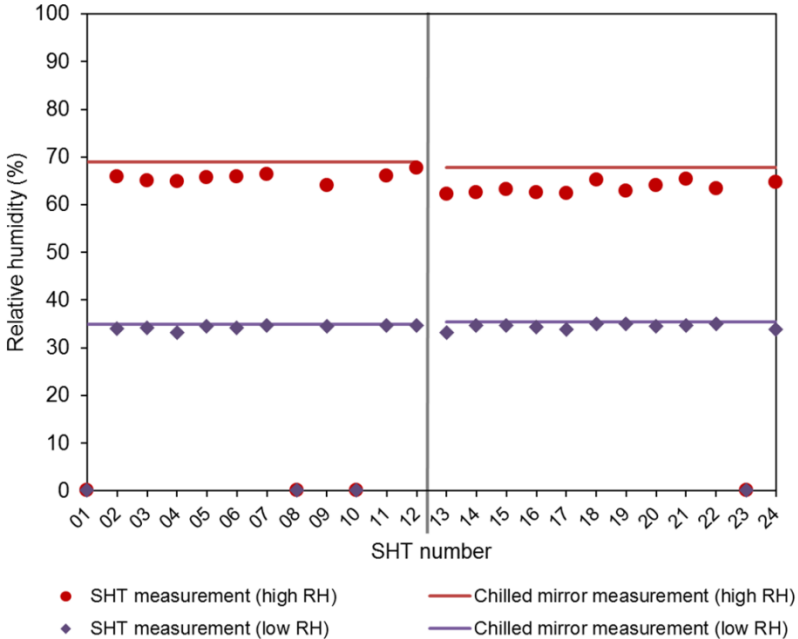


Figure 6.24 – Stationary tests on 24 SHT 75 sensors at high (70%) and low (35%) relative humidity

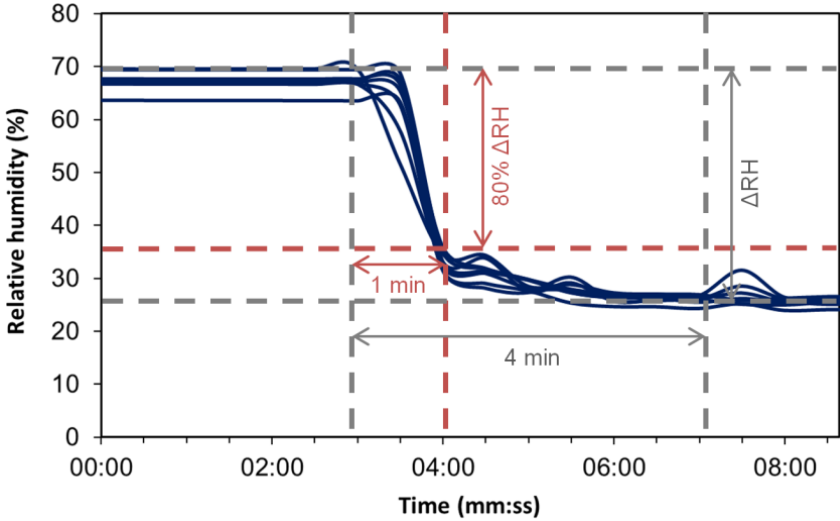


Figure 6.25 – Dynamic test on 9 SHT 75

**Intrusiveness study on the SAPIE box**

The intrusiveness of the SHT 75 sensors was tested in the SAPIE box, similarly to the test with thermocouples previously described. The SHT 75 need however to be attached to the building component because of its weight and can therefore not be easily pulled out one by one. As a result for this test, the sensors were added and not removed from the wall assembly while the pressure was monitored. The results are presented in Table 6.8. Unlike for the thermocouple there is a clear impact on the addition of the sensors with a pressure decrease of 27% by adding 2 sensors, and 35% with 8 sensors.

Table 6.8 – Intrusiveness test on the SHT 75

Nb SHT 75	0	2	4	8
$\Delta P$ (Pa)	510	370	350	330

However one should note that the small size of the SAPI box with a cross-section area of 15 cm x 15 cm compounds the intrusiveness issue, since a significant part of the tested wall – box wall interface sealing is impacted by the passage of the sensors' wires.

### 6.4.2. Description of the tests

#### Wall assembly instrumentation

The tests are carried out on the same three configurations than for the thermocouples tests, and a similar 3-D grid of RH sensors is implemented as described in Figure 6.26. The thermocouples are not removed during these tests since their intrusiveness is not significant compared to the SHT ones. The number of RH sensors is however smaller to minimize the impact on the flow behavior, with only 22 sensors. There is for example only one RH sensor at the last junction  $J_3$  since it has been observed with thermocouples that it was the only one detecting a temperature change.

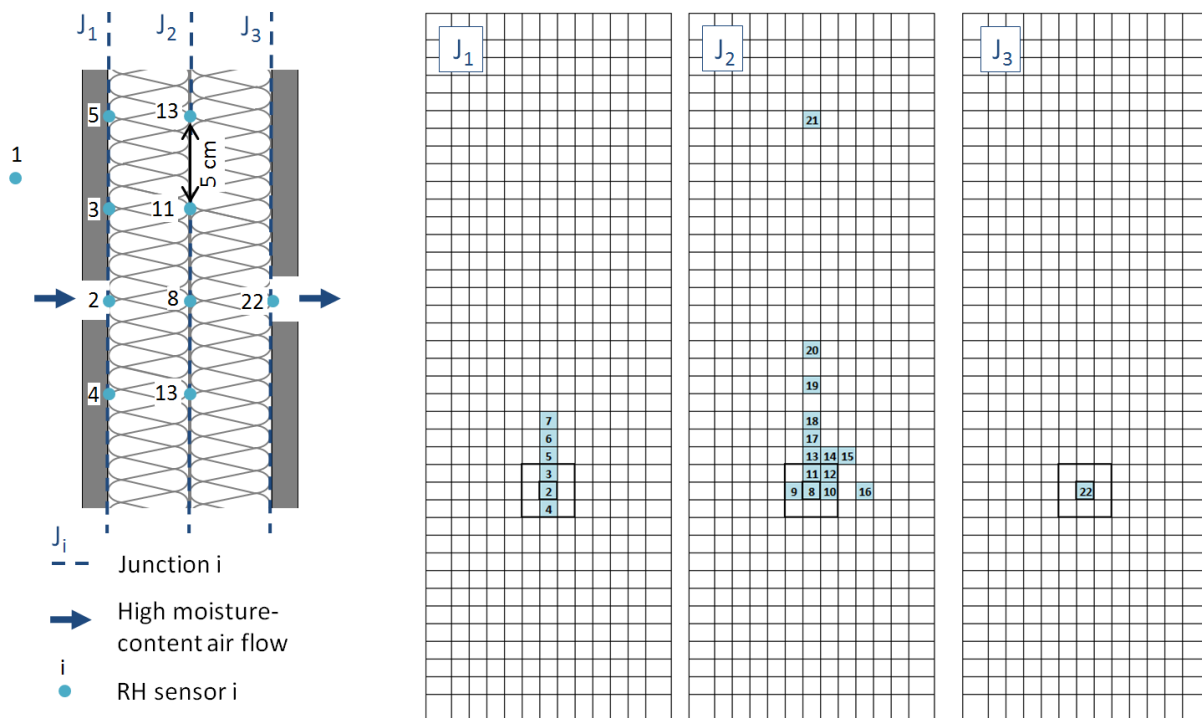


Figure 6.26 – Position of the 22 relative humidity sensors (SHT 75)

For  $J_1$  and  $J_3$ , the junctions between the gypsum boards and the glass wool, the RH sensors are placed against the gypsum board with tape, just as the thermocouples. For the  $J_2$  junction between the two layers of glass wool, the RH sensors are also attached on the 0.5 mm thick straight wires but staples are added because of the heavier weight. This is illustrated in Figure 6.27, as well as the impact of the sensor wires on the sealing between the glass wool and the APIE box wall.

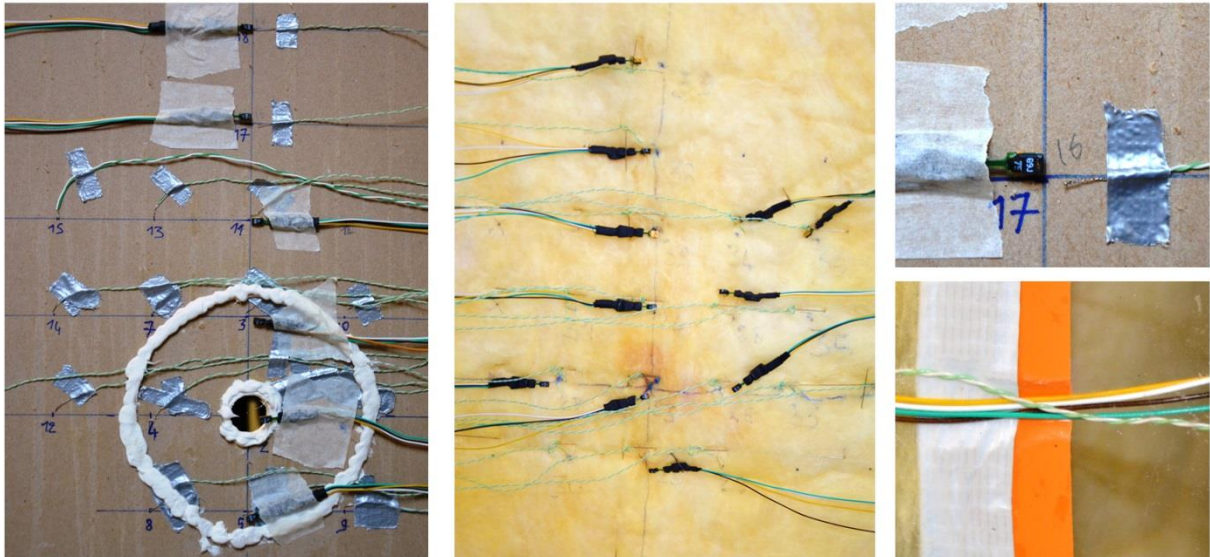


Figure 6.27 – RH sensors fixing on the building components

### Acquisition

The 22 RH sensors are connected to two DaqBox and measurements are taken every 30 seconds, which is the minimum time step offered by the software. Meanwhile, the 60 thermocouples are still connected to another data acquisition unit with temperature measurements every 3 seconds.

An air flow rate of 7.5 m<sup>3</sup>/h pressurizes the upstream side of the APIE box and a steamer enables to significantly increase the air relative humidity within a few seconds after the acquisition starts ( $t=t_0$ ). Since the steam is close to 100°C, its injection warms up the air of a few degrees and it is also possible to track this warm air flow by both the SHT temperature sensor and the thermocouples.

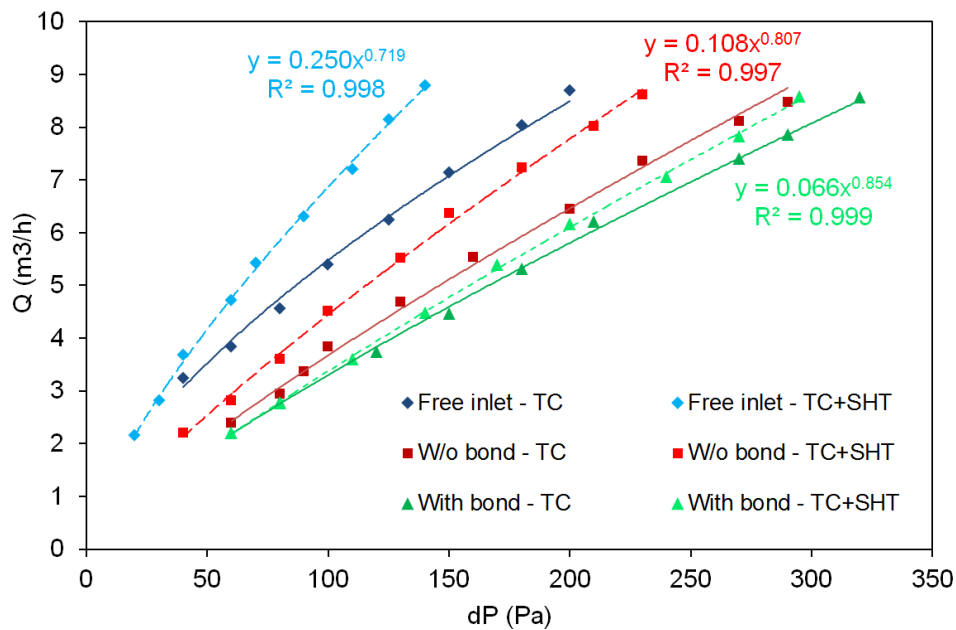


Figure 6.28 – Pressurization tests on the three configurations with 60 thermocouples and 22 RH sensors

Pressurization tests on the three instrumented wall assemblies are carried out to evaluate the impact of the RH sensors on the air permeability. The results are presented in Figure 6.28. The plain lines are

the results previously presented with only the thermocouples inside the wall assemblies, and the dotted lines correspond to the tests after the implementation of the 22 RH sensors. For the three configurations, the air permeability has clearly increased, which confirms that the intrusiveness of these sensors is significant.

### Data analysis

For the analysis, the relative humidity RH and temperature T are taken at time  $t=t_m$  corresponding to the RH peak recorded by the sensor SHT1 in the upstream air volume. This occurs about 2 minutes after the steam is introduced because of the response time mentioned before. After  $t_m$  the RH decreases slowly since dry air is continuously entering the upstream box to maintain a constant pressure. For each test, the RH difference between  $t_0$  and  $t_m$  recorded by the sensor SHT 22 at the outlet of the hole was between 17.7% (configuration 1) and 76.0% (configuration 2).

Because the flow is non-isothermal, the relative humidity is not the most appropriate parameter to track the vapor transport. For a constant mass of water, its value varies indeed significantly with the temperature. The vapor pressure  $p_v$  (Pa) is used instead, it is calculated for each SHT sensor  $i$  as follow:

$$p_{v,i} = \frac{RH_i}{100} \times P_{vs,i} \quad (4)$$

The saturation vapor pressure  $p_{vs}$  (Pa) is given by [166]:

$$p_{vs,i} = 610.78 \times \exp\left(\frac{T_i}{T_i + 238.3} \times 17.2694\right) \quad (5)$$

With T the temperature in °C. One should note that this formula is a good and commonly used approximation but for high accuracy studies, more accurate formulae can be found in standard reference works (e.g. Smithsonian Tables).

In order to obtain a mapping of the humid air leakage in the wall assembly, the parameter  $\Delta p_{vr}$  (relative  $p_v$  difference) is calculated for each sensor  $i$  at the junction  $J_j$  as follow:

$$\Delta p_{vr,i,J_j} = \frac{p_{v,i,t_m} - p_{v,i,t_0}}{\max(p_{v,i,t_m} - p_{v,i,t_0})} \quad (6)$$

However, since dry compressed air is used the RH is almost equal to 0 at  $t_0$ . As a result:

$$\Delta p_{vr,i,J_j} \approx \frac{p_{v,i,t_m}}{\max(p_{v,i,t_m})} \quad (7)$$

For a comparison purpose, the relative RH difference is also calculated for each sensor  $i$  at the junction  $J_j$ :

$$\Delta RH_{r,i,J_j} = \frac{RH_{i,t_m} - RH_{i,t_0}}{\max(RH_{i,t_m} - RH_{i,t_0})} \quad (8)$$



### 6.4.3. Results

The raw results at each junction are given for each test and each measurement: the relative humidity, the temperature monitored by the SHT sensors and the one monitored by the thermocouples. The “averaged results” are also presented with the  $\Delta RH_r$  averaged between sensors equidistant from the hole (considering axial symmetry). One should note that if the max  $\Delta RH$  is not in the center, it may change in the averaged results and therefore modify the other normalized values. The results for the junction  $J_3$  are not presented below since only there was only one SHT sensor (SHT 22) and the thermocouple facing the outlet (T43) hole was the only one detecting a significant temperature change.

The results for the first configuration with a free inlet are presented in Figure 6.29. As shown on the graph the analysis is made at  $t_m = 2$  min, since after the RH decreases in the upstream air volume (SHT1). This is only 15 seconds less than the  $t_m$  of the thermocouple tests, but the results are quite different.

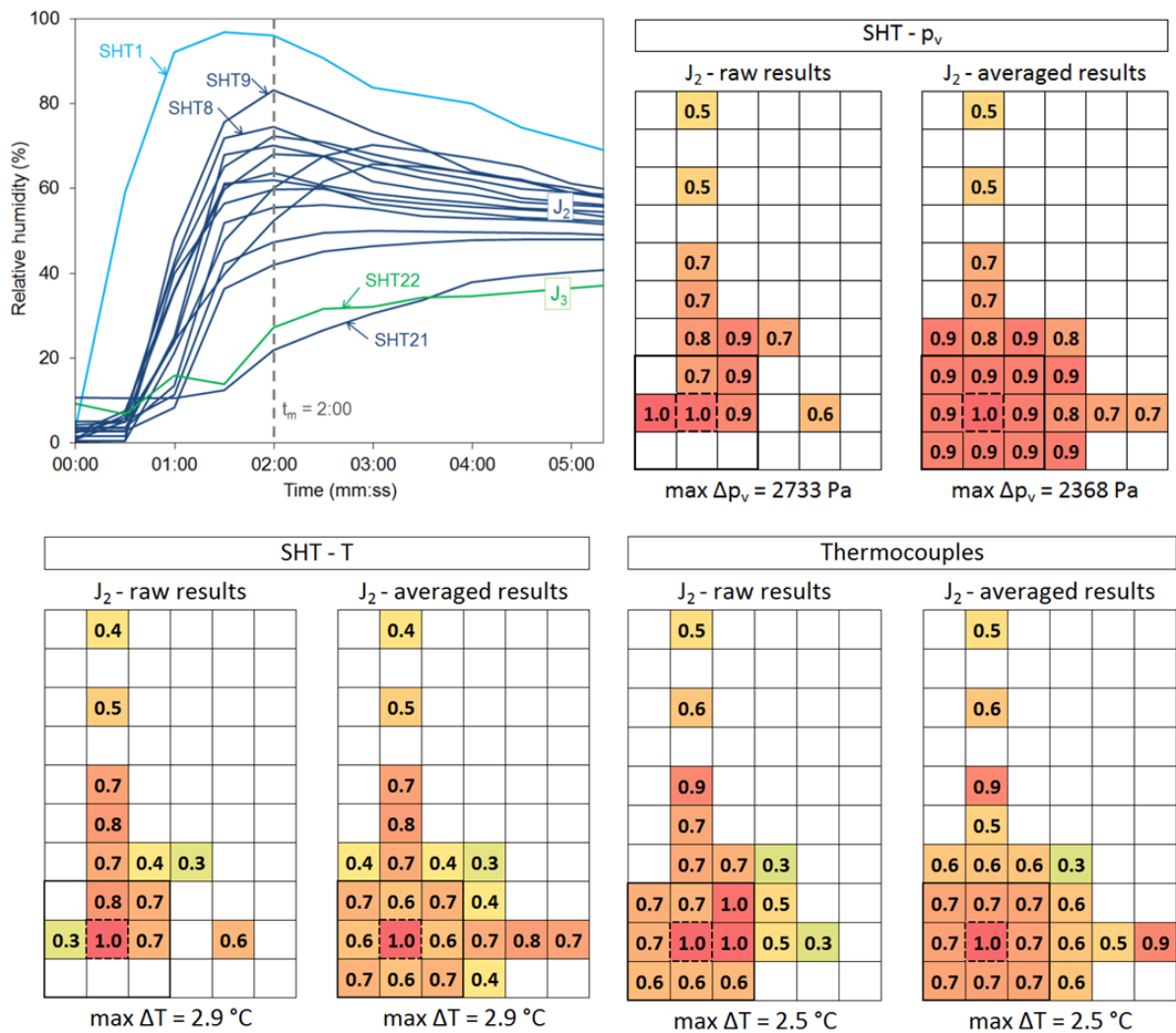


Figure 6.29 – Relative humidity measurement and  $\Delta RH_r$  and  $\Delta T_r$  mapping for the configuration 1 (free inlet)

The good point is the very low inertia since the glass wool is not a hygroscopic material. This can be clearly seen on the graph of the Figure 6.29, with a relative humidity at  $J_2$  near the hole (SHT 8 & SHT





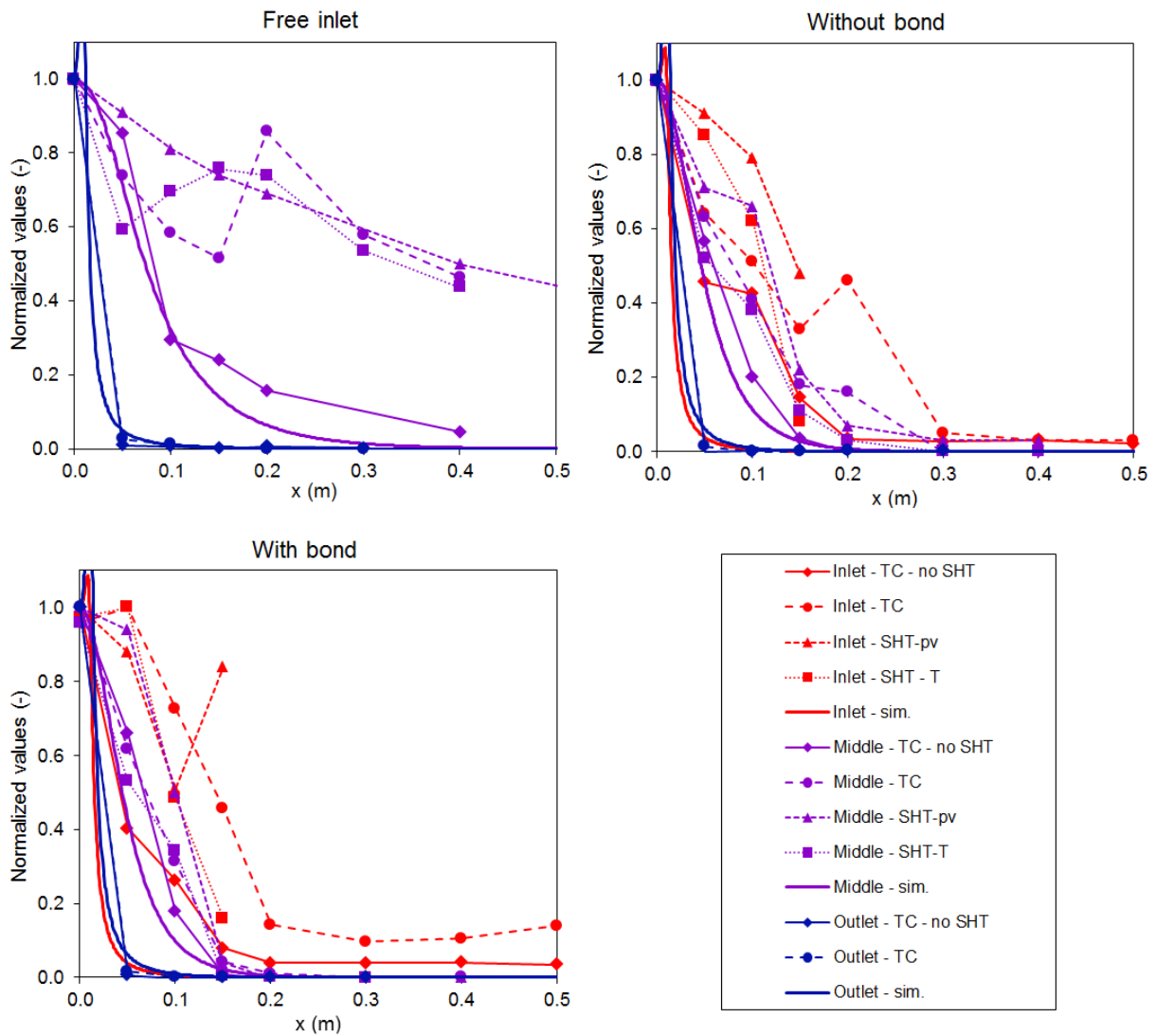


Figure 6.32 – Comparison between the thermocouples, SHT and simulation results for the three tested configurations

### 6.4.5. Conclusion

The air path investigation by the heat transfer with thermocouples and the moisture transfer with RH sensors are two approaches with different advantages and drawbacks. The thermocouples are smaller which reduces significantly the intrusiveness; they have a better accuracy and a very small response time. These three properties make them more appropriate to the air path study inside a wall assembly, especially at interfaces with flat and rigid surfaces. However the heat transfer presents too issues: the thermal inertia and the conduction that make difficult to find the appropriate measurement time  $t_m$  for the analysis, and prevent from having a direct relation between the  $\Delta T$ , mapping and the air flow rate distribution.

As mentioned before, these two techniques are also characterized by local measurements which increase the uncertainties due to spatial and temporal flow fluctuations. Moreover the intrusiveness is higher with the RH sensors but is also an issue with thermocouples as it would be with any sensor. In order to overcome these two problems, an additional technique using fluorescein to track the air path is presented below.

## 6.5. Fluorescein study

### 6.5.1. Fluorescein tests

#### Description of the tests

The air path through the three wall assemblies studied through this chapter was also investigated using fluorescein as tracer particle as presented in the Chapter 5. The pressure, the flow rate and the generation time are presented in Table 6.9. The generation time corresponds to the number of hours the fluorescein-laden air was infiltrating the wall assembly before the analysis.

Table 6.9 - Summary of the fluorescein tests

Tested configuration	dP (Pa)	Q (m <sup>3</sup> /h)	Generation time
1 (free inlet)	230	3.0	7h20
2 (without bond)	340	2.5	7h
3 (with bond)	460	2.8	6h45

For the free inlet configuration it has been noticed that a large amount of fluorescein micro-particles were depositing on the APIE box walls due to static electricity. In order to avoid this issue for the two other configurations, the outlet of the SAPIE box was placed around the inlet calibrated hole on the tested wall assembly. The fluorescein-laden air was injected into this smaller box to reduce the risk of particle deposition.

As mentioned in Chapter 5, it has been noticed that the air flow velocity should not exceed 3 m/s to prevent a high collection efficiency that would stop most of the particles in the first millimeters of the glass wool. In configurations 2 and 3 the air flow rate of 2.8 m<sup>3</sup>/h corresponds to a velocity of 2.5 m/s at the inlet hole which is below the limit. In configuration 1, the air velocity remains very low due to non-restricted air inlet.

After about 7 hours of generation time, the tested wall assembly is disassembled and the two layers of glass wool  $A_{tot}$  and  $B_{tot}$  are cut into 5 cm x 5 cm squared pieces as illustrated in Figure 6.33. For the configurations 2 and 3, each glass wool layer is cut at half its thickness which makes 4 analyzed layers:  $A_1$ ,  $A_2$ ,  $B_1$  and  $B_2$ .

The amount of fluorescein micro-particles is quantified in each piece of insulation material by following the protocol described in paragraph 5.1.5. In order to obtain a mapping of the fluorescein-laden air leakage in the wall assembly, the mass of fluorescein for each piece of glass wool is divided by the maximum mass measured in the glass wool layer:  $\max(m_{fluor})$ . The results of the three tests are presented below. The measurement that is far from the hole ( $x = 1$  m) is not shown because no fluorescein was detected at that distance for all configurations and any glass wool layer.

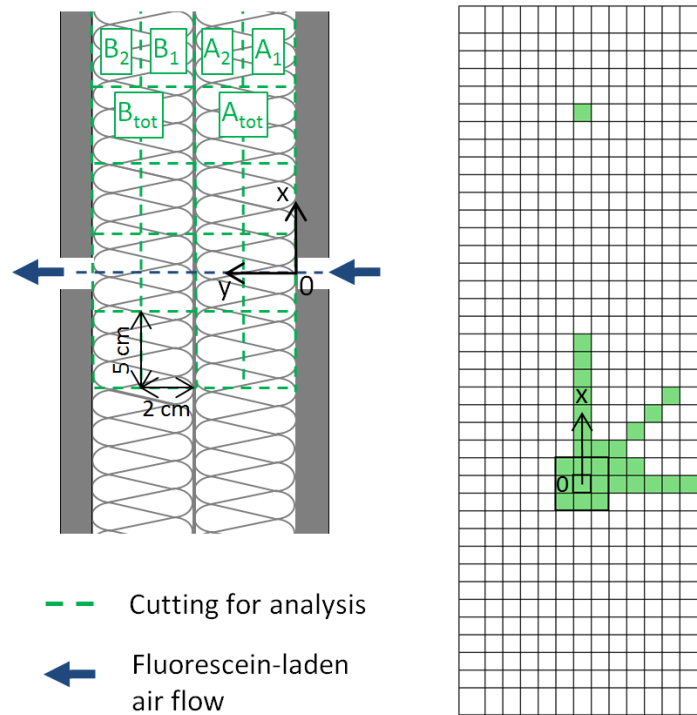


Figure 6.33 – Cutting for the fluorescein analysis

### Air inlet dispersion

The first point of interest is the air dispersion at the inlet of the glass wool depending on the configuration. For this purpose, the results for the most upstream glass wool layer are presented in Figure 6.34. It shows as expected a larger air dispersion for the free inlet configuration with still 30% of the  $\max(m_{\text{fluo}})$  measured 15 cm away from the hole ( $x=15$  cm), and more surprisingly, still 10% at  $x=40$  cm.

The two other configurations with gypsum board at the inlet have smaller air dispersions with in both cases less than 5% of  $\max(m_{\text{fluo}})$  at  $x=15$  cm. For the configuration with bond, the dispersion is even smaller, but there is still a significant amount of fluorescein found 5 cm from the hole. This is mainly due to the air diverging right after the inlet hole, but it could also be due to a non-perfect contact between the gypsum board and the glass wool. As mentioned in paragraph 5.1 it is difficult to guarantee the absence of air gap despite the two circles of glue since the air flow is pushing the glass wool away from the gypsum board.

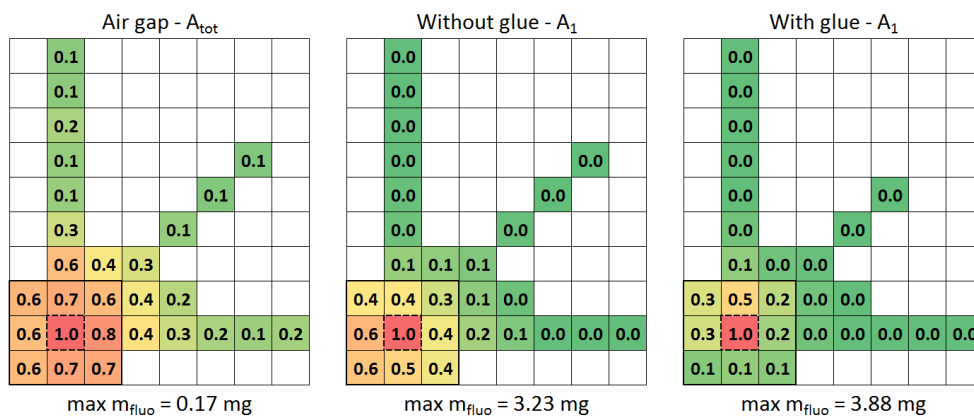


Figure 6.34 – Air inlet dispersion for the three fluorescein tests (raw results)

One can note that there is a better symmetry in the fluorescein results than for the thermocouples and RH sensors measurements. This is due to the fact that the measurement is no longer local but made on 5 cm x 5 cm x 2/4 cm volumes. Moreover it is not subject to the temporal fluctuations since the generation time was about 7 hours. This means that the asymmetries of fluorescein mass measurements are reflecting the real mean behavior of the flow. There is a small uncertainty due to the cutting accuracy but for example on the configuration 3 the air is clearly going up after entering the wall assembly. This is probably due to a local air gap between the gypsum board and the glass wool and possibly also to the non-homogeneity within the insulation material.

**Air dispersion around a direct air path**

The other focus of this study is on the air dispersion around the direct air path for the configurations 2 and 3, that is to say the dispersion of the air flow around the axis drawn between the inlet and the outlet holes. For this purpose the results of these two tests with the four glass wool layers are presented in Figure 6.35.

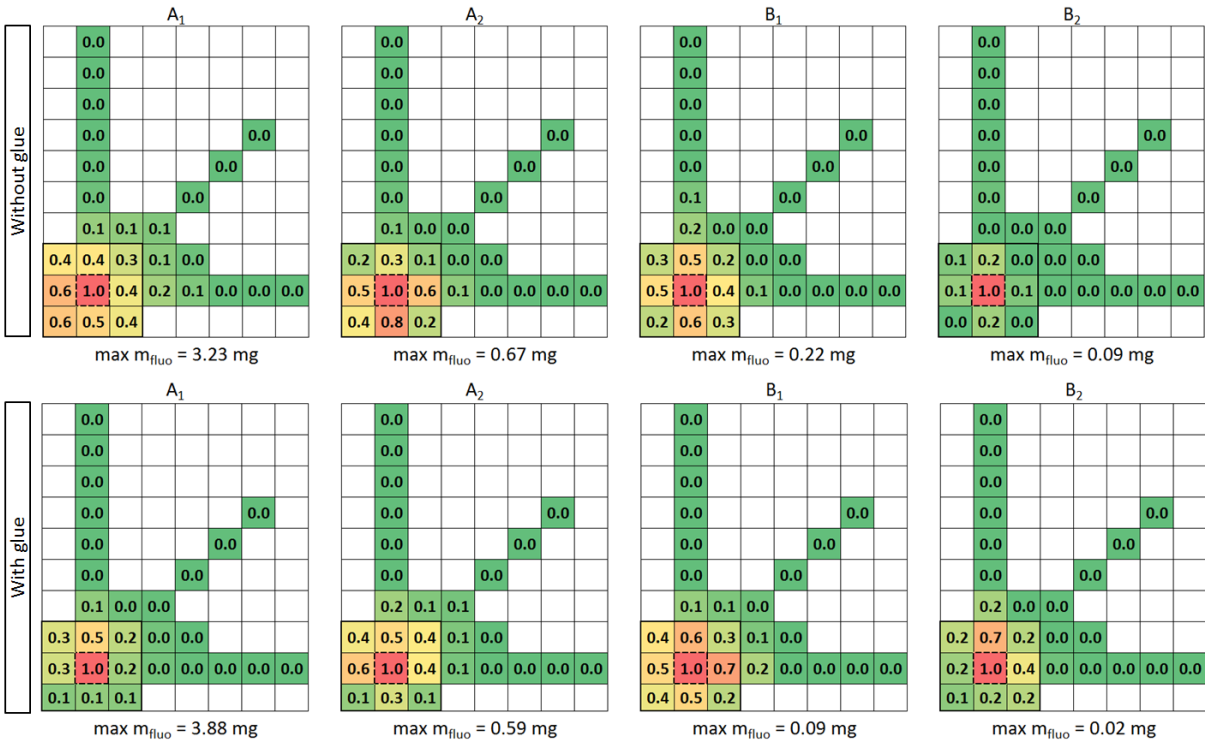


Figure 6.35 – Air dispersion inside the glass wool for the fluorescein tests 2 (without bond) and 3 (with bond)

These mappings shows that the no fluorescein was found further than 15 cm away from the direct path. The glue limit the air dispersion on the first layer of glass wool as mentioned previously, but it does not have a very significant impact on the following ones. The last one before the air outlet seems even to have a larger air dispersion than for the configuration without bond. However, the mass of fluorescein is very small, with only 0.02 mg near the hole. This means that the absorbance measured in that layer were below 0.060 which is too low to be very precise, considering that the glass wool fibers without fluorescein can color the water up to an absorbance of 0.020.

Moreover, the air dispersion on B<sub>1</sub> is slightly larger than on A<sub>2</sub> for the case with bond that is supposed to be symmetrical (same inlet as outlet). This is due to the fact that the concentration of

fluorescein in the air decreases as the particles are captured along the air path. Similarly, there are more particles filtrated in  $A_1$  than  $A_2$  and in each small volume of glass wool analysed, there are more particles on its upstream part. As a result, the measurements are not representative of the average of their thickness but of a plane closer to the upstream boundary. Consequently,  $A_2$  corresponds to a plane further from the interface between the two glass wool layers than  $B_1$ .

Complementary results are presented in Appendix L, with also the averaged values by axial symmetry.

## Conclusion

To conclude, the fluorescein technique gives consistent results for the air path study inside a timber frame wall assembly. It has the advantage of being non-intrusive, and not be subject to the temporal and spatial fluctuations. As a result it is possible to observe singularities that are difficult to study by simulation, such as the impact of the bound between the gypsum board and the glass wool or the asymmetry due to the non-homogeneity of the materials and the workmanship.

However, even though the fluorescein mapping gives a good indication on the air path, it does not give directly fully accurate air dispersion, especially when rather long air paths are involved. As most of the techniques investigated previously, an association with a numerical model is needed in order to deepen the analysis.

### 6.5.2. Comparison with the numerical study

The experimental results are compared with the numerical simulation in Figure 6.36. Three normalized profiles are plotted for each configuration and each analyzed GW layer:

- *Fluo – exp.*: the relative fluorescein mass measured experimentally and averaged by axial symmetry.
- *Velocity – sim.*: the normalized velocity taken at the middle of the GW layer, e.g.  $y=10$  mm for  $A_1$ ,  $y=30$  mm for  $A_2$ ,  $y=20$  mm for  $A_{tot}$ , etc. As previously discussed in Chapter 5, the concentration of fluorescein in the air decreases as the particles are captured along the air path and the mapping is therefore not exactly representative of the middle of the analysed layer.
- *Fluo – sim.*: The relative fluorescein concentration obtained by simulation. The model presented in paragraph 5.3.2 is coupled to the air transfer model to simulate the fluorescein micro-particles transport through the insulation, with no filtration in the air gap regions. The same 'cutting' is then applied as for the experiment, and the fluorescein concentration is integrated over each "sample". This enables to link more easily the experimental results to the air flow pattern inside the wall assembly. To this end similar coupling (heat-air transfer or moisture-air transfer) could also be implemented for the temperature and RH monitoring studies, but it was out of this study's scope.



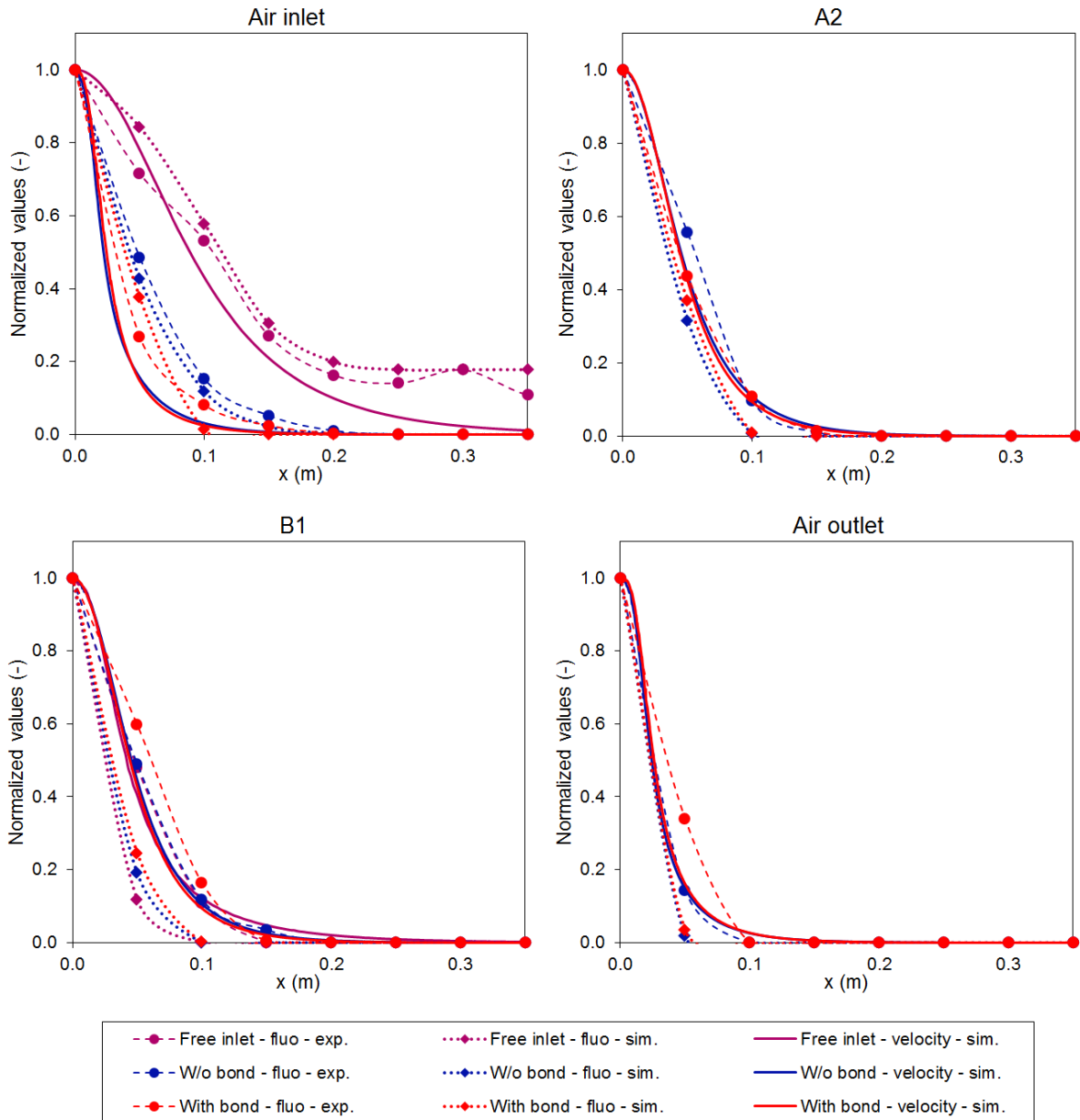


Figure 6.36 – Comparison of the experimental and numerical results for the fluorescein tests

Overall, these graphs show a better agreement between the experimental and numerical results than for the temperature and relative humidity monitoring. The normalized profiles are also smoother, since the fluorescein measurements are made on small GW volumes rather than on a local point, and the temporal fluctuations are not visible thanks to a long duration of the experiment.

At the air inlet, the experimental fluorescein measurements show larger air dispersion than the velocity profiles obtained with the simulation. However, the experimental and numerical fluorescein profiles are in good agreement for the three configurations. These results tend to confirm the necessity of coupled-model to compare experimental results with air flow patterns.

For A<sub>2</sub> all the profiles are close to each other but the numerical fluorescein profiles show slightly smaller air dispersion than the experimental ones. This tendency is more pronounced for B<sub>1</sub> and the

outlet of the wall assembly with numerical fluorescein profiles below the velocity curves and the experimental ones slightly above them.

These results show that the filtration model gives similar results to experimental measurements. However some differences are noticed. The model has indeed been validated for a relative small velocity range (0.2 – 1.5 m/s) because of technical experimental limitations, but since the maximum velocities are 2.5 m/s, most of the air flow inside the GW is below this range, especially far from the holes. Moreover, the average fluorescein micro-particles diameter is known to be in the vicinity of 0.18  $\mu\text{m}$  but the distribution is not known. Since the filtration model is quite sensitive to this parameter it could be helpful to determine the size distribution of the fluorescein particles and add it as a model input.

## **6.6. Comparison of the methods and discussion**

The main conclusions of this study are brought together in Table 6.10. Two experimental methods have been tested for the determination of the air inlets/outlets only: the infrared thermography (IRT) and the particle image velocimetry (PIV). In order to track the air path inside the timber frame wall assembly, three additional experimental methods have been compared: a 3-D grid temperature monitoring with thermocouples (TC), a 3-D relative humidity monitoring with SHT sensors and the use of fluorescein micro-particles.

For the air inlets and outlets identification, the IRT is much easier to implement than the PIV technique. It only requires heating and pressurizing one side of the tested wall and capturing thermographs on the other side with a specific IR camera. Since it is non-intrusive a visual diagnostic can even be done in-situ. This is the only one of the 5 tested techniques that does not require a laboratory set-up. The correlation between the thermographs and the air dispersion at the outlet is however not so easy since the air transfer is studied through the heat transfer. It raises the issues of the thermal inertia of the building materials that lead to an underestimation of the air dispersion and the possible heat conduction that may overestimate it. Moreover both the IRT and the PIV techniques give information only on the air inlet/outlet of the wall assembly and not on the flow behavior inside it.

On the other hand, the main advantage of the PIV technique is that it is the only approach in this study that actually measures the air velocity. The air dispersion at the inlet of the wall assembly can therefore be deduced directly. Moreover it enables to quantify or at least compare the air flow rates for different configurations. This technique has however some limitations other than the difficult implementation. The flow rate range is restricted since the infiltration velocity has to be significantly higher than the surrounding convection flow but not too high to avoid the obstruction of the air path by the tracer particles. In this study it also required an absence of sealing between the wall assembly and the test box in some areas both for the camera to capture the flow as close as possible to the wall and for the laser sheet to arrive on it. The air can therefore possibly infiltrate the wall assembly in these areas, and despite these precautions it is difficult to visualize the flow exactly at the interface with the wall assembly because of the light reflection on the wall materials and the non-planarity of some surfaces. One should note however that this last limitation does not necessarily apply for any experimental set-up, and solution may be found to ensure a good sealing despite the PIV constraints.

Concerning the air path identification inside the wall assembly, the use of thermocouples enables to limit as much as possible the intrusiveness. They also have a good accuracy and responsiveness which makes them the best option among the sensors. However, despite their very small dimensions, the comparison of the results with the simulation shows an overestimation of the air dispersion on the inlet side which could reflect the intrusiveness of the large amount of TC placed against a flat and rigid surface. A coupled heat and air transfer model would however be necessary to clarify this causal relationship. This problem can be overcome only by decreasing the number of sensors, but the local nature of the measurements makes them subject to the flow fluctuations and a relatively fine grid is therefore necessary. Moreover, as for the IRT, this method is based on the heat transfer study to track the air path which raises the issues of thermal inertia and conduction.

In order to avoid these problems, the use of SHT has been tested to monitor the infiltration of a humid air inside the wall assembly. The glass wool is indeed a non-hygroscopic material so there should be a direct relation between the relative vapor pressure mapping and the air dispersion. These sensors were chosen because of their small dimensions but they turned out to be strongly intrusive with much larger air dispersion than predicted by the simulation but also than monitored with the TC study. The relative humidity mappings were close to the temperature ones with slightly larger air dispersions. This shows that the thermal inertia issue probably prevails over the conduction one but the measurement duration seems to be rather well chosen to minimize both effects. Moreover the differences between the temperatures monitored by the TC and the SHT sensors confirmed that one-off and local measurements are subject to the temporal and spatial flow fluctuations. It may be useful to monitor these fluctuations but they complicate the establishment of air dispersion profiles for a comparison with numerical models.

As an alternative to potentially intrusive sensors, the last method tested is the use of fluorescein micro-particles. It gives volume-averaged results which in addition to the long generation time decreases the impact of the flow fluctuations. It has however one major limitation: its ability to track the air flow is strongly linked with the insulation filtration properties and the flow velocity (ideal velocity range of 0.1 - 1m/s). Actually, the absence of fluorescein in a sample far from the air inlet can reflect an absence of flow rate but can also result from the total fluorescein filtration along the air path. In order to avoid this confusion, the air transfer model can be coupled to a filtration one. A good knowledge of the micro-particles collection efficiency as a function of the air velocity is however required which is not easy to determine. In this study the velocity range covered by preliminary tests was smaller than the one encountered in the real-scale tests. The collection efficiency out of this range was predicted by the model but it could not be validated. For the three configurations there was indeed a good agreement between the numerical and experimental results on the upstream half but more significant errors were found for the other half. Overall this method seems to provide the best results but it is also the most complex and time-consuming one.

To conclude, the air path investigation in a wall assembly is not an easy task but the methods presented in this study gave some consistent results. Each of them has advantages and drawbacks that were pointed out thanks to the tests carried out and the comparison with the simulation. As a result the most adequate method can vary depending on the research objective.

Table 6.10 - Summary of the experimental methods for the air path study in timber frame wall assemblies

Method	Infrared thermography (IRT)	Particle image velocimetry (PIV)	Thermocouples (TC)	Relative humidity sensors (SHT)	Fluorescein
Scope	Air inlets / outlets identification		Air path study inside the wall assembly		
Measurement accuracy	+	+	+	-	+
Non-intrusiveness	++	-	-	--	++
Ease of use	++	-	+	-	--
Destructive?	No	Yes	No	No	Yes
Local/averaged results	Local <sup>4</sup>	Local <sup>1</sup>	Local	Local	Volume averaged
Ease of correlation with the air path	-	+	-	+	-
Main advantage	Non-intrusive	Velocity field obtained near the wall	Good measurement accuracy and responsiveness	Easy correlation with the air path	Non-intrusive
Main drawback	Thermal inertia & conduction	Difficult implementation	Thermal inertia & conduction	Intrusiveness	Filtration effect
Comparison with the simulation (isothermal air flow only)	Good agreement for one GW layer; underestimation of the air dispersion for two GW layers	Good agreement (only one case compared)	Relatively good agreement; intrusiveness issue revealed on the inlet side	Bad agreement: air dispersion strongly overestimated due to the important sensors intrusiveness	Good agreement except on the inlet side <sup>5</sup>

<sup>4</sup> For the IRT and the PIV techniques the measurements are local but the respectively temperature and velocity fields are directly obtained. On the contrary the TC and SHT give one measurement point per sensor.

<sup>5</sup> With the filtration model: good agreement on the upstream half, but not on the downstream one



# Conclusion

## General conclusion

Poor airtightness in buildings can lead to an over-consumption of energy and to many issues such as moisture damage and poor indoor climate. The timber frame constructions are particularly subject to air leakage and further knowledge in this field is needed to meet the regulation requirements tightened by the development of low-energy and passive houses.

Airtightness is commonly considered at the building scale, at least in the standards, with an air permeability measurement of the whole envelope. A first study has been presented at this scale on how to include the infiltration rate due to this air permeability in the calculation of the total ventilation rate when an unbalanced mechanical ventilation system disrupts the naturally-established pressure field inside the building. A wide range of weather and housing conditions (864 configurations) were simulated over a year with REGCAP resulting in 7.5 million hourly averaged data points. Three models from the literature were compared with this large data, giving errors up to 30% in the total ventilation rate prediction. A number of new models were developed and it has been found in particular that the sub-additivity ones reduce biases to 1% or less and work across the whole air tightness spectrum.

For the rest of the study, the airtightness was considered at a smaller scale with the characterization of timber frame wall assemblies, components and construction details. The APIE box was built to test relatively large walls with dimensions comparable to the space between two wood studs (2 m x 0.7 m). It was designed to facilitate the use of several experimental techniques implemented in this study, in particular the PIV with two transparent side walls.

A number of pressurization tests have been carried out on three experimental facilities: the APIE box; the SAPI box also built for this study enabling to test 15 cm x 15 cm components; and the AEV test bench for real-scale wall assembly tests. The results put together contribute to quantifying the impact of workmanship on timber-frame wall airtightness such as the choice of the insulation material with an air permeability three times higher for a soft glass wool than a rigid one; or the bond between two layers such as the gypsum board and the glass wool which was found to have a significant impact on the resulting pressure-flow law. It has also been noted that the direction of the airflow through the wall layers has also an influence for high pressure differences. The tests carried out on a real timber-frame wall assembly showed that when the sealing is properly achieved on one side of the wall, the impact of an airtightness defect on the other side (no sealing between the gypsum boards and between the vapor barrier and the bottom plate) is not very significant on the airflow through the wall (<10%). On the other hand it has been shown that a proper sealing on both sides of a window is required. In our configuration the addition of a window with only the exterior

sealing has more than doubled the air leakage, whereas a both side sealed window had an impact lower than 20%.

Such pressurization tests enable to quantify the additional air flow induced by a particular airtightness defect at a given pressure difference. It is however necessary to also investigate the air path inside the wall assembly for a finer analysis of the hygro-thermal performance of the envelope. The air dispersion inside the wall has indeed a significant impact on the heat and moisture transfer. The longer the air path, the greater the heat transfer between the infiltrating air and the walls. Moreover wood is hygroscopic unlike other wall components such as glass wool, and the impact of humid air leakage on the moisture risks depends therefore on which materials are in contact with the air flow.

The review on the experimental technique for the airtightness study showed that there are very few studies on the air path investigation inside wall assemblies and the only approach tested seems to be the implementation of 2-D or 3-D grid temperature and moisture content monitoring. An alternative method was therefore developed, consisting of seeding the air with fluorescein micro-particles to track its path inside the insulation layer. The particles are collected in the porous insulation material along the air flow, the insulation is then cut into small volumes and the fluorescein concentration is measured in each of them by spectrometry.

This method is time consuming and destructive but it has the great advantage of not being intrusive unlike the use of any type of sensor. It was tested on a number of preliminary tests which showed consistent results and a good repeatability of the measurement. They also pointed out a limitation due to relatively high collection efficiency: the absence of fluorescein far from the air inlet in the wall cannot be only explained by the absence of air flow but also possibly by a total upstream filtration of the particles. A fluorescein transport model was therefore developed to facilitate the comparison between the experimental fluorescein concentration mappings and the numerical velocity fields. The collection efficiency was measured experimentally for a range of velocity (0.2 – 1.5 m/s). It was found to be in good agreement with the Miecret and Gustavsson model that was therefore used for the extrapolation at smaller and higher velocities.

This method was then applied to a specific configuration: an air channel in contact with porous media. A simple analysis of the resulting fluorescein concentration mappings enabled to draw some conclusions on the impact of parameters such as the flow velocity or the insulation material on the air infiltration in the glass wool. It has also given evidences of phenomena such as the appearance of thin air gaps between the components of the wall assembly. The results were compared to a numerical study on COMSOL with the fluorescein transport model coupled to a CFD model. This enabled to point out significant differences in the air flow patterns. For angled air channels, the air infiltration was more concentrated in the corner than predicted by the simulation. The air dispersion inside the glass wool was also much smaller for the case without an airtight layer on the inlet side. And concerning straight channels, some fluorescein was found experimentally in the GW whereas the simulation does not predict an air infiltration.

Finally a case study was carried out to compare experimental techniques to each other and with the results of a numerical study. The tested configurations were simple wall assemblies made of glass wool and gypsum boards with a 20 mm in diameter hole. Two techniques enabled to investigate the air dispersion at the inlet/outlet of the insulation: the commonly used infrared thermography and

the PIV which was found to be also appropriate to such laboratory studies. The comparison with the numerical simulation showed a good agreement for the configuration with only one layer of glass wool: the air dispersion measured with both experimental techniques is similar to the area with velocities higher than 5% of  $v_{max}$  obtained numerically. However for the two insulation layer configuration the infiltrating flow velocities were too small compared to the convection flow to be measured by PIV, and the air dispersion measured by IRT was smaller than predicted numerically (by 31% for 5% of  $v_{max}$ ). Indeed, the smaller the velocities, the longer it takes for the flow to warm up the insulation material, and the less significant the temperature differences are since the insulation is cooled down by the ambient air at the meantime.

The air path inside the insulation layer was then investigated using three experimental approaches: a temperature monitoring with thermocouples; a relative humidity monitoring with capacitive sensors SHT 75; and the previously tested use of fluorescein tracer micro-particles. These experimental methods were again compared with each other and with a numerical model, to identify their respective benefits and limitations. It was found that the use of thermocouples enables a low intrusiveness, a good accuracy and responsiveness. However, as for the IRT, this method is based on the heat transfer study to track the air path which raises the issues of thermal inertia and conduction. On the other hand, the relative humidity sensor allow a relative vapor pressure mapping that can more easily be correlated with the air path in non-hygroscopic materials, but the significant intrusiveness was demonstrated by pressurization tests and observed in the resulting mappings with wider air dispersion. Finally the main advantage of the use of fluorescein micro-particles is that it is a non-intrusive method. However, as for the temperature, the concentration mapping is not very easily correlated with the velocity field. The absence of fluorescein far from the air inlet can indeed reflect an absence of flow rate but can also result from the total fluorescein filtration along the air path. In order to avoid this confusion, the air transfer model can be coupled to a filtration one, but a good knowledge of the micro-particles collection efficiency as a function of the air velocity is required.

## **Contribution of the work and perspectives**

This study contributes to evaluating the impact of air infiltration on building's performance on several aspects and scales, as summarized below.

### **Models for combining natural infiltration and mechanical ventilation**

At the building scale, models were developed to combine natural infiltration with unbalanced mechanical ventilation. They can be used for different applications depending on whether the time-period of concern is short or long and whether it is a forward or inverse problem:

- Hourly, Forward Case: for the hourly air change rate prediction; useful for estimating energy loads and needed for relative exposure calculations.
- Annual, Forward Case: predicting the annual effective ventilation given the effective infiltration and a fixed (or effective) fan flow; for indoor air quality (IAQ) purposes.
- Hourly, Inverse Case: when one wants to vary the fan size each hour to compensate for varying hourly infiltration in order to keep the total ventilation constant. This could be used in future smart ventilation system controls.



- Annual, Inverse Case: for finding the fixed fan size that will combine with effective infiltration to produce a desired total ventilation; useful for building codes/standards applications such as ASHRAE Standard 62.2.

### **Contribution to quantifying the air leakage induced by specific construction details**

The results of the pressurization tests presented in this study can be directly used to evaluate the impact of specific wall assemblies and construction details on the air permeability. As an example, the additional air leakage due to the absence of sealing between the gypsum boards may be linearized by the length of the junction, which enables to estimate the airflow rate per meter of unsealed junctions at a given pressure. These results may also be used for building scale numerical simulations.

### **Feasibility of experimental methods for the air path study within the wall assembly**

Due to very few previous experimental studies for the air path investigation within a wall assembly, several methods were developed and tested for this application. Fluorescein micro-particles are commonly used as tracer particles but the applicability was verified to track the airflow inside a porous insulation material, and a specific experimental protocol was developed. It was also verified that the PIV technique can be used to visualize the air infiltration despite rather large tracer particles.

### **Help in the selection of the experimental method for the air path study**

This study has shown that each experimental method has benefits but also disadvantages, and there is therefore no perfect method that can be applied to any configuration. The choice of the most appropriate approach depends strongly on the scope of the study. As an example, for in-situ measurements IRT will be preferred to PIV, and while the wall can possibly be instrumented with temperature and RH sensors during the construction phase, the use of the fluorescein method is inconceivable since it is destructive. On the other hand fluorescein measurements may be a better option for relatively short air path studies to avoid any intrusiveness or if volume and time averaged results are preferred to local measurements.

### **Numerical model validation**

Furthermore, it has been pointed out that timber-frame wall assemblies differ from one building to another, and if common sources of air leakage are well-known, there are a countless number of airtightness defects configurations. It is therefore inconceivable to characterize experimentally every single construction detail but reliable experimental data on specific configurations are of interest for numerical model validations. It is however not possible to measure directly the air velocity inside the wall assembly since the sensors would be too intrusive. As an alternative temperature, vapor pressure and fluorescein concentrations mappings can be obtained but the relation is not direct between these parameters and the velocity fields. A micro-particles collection efficiency model was developed to facilitate this comparison for the use of fluorescein, but it can be further improved, in particular with a better characterization of the particles size dispersion. Concerning the temperature and RH monitoring, it is also possible to use coupled heat air and moisture models for a finer analysis.

In this study many experimental configurations were tested and each time the parameters have been explicitly specified. It is therefore possible to simulate these tests with any numerical model and compare the results with the experimental measurements.

### **Transport of outdoor air contaminants through the wall assembly**

The experimental investigation of the air transfer inside timber frame wall assemblies is therefore of interest both to characterize the impact of specific construction details and to validate numerical tools with which many more configurations can be tested. Another practical application is the indoor air quality, and more specifically the transport of outdoor air contaminants through the wall assembly. It has not been discussed in this study, but this problematic is closely linked with the fluorescein transport. Fluorescein tests results, together with detailed parameters of the glass wool material, can therefore allow for filtration models validation. The Miecret and Gustavsson model used in this study seems to show that the percentage of particles passing through a 10 cm thick glass wool (HPGW) layer is possibly significant (> 5%) only for small particles ranging from 0.05  $\mu\text{m}$  to 0.5  $\mu\text{m}$  and a flow velocity ranging from 0.1 m/s to 3 m/s. Such models can be applied to various insulation materials, thicknesses, infiltration velocities and pollutants to evaluate the risk of contamination from the outdoor air in specific configurations.



# Publications

## Journal Publications

- Nolwenn Hurel, Max H. Sherman, and Iain S. Walker, "Sub-additivity in combining infiltration with mechanical ventilation for single zone buildings," *Building and Environment*, vol. 98, pp. 89–97, Mar. 2016.
- Nolwenn Hurel, Mickaël Pailha, and Monika Woloszyn, "Impact of different construction details on air permeability of timber frame wall assemblies: some experimental evidences from a three-scale laboratory study," *Journal of Building Physics*, Nov. 2016.

## Publication in Proceedings of International Conferences

- Nolwenn Hurel, Max H. Sherman, and Iain S. Walker, "Simplified Methods for Combining Natural and Mechanical Ventilation," in *Proceedings of the 36th AIVC Conference*, Madrid, Spain, 2015, pp. 840–850.
- Nolwenn Hurel, Mickaël Pailha, Géraldine Garnier, Clément Belleudy, and Monika Woloszyn, "Contribution to the Wooden-Frame Wall Assemblies Airtightness Tests: a Three-scale Laboratory Study," in *Proceedings of the 12th REHVA World Congress (CLIMA)*, Aalborg, Denmark, 2016, vol. 2.
- Nolwenn Hurel, Mickaël Pailha, and Monika Woloszyn, "Innovative use of fluorescein microparticles for the air path study through airtightness defects in timber frame wall assemblies," in *Proceedings of the 14th International Conference of Indoor Air Quality and Climate (INDOOR AIR)*, Ghent, Belgium, 2016.

## Publication in Proceedings of National Conferences

- Clément Belleudy, Nolwenn Hurel, Marx Chhay, Mickaël Pailha, Monika Woloszyn, Daniel Quenard, Géraldine Garnier, "Démarche pour l'étude de l'impact des transferts d'air liés aux défauts d'étanchéité sur le comportement de l'enveloppe des bâtiments à ossature bois", Conférence IBPSA France, Arras, May 2014  
(Best paper award)

## **Report Publication**

- Nolwenn Hurel, Max H. Sherman, and Iain S. Walker, "Simplified Methods for Combining Natural and Mechanical Ventilation," *Rep. Number LBNL-184001*, 2015.

# References

- [1] ADEME, “Mix électrique 100% renouvelable ? Analyses et optimisations,” 2015.
- [2] L. Pérez-Lombard, J. Ortiz, and C. Pout, “A review on buildings energy consumption information,” *Energy Build.*, vol. 40, no. 3, pp. 394–398, 2008.
- [3] R. Carrié, R. Jobert, M. Fournier, S. Berthault, and H. Van Elslande, “Perméabilité à l’air de l’enveloppe des bâtiments- généralités et sensibilisation,” CETE de Lyon, ISRN EQ-CT69-DVT/RE, 2006.
- [4] J. M. Logue, M. H. Sherman, I. S. Walker, and B. C. Singer, “Energy impacts of envelope tightening and mechanical ventilation for the U.S. residential sector,” *Energy Build.*, vol. 65, pp. 281–291, Oct. 2013.
- [5] B. Jones *et al.*, “Assessing uncertainty in housing stock infiltration rates and associated heat loss: English and UK case studies,” *Build. Environ.*, vol. 92, pp. 644–656, Oct. 2015.
- [6] A. Litvak, “Campagne de mesure de l’étanchéité à l’air de 123 logements,” CETE Sud Ouest, DAI.GVCH.05.10. ADEME-DGUHC, 2005.
- [7] M. Airaksinen, P. Pasanen, J. Kurnitski, and O. Seppänen, “Microbial contamination of indoor air due to leakages from crawl space: a field study,” *Indoor Air*, vol. 14, no. 1, pp. 55–64, Feb. 2004.
- [8] P. I. Sandberg and E. Sikander, “Airtightness issues in the building process,” in *Proceedings to the 7th Symposium on Building Physics in the Nordic Countries*, Reykjavik, 2005.
- [9] V. Iordache and T. Catalina, “Acoustic approach for building air permeability estimation,” *Build. Environ.*, vol. 57, pp. 18–27, Nov. 2012.
- [10] S. Tykkä *et al.*, “Development of timber framed firms in the construction sector — Is EU policy one source of their innovation?,” *For. Policy Econ.*, vol. 12, no. 3, pp. 199–206, Mar. 2010.
- [11] P. CORCIER, “Maison à ossature bois Présentation,” *Tech. Ing. Tech. Bâtim. Constr. Dév. Durable*, vol. base documentaire : TIE820DUO., no. ref. article : tba1720, 2016.
- [12] L. Gustavsson and R. Sathre, “Variability in energy and carbon dioxide balances of wood and concrete building materials,” *Build. Environ.*, vol. 41, no. 7, pp. 940–951, Jul. 2006.
- [13] T. Goverse, M. P. Hekkert, P. Groenewegen, E. Worrell, and R. E. H. . Smits, “Wood innovation in the residential construction sector; opportunities and constraints,” *Resour. Conserv. Recycl.*, vol. 34, no. 1, pp. 53–74, Dec. 2001.
- [14] J. Langmans, “Feasibility of exterior air barriers in timber frame construction,” KU Leuven, 2013.
- [15] B. Hrubá, P. Oravec, and J. Labudek, “Diagnostics and optimalization of airtightness in experimental wooden structures,” *Adv. Mater. Res.*, no. 1020, p. 540, Sep. 2014.
- [16] R. Jobert, *Perméabilité à l’air de l’enveloppe. Réglementation, risques, mesure et amélioration. En application de la RT 2012*. CSTB, 2012.
- [17] M. H. Sherman and L. Palmiter, “Uncertainties in fan pressurization measurements,” in *Airflow Performance of Building Envelopes, Components, and Systems*, 1995, pp. 266–283.
- [18] M. H. Sherman and R. Chan, “Building Airtightness: Research and Practice,” Berkeley, USA, Lawrence Berkeley national laboratory report no. LBNL-53356, 2004.

- [19] M. W. Liddament, *A guide to energy efficient ventilation*. Coventry, UK: AICV, AIC-TN-VENTGUIDE, 1996.
- [20] I. S. Walker, M. H. Sherman, J. Joh, and W. R. Chan, "Applying Large Datasets to Developing a Better Understanding of Air Leakage Measurement in Homes," *Int. J. Vent. VEETECH Ltd*, vol. 11–4, pp. 323–338, Feb. 2013.
- [21] A. Persily, "Repeatability and Accuracy of Pressurization Testing," in *ASHRAE/DOE Conference "Thermal performance of the exterior envelope of the building II,"* USA, 1982, pp. 380–390.
- [22] F. . Carrié and V. Leprince, "Model error due to steady wind in building pressurization tests," in *35th AIVC Conference " Ventilation and airtightness in transforming the building stock to high performance,"* Poznań, Poland, 2014.
- [23] T. Kalamees, "Air tightness and air leakages of new lightweight single-family detached houses in Estonia," *Build. Environ.*, vol. 42, no. 6, pp. 2369–2377, Jun. 2007.
- [24] S. Molleti, B. A. Baskaran, P. Beaulieu, and D. Van Reenen, "Air intrusion and its impact on energy performance of roofing assemblies," *Energy Build.*, vol. 42, no. 1, pp. 123–135, Jan. 2010.
- [25] A. Bailly, G. Guyot, and V. Leprince, "6 years of envelope airtightness measurements performed by French certified operators: analyses of about 65,000 tests," in *36th AIVC Conference " Effective ventilation in high performance buildings,"* Madrid, Spain, 2015.
- [26] M. Pinto, J. Viegas, and V. P. de Freitas, "Air permeability measurements of dwellings and building components in Portugal," *Build. Environ.*, vol. 46, no. 12, pp. 2480–2489, Dec. 2011.
- [27] W. R. Chan, J. Joh, and M. H. Sherman, "Analysis of air leakage measurements of US houses," *Energy Build.*, vol. 66, pp. 616–625, Nov. 2013.
- [28] A. K. Kim and C. Y. Shaw, "Seasonal Variation in Airtightness of Two Detached Houses," in *Measured Air Leakage of Buildings*, H. R. Trechsel and P. L. Lagus, Eds., American Society for Testing and Materials, 1986, pp. 17–32.
- [29] C. Delmotte and J. Laverge, "Interlaboratory Tests for the Determination of Repeatability and Reproducibility of Buildings Airtightness Measurements," in *AIVC Conference*, Brussels, Belgium, 2011.
- [30] W. Bracke, J. Laverge, N. V. D. Bossche, and A. Janssens, "Durability and Measurement Uncertainty of Airtightness in Extremely Airtight Dwellings," *Int. J. Vent.*, vol. 14, no. 4, pp. 383–394, Mar. 2016.
- [31] J. T. Reardon, "Balanced fan depressurization method for measuring component and overall air leakage in single- and multifamily dwellings," *ASHRAE Trans.*, vol. 93, no. 2, pp. 137–152, 1987.
- [32] S. Gustavsen, "Interzonal airflows in five Danish homes during two seasons," 2012.
- [33] G. Guyot, J. Ferlay, E. Gonze, M. Woloszyn, P. Planet, and T. Bello, "Multizone air leakage measurements and interactions with ventilation flows in low-energy homes," *Build. Environ.*, vol. 107, pp. 52–63, Oct. 2016.
- [34] CEN, "BS EN 15242:2007-Ventilation for Buildings. Calculation Methods for the Determination of Air Flow Rates in Buildings Including Infiltration." 2007.
- [35] JO, "Annexe à l'arrêté portant approbation de la méthode de calcul Th-BCE 2012," in *Méthode de calcul Th-BCE 2012*, 2011, p. 1377.
- [36] E. L. Hult and M. H. Sherman, "Estimates of Uncertainty in Multi-Zone Air Leakage Measurements," *Int. J. Vent.*, vol. 12, no. 4, pp. 359–368, Mar. 2014.
- [37] M. Labat, M. Woloszyn, G. Garnier, and J. J. Roux, "Assessment of the air change rate of airtight buildings under natural conditions using the tracer gas technique. Comparison with numerical modelling," *Build. Environ.*, vol. 60, pp. 37–44, Feb. 2013.
- [38] M.-H. Kim, J.-H. Jo, and J.-W. Jeong, "Feasibility of building envelope air leakage measurement using combination of air-handler and blower door," *Energy Build.*, vol. 62, pp. 436–441, Jul. 2013.

- [39] J.-W. Jeong, J. Firrantello, W. P. Bahnfleth, J. D. Freihaut, and A. Musser, "Case studies of building envelope leakage measurement using an air-handler fan pressurisation approach," *Build. Serv. Eng. Res. Technol.*, vol. 29, no. 2, pp. 137–155, May 2008.
- [40] Y. Billard, G. Debicki, and L. Coudert, "Leakage rate through a non-cracked concrete wall, comparison between two situations: Air pressure test and accident conditions," *Nucl. Eng. Des.*, vol. 235, no. 17–19, pp. 2109–2123, Aug. 2005.
- [41] T.-O. Relander, G. Bauwens, S. Roels, J. V. Thue, and S. Uvsløkk, "The influence of structural floors on the airtightness of wood-frame houses," *Energy Build.*, vol. 43, no. 2–3, pp. 639–652, Feb. 2011.
- [42] T.-O. Relander, B. Heiskel, and J. S. Tyssedal, "The influence of the joint between the basement wall and the wood-frame wall on the airtightness of wood-frame houses," *Energy Build.*, vol. 43, no. 6, pp. 1304–1314, Jun. 2011.
- [43] T. Z. Desta, J. Langmans, and S. Roels, "Experimental data set for validation of heat, air and moisture transport models of building envelopes," *Build. Environ.*, vol. 46, no. 5, pp. 1038–1046, May 2011.
- [44] C. Inard, E. Liberge, O. Martin, and D. Covalet, "Rapport d'étude sur l'étude expérimentale des infiltrations et intégration numérique à l'échelle du bâtiment," Livrable de la tâche 2.2 du projet PREBAT-MININFIL, 2011.
- [45] M. H. Sherman, D. T. Grimsrud, and R. C. Sonderegger, "The Low Pressure Leakage Function of a Building," in *ASHRAE-DOE Conference on Thermal Performance of Exterior Envelopes of Buildings*, 1979, vol. 28.
- [46] K. Siren, "A modification of the power-law equation to account for large scale wind turbulence," in *18th AIVC Conference "Ventilation and Cooling"*, Athens, Greece, 1997.
- [47] Y. Watanabe, H. Kobayashi, and Y. Utsumi, "Development of validation of AC-pressurization measuring of leakage area of houses," in *Building Simulation '99*, Kyoto, Japan, 1999, pp. 807–814.
- [48] S. Sharples and D. Thompson, "Experimental study of crack flow with varying pressure differentials," in *17th AIVC Conference "Optimum Ventilation and Air Flow Control in Buildings"*, Gothenburg, Sweden, 1996.
- [49] T. Nishioka, Q. Chen, N. Arai, K. Fujiwara, N. Umemiya, and R. Okura, "Unsteady pressurization method to measure the airtightness of the building envelope," in *Research in building physics international conference*, 2003, pp. 771–776.
- [50] B. Mattsson and J. Claesson, "A transient pressurization method for measurements of airtightness (English)," *J. Build. Phys.*, vol. 31, no. 1, pp. 35–53, 2007.
- [51] P. S. Carey and D. W. Etheridge, "Leakage measurements using unsteady techniques with particular reference to large buildings," *Build. Serv. Eng. Res. Technol.*, vol. 22, no. 2, pp. 69–82, May 2001.
- [52] E. W. Cooper and D. W. Etheridge, "Measurement of building leakage by unsteady pressurisation," in *25th AIVC Conference "Ventilation and retrofitting"*, Prague, Czech Republic, 2004.
- [53] E. Cooper *et al.*, "Field trialling of a new airtightness tester in a range of UK homes," in *36th AIVC Conference "Effective ventilation in high performance buildings"*, Madrid, Spain, 2015.
- [54] M. H. Sherman, "Uncertainty in air flow calculations using tracer gas measurements," *Build. Environ.*, vol. 24, no. 4, pp. 347–354, 1989.
- [55] P. Wegerer and T. Bednar, "Method for measuring the air-tightness of facing formworks," in *10th Nordic Symposium on Building Physics*, Lund, 2014, pp. 102–109.
- [56] M. Sherman, "The Use of Blower-Door Data1," *Indoor Air*, vol. 5, no. 3, pp. 215–224, 1995.
- [57] A. Sfakianaki *et al.*, "Air tightness measurements of residential houses in Athens, Greece," *Build. Environ.*, vol. 43, no. 4, pp. 398–405, Apr. 2008.
- [58] G. Benedetto, *A relation between transmission loss and air infiltration characteristics in windows*, 1. ed. Ist. Elettrotecn. Nazion. G. Ferraris, 1980.



- [59] T. Sonoda and F. Peterson, "A sonic method for building air-leakage measurements," *Appl. Energy*, vol. 22, no. 3, pp. 205–224, 1986.
- [60] O. A. B. Hassan, "An alternative method for evaluating the air tightness of building components," *Build. Environ.*, vol. 67, pp. 82–86, Sep. 2013.
- [61] K. Varshney, J. E. Rosa, I. Shapiro, and D. Scott, "Air-Infiltration Measurements in Buildings Using Sound Transmission Loss Through Small Apertures," *Int. J. Green Energy*, vol. 10, no. 5, pp. 482–493, May 2013.
- [62] X. Maldague, "Applications Of Infrared Thermography In Nondestructive Evaluation," 2000.
- [63] A. Kyllili, P. A. Fokaides, P. Christou, and S. A. Kalogirou, "Infrared thermography (IRT) applications for building diagnostics: A review," *Appl. Energy*, vol. 134, pp. 531–549, Dec. 2014.
- [64] C. A. Balaras and A. A. Argiriou, "Infrared thermography for building diagnostics," *Energy Build.*, vol. 34, no. 2, pp. 171–183, Feb. 2002.
- [65] T. Taylor, J. Counsell, and S. Gill, "Energy efficiency is more than skin deep: Improving construction quality control in new-build housing using thermography," *Energy Build.*, vol. 66, pp. 222–231, Nov. 2013.
- [66] G. Desmarais, "Impact of added insulation on the hygrothermal performance of leaky exterior wall assemblies," masters, Concordia University, 2000.
- [67] G. Desmarais, D. Derome, and P. Fazio, "Mapping of Air Leakage in Exterior Wall Assemblies," *J. Build. Phys.*, vol. 24, no. 2, pp. 132–154, Oct. 2000.
- [68] T. Ojanen and C. Simonson, "Convective Moisture Accumulation in Structures with Additional Inside Insulation," in *Proceedings of Thermal Performance of the Exterior Envelopes of Buildings VI*, Clearwater Beach, 1995, pp. 745–752.
- [69] K.-E. Peiponen, V. V. K. Karppinen, and R. Varonen, "The visualization of leakage flow through building cracks by means of holographic interferometry," *Opt. Laser Technol.*, vol. 18, no. 2, pp. 101–102, Apr. 1986.
- [70] K.-E. Peiponen and T. Hartikainen, "Visualization of simulated leakage flow from buildings using a pulsed laser," *Opt. Lasers Eng.*, vol. 10, no. 2, pp. 127–132, 1989.
- [71] K.-E. Peiponen, T. Hartikainen, and R. M. K. Hämäläinen, "Visualization of leakage flow in buildings," *Opt. Laser Technol.*, vol. 21, no. 4, pp. 273–275, Aug. 1989.
- [72] "EN ISO 9972, Determination of air permeability of buildings - Fan pressurization method." 2015.
- [73] H. M. Künzle, "Simultaneous heat and moisture transport in building components. One- and two-dimensional calculation using simple parameters," Fraunhofer IBP, 1995.
- [74] C. R. Buchanan and M. H. Sherman, "A mathematical model for infiltration heat recovery," Lawrence Berkeley National Laboratory, May 2000.
- [75] C.-E. Hagentoft *et al.*, "Assessment Method of Numerical Prediction Models for Combined Heat, Air and Moisture Transfer in Building Components: Benchmarks for One-dimensional Cases," *J. Therm. Envel. Build. Sci.*, vol. 27, no. 4, pp. 327–352, Apr. 2004.
- [76] F. Tariku, K. Kumaran, and P. Fazio, "Transient model for coupled heat, air and moisture transfer through multilayered porous media," *Int. J. Heat Mass Transf.*, vol. 53, no. 15–16, pp. 3035–3044, Jul. 2010.
- [77] C. Belleudy, M. Woloszyn, M. Chhay, and M. Cosnier, "A 2D model for coupled heat, air, and moisture transfer through porous media in contact with air channels," *Int. J. Heat Mass Transf.*, vol. 95, pp. 453–465, Apr. 2016.
- [78] L. Soudani, M. Woloszyn, A. Fabbri, A.-C. Grillet, and J.-C. Morel, "Energy evaluation of rammed earth wall with long term in situ measurements," in *CLIMA 2016 - 12th REHVA World Congress*, Aalborg, Denmark, 2016, vol. 3.
- [79] A.-M. Stefanoiu, M. Woloszyn, A. Jay, E. Wurtz, and C. Buhé, "A Methodology to Assess the Ambient Temperature of a Building using a Limited Number of Sensors," *6th Int. Build. Phys. Conf.*, 2015.

- [80] A. Tenwolde, C. Carll, and V. Malinauskas, "Airflows and moisture conditions in walls of manufactured homes," *ASTM STP 1255*, pp. 137–155, 1995.
- [81] W. Maref, M. Armstrong, M. Rousseau, and W. Lei, "A field monitoring investigation of the effect of adding different exterior thermal insulation materials on the hygrothermal Response of Wood-Frame Walls in a Cold Climate," presented at the BEST conference, Portland, 2010, pp. 1–15.
- [82] Z. Pavlik, J. Pavlik, M. Jirickova, and R. Cerny, "System for Testing the Hygrothermal Performance of Multi-Layered Building Envelopes," *J. Build. Phys.*, vol. 25, no. 3, pp. 239–249, Jan. 2002.
- [83] M. Hall and G. Hauser, "In situ Quantifizierung von Leckagen bei Gebäuden in Holzbauart," Universität Kassel, AIF-Forschungsvorhaben Nr. 12611 N, 2003.
- [84] J. Vinha, "Hygrothermal performance of timber-framed external walls in Finnish Climatic Conditions," PhD thesis, Tampere University of Technology, 2007.
- [85] P. Talukdar, S. O. Olutmayin, O. F. Osanyintola, and C. J. Simonson, "An experimental data set for benchmarking 1-D, transient heat and moisture transfer models of hygroscopic building materials. Part I: Experimental facility and material property data," *Int. J. Heat Mass Transf.*, vol. 50, no. 23–24, pp. 4527–4539, Nov. 2007.
- [86] A. Alturkistani, P. Fazio, J. Rao, and Q. Mao, "A new test method to determine the relative drying capacity of building envelope panels of various configurations," *Build. Environ.*, vol. 43, no. 12, pp. 2203–2215, Dec. 2008.
- [87] Q. Mao, P. Fazio, and J. Rao, "In-cavity evaporation allowance—A drying capacity indicator for wood-frame wall system," *Build. Environ.*, vol. 44, no. 12, pp. 2418–2429, Dec. 2009.
- [88] D. David, "Étude expérimentale de la convection naturelle aux abords de parois contenant des matériaux à changement de phase," Institut National des Sciences Appliquées de Lyon, CETHIL, 2010.
- [89] T. Kalamees and J. Kurnitski, "Moisture Convection Performance of External Walls and Roofs," *J. Build. Phys.*, vol. 33, no. 3, pp. 225–247, Jan. 2010.
- [90] M. Van Belleghem, M. Steeman, A. Willockx, A. Janssens, and M. De Paepe, "Benchmark experiments for moisture transfer modelling in air and porous materials," *Build. Environ.*, vol. 46, no. 4, pp. 884–898, Apr. 2011.
- [91] S. Pinard, *Etude d'une paroi ventilée multifonctionnelle adaptée à la rénovation énergétique des bâtiments par l'intérieur*. Grenoble, 2012.
- [92] H. M. Rafidiarison, *Etudes expérimentales des transferts de masse et de chaleur dans les parois des constructions en bois, en vue de leur modélisation. Applications aux économies d'énergie et au confort dans l'habitat*. Université de Lorraine, 2012.
- [93] Z. Slimani, "Analyse expérimentale et numérique du comportement hygrothermique de parois fortement hygroscopiques," Université de Lyon, Lyon, France, 2015.
- [94] C. Sanjuan, M. J. Suárez, E. Blanco, and M. del R. Heras, "Development and experimental validation of a simulation model for open joint ventilated façades," *Energy Build.*, vol. 43, no. 12, pp. 3446–3456, Dec. 2011.
- [95] B. Cretinon, "Hygromètres," *Tech. Ing. Mes. Gd. Thermophysiques*, vol. base documentaire : TIB544DUO., 2004.
- [96] T. Kalamees and J. Vinha, "Hygrothermal calculations and laboratory tests on timber-framed wall structures," *Build. Environ.*, vol. 38, no. 5, pp. 689–697, May 2003.
- [97] V. Ž. Leskovar and M. Premrov, "Influence of glazing size on energy efficiency of timber-frame buildings," *Constr. Build. Mater.*, vol. 30, pp. 92–99, May 2012.
- [98] M. Labat, *Chaleur – Humidité – Air dans les maisons à ossature bois : Expérimentation et modélisation*. Lyon, INSA, 2012.
- [99] M. Labat, M. Woloszyn, G. Garnier, and J. J. Roux, "Dynamic coupling between vapour and heat transfer in wall assemblies: Analysis of measurements achieved under real climate," *Build. Environ.*, vol. 87, pp. 129–141, May 2015.

- [100] R. McClung, H. Ge, J. Straube, and J. Wang, "Hygrothermal performance of cross-laminated timber wall assemblies with built-in moisture: field measurements and simulations," *Build. Environ.*, vol. 71, pp. 95–110, Jan. 2014.
- [101] J. Jokisalo, J. Kurnitski, M. Korpi, T. Kalamees, and J. Vinha, "Building leakage, infiltration, and energy performance analyses for Finnish detached houses," *Build. Environ.*, vol. 44, no. 2, pp. 377–387, Feb. 2009.
- [102] T.-O. Relander, J. V. Thue, and A. Gustavsen, "Air tightness performance of different sealing methods for windows in wood-frame buildings," *Nord. Symp. Build. Phys. Cph. Den.*, 2008.
- [103] N. Hurel, M. H. Sherman, and I. S. Walker, "Simplified Methods for Combining Natural and Mechanical Ventilation," *Rep. Number LBNL-184001*, 2015.
- [104] N. Hurel, M. H. Sherman, and I. S. Walker, "Sub-additivity in combining infiltration with mechanical ventilation for single zone buildings," *Build. Environ.*, vol. 98, pp. 89–97, Mar. 2016.
- [105] ASHRAE Standard 62.2-2013, "Ventilation and Acceptable Indoor Air Quality in Low-Rise Residential Buildings." Atlanta, GA: ASHRAE, 2013.
- [106] ASHRAE, *ASHRAE Handbook of Fundamentals*. Atlanta, GA, 2013.
- [107] Y. Li, "Simplified Method of Combining Natural and Exhaust Ventilation," *Clim. Build.*, vol. 2, pp. 29–35, 1990.
- [108] L. Palmiter and T. Bond, "Interaction of mechanical systems and natural infiltration," in *12th AIVC Conference*, Ottawa, Canada, 1991, pp. 285–295.
- [109] M. Modera and F. Peterson, "Simplified Methods for Combining Mechanical Ventilation and Natural Infiltration," Lawrence Berkeley National Laboratory, LBNL Paper LBL-18955, 1985.
- [110] D. Kiel and D. J. Wilson, "Influence of natural infiltration on total building ventilation dominated by strong fan exhaust," *ASHRAE Trans.*, vol. 93 (Part 2), 1987.
- [111] D. J. Wilson and I. S. Walker, "Combining Air Infiltration And Exhaust Ventilation," in *Indoor Air '90*, Toronto, Canada, 1990, pp. 467–472.
- [112] W. P. Levins, "Measured Effect of Forced Ventilation on House Infiltration Rate," presented at the ASHRAE/DOE Thermal Performance of the Exterior Envelopes of Buildings II Conference, Las Vegas, 1982.
- [113] C. Y. Shaw, "Methods for Estimating Air Change Rates and Sizing Mechanical Ventilation Systems for Houses," Division of Building Research, National Research Council of Canada, Building Research Note 237(5th edition), 1985.
- [114] W. J. N. Turner and I. S. Walker, "Using a ventilation controller to optimise residential passive ventilation for energy and indoor air quality," *Build. Environ.*, vol. 70, pp. 20–30, Dec. 2013.
- [115] I. Walker, "Attic Ventilation, Heat and Moisture Transfer," University of Alberta, Edmonton, Alberta, Canada., 1993.
- [116] M. H. Sherman and D. J. Wilson, "Relating actual and effective ventilation in determining indoor air quality," *Build. Environ.*, vol. 21, no. 3–4, pp. 135–144, 1986.
- [117] N. Hurel, M. Pailha, G. Garnier, and M. Woloszyn, "Impact of different construction details on air permeability of timber frame wall assemblies: Some experimental evidences from a three-scale laboratory study," *J. Build. Phys.*, Nov. 2016.
- [118] C. Belleudy *et al.*, "Démarche pour l'étude de l'impact des transferts d'air liés aux défauts d'étanchéité sur le comportement de l'enveloppe des bâtiments à ossature bois," presented at the IBPSA France, Arras, France, 2014.
- [119] CETE de Lyon, "Carnets Prebat Minifil, Mémento étanchéité - Construction Ossature Bois - Isolation Thermique Intégrée," Nov. 2010.
- [120] S. K. Suneja and C. H. Lee, "Aerosol filtration by fibrous filters at intermediate reynolds number (<100)," *Atmos. Environ.*, vol. 8, pp. 1081–1094, 1974.
- [121] D. Thomas, "Etude de la filtration des aerosols par des filtres à fibres," Université Henri Poincare, Laboratoire des sciences du génie chimique CNRS, 2001.

- [122] A. Tamayol and M. Bahrami, "Numerical investigation of flow in fibrous porous media," presented at the ECI International Conference on Heat Transfer and Fluid Flow in Microscale, Whistler, 2008.
- [123] Z. Zeng and R. Grigg, "A Criterion for Non-Darcy Flow in Porous Media," *Transp. Porous Media*, vol. 63, no. 1, pp. 57–69, Apr. 2006.
- [124] J. Langmans, R. Klein, and S. Roels, "Hygrothermal risks of using exterior air barrier systems for highly insulated light weight walls: A laboratory investigation," *Build. Environ.*, vol. 56, pp. 192–202, Oct. 2012.
- [125] J. Kronvall, *Air flows in building components*. Division of Building Technology, Lund Institute of Technology, 1980.
- [126] M. K. Kumaran, "Heat, Air and Moisture Transport. Final Report, Vol 3, Task 3: Material Properties," Laboratorium Bouwfysica, K.U., Leuven, Belgium, International Energy Agency Annex 24, 1996.
- [127] Ø. Økland, "Convection in highly-insulated building structures," PhD thesis, Norwegian University of Science and Technology, Trondheim, Norway, 1998.
- [128] L. Marmoret, M. Lewandowski, and A. Perwuelz, "An Air Permeability Study of Anisotropic Glass Wool Fibrous Products," *Transp. Porous Media*, vol. 93, no. 1, pp. 79–97, May 2012.
- [129] F. A. Dullien, *Porous Media, Fluid Transport and Pore Structure*, Academic Press. 1992.
- [130] S. Roy, M. Junk, and S. Sundar, "Understanding the porosity dependence of heat flux through glass fiber insulation," *Math. Comput. Model.*, vol. 43, no. 5–6, pp. 485–492, Mar. 2006.
- [131] R. Vallabh, P. Banks-Lee, and A. M. Seyam, "New approach for determining tortuosity in fibrous Porous Media," *J. Eng. Fibers Fabr.*, vol. 5, no. 3, 2010.
- [132] A. Piot, M. Woloszyn, J. Brau, and C. Abele, "Experimental wooden frame house for the validation of whole building heat and moisture transfer numerical models," *Energy Build.*, vol. 43, no. 6, pp. 1322–1328, Jun. 2011.
- [133] M. H. Sherman and I. S. Walker, "Heat Recovery in Building Envelopes," *Lawrence Berkeley Natl. Lab.*, Jan. 2001.
- [134] Z. Gao and J. S. Zhang, "Modeling Particle Penetrations Through Wall Assemblies Using Computational Fluid Dynamics," *Aerosol Sci. Technol.*, vol. 49, no. 3, pp. 167–178, Mar. 2015.
- [135] K. W. Cheong, "Airflow measurements for balancing of air distribution system — tracer-gas technique as an alternative?," *Build. Environ.*, vol. 36, no. 8, pp. 955–964, Oct. 2001.
- [136] L. Gutowski, O. Olsson, J. Lange, and K. Kümmerer, "Photolytic transformation products and biological stability of the hydrological tracer Uranine," *Sci. Total Environ.*, vol. 533, pp. 446–453, Nov. 2015.
- [137] M. S. El-Shobokshy, "Experimental measurements of aerosol deposition to smooth and rough surfaces," *Atmospheric Environ. 1967*, vol. 17, no. 3, pp. 639–644, Jan. 1983.
- [138] M. R. Sippola and W. W. Nazaroff, "Experiments Measuring Particle Deposition from Fully Developed Turbulent Flow in Ventilation Ducts," *Aerosol Sci. Technol.*, vol. 38, no. 9, pp. 914–925, Sep. 2004.
- [139] D. Maro *et al.*, "Aerosol dry deposition in the urban environment: Assessment of deposition velocity on building facades," *J. Aerosol Sci.*, vol. 69, pp. 113–131, Mar. 2014.
- [140] G. Menard, "Contribution a l'étude de la microfiltration tangentielle des gaz," Université de Savoie, Chambéry, France, 1990.
- [141] R. Boichot, "Filtration des particules issues des moteurs Diesel par matrices fibreuses plongées dans un champ électrique," Université de Savoie, 2005.
- [142] R. Sjöback, J. Nygren, and M. Kubista, "Absorption and fluorescence properties of fluorescein," *Spectrochim. Acta. A. Mol. Biomol. Spectrosc.*, vol. 51, no. 6, pp. L7–L21, Jun. 1995.
- [143] P. L. Smart and I. M. S. Laidlaw, "An evaluation of some fluorescent dyes for water tracing," *Water Resour. Res.*, vol. 13, no. 1, pp. 15–33, Feb. 1977.
- [144] C. Y. Chen, "Filtration of Aerosols By Fibrous Media," *Chem. Rev.*, vol. 55, no. 3, pp. 595–623, Jun. 1955.

- [145] A. F. Miguel, "Porous Media and Filtration," in *Emerging Technologies and Techniques in Porous Media*, D. B. Ingham, A. Bejan, E. Mamut, and I. Pop, Eds. Springer Netherlands, 2004, pp. 419–431.
- [146] M. M. El-Halwagi, "Mathematical Modeling of Aerosol Collection in Fluidized-Bed Filters," *Aerosol Sci. Technol.*, vol. 13, no. 1, pp. 102–115, Jan. 1990.
- [147] G. Miecret and J. Gustavsson, "Mathematic expression of HEPA and ULPA filters efficiency experimental verification - Practical alliance to new efficiency test methods," presented at the Contaminexpert, Versailles, France, 1989.
- [148] C. N. Davies, *Air filtration*, Academic Press-London-New York. 1973.
- [149] N. A. Fuchs, *The mechanics of aerosols*, Pergamon Press. Oxford, 1964.
- [150] I. B. Stechkina, A. A. Kirsh, and N. A. Fuchs, "Investigations of fibrous filters for aerosols calculation of aerosols deposition in model filters in the region of maximum particle breakthrough," vol. 31, pp. 121–126, 1969.
- [151] B. S. Kuwabara, "The forces experienced by randomly distributed parallel circular cylinders or spheres in a viscous flow at small reynolds numbers," *J. Phys. Soc. Jpn.*, vol. 14, no. 4, pp. 527–532, 1959.
- [152] P.-X. Thivel, *Contribution a l'etude des lits fluidises stabilises magnetiquement ; application a la filtration des gaz*. Chambéry, 1998.
- [153] R. Hall, L. Murdoch, R. Falta, B. Looney, and B. Riha, "Evaluation of liquid aerosol transport through porous media," *J. Contam. Hydrol.*, vol. 190, pp. 15–28, Jul. 2016.
- [154] A. Einstein, "Über die von der molekularkinetischen Theorie der Wärme geforderte Bewegung von in ruhenden Flüssigkeiten suspendierten Teilchen," *Ann. Phys.*, vol. 322, pp. 549–560, 1905.
- [155] R. E. Ewing and H. Wang, "A summary of numerical methods for time-dependent advection-dominated partial differential equations," *J. Comput. Appl. Math.*, vol. 128, no. 1–2, pp. 423–445, Mar. 2001.
- [156] C. Belleudy, "Modélisation des transferts d'air et leur impact sur le comportement hygrothermique de l'enveloppe des bâtiments," Université Grenoble Alpes, LOCIE, Chambéry, France, 2016.
- [157] H. C. Brinkman, "A calculation of the viscous force exerted by a flowing fluid on a dense swarm of particles," *Flow Turbul. Combust.*, vol. 1, no. 1, p. 27, Dec. 1949.
- [158] C. E. Willert and M. Gharib, "Three-dimensional particle imaging with a single camera," *Exp. Fluids*, vol. 12, no. 6, pp. 353–358, Apr. 1992.
- [159] A. Omrane, P. Petersson, M. Aldén, and M. A. Linne, "Simultaneous 2D flow velocity and gas temperature measurements using thermographic phosphors," *Appl. Phys. B*, vol. 92, no. 1, pp. 99–102, May 2008.
- [160] A. Melling, "Tracer particles and seeding for particle image velocimetry," *Meas. Sci. Technol.*, vol. 8, no. 12, p. 1406, 1997.
- [161] G. Cao, M. Sivukari, J. Kurnitski, M. Ruponen, and O. Seppänen, "Particle Image Velocimetry (PIV) application in the measurement of indoor air distribution by an active chilled beam," *Build. Environ.*, vol. 45, no. 9, pp. 1932–1940, Sep. 2010.
- [162] L. H. Mortensen, C. Rode, and R. Peuhkuri, "Investigation of airflow patterns in a microclimate by particle image velocimetry (PIV)," *Build. Environ.*, vol. 43, no. 11, pp. 1929–1938, Nov. 2008.
- [163] P. Karava, T. Stathopoulos, and A. K. Athienitis, "Airflow assessment in cross-ventilated buildings with operable façade elements," *Build. Environ.*, vol. 46, no. 1, pp. 266–279, Jan. 2011.
- [164] C. Sanjuan, M. N. Sánchez, R. Enríquez, and M. del R. H. Celemín, "Experimental PIV Techniques Applied to the Analysis of Natural Convection in Open Joint Ventilated Facades," *Energy Procedia*, vol. 30, pp. 1216–1225, 2012.
- [165] A. Trabelsi *et al.*, "Analyse de la réponse des capteurs," Projet ANR- 10-HABISOL-005 TACHE 1.3.1., 2013.

[166] O. Tetens, "Über einige meteorologische Begriffe," *Z. Für Geophys.*, vol. 6, pp. 297–309, 1930.



# Appendices





## A. Optimization of the advanced quadrature model

The advanced quadrature is similar to the quadrature model but with an additional correction term driven by the coefficient  $\beta$ :

$$Q_t = \sqrt{Q_f^2 + Q_{inf}^2 + \beta Q_f Q_{inf}} \quad (1)$$

If  $\beta=2$  this is the additivity model that will always overpredict  $Q_t$ . If  $\beta=0$  this is the simple quadrature model that tends to underpredict  $Q_t$ . So by taking intermediate values of  $\beta$  it is possible to get better predictions of  $Q_t$ .

For the forward model, the ideal advanced quadrature coefficient  $\beta$  verifying (21) is defined as follows:

$$\beta = \frac{Q_t^2 - Q_f^2 - Q_{inf}^2}{Q_f \cdot Q_{inf}} \quad (2)$$

As presented in Figure 1, the REGCAP simulation results were used to plot this coefficient for the hourly and annual data. The equally weighted averages are  $\bar{\beta} = 0.271$  for the hourly data and  $\bar{\beta} = 0.461$  for the annual one, but we can observe that the value depends highly on the infiltration fraction.

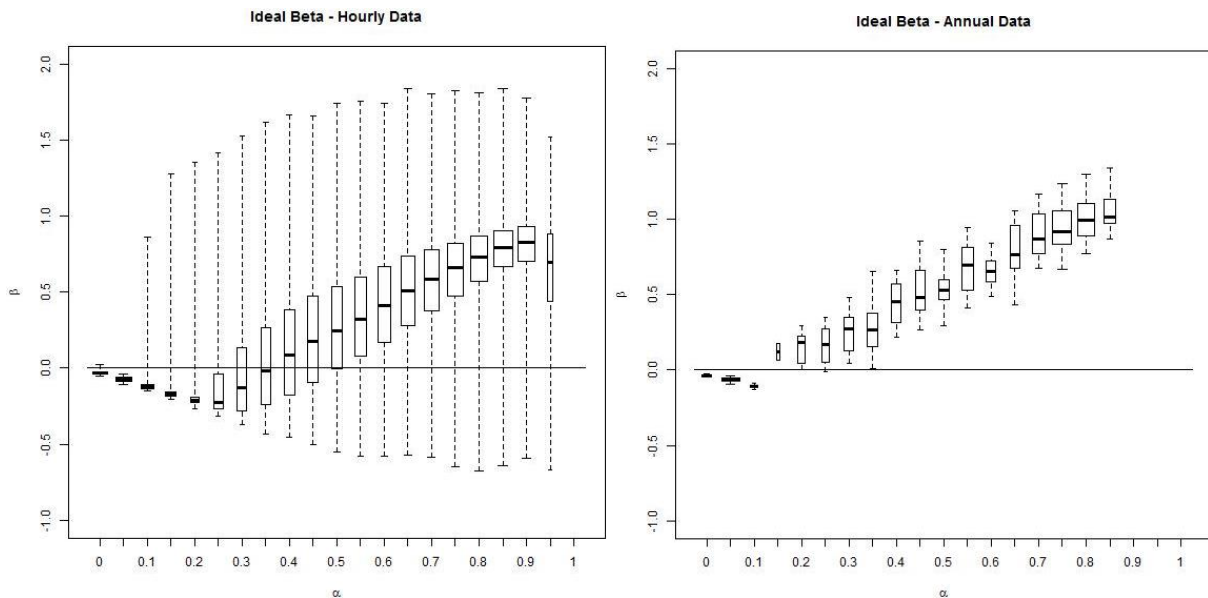


Figure 1 - Hourly and annual ideal advanced quadrature coefficient ( $\beta$ ) obtained with REGCAP

These averages give an idea of the best values to use, but a more detailed analysis of the biases and RMS errors presented in Figure 2 enables to select slightly better coefficients.

For the hourly data,  $\beta=0.3$  minimizes both the bias and RMS error for the forward model, and is also pretty close to the optimum point for the inverse one. Concerning the annual data,  $\beta=0.6$  minimizes

both the bias and RMS error for the inverse model, and is pretty close to the optimum point for the forward one.

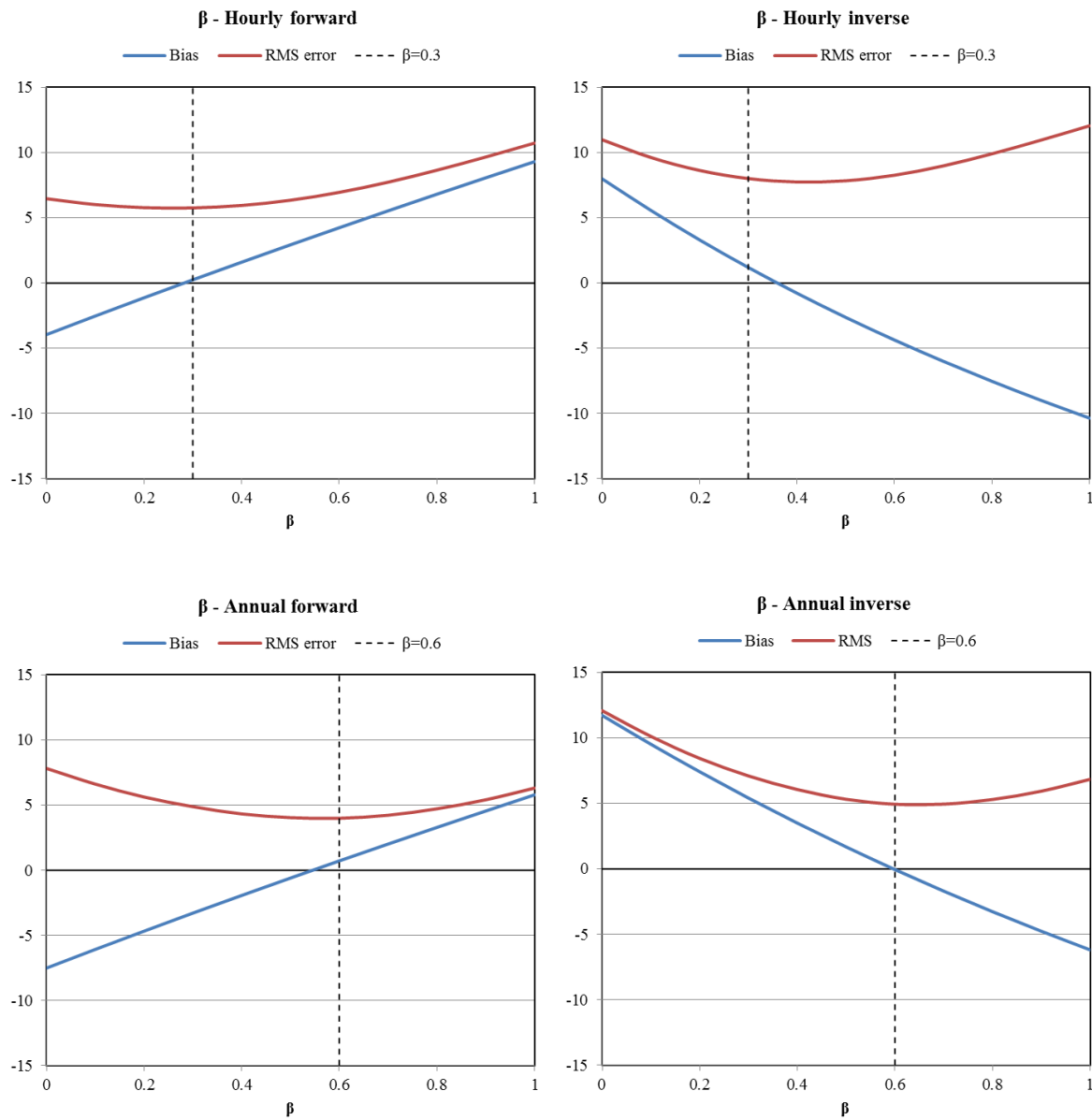


Figure 2 - Impact of the advanced quadrature coefficient  $\beta$  on the bias and RMS error for the forward and inverse models compared with the hourly and annual REGCAP data

## B. Optimization of the exponential models

We suggested three exponential superposition models:

- the exponential forward sub-additivity (EFSA):  $Q_t = Q_f + \exp\left(-k_{fw} \frac{Q_f}{Q_{inf}}\right) Q_{inf}$
- the exponential inverse sub-additivity (EISA):  $Q_f = Q_t - \exp\left(-k_{inv} \left(\frac{Q_t}{Q_{inf}} - 1\right)\right) Q_{inf}$
- the modified Levins sub-additivity (MLSA):  $Q_t = \exp\left(-k'_{fw} \frac{Q_{inf}}{Q_f}\right) Q_f + Q_{inf}$

The exponential coefficients  $k_{fw}$ ,  $k_{inv}$  and  $k'_{fw}$  are optimized to best approximate the simulation results. We have calculated for each model, and for both hourly and annual data, the bias and RMS error induced as a function of the exponential coefficient. The results are presented in Figure 9. As shown in Table 10 the minimum of the bias and RMS errors are obtained for the same or very close exponential coefficient values. The only exception is the hourly MLSA model, but the RMS error for the coefficient minimizing the bias is very close to the lowest one.

We chose to express the exponential coefficients as fractions. The only model for which it could be critical is the hourly EFSA with a selected coefficient of  $2/3$  instead of  $0.6$ . However, the RMS error are almost the same and the bias induced by the fraction is only 1%, which is considered small enough given the uncertainties due to the use of a simulation tool.

**Table 10: Optimized and selected values of the exponential coefficient for each model**

Model	Bias minimization	RMS error minimization	Selected coefficient
Hourly EFSA	$k_{fw} = 0.60$	$k_{fw} = 0.60$	$k_{fw} = \frac{2}{3} \approx 0.67$
Annual EFSA	$k_{fw} = 0.44$	$k_{fw} = 0.44$	$k_{fw} = \frac{4}{9} \approx 0.44$
Hourly EISA	$k_{inv} = 1.06$	$k_{inv} = 1.04$	$k_{inv} = 1$
Annual EISA	$k_{inv} = 0.66$	$k_{inv} = 0.67$	$k_{inv} = \frac{2}{3} \approx 0.67$
Hourly MLSA	$k'_{fw} = 0.69$	$k'_{fw} = 0.90$	$k'_{fw} = \frac{2}{3} \approx 0.67$
Annual MLSA	$k'_{fw} = 0.54$	$k'_{fw} = 0.58$	$k'_{fw} = 0.5$

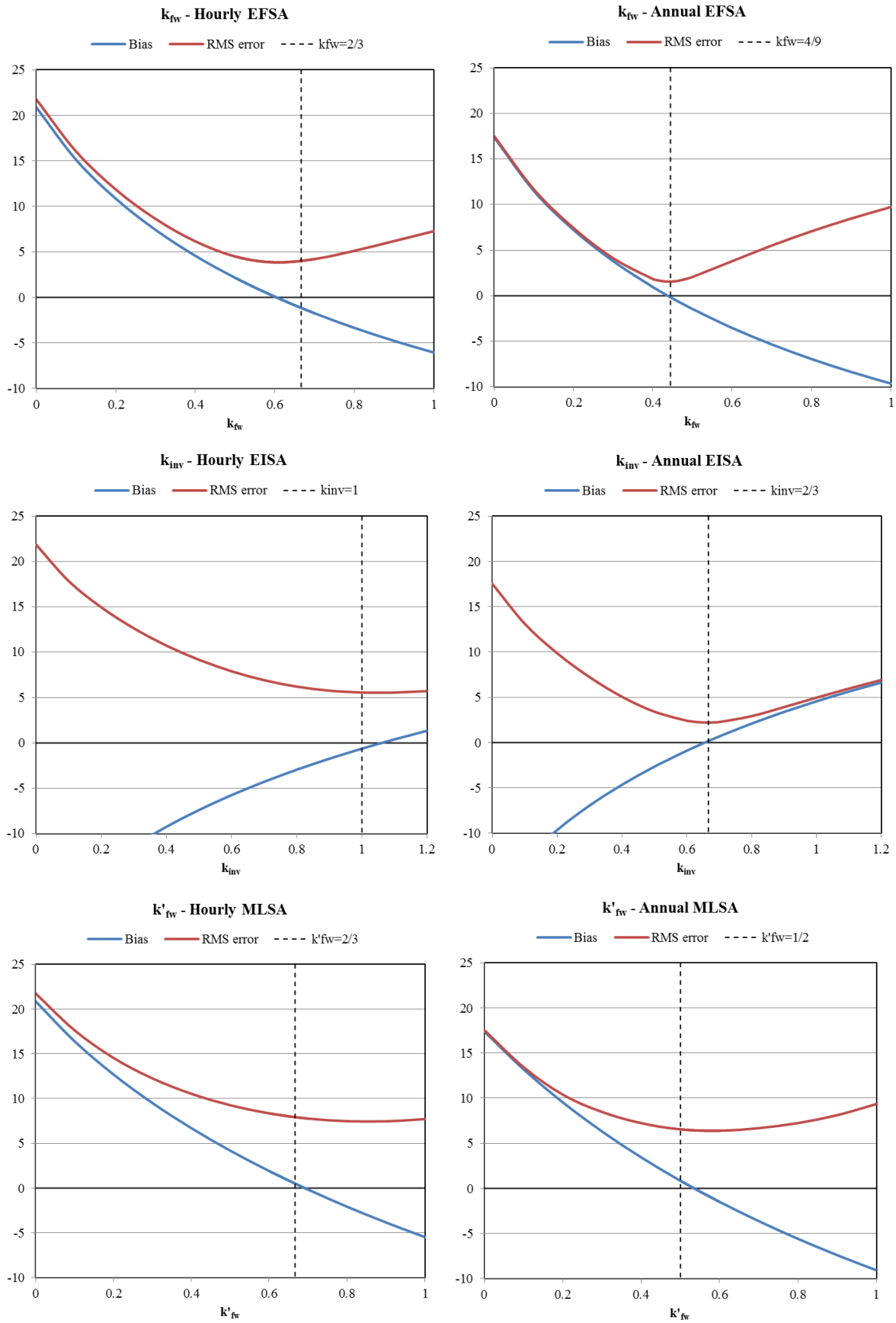


Figure 0.1 - Impact of the exponential coefficient on the bias and RMS error for the forward and inverse models compared with the hourly and annual REGCAP data

### C. Impact of the simulation parameters on the sub-additivity coefficients

In order to better understand the REGCAP simulation results, we have studied the impact of each input parameter on the sub-additivity coefficient. For this purpose, we used the annual data since it is much easier to display than the hourly one. Moreover, we used the forward case, which means that the coefficient is plot against  $\alpha_{fw} = Q_{inf}/(Q_t - Q_{inf})$ , but the inverse case would give the same conclusions.

The first plot shows the sub-additivity coefficient according to the airtightness level. The very tight houses with 0.6 ACH at 50Pa have a sub-additivity coefficient equal to zero: the total ventilation flow is the fan flow. This means that the fan induces a pressure difference between both sides of the envelope that is always bigger than the local dP induced by the stack and wind effect. As a result, for exhaust ventilation there will be no exfiltration through the envelope, and for supply ventilation there will be no infiltration. When the airtightness level decreases, a smaller fan flow is required. From 3 ACH,  $\Phi$  never equals to zero, which means that locally the wind and stack effects induce bigger pressure differences than the mechanical ventilation.

The second plot reveals two groups of data depending on the ventilation type. Simulations with supply fans give higher values of  $\Phi$  than the one with exhaust fans. This is due to the fact that the house is normally slightly depressurized in order to balance the flows under natural infiltration. Without mechanical ventilation the internal relative pressure is therefore negative. The exhaust fan makes it go more negative whereas the supply fan makes it go more towards zero and then positive. Because of the non-linear pressure-flow relationship and the interactions with the different leak locations, this leads to different effects for supply and exhaust systems. It means that two separate models could be created depending on the ventilation type. However, this distinction is not very relevant, because the differences in the two groups are small compared to the uncertainties due to the use of a simulation tool.

The number of stories has also a visible impact. The stack effect is amplified with the height of the building, which increases the infiltrations and therefore  $\alpha$ . On the contrary, the foundation type does not seem to have a big impact. Finally, in the last plot three cities are displayed among the eight simulated. Cold climates such as in Fairbanks, Alaska induce bigger temperature differences between the inside and outside of the house, which also increases the stack effect and therefore  $\alpha$ .

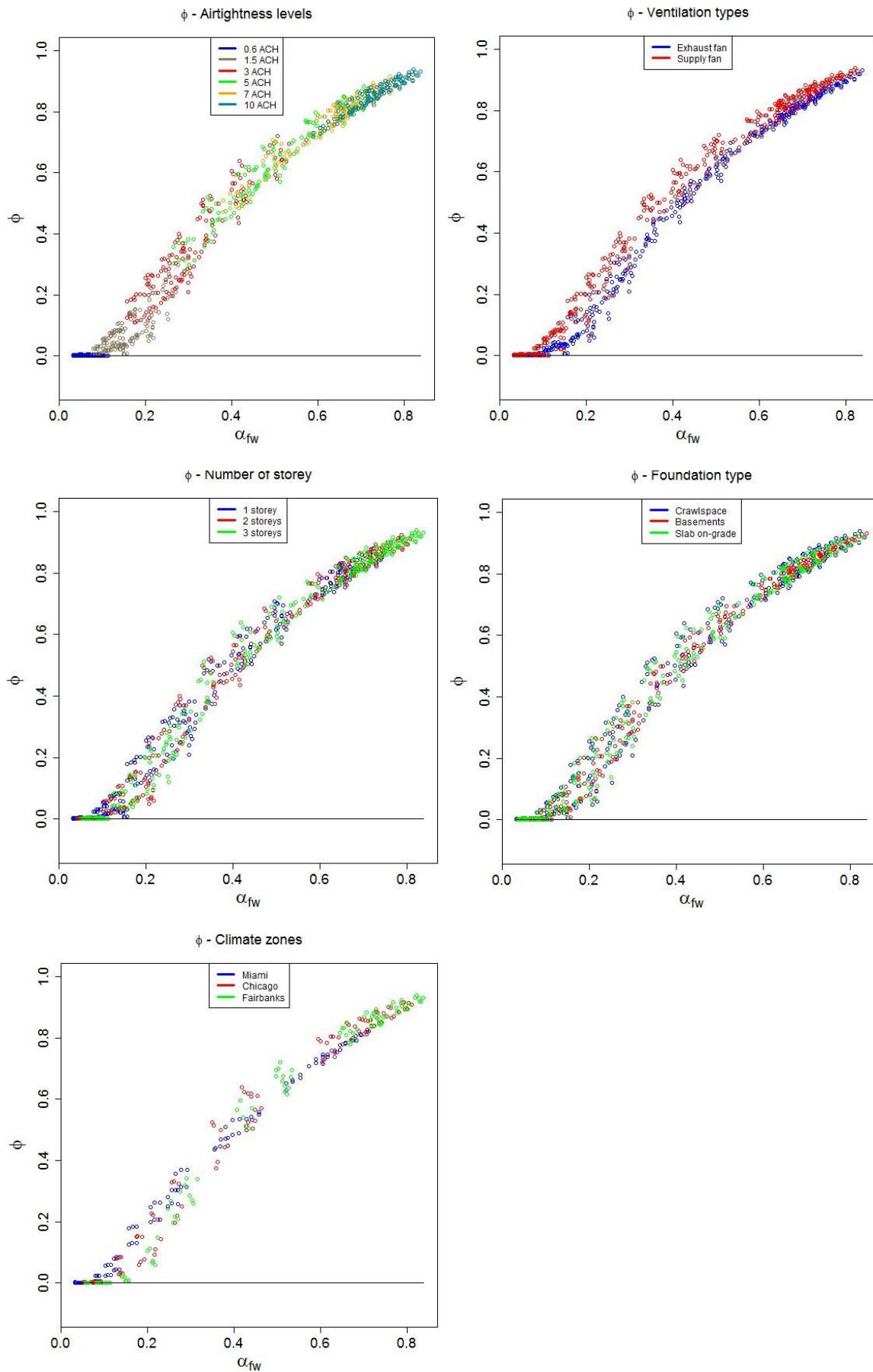


Figure 0.2 - Impact of the input parameters on the sub-additivity coefficient ( $\Phi$ )

## D. APIE box sizing using CFD (OpenFoam)

- **Objective of the simulation**

The aim of the simulation is to identify the easiest geometry to implement that ensures a good homogeneity in the pressure field near the tested wall on the upstream side of the box. The objective is to be able to consider identical flow characteristics near an airtightness defect on the tested wall whatever its location is.

One key point of the design issue is the geometry of the air inlets and outlets in the box. Straight enlargements are easier to implement than building a divergent duct for the air inlet and a converging one for the air outlet, but they don't facilitate the homogeneity of the pressure field near the tested wall. The location of these air inlets and outlets is also important.

- **Method**

The simulation is carried out on the 3D experimental geometry, including the two air cavity separated by the air wall and the inlet and outlet air ducts.

The following software has been used:

- *Salome* for the construction of the geometry and the meshing
- *OpenFoam* for the simulation
- *Paraview* for the visualization and exploitation of the results

A first simulation is run with straight enlargements of the air inlet and outlet, and a location half-way up. On this first geometry a number of tests were carried out to set appropriate parameters for the simulation (mesh size, turbulence model...).

- **Simulation parameters**

The main parameters are the following ones:

- The chosen solver is *PorousSimpleFoam*. It gives a stationary solution for turbulent and incompressible flows going through a porous region
- The turbulence model is  $k-\varepsilon$
- The mesh contains 86960 cells. It is generated from the geometry thanks to the *Salome* function *3D Automatic Tetrahedralization* (Figure 1)
- The tested wall located in the center of the air cavity is modeled by a porous volume. The parameters used to characterize this region are those of the glass wool<sup>6</sup>, that is to say a porosity  $\varphi=0.95$  and a permeability coefficient  $k=(5.10^{-10}, 3.10^{-10}, 5.10^{-10})$
- The simulations run with the boundary conditions listed in the Table 1.

---

<sup>6</sup> L. Marmoret, M. Lewandowski, and A. Perwuelz, "An Air Permeability Study of Anisotropic Glass Wool Fibrous Products," *Transp. Porous Media*, vol. 93, no. 1, pp. 79–97, May 2012.



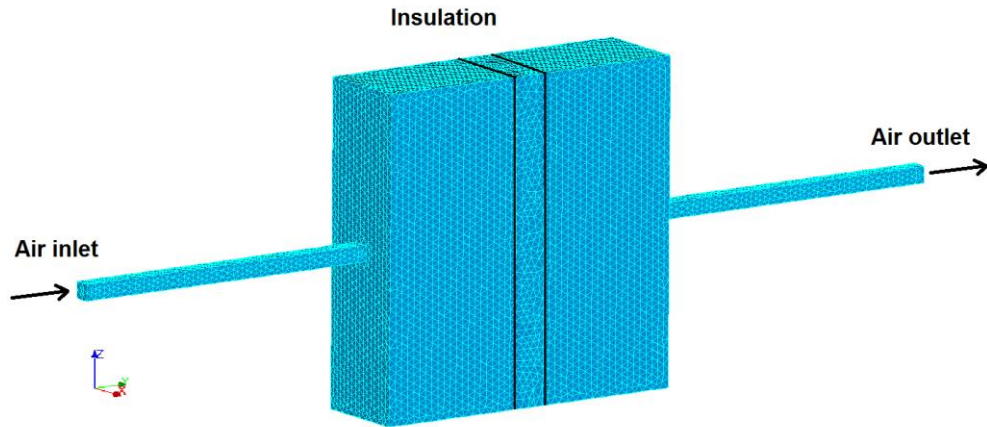


Figure 1 – Mesh of the experimental geometry sing Salome (86960 cells)

Table 1 – Boundary conditions

Parameters	Inlet	Outlet	Walls
P (Pa)	Zero gradient	0	Zero gradient
V (m/s)	(0, 0.3, 0)	Zero gradient	(0,0,0)
k (m <sup>2</sup> /s <sup>2</sup> )	3.66.10 <sup>-4</sup>	Zero gradient	3.66.10 <sup>-4</sup>
E (m <sup>2</sup> /s <sup>3</sup> )	1.15.10 <sup>-4</sup>	Zero gradient	1.15.10 <sup>-4</sup>

- **Simulation Results**

The results of the CFD simulation with straight enlargements of the air inlet and outlet and a location half-way up are shown in Figure2.

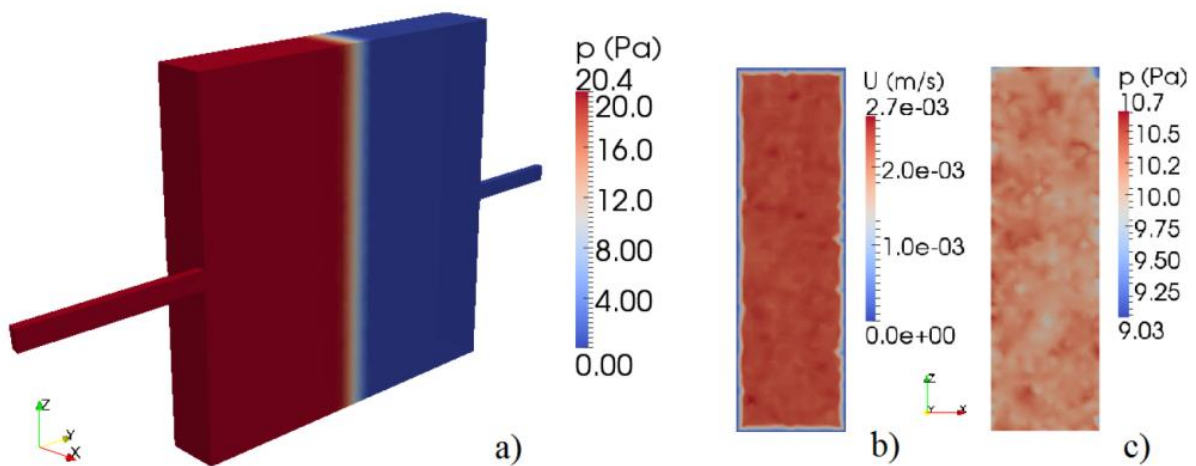


Figure 2 - Results of the CFD simulation: pressure field inside the box (a); velocity (b) and pressure (c) fields in a vertical cross-section in the middle of the insulation material

It appears that the pressure field is homogeneous in cross-sections perpendicular to the flow direction. With a pressure difference between the inlet and the outlet of 20 Pa, in the vertical cross section in the middle of the porous insulation material the pressure values mostly ranges from 9.75 Pa to 10.5 Pa.

This pressure homogeneity is linked with the velocity homogeneity. Apart from the regions near the wall boundaries where the velocity decreases to zero, the velocity values are also homogeneous in cross-sections perpendicular to the flow direction.

There is therefore no need to implement diverging and converging ducts for the air inlet and outlet.

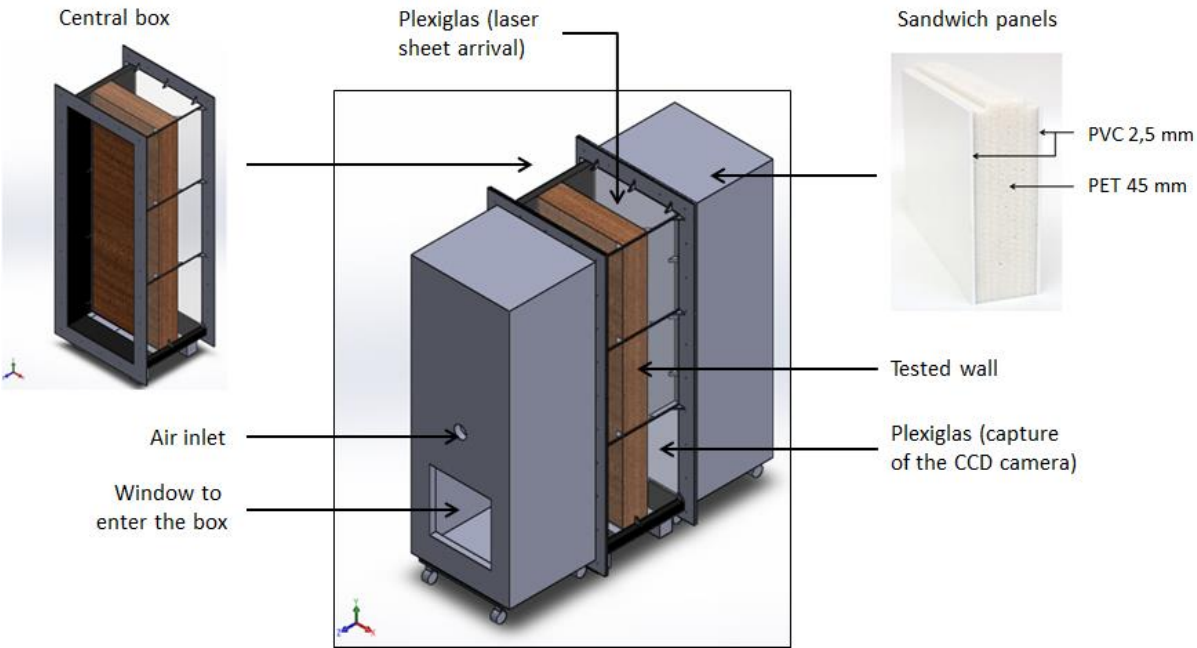
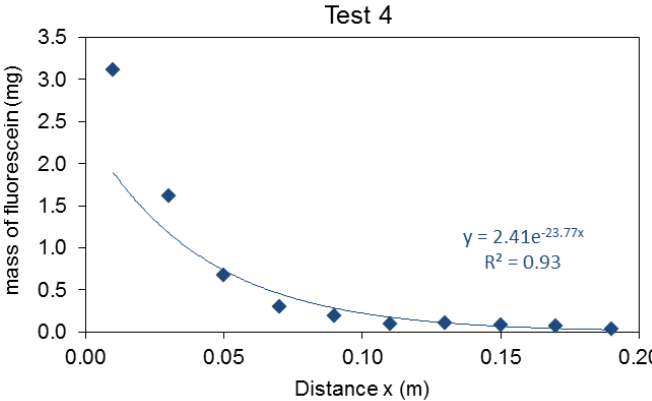
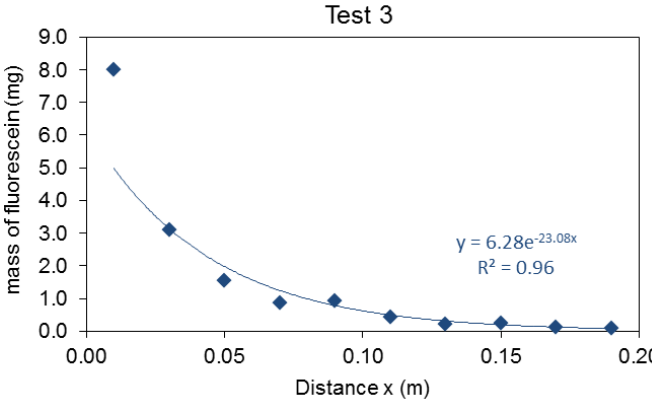
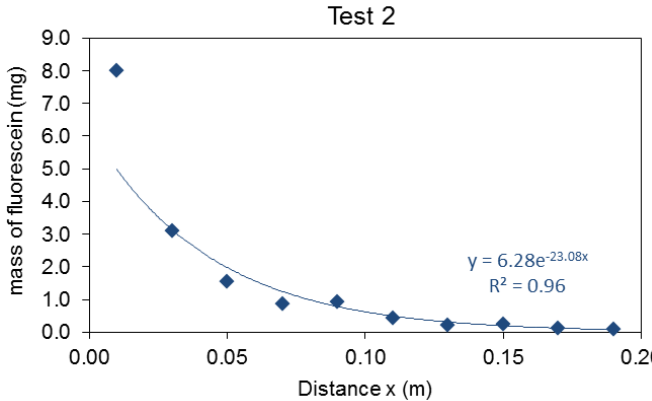
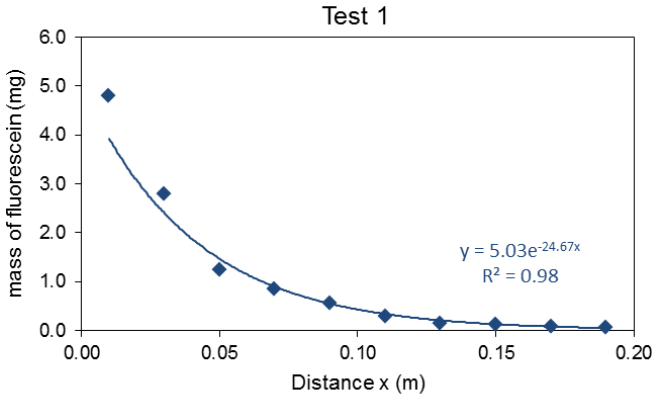
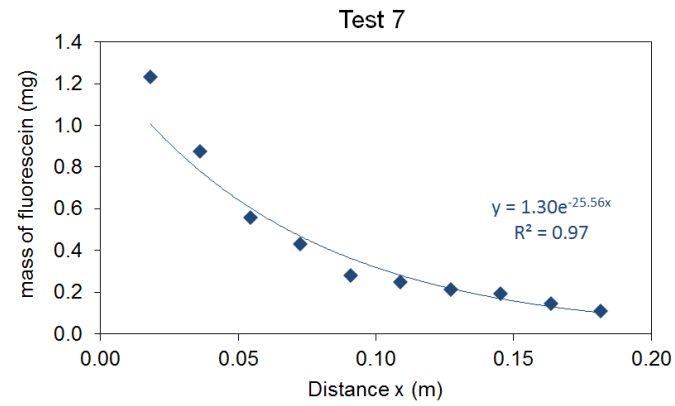
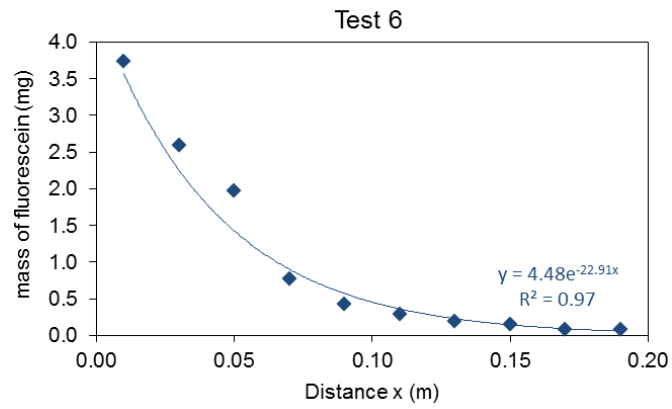
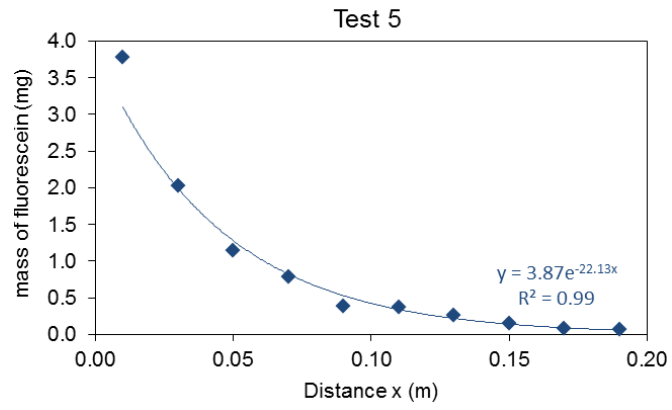


Figure 3 – Geometry of the APIE box designed with Solidworks

### E. Full results of the CETT fluorescein tests





## F. Full results of the COMSOL simulation for the air channel study

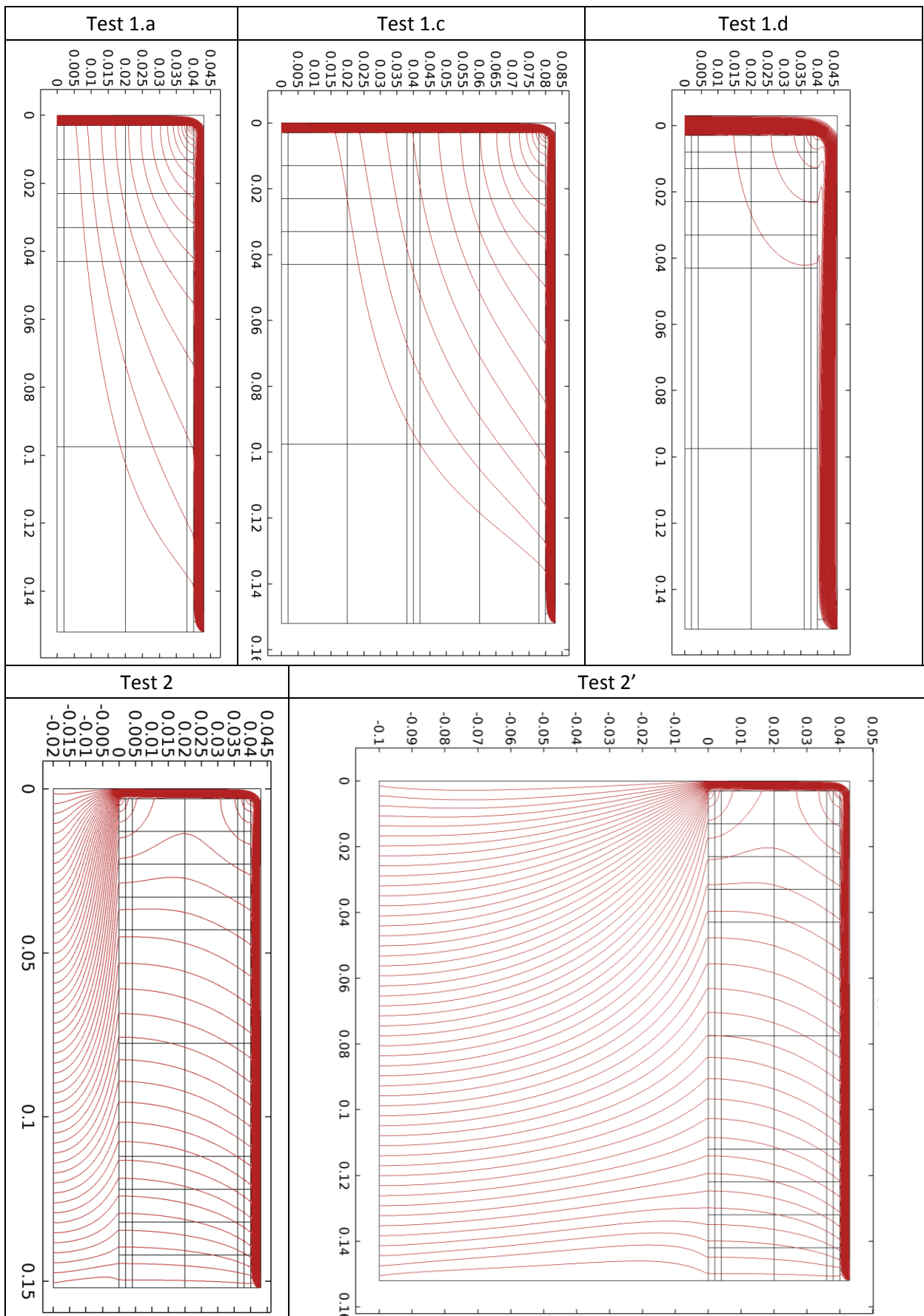
The 11 experimental tests presented in paragraph 5.4.1 are simulated in COMSOL with the exception of Test 1.a' (repeatability test) and Test 1.c because of a lack of reliable data on the collection efficiency of the LPGW. The test 2 is carried out both with a 20 mm and a 100 mm thick air cavity to check that the flow behavior is not impacted by its dimension. The tests 3.b and 3.c were simulated by inverting the parallel and perpendicular permeability components ( $k_{\perp}$  and  $k_{//}$ ). As shown on the streamlines results, this had no impact on the flow behavior (no air infiltration in the glass wool), and the results are therefore not displayed for the velocity field and the fluorescein concentration.

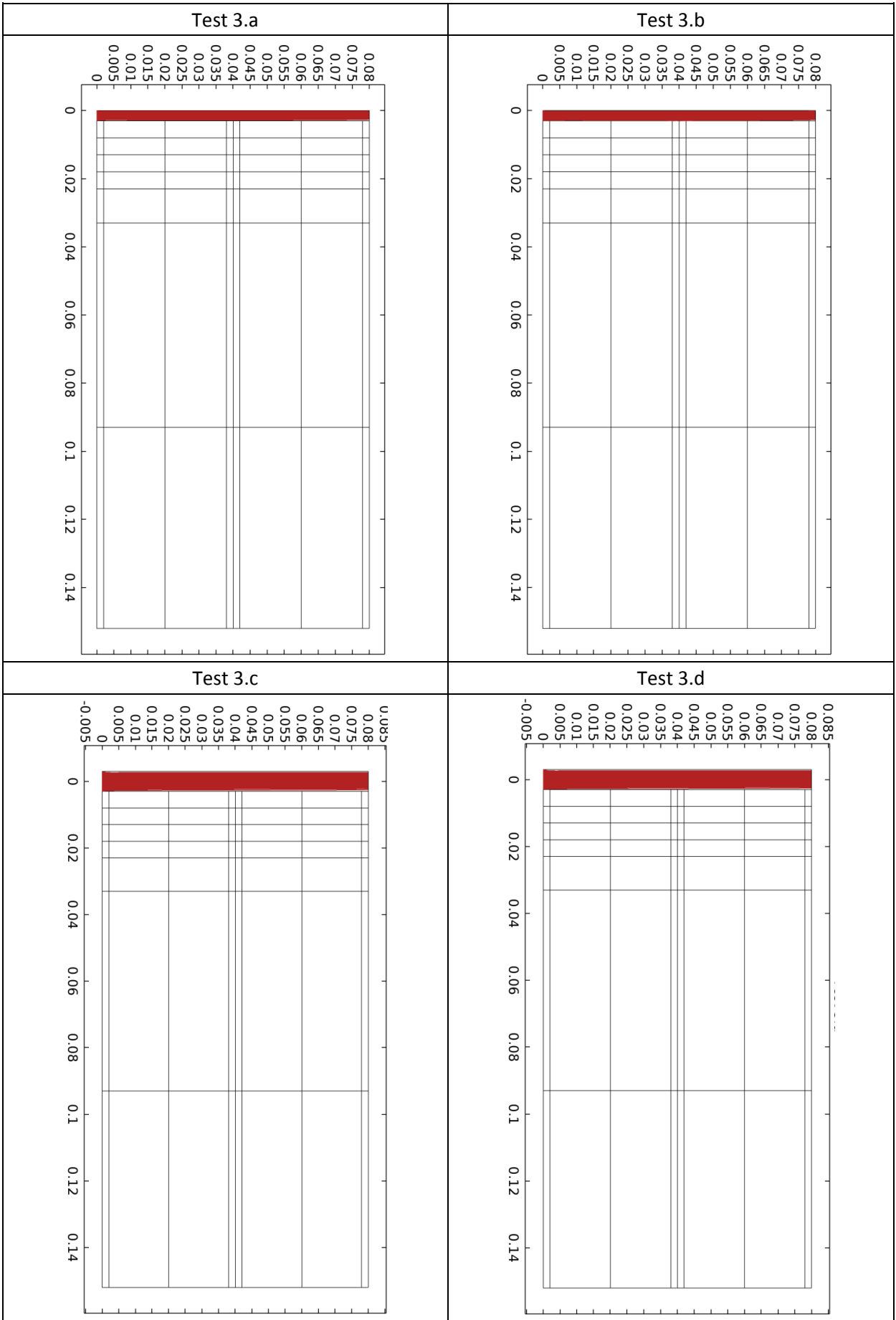
Test	Specificity	$t_{GW}$ (mm)	$t_{AC}$ (mm)	$t_{AG}$ (mm)	Q (m <sup>3</sup> /h)	$v_{in}$ (m/s)	
1.a	Reference 1	40	3	-	4.00	2.52	
1.a'	Repeatability				3.67	2.31	
1.b	LPGW				60	3.84	2.42
1.c	2 layers of GW				80	3.37	2.12
1.d	Larger air channel	40	6		3.07	0.97	
2	Reference 2	40	3	20	3.86	-	
2'	Larger air gap			100			
3.a	Reference 3	80	3	-	3.96	2.49	
3.b	GW // to the flow				3.92	2.47	
3.c	Larger air channel				2.99	0.94	
3.d	Larger air channel + GW // to the flow		6		4.12	1.30	

Five representations are given for each simulation result:

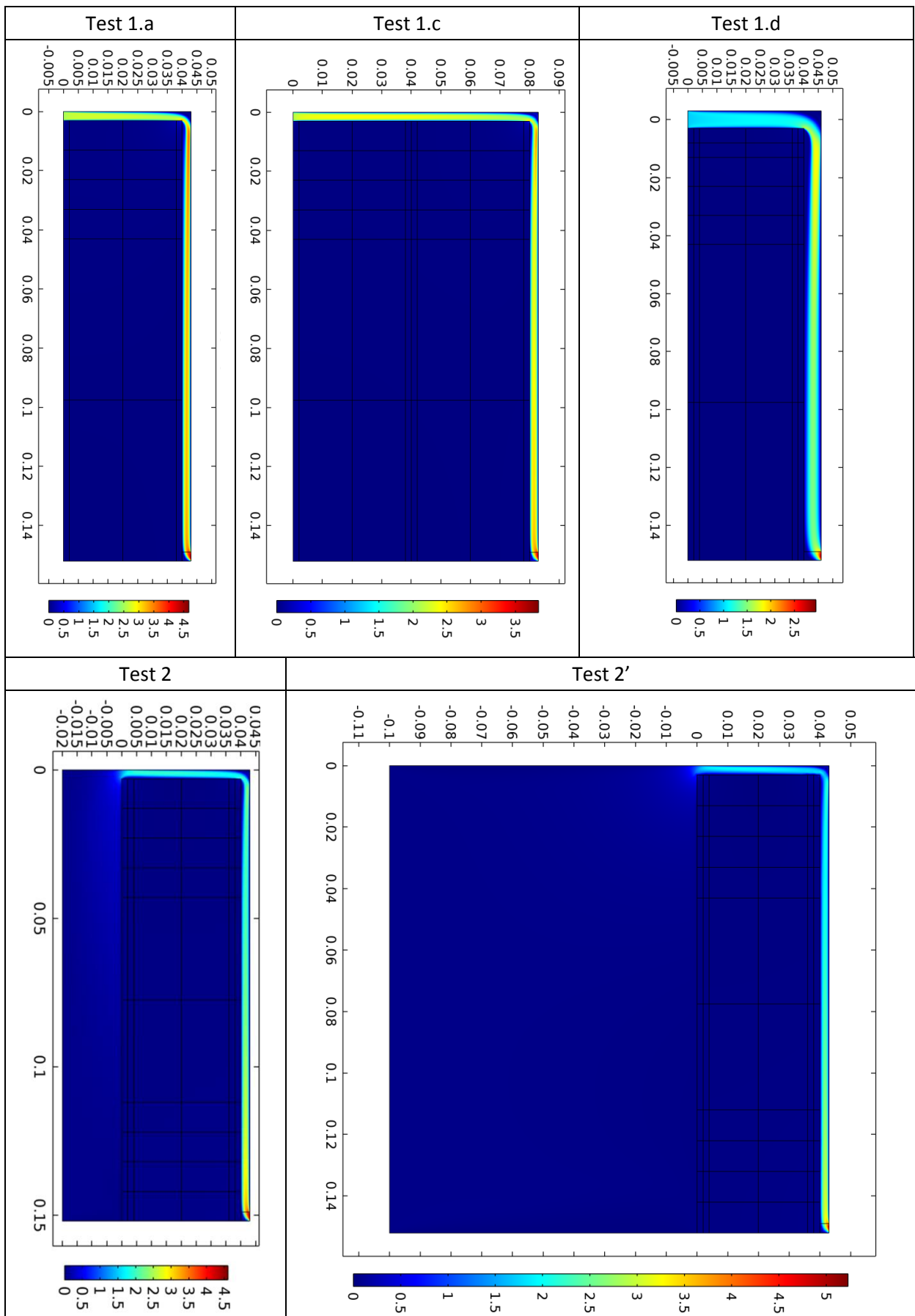
- The streamlines to evaluate the air flow penetration in the HPGW. They represent the path of 50 equidistant points taken on the inlet boundary.
- The velocity field which complements the streamline representation. It enables to see that for each test the air velocity inside the porous medium is much smaller than in the air channel.
- The velocity field with a restricted range from 0 m/s to 10% of  $v_{in}$  in order to visualize better the air velocity inside the porous medium.
- The fluorescein concentration field which differs from the velocity one since the particles get collected only in the porous medium: the maximum concentration in the GW is therefore the same as in the air channel. The absolute values are not of interest.
- The surface-averaged fluorescein concentrations with the same control volumes as in the experiment for a direct comparison. The values given are relative concentrations which were calculated in order to obtain identical experimental and numerical total mass of fluorescein for the reference test 1.a.

# Streamlines

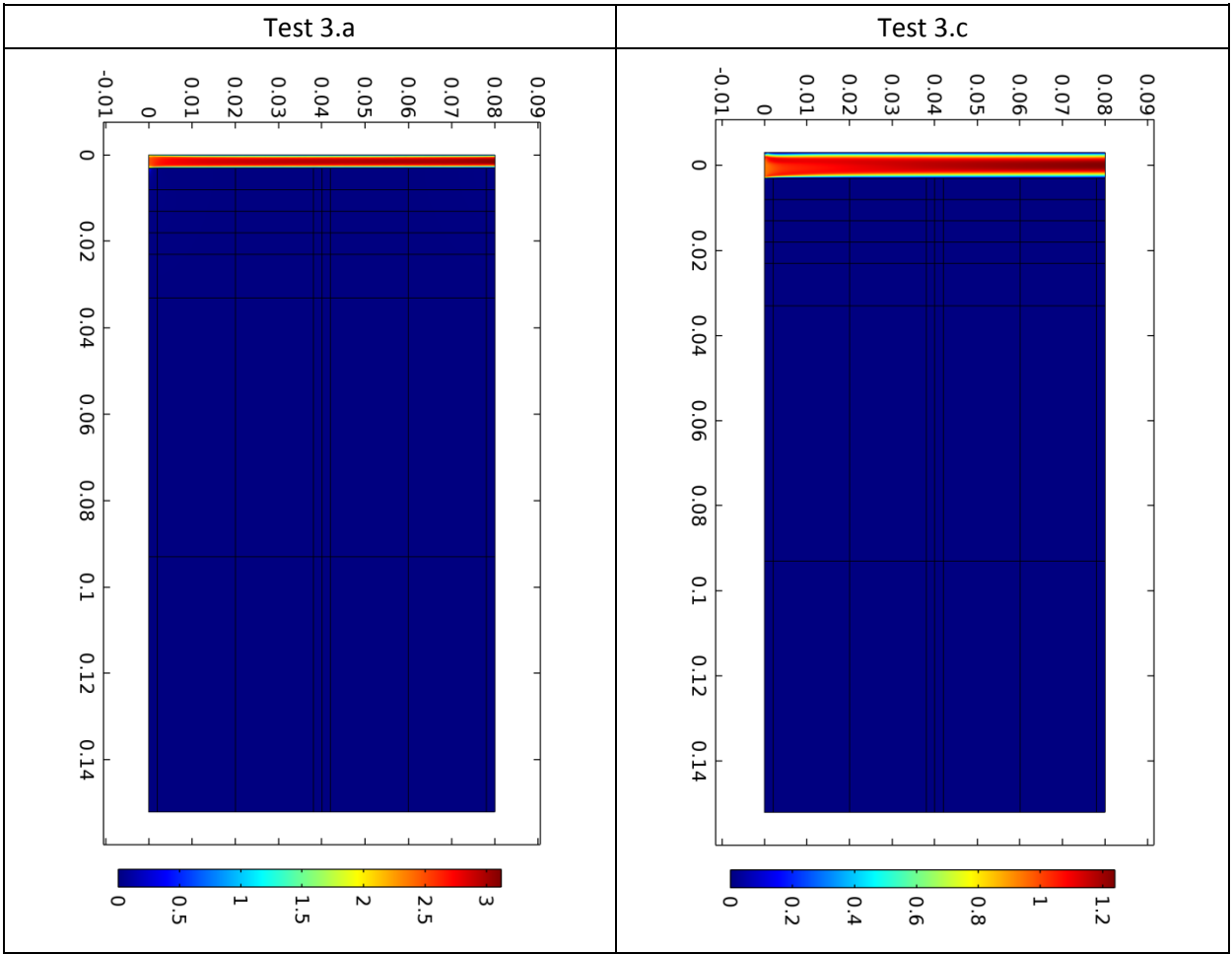




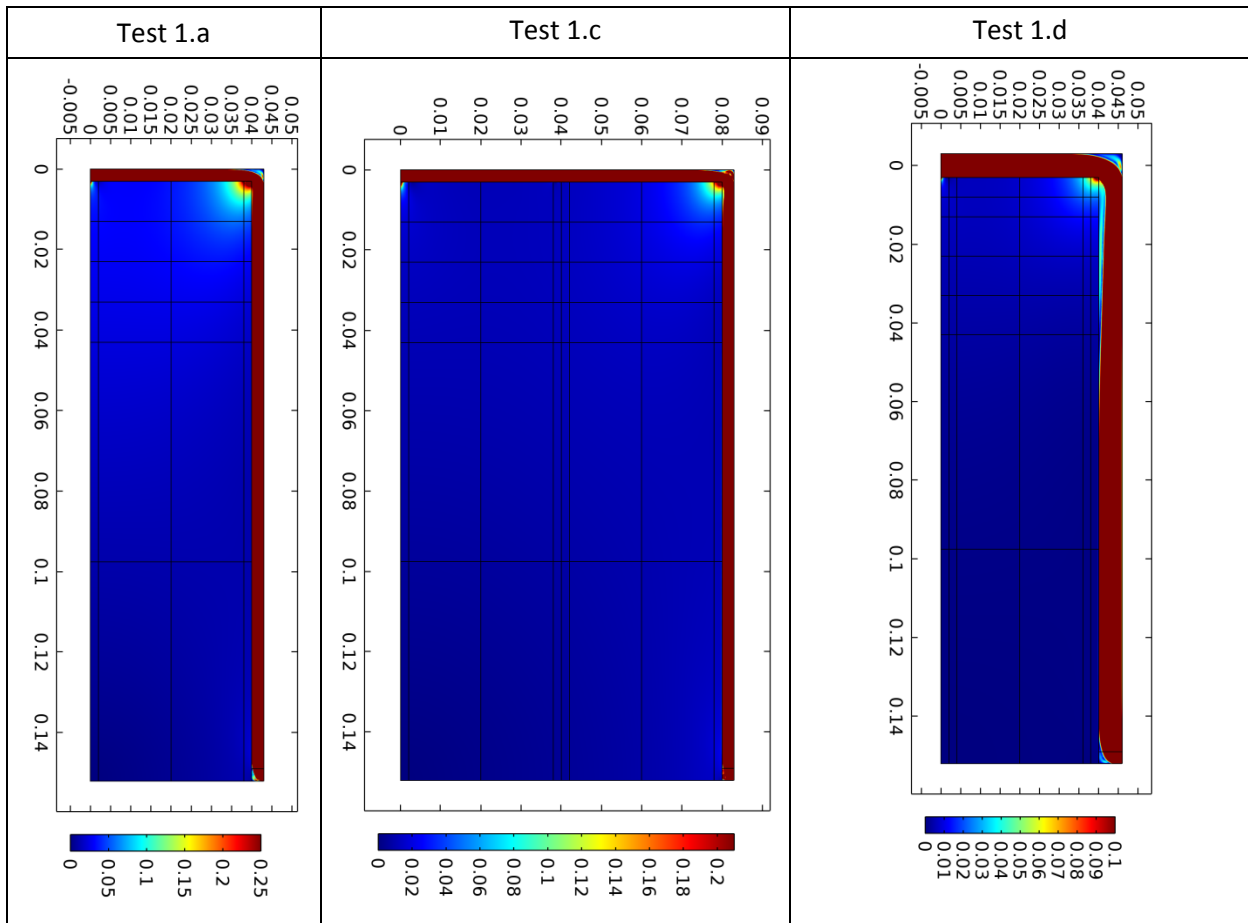
### Velocity fields

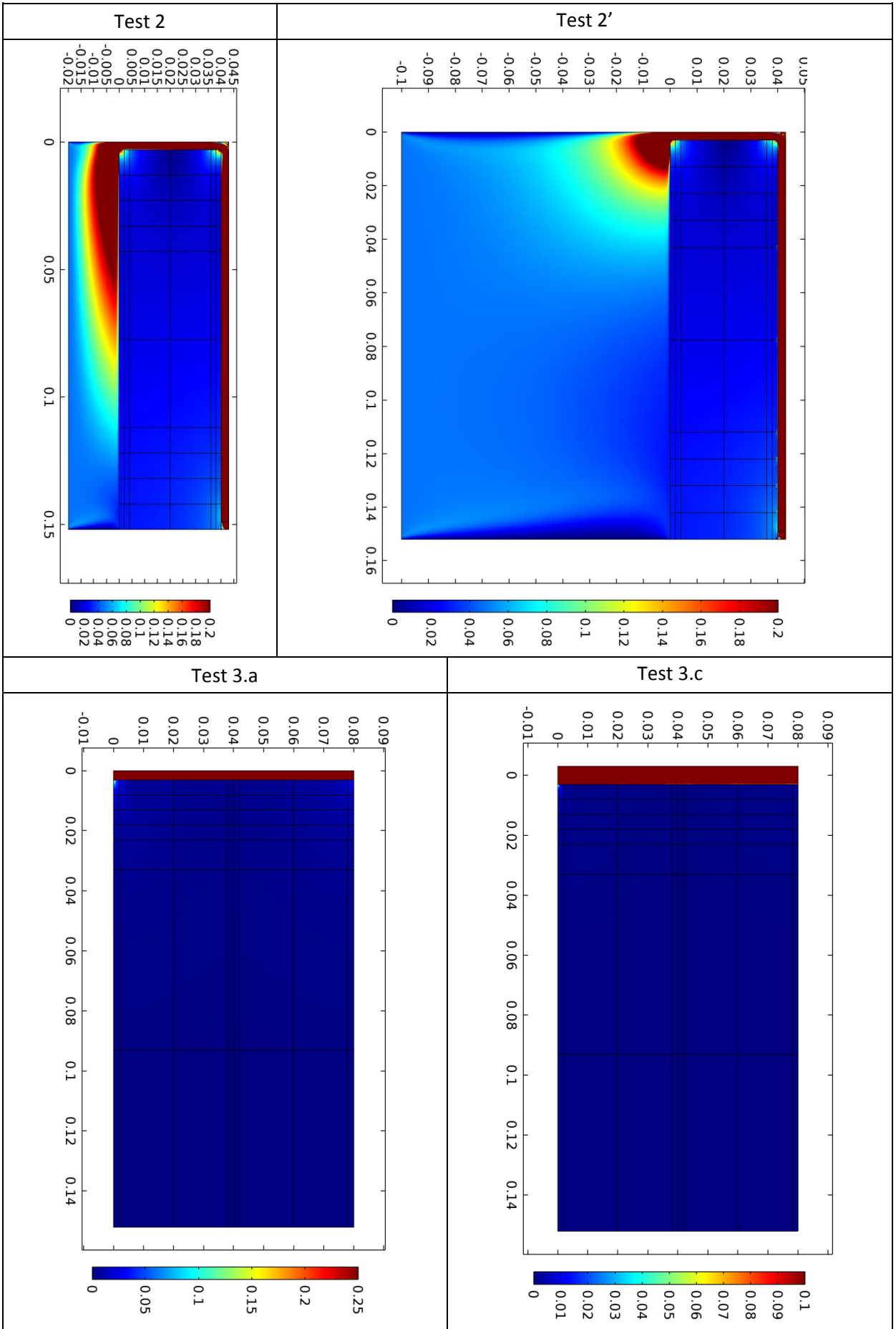




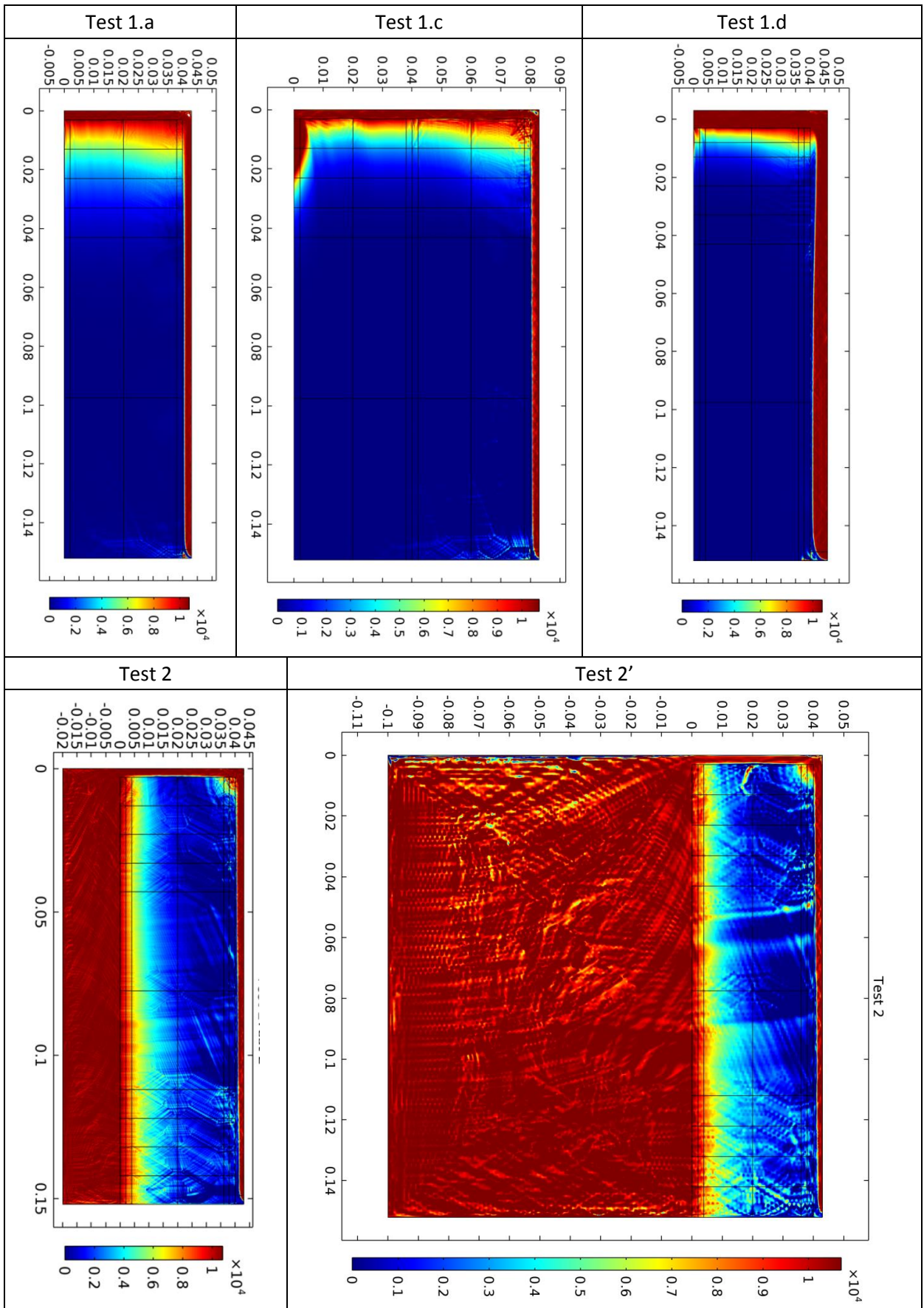


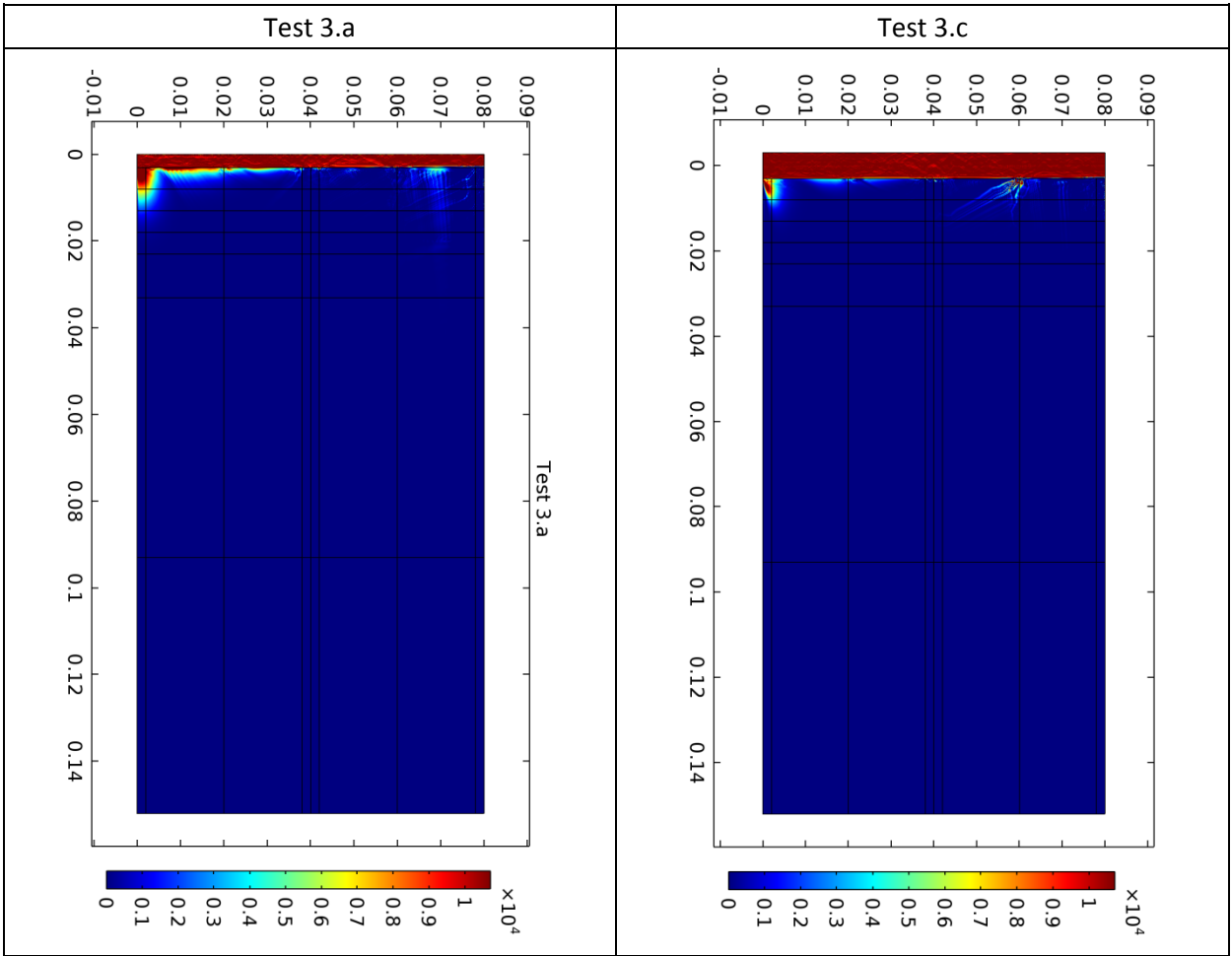
Velocity fields – restricted range:  $0 - 0.1 v_{in}$  (m/s)





Fluorescein concentration fields









## G. COMSOL simulation results

The experimental tests are simulated in COMSOL as explained in paragraph 6.1.2.

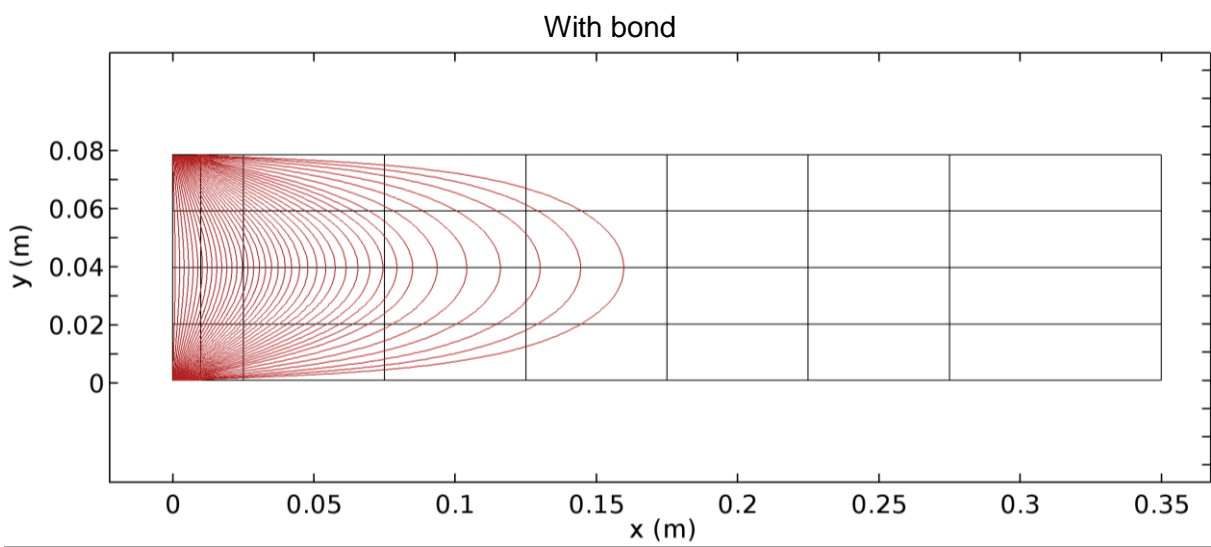
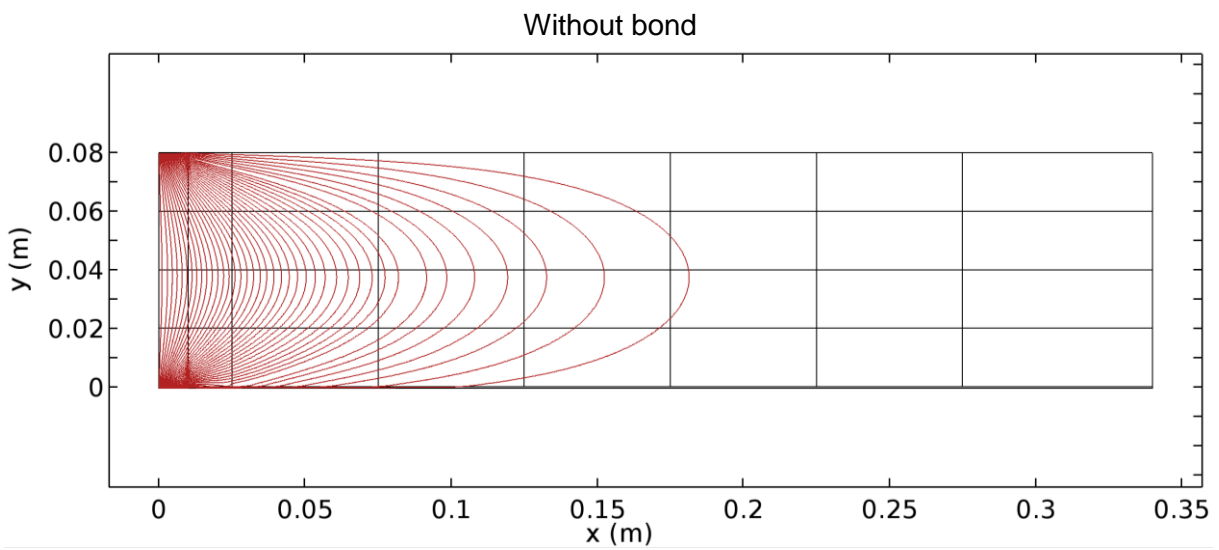
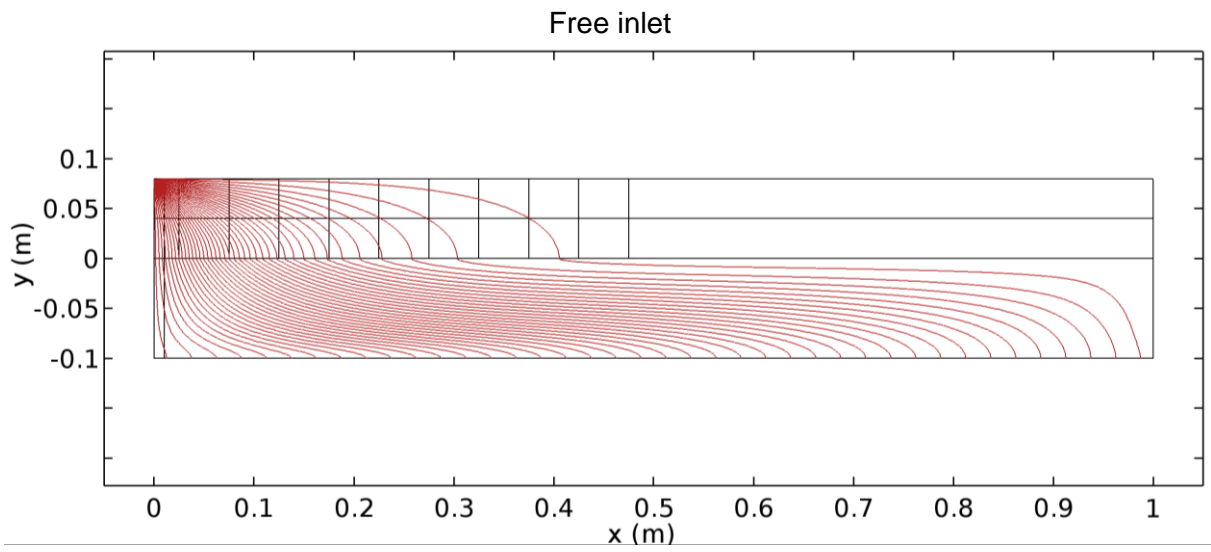
Two representations are given for each simulation result:

- The streamlines to evaluate the air flow dispersion in the HPGW. They represent the path of 40 equidistant points taken on the inlet boundary.
- The relative fluorescein concentration field velocity field with the value of  $C_{flu0}$  divided by  $C_0$ .

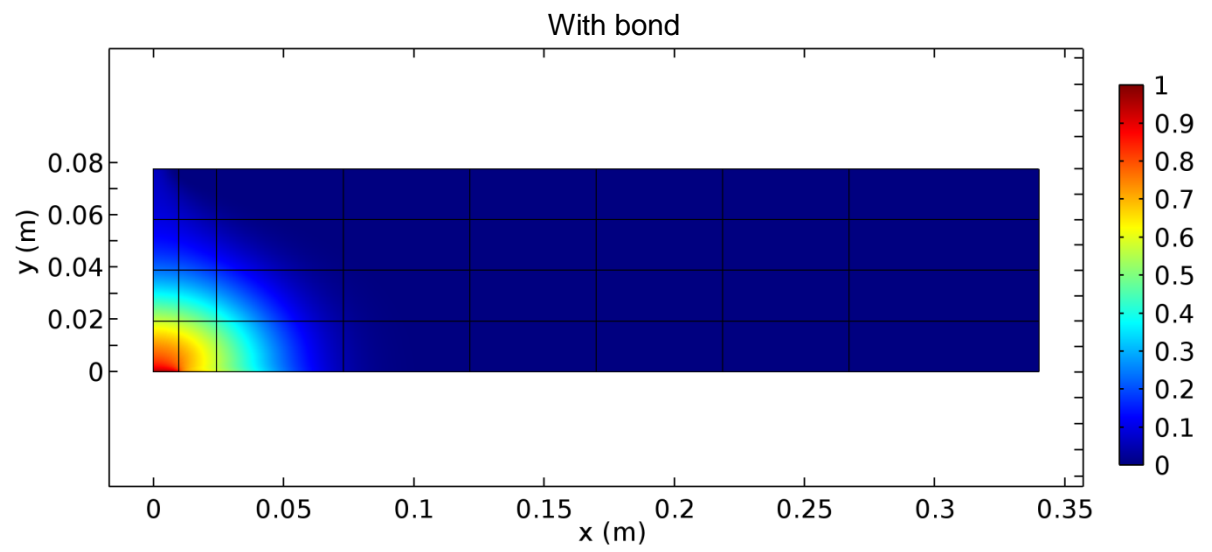
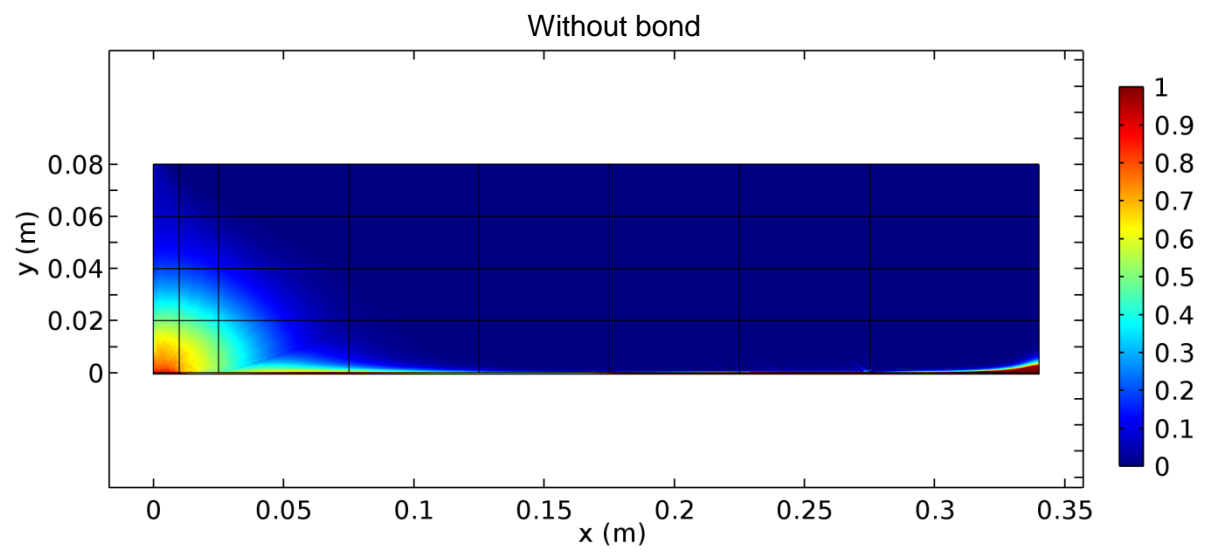
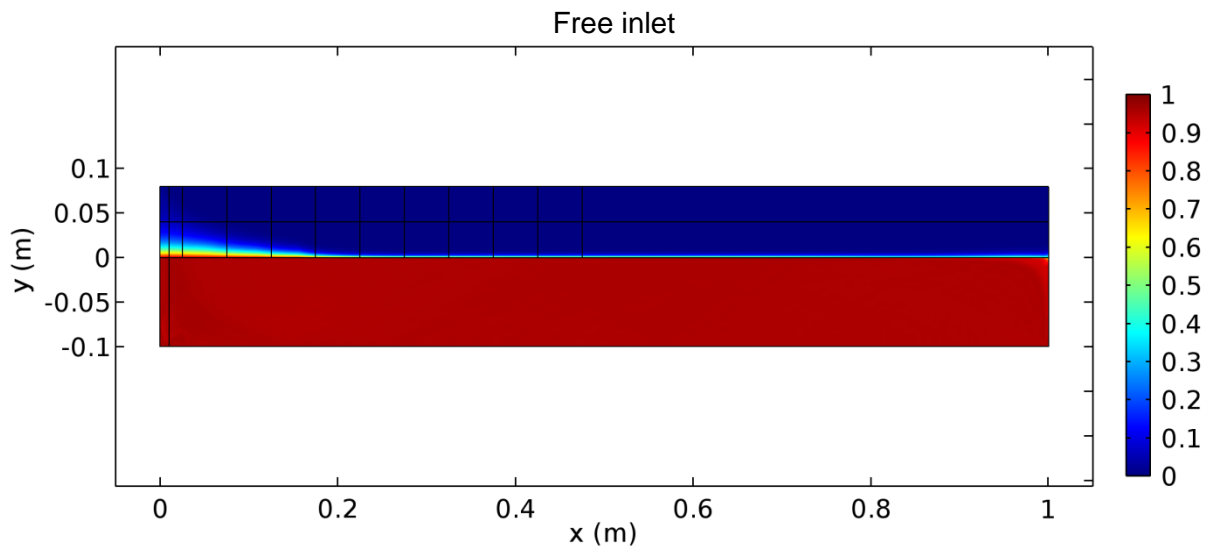
As illustrated above, the origin of the coordinate system is at the air inlet in the glass wool at the height of the hole(s) center(s).



## Streamlines

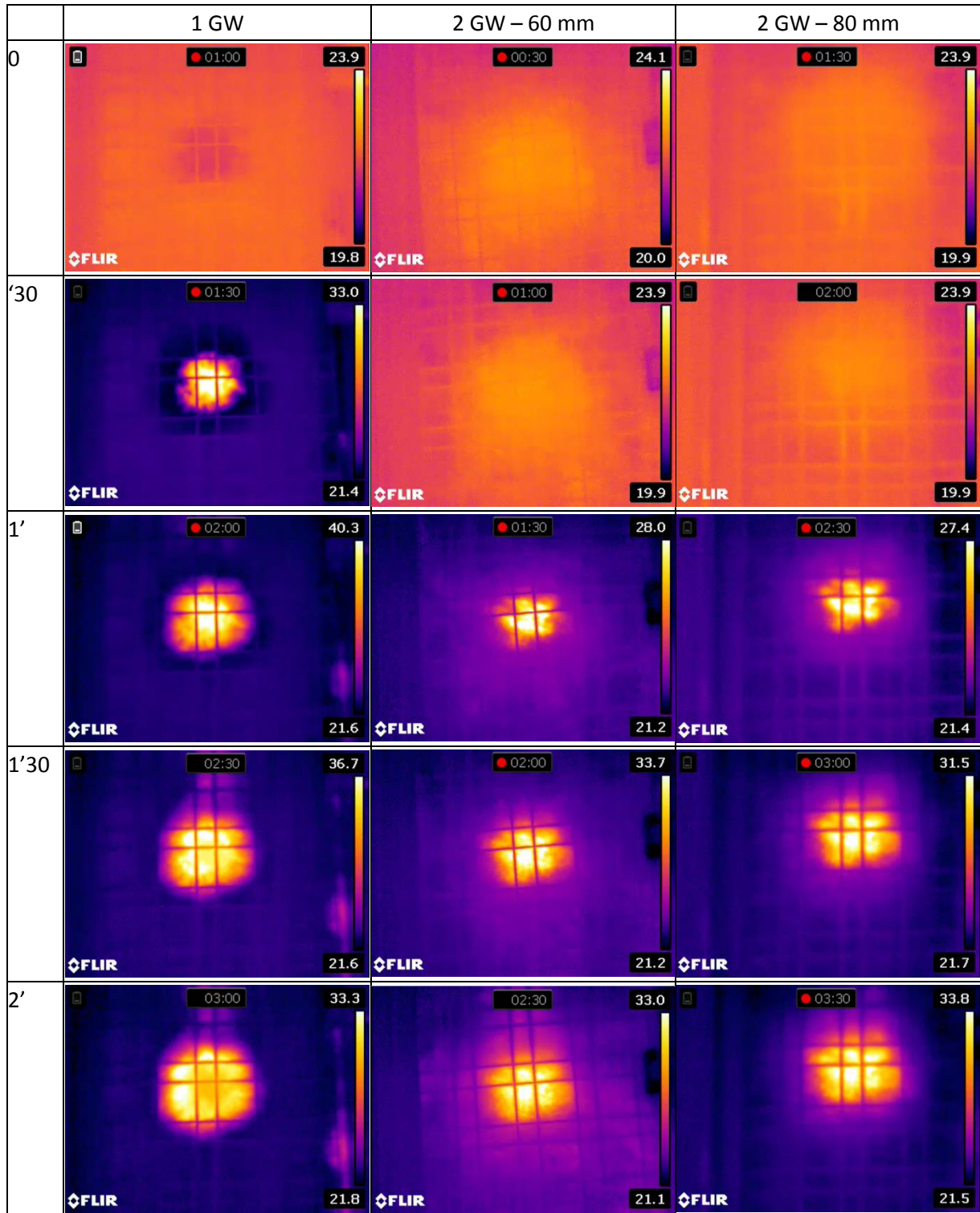


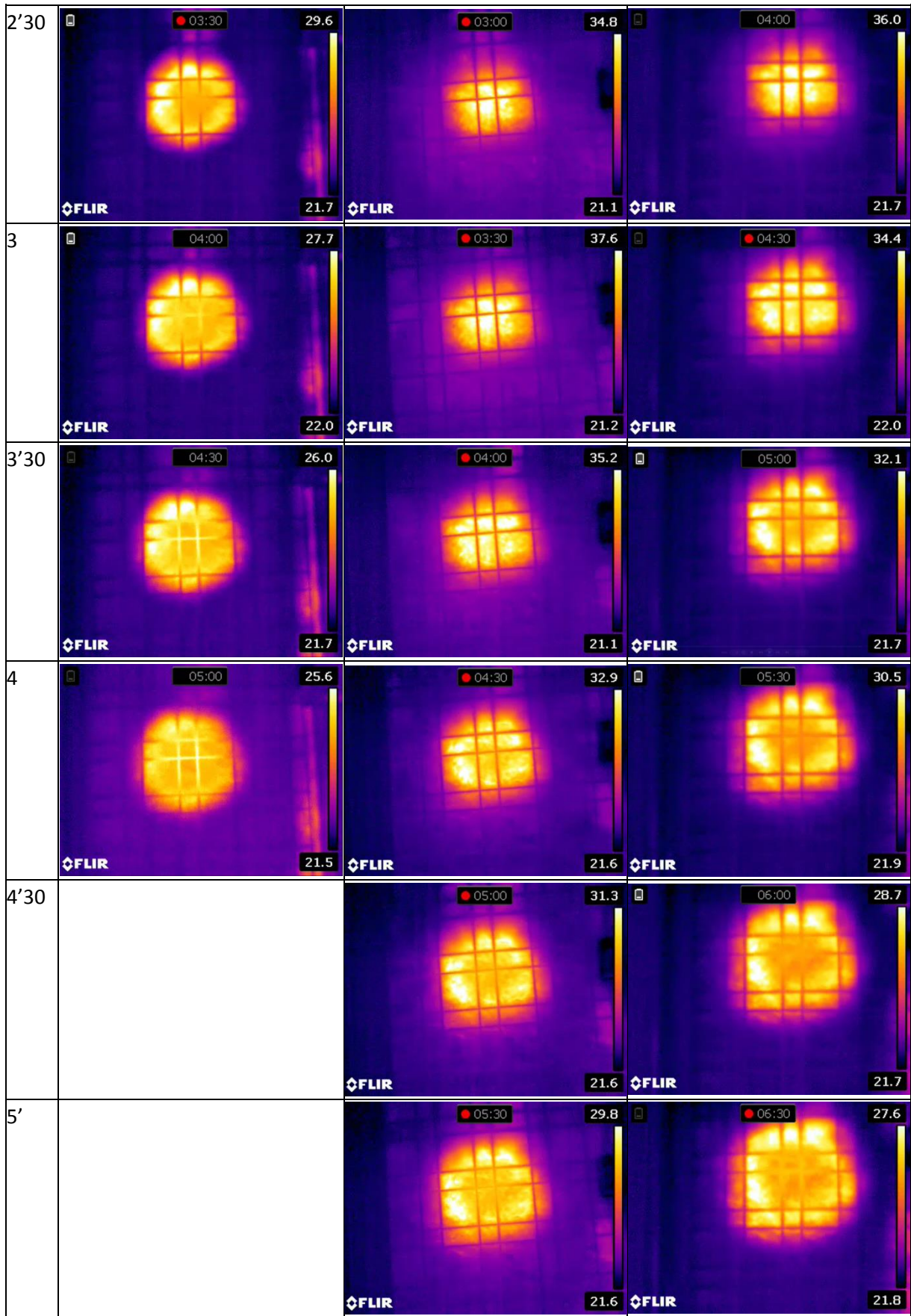
## Relative concentration field



## H. Full results of IR thermography tests

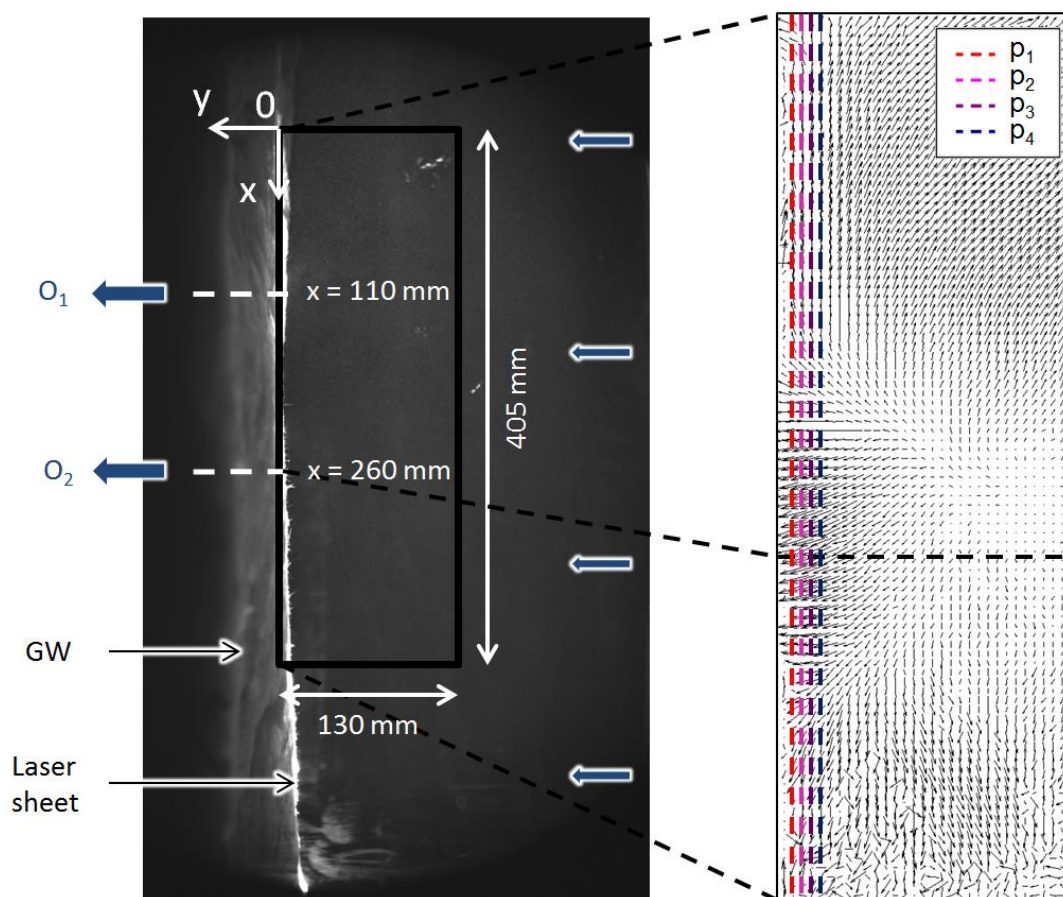
The results of the IR thermography tests presented in paragraph 6.2.1 are presented below, with instant pictures every 30 seconds. The size of each picture corresponds to a 75 cm x 56 cm glass wool area.



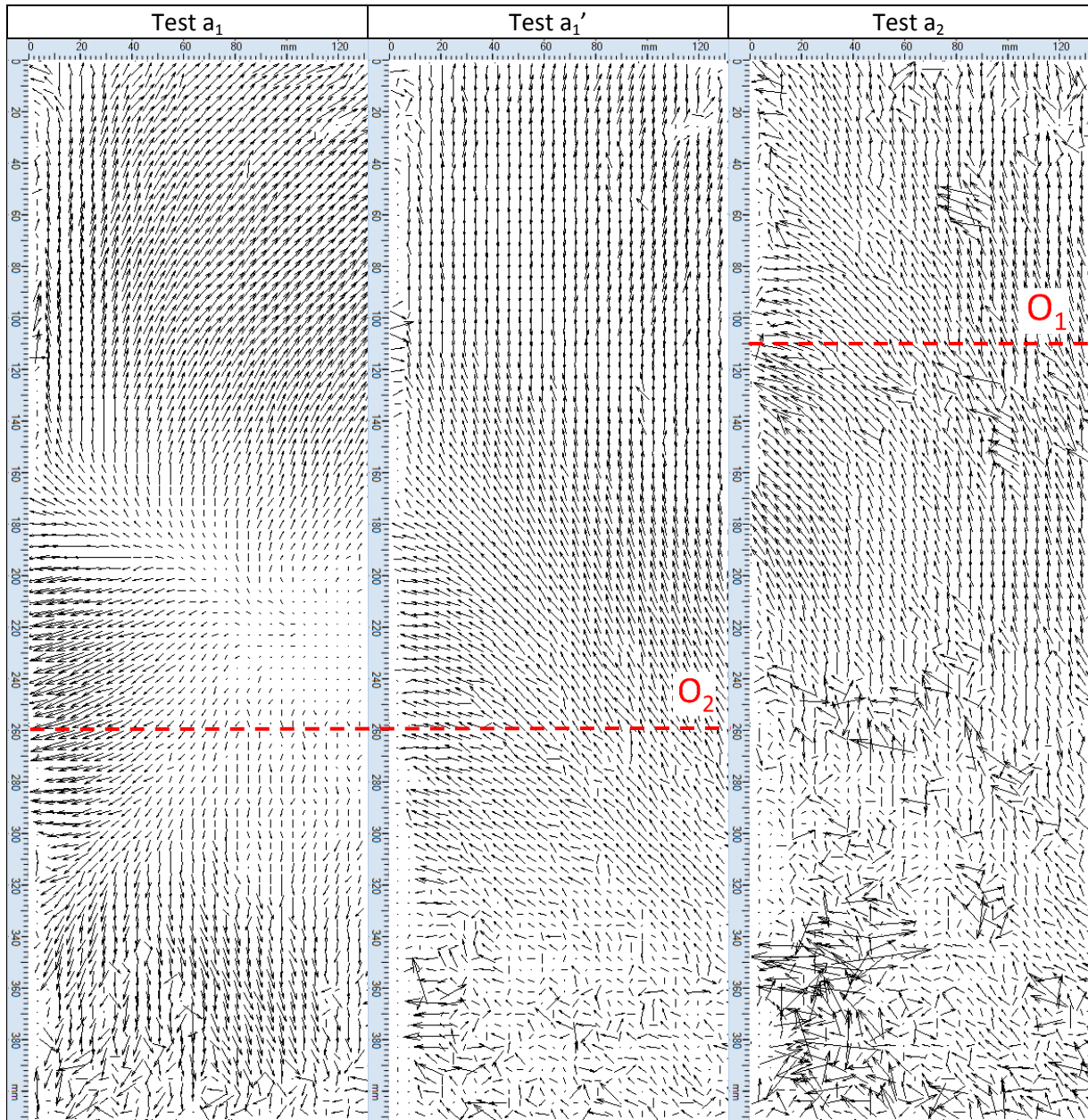


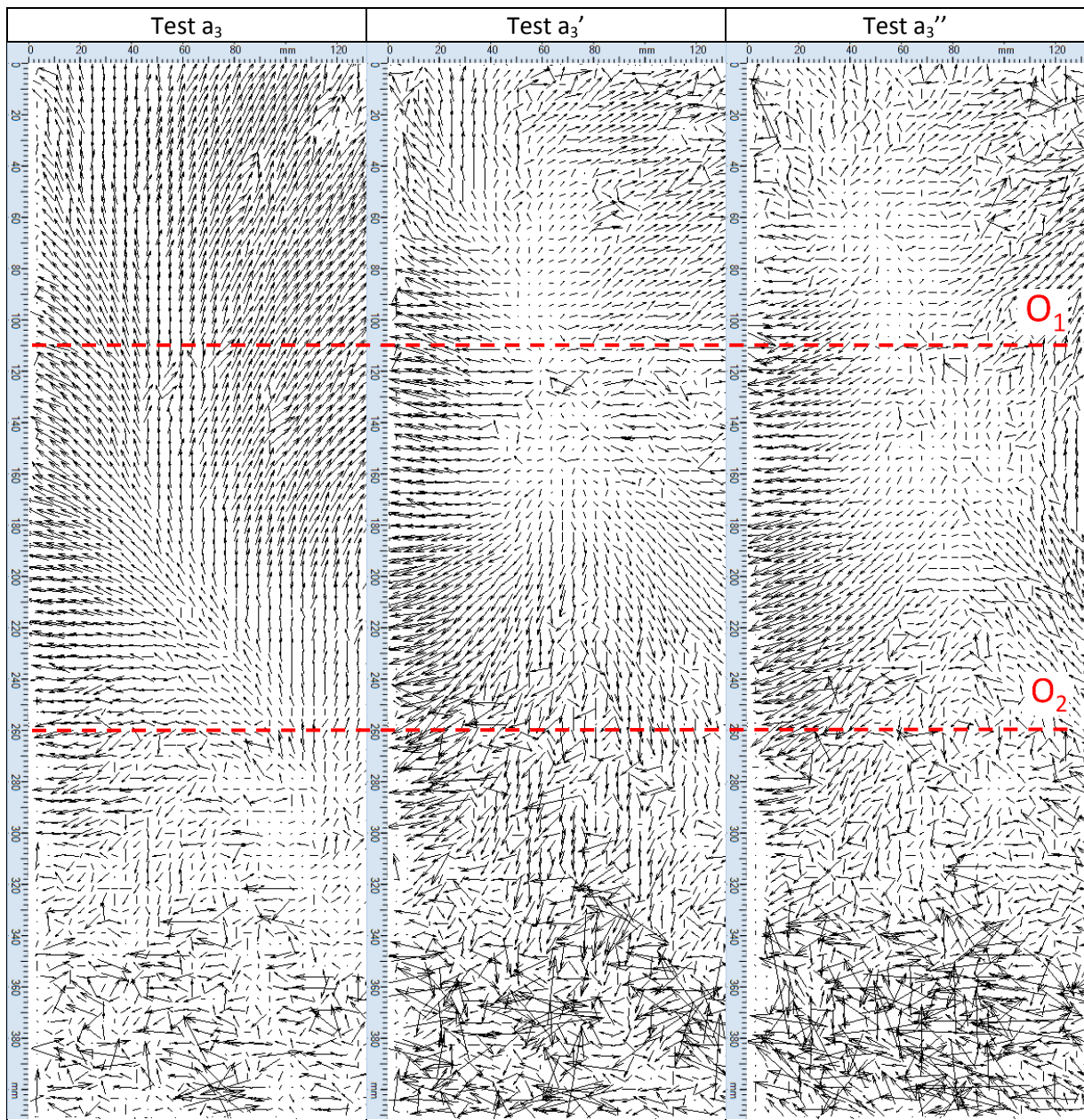
## I. Full results of PIV Tests

	Test	Inlet	Outlet	$n_{ppi}$	$f_{acq}$ ( $s^{-1}$ )	$t_{acq}$
Free inlet	$a_1$	-	$O_2$	500	2	4 min 10
	$a_1'$			200	3	1 min 07
	$a_2$		$O_1$	500	2	4 min 10
	$a_3$		$O_1, O_2$	600	2	5 min
	$a_3'$			500	2	4 min 10
	$a_3''$			200	3	1 min 07
Restricted inlet	$b_1$	$l_2$	$O_2$	200	3	1 min 07
	$b_2$	$l_1$				

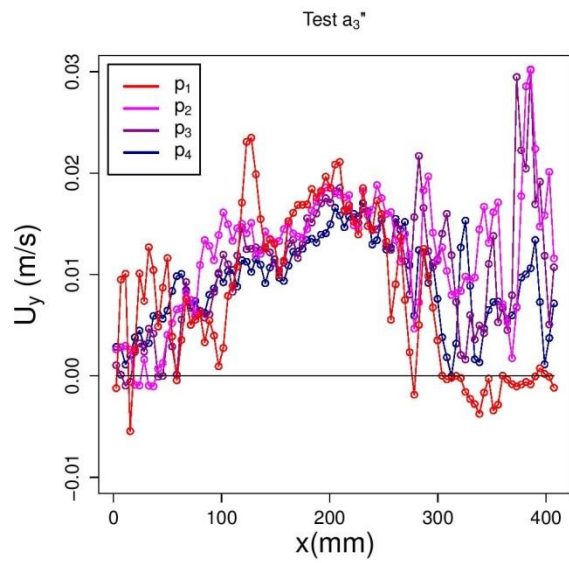
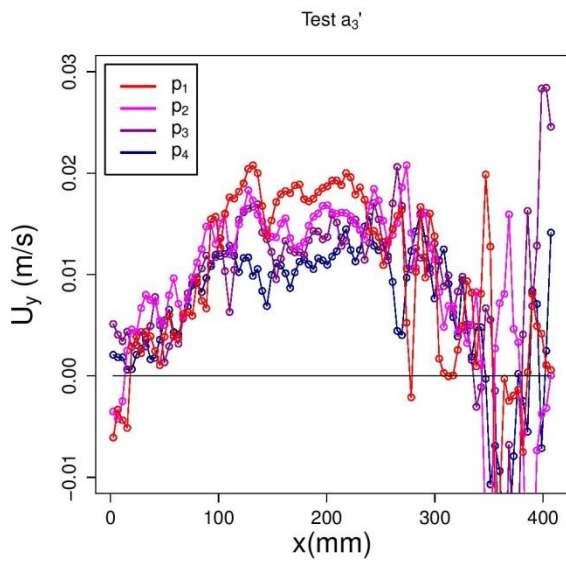
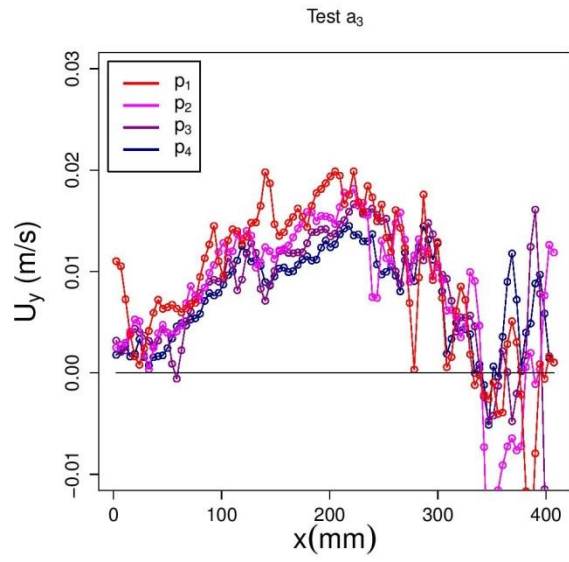
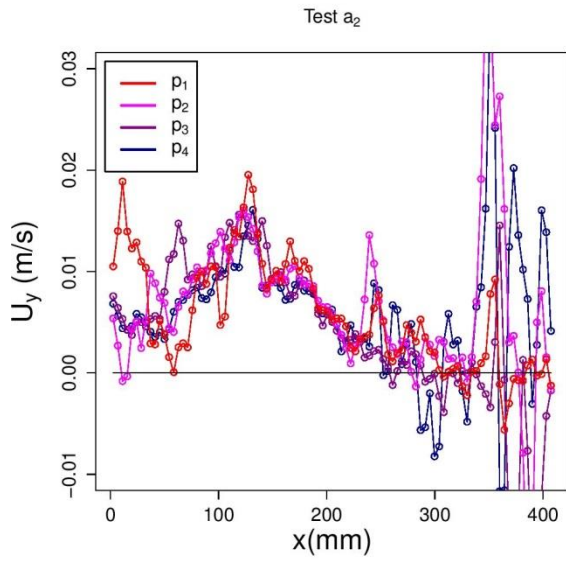
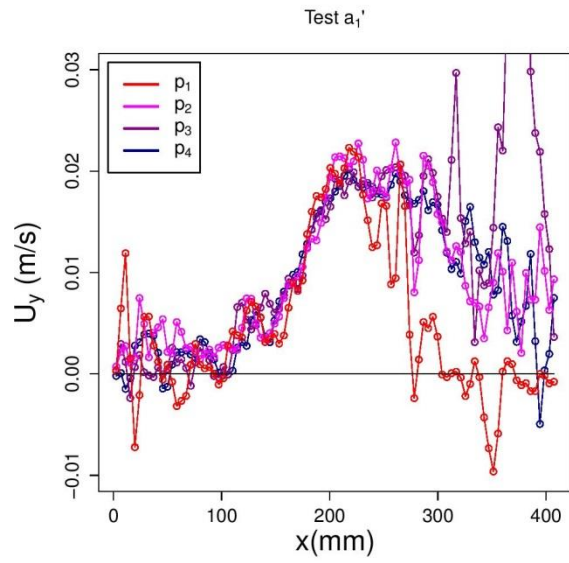
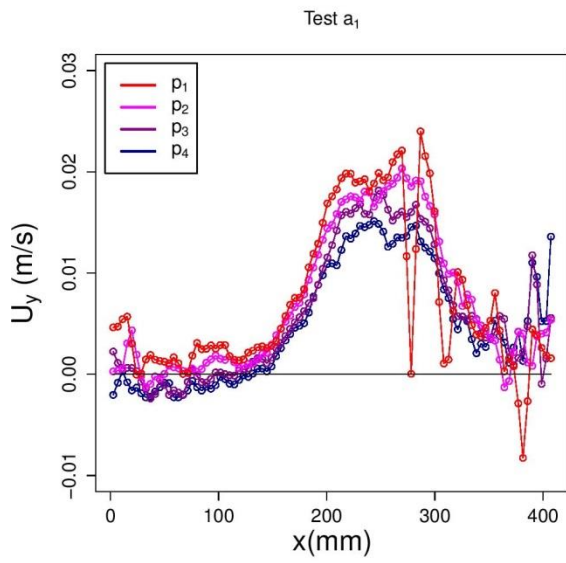


- Free inlet

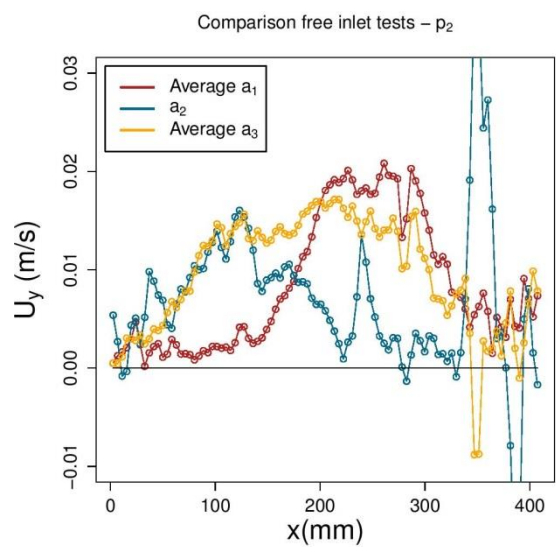
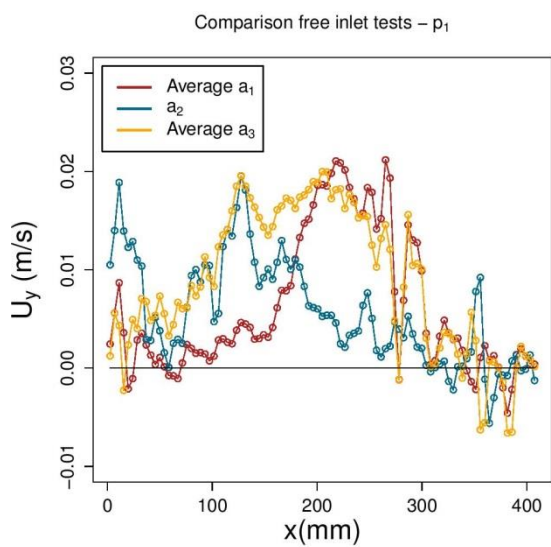
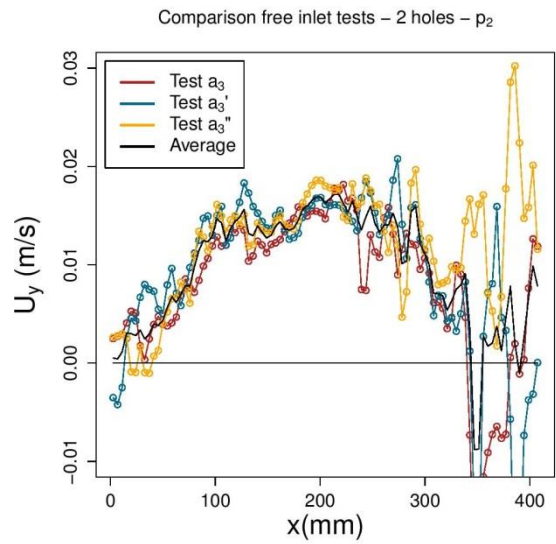
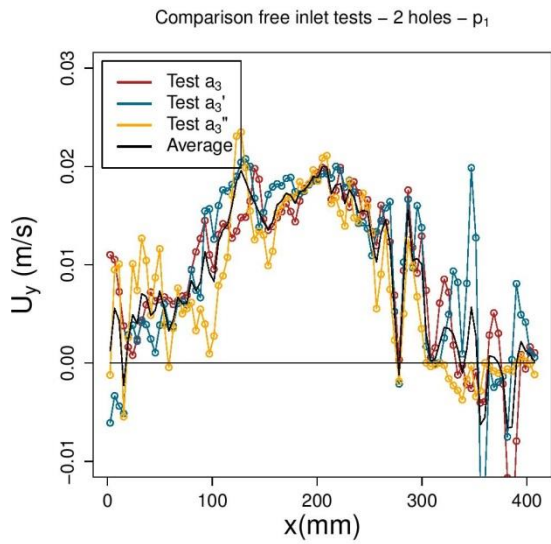
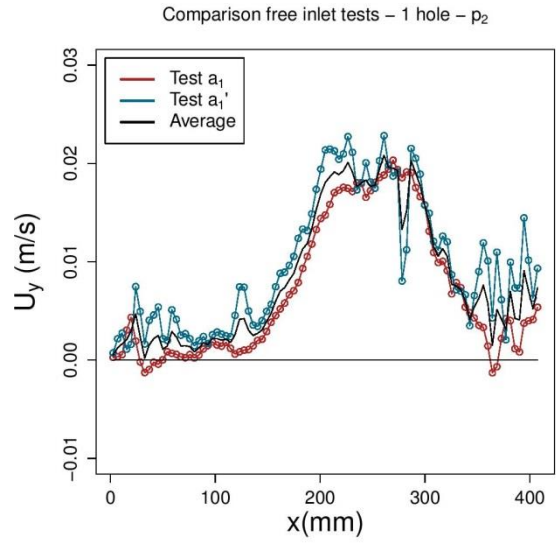
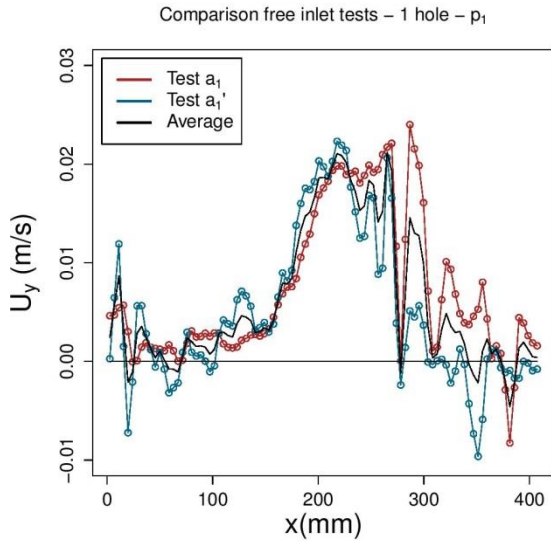




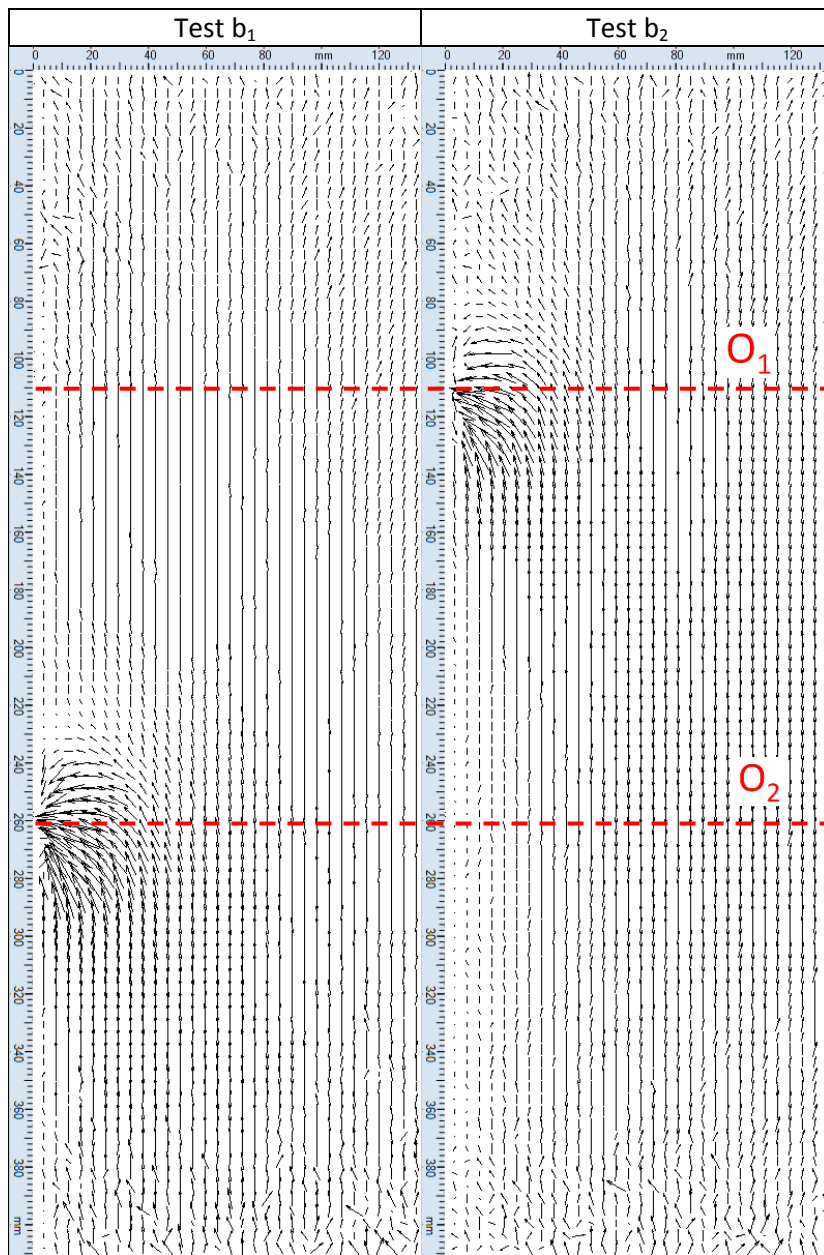
- **Velocity profiles**

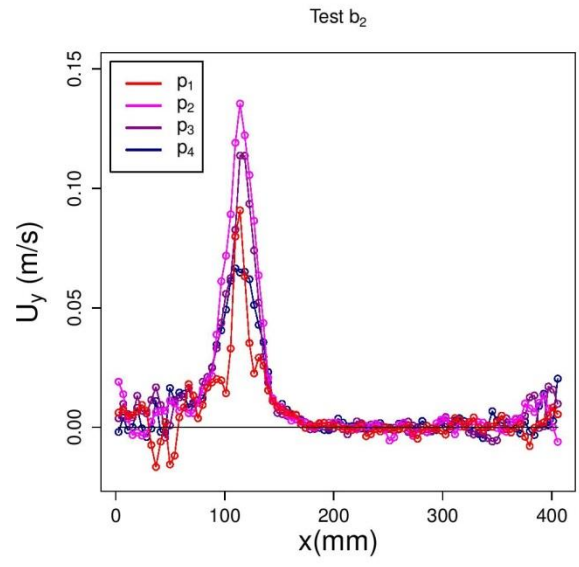
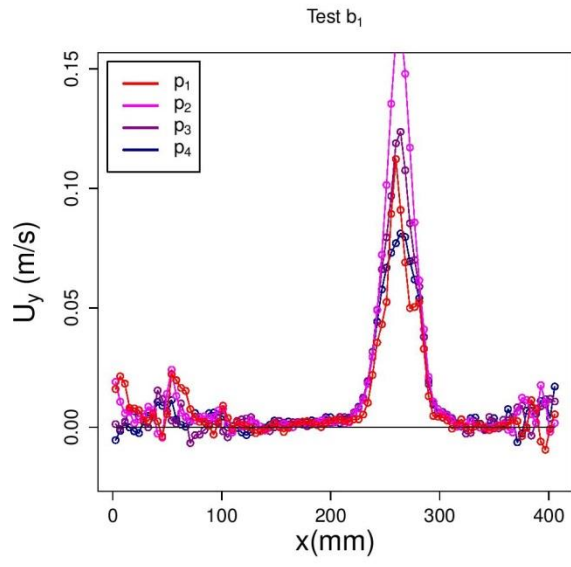




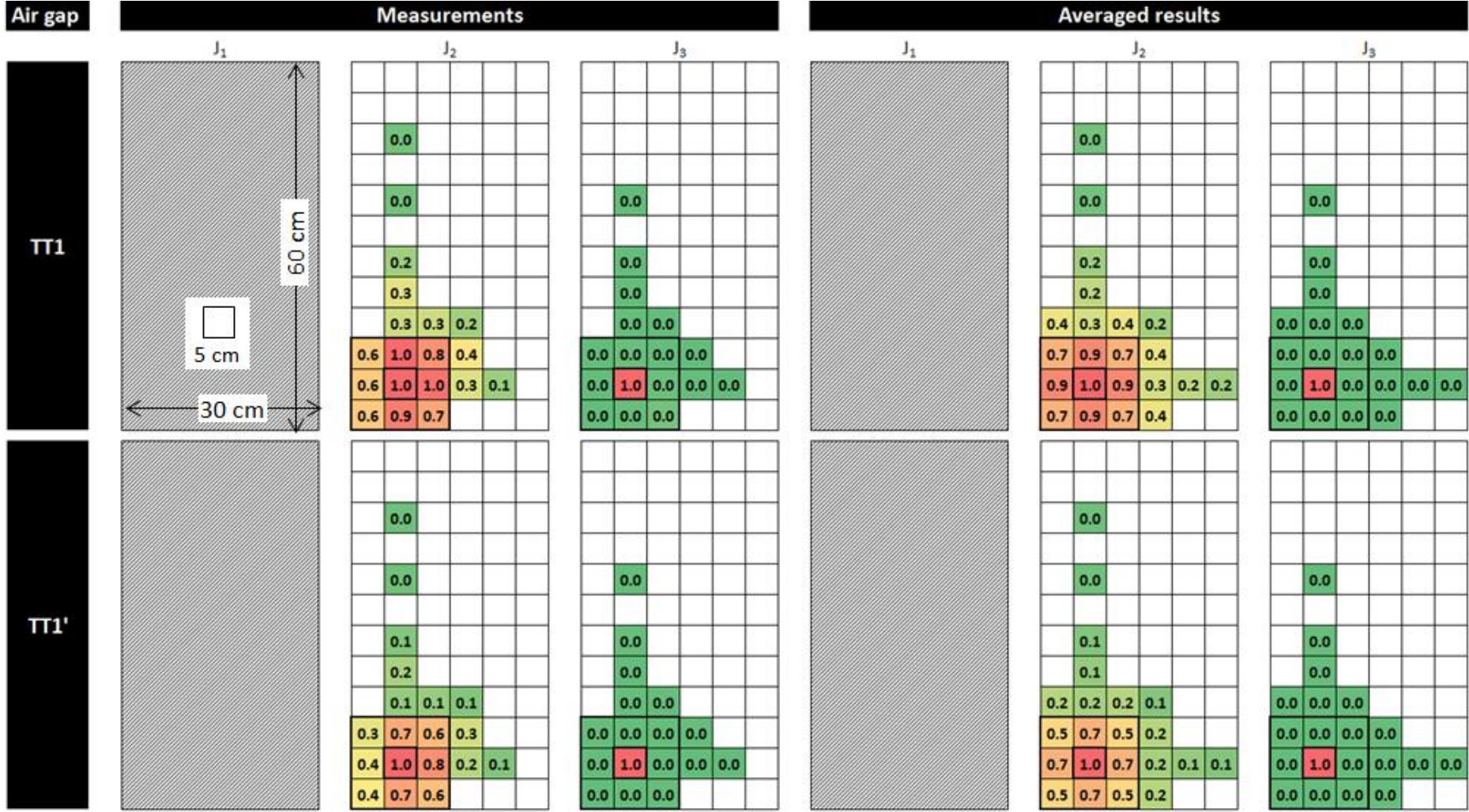


- Restricted inlet





### J. Full results of the 3-D thermocouple grid tests



No Glue

Measurements

Averaged results

TT2

$J_1$

0.0				
0.0				
0.0				
0.0				
0.3				
0.7	0.0	0.0		
0.2	0.5	0.1	0.0	
0.5	1.0	0.2	0.2	0.0
0.4	0.5	0.1		

$J_2$

0.0				
0.0				
0.0				
0.1				
0.3	0.1	0.0		
0.2	0.8	0.5	0.1	
0.2	1.0	0.8	0.1	0.0
0.1	0.5	0.7		

$J_3$

0.0				
0.0				
0.0				
0.0	0.0			
0.0	0.0	0.0		
0.0	1.0	0.0	0.0	0.0
0.0	0.0	0.0		

$J_1$

0.0					
0.0					
0.0					
0.0					
0.1					
0.0	0.4	0.0	0.0		
0.2	0.5	0.2	0.0		
0.5	1.0	0.5	0.4	0.1	0.0
0.2	0.5	0.2	0.0		

$J_2$

0.0					
0.0					
0.0					
0.0					
0.1	0.2	0.1	0.0		
0.4	0.6	0.4	0.1		
0.6	1.0	0.6	0.2	0.0	0.0
0.4	0.6	0.4	0.1		

$J_3$

0.0					
0.0					
0.0					
0.0	0.0	0.0			
0.0	0.0	0.0	0.0		
0.0	1.0	0.0	0.0	0.0	0.0
0.0	0.0	0.0	0.0		

TT2'

$J_1$

0.0				
0.0				
0.0				
0.0				
0.3				
0.7	0.0	0.0		
0.2	0.5	0.1	0.0	
0.5	1.0	0.2	0.2	0.0
0.3	0.6	0.1		

$J_2$

0.0				
0.0				
0.0				
0.1				
0.3	0.1	0.0		
0.2	0.8	0.6	0.1	
0.2	1.0	0.8	0.2	0.0
0.1	0.5	0.7		

$J_3$

0.0				
0.0				
0.0				
0.0	0.0			
0.0	0.0	0.0		
0.0	1.0	0.0	0.0	0.0
0.0	0.0	0.0		

$J_1$

0.0					
0.0					
0.0					
0.0					
0.1					
0.0	0.4	0.0	0.0		
0.2	0.5	0.2	0.0		
0.5	1.0	0.5	0.4	0.1	0.0
0.2	0.5	0.2	0.0		

$J_2$

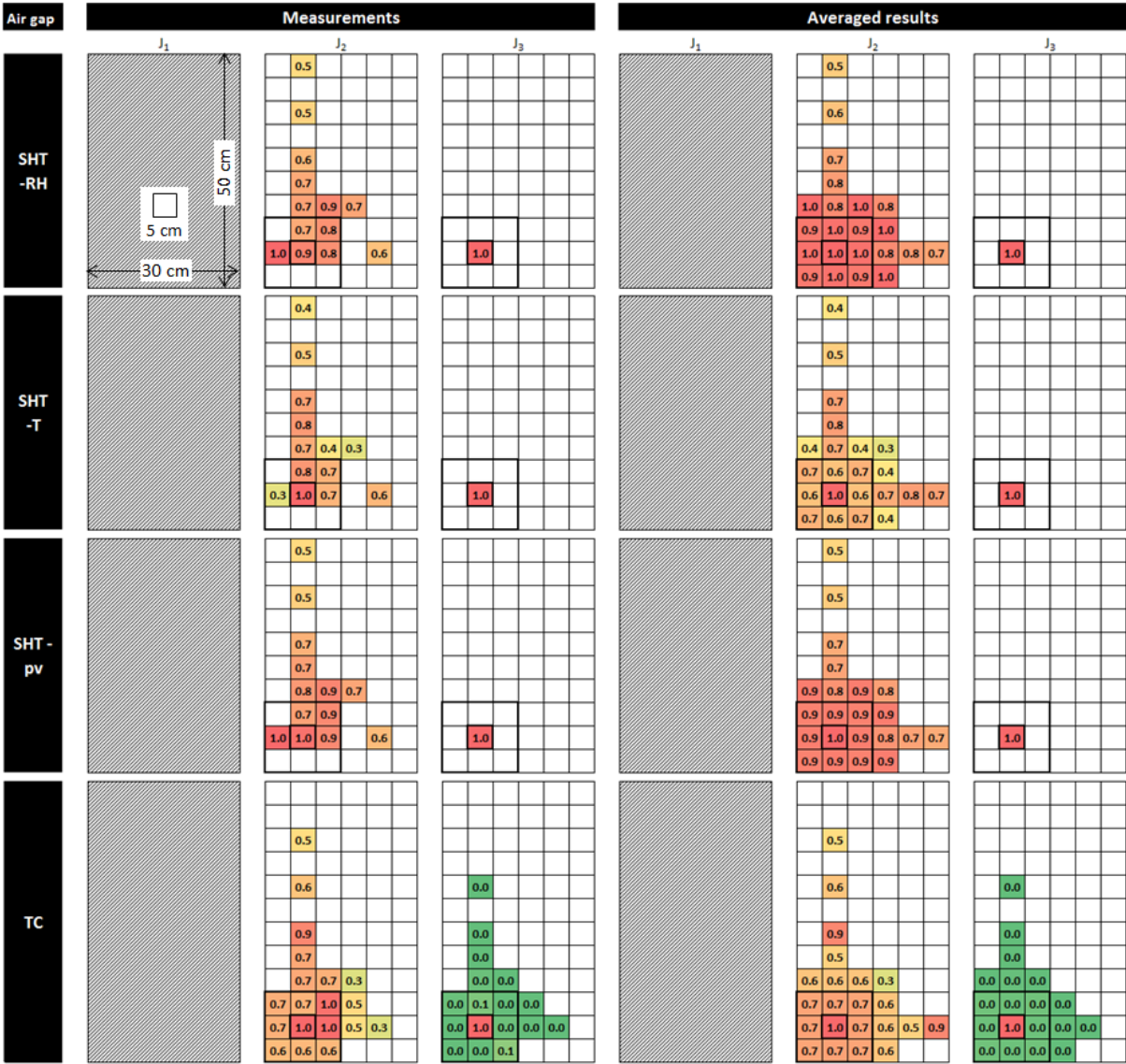
0.0					
0.0					
0.0					
0.0					
0.1	0.2	0.1	0.0		
0.4	0.6	0.4	0.1		
0.6	1.0	0.6	0.2	0.0	0.0
0.4	0.6	0.4	0.1		

$J_3$

0.0					
0.0					
0.0					
0.0	0.0	0.0			
0.0	0.0	0.0	0.0		
0.0	1.0	0.0	0.0	0.0	0.0
0.0	0.0	0.0	0.0		



### K. Full results of the 3-D relative humidity sensors grid tests











Without glue

### Measurements

A<sub>1</sub>

		0.00			
		0.01			0.00
		0.03		0.01	
		0.14	0.12	0.08	
0.42	0.43	0.28	0.11	0.03	
0.64	1.00	0.37	0.17	0.07	0.01
0.57	0.51	0.36			

A<sub>2</sub>

		0.01			
		0.08	0.04	0.01	
0.19	0.34	0.14	0.03	0.01	
0.53	1.00	0.58	0.11	0.01	
0.39	0.77	0.24			

B<sub>1</sub>

		0.06			
		0.15	0.04		
0.25	0.52	0.22	0.02		
0.46	1.00	0.41	0.08	0.01	
0.24	0.56	0.30			

B<sub>2</sub>

0.08	0.21	0.00			
0.13	1.00	0.08			
0.00	0.16	0.00			

### Averaged results

A<sub>1</sub>

		0.00			
		0.01			0.00
		0.03	0.05	0.03	0.01
		0.11	0.15	0.11	0.08
0.41	0.49	0.41	0.11	0.03	
0.49	1.00	0.49	0.15	0.05	0.01
0.41	0.49	0.41	0.11	0.03	

A<sub>2</sub>

		0.01	0.01	0.01	
		0.04	0.10	0.04	0.01
0.24	0.56	0.24	0.04	0.01	
0.56	1.00	0.56	0.10	0.01	
0.24	0.56	0.24	0.04	0.01	

B<sub>1</sub>

		0.04			
		0.03	0.12	0.03	
0.25	0.49	0.25	0.03		
0.49	1.00	0.49	0.12	0.04	
0.25	0.49	0.25	0.03		

B<sub>2</sub>

0.02	0.14	0.02			
0.14	1.00	0.14			
0.02	0.14	0.02			

With glue

**Measurements**

A<sub>1</sub>

		0.00				
		0.00				
		0.04			0.00	
		0.12	0.04	0.01		
0.31	0.50	0.23	0.05	0.00		
0.28	1.00	0.16	0.04	0.01	0.00	
0.10	0.13	0.10				

A<sub>2</sub>

		0.00				
		0.02				
		0.16	0.08	0.05		
0.37	0.49	0.39	0.07	0.04		
0.57	1.00	0.40	0.06	0.00		
0.13	0.30	0.12				

B<sub>1</sub>

		0.01				
		0.13	0.07	0.03		
0.44	0.65	0.26	0.07			
0.50	1.00	0.75	0.20			
0.35	0.50	0.23				

B<sub>2</sub>

		0.18				
0.24	0.67	0.22				
0.16	1.00	0.36	0.03			
0.11	0.18	0.22				

**Averaged results**

A<sub>1</sub>

		0.00				
		0.00				
		0.00	0.02	0.00		0.00
		0.04	0.08	0.04	0.01	
		0.19	0.27	0.19	0.04	0.00
0.27	1.00	0.27	0.08	0.02	0.00	
0.19	0.27	0.19	0.04	0.00		

A<sub>2</sub>

		0.00				
		0.04	0.01	0.04		
		0.08	0.11	0.08	0.05	
		0.25	0.44	0.25	0.08	0.04
0.44	1.00	0.44	0.11	0.01		
0.25	0.44	0.25	0.08	0.04		

B<sub>1</sub>

		0.00				
		0.07	0.16	0.07		
0.32	0.60	0.32	0.07			
0.60	1.00	0.60	0.16	0.00		
0.32	0.60	0.32	0.07			

B<sub>2</sub>

0.20	0.34	0.20				
0.34	1.00	0.34				
0.20	0.34	0.20				

